Acoustic streaming in microchannels

The trinity of analytics, numerics and experiments

Tribler, Peter Muller

Publication date:
2015

Document Version
Publisher's PDF, also known as Version of record

DTU Physics
Department of Physics

Acoustic streaming in microchannels

The trinity of analytics, numerics and experiments

Peter Muller Tribler

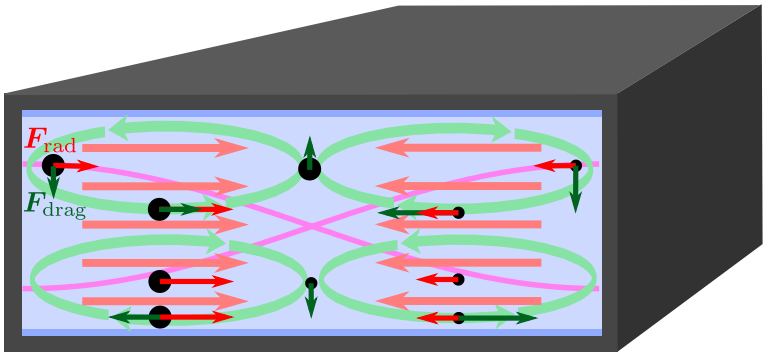

PhD thesis, 10 September 2015

Advised by Professor Henrik Bruus

Cover illustration: Illustration of forces on particles suspended in a microchannel supporting a standing acoustic wave.

Acoustic streaming in microchannels — The trinity of analytics, numerics, and experiments

Email contact: peter.muller.tribler@gmail.com
Typeset using LaTeX and MATLAB

http://www.fysik.dtu.dk/microfluidics

Til min hustru Line,
for altid og evigt.

Abstract

This thesis presents studies of boundary-driven acoustic streaming in microfluidic channels, which is a steady flow of the fluid initiated by the interactions of an oscillating acoustic standing wave and the rigid walls of the microchannel. The studies present analysis of the acoustic resonance, the acoustic streaming flow, and the forces on suspended microparticles. The work is motivated by the application of particle focusing by acoustic radiation forces in medical, environmental and food sciences. Here acoustic streaming is most often unwanted, because it limits the focusability of particles smaller than a given critical size. One of the main goals of this thesis work has been to overcome this limitation.

The main text of this thesis serves to give an introduction to the theory and numerical models applied in the five journal papers supplied in the Appendixes, which constitute this thesis work.

Based on first- and second-order perturbation theory, assuming small acoustic amplitudes, we derived the time-dependent governing equations under adiabatic conditions. The adiabatic first- and second-order equations are solved analytically for the acoustic field between two orthogonally oscillating plates. Furthermore, under general thermodynamic conditions, we derive the time-dependent first- and second-order equations for the conservation of mass, momentum, and energy. The coupling from fluid equations to particle motion is achieved through the expressions for the streaming-induced drag force and the acoustic radiation force acting on particles suspended in the fluid. Lastly, the numerical method is discussed, with emphasis on how proper numerical convergence is ensured.

Three numerical studies are presented, in which the acoustic resonance and the acoustic streaming flow are investigated, both in the transient regime and in the purely periodic state. The solutions for the periodic acoustic resonance and the steady streaming flow are used to simulate the motion of suspended particle in a Lagrangian description, which mimics experimental particle tracking velocimetry.

In the forth study, the numerical model is used to engineer a single roll streaming flow, which does not counteract the focusing by the acoustic radiation force, contrary to the usual quadrupolar streaming flow. The single roll streaming flow is observed experimentally in a nearly-square channel, and acoustophoretic focusing of E. coli bacteria and 0.6 µm particles is achieved. These particles are considerably smaller than the critical particle size of approximately 2 µm for the usual half-wavelength resonance in a rectangular channel.

The fifth study presents a quantitative comparison of analytical, numerical, and experimental results for the streaming-induced drag force dominated motion of particles suspended in a water-filled microchannel supporting a transverse half-wavelength reso-

nance. The experimental and theoretical results agree within a mean relative difference of approximately 20%, a low deviation given state-of-the-art in the field. Furthermore, the analytical solution for the acoustic streaming in rectangular channels with arbitrary large height-to-width ratios is derived. This accommodates the analytical theory of acoustic streaming to applications within acoustofluidics.

Resumé

Afhandlingen *Acoustic streaming in microchannels – The trinity of analytics, numerics, and experiments*, *Akustisk strømning i mikrokanaler – Treenigheden bestående af analytisk, numerisk og eksperimentiel analyse* beskriver et studie af væske- og partikkelbevægelse forårsaget af lydbølger i en mikrokanal.

Bevægelse af partikler ved brug af lyd kaldes akustoforese. En lydbølge påvirker en partikel i en væske direkte og indirekte. Den direkte påvirkning sker ved at lydbølgen spredes på partiklen, hvis partiklen og væsken har forskellig massetæthed eller sammentrykkelighed. Partiklen vil heraf opleve en kraftpåvirkning kaldet den akustiske strålingskraft. Den indirekte påvirkning sker ved at lydbølgen dæmpes på sin vej gennem væsken, hvilket skaber en strømning i væsken kaldet den akustiske strømning. Den akustiske strømning trækker partiklerne i væsken med sig, og derved påvirker lydbølgen indirekte partiklerne med en trækkraft. Strålingskraften og trækkraften afhænger på forskellig vis af partiklens størrelse, sådan at store partikler primært bliver påvirket af strålingskraften og små partikler primært bliver påvirket af trækkraften.

Akustoforese er interessant fordi man kan anvende strålingskraften til at flytte rundt på partikler, såsom biologiske celler og bakterier, på kontrolleret vis. Dette gøres i praksis ved at have en opløsning af celler i vand som flyder igennem en meget smal kanal, hvis bredde svarer til tykkelsen af et menneskehår. Kanalen er ætset i en silicium plade, hvortil der kan tilsluttes væskeslanger. Pladen med væskekanalen placeres ovenpå en vibrator, hvorved der skabes lydbøger i væskekanalen. Strålingskraften skubber cellerne ind mod midten af kanalen, hvorved cellerne kan koncentreres eller forskellige celler kan skilles fra hinanden på baggrund af deres massetæthed og sammentrykkelighed. Trækkraften derimod får cellerne til at cirkulere rundt i kanalen og modvirker derved strålingskraften, særligt for små celler. Det er interessant at forstå fysikken bag den akustiske strømning, så man kan undgå eller mindske trækkraftens indflydelse på bevægelsen af cellerne.

Denne afhandling præsenterer en computermodel til beregning af den lydbølge, der opbygges i en væskekanal som følge af en vibration af kanalens vægge, samt den resulterende strålingskraft og trækkraft på partikler i væsken. Modellen kan forudsige partiklers bevægelse i kanalen, og dens resultater viser god overensstemmelse med de i afhandlingen præsenterede eksperimentelle målinger.

Gennem teoretiske beregninger og eksperimentelle målinger demonstreres hvordan der i en kvadratisk væske kanal, ved et bestemt valg af lydbølgens frekvens, kan opnås en væskestrømning der ikke modarbejder den akustiske strålingskraft. Herved skabes der mulighed for at kontrollere bevægelsen af små partikler, som hidtil ikke var muligt. Dette er bl.a.

interessant i forhold til måling af små bakterier i drikkevand.

Computermodellen og den i afhandlingen præsenterede teoretiske analyse af akustoforese systemer udgør et vigtigt redskab til udvikling af fremtidige anvendelser af akustoforese.

Preface

This thesis is submitted as partial fulfillment for obtaining the degree of Doctor of Philosophy (PhD) at the Technical University of Denmark (DTU). The PhD project was financed by the Danish Council for Independent Research, Technology and Production Sciences, Grant No. 11-107021. The project was carried out at the Department of Physics, DTU Physics, as a member of the Theoretical Microfluidics Group (TMF) during a three-year and five month period from April 2012 to September 2015. The project was supervised by Professor Henrik Bruus, leader of the TMF group at DTU Physics. During all three project years I have made short visits to the lab of Professor Thomas Laurell at Lund University, Sweden, where the experiments for two of the papers in this thesis have been performed.

I would like to thank the following people:
My supervisor Henrik Bruus, for teaching me some humility during our first supervisor meetings, which any straight-A student needs once in a while, for giving me the opportunity to experience the joys of being a PhD-student, and for teaching me what good and thorough physics is.

The people at Bläcklabbet, especially Thomas, Per, Maria, and Pelle, for good discussions and Swedish food. The researchers in the acoustofluidic community for great conference memories, discussions and motivation to provide theoretical insight. Current and former members of the TMF group: Christoffer, Jonas, Mikkel, Rayisa, Fabio, Søren, Mathias and Rune, for good discussions and moose adventures. My collaborators Alvaro, Massimiliano, Per and Rune, for giving me the opportunity to join their great physics quest to make a quantitative theoretical-experimental comparison of the acoustic streaming flow. Comsol Mads for insightful discussions during and after our collaboration, and a vital source of information to what goes on inside the stomach of Comsol.

My friend and collaborator Per Augustsson for teaching me the best of Swedish irony, for never using smileys, and for giving me constructive feedback on the thesis. My friend and former colleague Rune Barnkob, for welcoming me into the TMF group and the world of acoustofludics, for influencing me with his fascination of physics, for always being a positive soul and a bundle of joy, and for great hugs.

My friends in Homogrotten for boardgaming and challenging my memory of the fundamentals of physics through experiments with liquid substances. My family for support and hygge. My children Aske and Ronja for being the best distraction from the world of theoretical physics. My lovely wife Line for reminding me that any inconsistency is prob-

ably due to a sign error, for challenging my ability to explain my work to a non-physicist, and for reminding me that there are other important things in life than physics.

Ringsted, 10 September 2015

Peter Muller Tribler

Table of Contents

List of Figures

List of symbols

Symbol	Description	Unit
$\mathbf{1}$	Unit matrix	
a	Microparticle radius	m
a_c	Critical particle radius	m
A	Area	m^2
c_s	Isentropic speed of sound	$\mathrm{m\,s^{-1}}$
$C\,(g)$	Numerical convergence parameter	
c_p	Specific heat capacity at constant pressure	$\mathrm{J\,kg^{-1}\,K^{-1}}$
c_V	Specific heat capacity at constant volume	$\mathrm{J\,kg^{-1}\,K^{-1}}$
$\mathbf{e}_i$	Unit vector in the direction $i = x, y, z$	
E_ac	Acoustic energy density	Pa
f	Frequency	$\mathrm{s^{-1}}$
f_res	Resonance frequency	$\mathrm{s^{-1}}$
Δf	Resonance full width at half maximum	$\mathrm{s^{-1}}$
f_0, f_1	Acoustic scattering coefficients	
$\boldsymbol{F}^\mathrm{drag}$	Viscous Stokes drag force	N
$\boldsymbol{F}^\mathrm{rad}$	Acoustic radiation force	N
g	Gibbs free energy per unit mass	$\mathrm{J\,kg^{-1}}$
g	General field	
g_ref	Numerical reference solution	
i	Unit imaginary number	
$k_0 = \frac{2\pi}{\lambda} = \frac{\omega}{c}$	Undamped acoustic wavenumber	$\mathrm{m^{-1}}$
k	Damped acoustic wavenumber	$\mathrm{m^{-1}}$
k^th	Thermal conductivity	$\mathrm{W\,m^{-1}\,K^{-1}}$
l, w, h	Microchannel length, width, and height	m
m	Mass	kg
$\boldsymbol{n}$	Outward-pointing normal vector	
p	Pressure	Pa
$Q = \frac{f_\mathrm{res}}{\Delta f}$	Resonance quality factor	
s	Entropy per unit mass	$\mathrm{J\,K^{-1}\,kg^{-1}}$
t	Time	s
$t_0 = \frac{1}{f}$	Oscillation period	s

Symbol	Description	Unit
T	Temperature	K
$\boldsymbol{u}$	Acoustophoretic particle velocity	$\mathrm{m\,s^{-1}}$
$\boldsymbol{v}$	Fluid velocity vector	$\mathrm{m\,s^{-1}}$
v	Fluid velocity magnitude	$\mathrm{m\,s^{-1}}$
$\boldsymbol{v}^{\mathrm{ext}}$	Velocity vector of external flow	$\mathrm{m\,s^{-1}}$
v_{bc}	Amplitude of oscillatory boundary velocity	$\mathrm{m\,s^{-1}}$
V	Volume	$\mathrm{m^3}$
(x, y, z)	Cartesian coordinates	m
α_p	Isobaric thermal expansion	$\mathrm{K^{-1}}$
δ_{s}	Viscous boundary layer thickness	m
δ_{t}	Thermal boundary layer thickness	m
ε	Internal energy per unit mass	$\mathrm{J\,kg^{-1}}$
η	Dynamic viscosity	$\mathrm{Pa\,s}$
η^{b}	Bulk viscosity	$\mathrm{Pa\,s}$
$\gamma = c_p/c_v$	Ratio of specific heat capacities	
Γ	Viscous damping factor, 1D wave	
Γ'	Viscous damping factor, general	
κ_T	Isothermal compressibility	$\mathrm{Pa^{-1}}$
κ_s	Isentropic compressibility	$\mathrm{Pa^{-1}}$
λ	Acoustic wavelength	m
$\omega = 2\pi f$	Angular frequency	$\mathrm{s^{-1}}$
Ω	Domain	
$\partial\Omega$	Domain boundary	
Φ	Acoustic contrast factor in 1D $\boldsymbol{F}^{\mathrm{rad}}$	
Ψ	Acoustic streaming prefactor	
ψ_n	n'th basis function	
ρ	Mass density	$\mathrm{kg\,m^{-3}}$
$\boldsymbol{\sigma} = \boldsymbol{\tau} - p\,\mathbf{1}$	Stress tensor	Pa
$\boldsymbol{\sigma}^{\mathrm{ext}}$	Stress tensor of external flow	Pa
$\boldsymbol{\tau}$	Viscous stress tensor	Pa
∂_i	Partial derivative with respect to $i = x, y, z$	$\mathrm{m^{-1}}$
∂_t	Partial derivative with respect to time	$\mathrm{s^{-1}}$
$\mathrm{d}\square$	Infinitesimal change in $\square$	
$\square^*$	Complex conjugate of $\square$	
$\square_a$	Bulk amplitude of first-order field $\square$	
$\square_i$	i'th component of $\square$, $i = x, y, z$	
$\square_0, \square_1, \square_2$	0th-, 1st-, and 2nd-order perturbations of $\square$	
$\square_{\mathrm{in}}$	Incident acoustic field	
$\lvert\square\rvert$	Order of magnitude of $\square$	
$\sim$	Similar order of magnitude	
$\langle\square\rangle = \frac{1}{t_0}\int_{t-t_0/2}^{t+t_0/2}\square\,\mathrm{d}t,$	Time average of $\square$	

Symbol	Description	Unit
$(\square)^{2\omega}$	Oscillatory second-order field component	
$(\square)^{0}$	Steady second-order field component	
$\mathrm{Re}\,(\square)$	Real part of $\square$	
$\mathrm{Im}\,(\square)$	Imaginary part of $\square$	
$\mathcal{O}(\square)$	Remainder of relative order of magnitude $\square$	
$\boldsymbol{\nabla}$	Gradient vector operator	m^{-1}
$\boldsymbol{\nabla}\cdot$	Divergence scalar operator	m^{-1}
$\boldsymbol{\nabla}\times$	Rotation vector operator	m^{-1}
∇^2	Laplacian scalar operator	m^{-2}

Chapter 1

Introduction

This chapter presents a short description of the physical phenomena treated in this thesis along with a historic review of the development of the theoretical framework. It is a selection of studies that I find important for the basis and context of my thesis work, and by no means an exhaustive treatment. For a wider scope, the reader is referred to the tutorial series on acoustofluidics in Lab on a Chip [1] and the review article by Riley [2].

1.1 Acoustic streaming

Acoustic streaming is a steady fluid flow generated by an oscillating acoustic field. The magnitude of the steady streaming flow is usually much smaller than the amplitude of the oscillating velocity field. Acoustic streaming can be categorized by its generating mechanism into bulk-driven streaming and boundary-driven streaming, both illustrated in Fig. 1.1. Bulk-driven streaming originates from the bulk absorption of acoustic momentum, which result in a steady velocity in the direction of propagation of the acoustic wave. This is observed for traveling acoustic waves in configurations where the spatial dimension of the fluid domain is comparable to or longer than the absorption length of the acoustic wave. Boundary-driven streaming originates from the viscous stresses present in a thin region close to boundaries, known as the acoustic boundary layer, where the amplitude of the acoustic velocity oscillations has to transition from its bulk value to zero at the wall. Due to nonlinearity, the viscous stresses inside the acoustic boundary layer generate a steady velocity parallel to the wall, which drives a steady flow in the bulk of the fluid. The spatial periodicity of the steady velocity is twice that of the acoustic wave. For a rectangular channel cross section with a standing wave parallel to the top and bottom walls, as sketched in Fig. 1.1(b), we thus get four bulk flow rolls for each half acoustic wavelength. Bulk-driven streaming is also referred to as Eckart streaming, whereas boundary-driven streaming is also referred to as Rayleigh streaming in the bulk of the fluid and Schlichting streaming inside the boundary layers. In this thesis, only boundary-driven streaming is studied. Bulk absorption is included in the theoretical models, but it has a negligible effect, because the length scales of the fluid domains are much shorter than the absorption length.

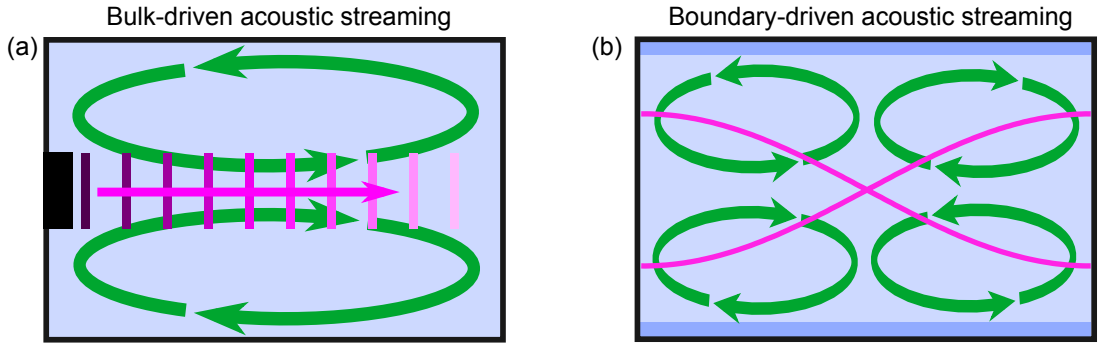

Figure 1.1: (a) Sketch of bulk-driven acoustic streaming in a rectangular fluid chamber. The acoustic traveling wave (magenta) is generated by the vibrating transducer (black filled rectangle to the left) and absorbed in the fluid (blue). The absorption of acoustic momentum leads to a force on the fluid in the direction of propagation of the acoustic wave, generating a steady flow (green arrows) in the fluid chamber. This type of streaming is also referred to as Eckart streaming. (b) Sketch of boundary-driven acoustic streaming in the vertical cross section of a microchannel. The magenta lines represent a standing acoustic wave, with a pressure node in the center of the channel and pressure anti-nodes at the sidewalls. The non-linear interactions of the oscillating acoustic wave inside the boundary layers (dark blue) generate a steady rotational flow (green arrows) in the bulk of the fluid (light blue). This type of streaming is also referred to as Rayleigh streaming.

1.2 Acoustophoresis

Particles in an acoustic wave experience a force due to scattering of the acoustic wave on the particle, known as the acoustic radiation force $\boldsymbol{F}_{\text{rad}}$. In the case of a standing acoustic wave, the radiation force pushes "acoustically hard" particles towards the nodal points of the pressure oscillations, whereas "acoustically soft" particles are pushed towards the antinodal points. The "hardness" of a particle is determined by the relative density and compressibility of the particle and the suspending fluid. By default we assume the particles to be hard and focused at the pressure node, which is the case for most relevant particles and biological cells. Furthermore, besides gravitation and buoyancy, which we will disregard, the particles also experience a drag force $\boldsymbol{F}_{\text{drag}}$ from the acoustic streaming flow generated by the acoustic wave. The relative magnitude of the drag force and the radiation force depends largely on the particle size. The motion of large particles are dominated by the radiation force and focused at the pressure node, whereas small particles are dominated by the streaming-induced drag force and follow the rotational motion of the streaming flow. This is sketched in Fig. 1.2, where the directions and relative magnitudes of the drag force and the radiation force are shown on a large and a small particle in a standing acoustic wave.

1.3 Historic review

The theory of acoustic streaming was initially developed by Lord Rayleigh in 1884 [3], inspired by the observations of particle motion generated by a standing sound wave in

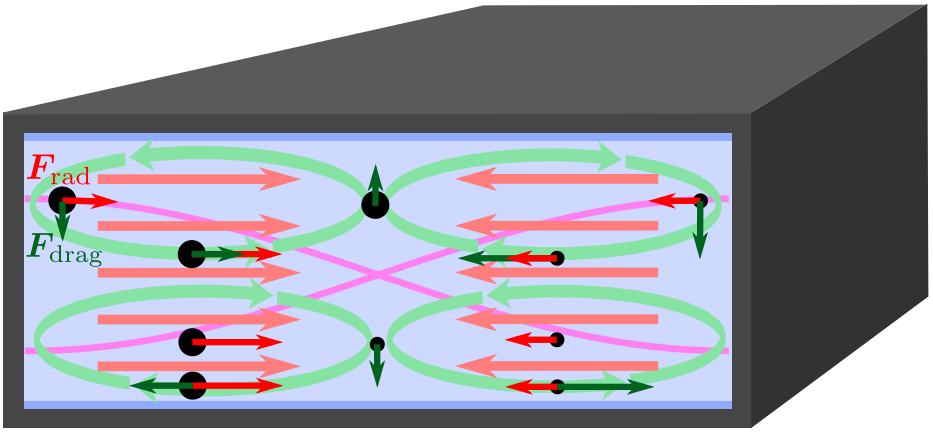

Figure 1.2: Forces on particles in a standing acoustic wave. F_{drag} is the drag force (dark green arrows) on the particle induced by the generated acoustic streaming flow (light green arrows), and F_{rad} is the acoustic radiation force (dark red arrows) induced by the scattering of the acoustic wave on the particle. The light red arrows indicate the directionality of the radiation force, working to focus the particles at the node of the standing pressure wave (magenta lines). In the left half of the channel examples of a large particle are shown, and in the right side of the channel examples of a small particle are shown. The two arrows on each particle indicate the relative magnitude of the two forces on that particle. The length of the arrows are scaled differently on the large and the small particles.

a gasfilled tube, known as Kundt's tube, by Kundt in 1866 [4]. Lord Rayleigh derived the framework for how a standing sound wave parallel to a wall can generate a steady streaming flow. In 1932 Sclichting [5] revised Rayleigh's theory and described the presence of flow rolls inside the boundary layer, which where responsible for driving the bulk flow. Nyborg presented in 1958 [6] a general treatment of the steady velocity generated along an arbitrary smooth wall, thus not limited to a planar wall, in terms of the bulk acoustic amplitude near the wall and the curvature of the wall. This theory was applicable to a wide range of streaming phenomena, and was later extended by Lee and Wang in 1989 [7] and by Rednikov and Sadhal in 2011 [8], and was referred to as the limiting velocity method.

The viscosity of the fluid plays a key role in the generation of acoustic streaming. Since the viscosity is dependent on the thermodynamic state of the fluid it will be slightly perturbed by the acoustic density and temperature oscillations, and in studies by Hamilton *et al.* [9] and Rednikov and Sadhal [8], this was shown to have significant influence on the magnitude of the acoustic streaming.

Lord Rayleigh's treatment of the boundary-driven acoustic streaming in a parallel plate channel is only valid for channels where the height of the channel h is much larger than the boundary layer thickness δ and much smaller than the acoustic wavelength λ, *i.e.* $\delta \ll h \ll \lambda$. These limitation of the theory was later solved when new applications of standing acoustic waves presented a need for it. Hamilton *et al.* [10] derived the solution for arbitrarily thin channels $\delta \sim h \ll \lambda$, relevant for applications within thermoacoustic engines, whereas Muller *et al.* [11] Appendix B derived the solution for arbitrarily tall channels $\delta \ll h \sim \lambda$, relevant for applications within microchannel acoustophoresis.

The acoustic radiation force had been observed in Kundt's tube in the nineteenth century but was not explained theoretically until 1934 by King [12]. The particle agglomeration at pressure nodes was similar to the observed agglomeration of particle on vibrating Cladni plates, at the points of least vibration. King's treatment was limited to an incompressible spherical particle in an inviscid fluid, and this was later extended to a compressible particle in an inviscid fluid by Yosioka and Kawasima [13] and Gorkov [14]. The effect of the viscous and thermal boundary layers around the particle was included in the theory by Settnes and Bruus [15], respectively, Karlsen and Bruus [16].

1.4 Acoustofluidics

The term acoustofludics refer to applications of acoustic pressure fields in microfluidic systems [17] and spans a wide range of applications involving manipulation of fluids and suspended particles, such as cell enrichment [18], separation of fat particles from blood [19], raw milk quality control [20], particle trapping using seed particles [21], mixing of cells and nutrients in multi-well plates [22], and acoustofluidic pumping using sharp channel edges [23]. A great effort has also been put into making experimental tools and measurements to test the theoretical hypotheses, such as investigation of channel resonances and radiation force dominated particle motion [24, 25], measurements of streaming dominated particle motion [26, 11], and direct measurements of acoustophoretic forces on particles using opti-

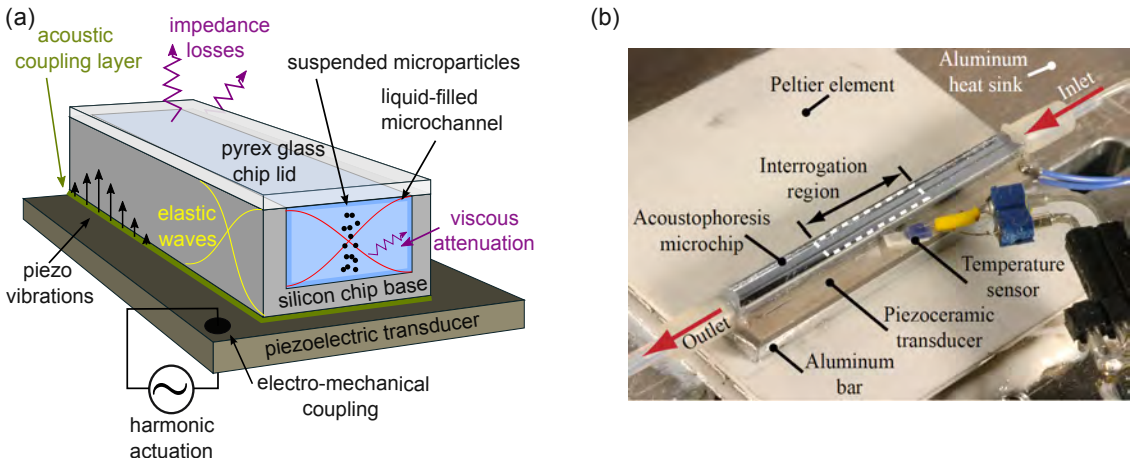

Figure 1.3: (a) Sketch of an acoustophoresis microchip, adopted from the PhD-thesis by Rune Barnkob Ref. [32]. (b) Image of an acoustophoresis microchip, adopted from Augustsson *et al.* Ref. [25].

cal trapping [27]. Figure 1.3 shows a sketch and an image of an acoustophoresis chip with a long straight microchannel with a rectangular cross section. This is the channel we have been modeling in the theoretical work presented in Refs. [28, 11, 29, 30] Appendixes A, B, D, and E, and this chip was used for the experimental study in Ref. [11] Appendix B. In Ref. [31] Appendix C a microchannel with a nearly-square cross section was used.

There are two approaches to numerical modeling of acoustic streaming in microchannels. (i) The boundary layer approach, in which the acoustic boundary layers are resolved and the acoustic fields and streaming flow are solved directly from the governing equations and a set of physical boundary conditions. (ii) The effective slip velocity approach, in which the acoustic boundary layers are not resolved, but instead the analytical effective slip velocity expression is used for the boundary condition for the streaming flow. The advantages of the boundary layer approach is that it correctly predicts the acoustic damping and gives insight into the physics of the acoustic boundary layer and the generation of the acoustic streaming flow. The effective slip velocity approach, on the other hand, requires much less computational effort and thus allows for analysis of streaming flows in more complicated three-dimensional systems.

The boundary layer approach was employed by Muller *et al.* to study the boundary layers of the the acoustic fields and the cross-over between radiation force and streaming-induced drag force dominated particle motion [28] Appendix A, the influence of viscosity perturbation on the acoustic streaming and transport of thermal energy in acoustophoresis systems [29] Appendix D, as well as the time-dependent build-up of the acoustic resonance and the streaming flow [30] Appendix E, all for bulk acoustic wave generation in a silicon-glass microfluidic chip. A similar study was done by Nama *et al.* [33], in which the acoustic resonance and particle motion was studied for a PDMS channel exited by surface acoustic waves.

The effective slip velocity approach has successfully been employed by Lei *et al.* [34, 35] to study the acoustic streaming in three-dimensional problems and streaming flows in the

pressure nodal plane. This is relevant for experimental applications, such as acoustic trapping [21], and they explained the puzzling streaming pattern observed in a flat microfluidic chamber by Hagsäter *et al.* [36].

To develop an approach that avoids the computational expensive resolution of the boundary layers but still predict the correct acoustic loss, Hahn *et al.* [37] developed a numerical model which utilizes analytical analysis of the boundary layer stresses and other loss mechanisms, and employ these loss factors in an artificial bulk damping factor. This results in a computational efficient model that correctly predicts the amplitude of the resonant acoustic field. Such a method was also employed by Hahn *et al.* [38] to make an optimization scheme that maximizes the amount of acoustic energy in a microfluidic chamber with respect to the geometrical dimensions of the chip and position of the piezo transducer.

1.5 Outline of the thesis

This thesis deals with the theory of fluid dynamics, acoustics, and thermodynamics. There are many good textbooks on these topics of which I can recommend; *Theoretical Microfluidics* by Henrik Bruus [17], *Course of Theoretical Physics* volume 5 *Statistical Physics* and volume 6 *Fluid Mechanics* by Landau and Lifshitz[39, 40]. For this thesis I wanted to give a presentation of the theory of acoustic streaming, and I have divided this into two chapters.

Chapter 2 is meant as an introduction to students not familiar with acoustics and thermodynamics. The topics of acoustic resonances and acoustic streaming are treated within the adiabatic acoustic theory, which simplifies the problem while still containing the fundamental parts of the theory. The problem of the acoustic wave between two orthogonally oscillating parallel plates are thoroughly treated, including derivations of the oscillating first-order velocity, the time-averaged second-order velocity, and the oscillating second-order velocity, for which the latter has not been treated before in the literature.

Chapter 3 treats the full thermodynamic theory in a rigorous way. It includes the thermodynamic relations, perturbations in material parameters due to the acoustic perturbations of the thermodynamic state, and governing equations for the second-order temperature perturbation. The theory is discussed through dimensional analysis of the governing equations, to estimate the orders of magnitude of the acoustic fields and the acoustic streaming flow, and to evaluate the error done by the adiabatic approximation. Furthermore, the possible ambiguity of the combination of linear thermodynamic relations and second-order perturbation theory is discussed.

Chapter 4 outlines the analytical framework for the calculation of the forces exerted on suspended particles by the scattering of the acoustic wave and the drag from the acoustic steaming flow.

Chapter 5 gives a brief introduction to the numerical methods applied in the studies of this thesis. The finite element method and the implementation of the governing equations are described, including a practical example. The spatial and temporal resolutions are discussed, with emphasis on how proper numerical convergence is ensured.

Chapter 6 presents an extended conclusion on this thesis work by summarizing the main results of the five journal papers and discussing their relations to each other and to the field of acoustofluidics.

Chapter 7 presents an outlook on the future opportunities and challenges in the field of acoustofluidics along the path of this thesis work.

1.6 Publications

This PhD-thesis is based on the work published in the following five peer-reviewed journal papers, all presented in their original form in the Appendixes A-E. The results and discussions of the papers are not reproduced in the main chapters of this thesis, only the main results of the papers are summarized in Chapter 6. The work has been presented in 18 contributions at international conferences (of which 12 involved peer-review) in the form of 13 talks and 5 posters.

1. P. B. Muller, R. Barnkob, M. J. H. Jensen, and H. Bruus. *A numerical study of microparticle acoustophoresis driven by acoustic radiation forces and streaming-induced drag forces.* Lab Chip **12**, 4617–4627 (2012). Enclosed in Appendix A.

2. P. B. Muller, M. Rossi, A. G. Marin, R. Barnkob, P. Augustsson, T. Laurell, C. J. Kähler, and H. Bruus. *Ultrasound-induced acoustophoretic motion of microparticles in three dimensions.* Phys Rev E **88**, 023006 (2013). Enclosed in Appendix B.

3. M. Antfolk, P. B. Muller, P. Augustsson, H. Bruus, and T. Laurell. *Focusing of submicrometer particles and bacteria enabled by two-dimensional acoustophoresis.* Lab Chip **14**, 2791 (2014). Enclosed in Appendix C.

4. P. B. Muller and H. Bruus. *Numerical study of thermoviscous effects in ultrasound-induced acoustic streaming in microchannels.* Phys Rev E **90**, 043016 (2014). Enclosed in Appendix D.

5. P. B. Muller and H. Bruus. *A theoretical study of time-dependent, ultrasound-induced acoustic streaming in microchannels.* Phys Rev E (submitted September 2015). Enclosed in Appendix E.

Chapter 2

Adiabatic theory

In this chapter we treat the theory of acoustic resonances and the generated acoustic streaming using the adiabatic thermodynamic approximation. The treatment is based on the textbooks *Theoretical Microfludics* by Henrik Bruus [17], *Course of Theoretical Physics* volume 5 *Statistical Physics* and volume 6 *Fluid Mechanics* by Landau and Lifshitz[39, 40]. Part of the theory presented in this chapter is also presented in Ref. [30] Appendix E. The purpose of this chapter is to give students, not familiar with the topics of acoustic resonances and acoustic streaming, an introduction to the topic in its most simple form and with some practical examples. After deriving the governing equations, the problem of the acoustic wave between two orthogonally oscillating parallel plates is thoroughly treated, including derivations of the first-order oscillating velocity, the second-order time-averaged velocity, and the second-order oscillating velocity, for which the latter has not previously been treated in the literature. Finally, we discuss the acoustic boundary layer and its role in the generation of boundary-driven acoustic streaming.

For an adiabatic process the entropy is conserved for each part of a system [39]. Thus for every little fluid volume we consider the entropy to be constant, and consequently the temperature and pressure oscillations of the acoustic wave can be expressed solely in terms of the density oscillations, and thus we need only consider acoustic perturbations in the density ρ and the velocity $\boldsymbol{v}$.

2.1 Governing equations

Without deriving it, we will take the Navier—Stokes equation, describing the conservation of momentum, and the continuity equation, describing the conservation of mass, as our starting point,[1]

$$\rho\partial_t\boldsymbol{v} + \rho\left(\boldsymbol{v}\cdot\boldsymbol{\nabla}\right)\boldsymbol{v} = -\boldsymbol{\nabla}p + \eta\nabla^2\boldsymbol{v} + \left(\tfrac{1}{3}\eta + \eta^{\mathrm{b}}\right)\boldsymbol{\nabla}\left(\boldsymbol{\nabla}\cdot\boldsymbol{v}\right), \tag{2.1a}$$

$$\partial_t\rho = -\boldsymbol{\nabla}\cdot\left(\rho\boldsymbol{v}\right), \tag{2.1b}$$

[1] In Chapter 3 the derivations of the conservation equations for mass, momentum, and energy are presented.

where ρ is the density of the fluid, η is the shear viscosity, and η^{b} is the bulk viscosity[2]. It is inherent in the physics of acoustics that we need to consider the fluid to be compressible, thus the divergence of the velocity field is non-zero, in contrast to most basic fluid dynamic problems. This means that the density should be considered a field just as the velocity and the pressure, contrary to being just a material parameter. We also need to include the bulk viscosity, which is a material parameter related to the viscous dissipation due to compression of the fluid.

As the density is now also a field variable, the equations (2.1) contains three variables, $\boldsymbol{v}$, p, and ρ, but only two equations, thus a third equation is needed to determine the problem. This third equation is an equation of state, which should describe the state of the fluid *i.e.* an equation that relates p and ρ. One example of an equation of state is the ideal gas law, which relates the pressure, volume, and temperature of an ideal gas. For a fluid in general, it is not possible to write down an analytical equation of state, however, we can use thermodynamics to relate the changes in the thermodynamic variables for small perturbations to a known equilibrium state. These relations will be described in detail in Chapter 3, for now we will postulate the result in the case of the adiabatic approximation,

$$\frac{\mathrm{d}\rho}{\rho_0} = \kappa_s \, \mathrm{d}p. \tag{2.2}$$

This equation states that the relative change in the local density $\frac{\mathrm{d}\rho}{\rho}$ equals the change in pressure times the isentropic compressibility of the fluid κ_s, which is valid for small perturbations $\mathrm{d}\rho$ and $\mathrm{d}p$ to an equilibrium state. Equation (2.2) follows directly from the definition of the isentropic compressibility

$$\kappa_s \equiv \frac{1}{\rho_0}\left(\frac{\mathrm{d}\rho}{\mathrm{d}p}\right)_s. \tag{2.3}$$

Here the subscript s implies that the differentiation is evaluated for constant entropy $\mathrm{d}s = 0$, which is the adiabatic approximation. Since the isentropic speed of sound is defined as $c_s^2 \equiv \left(\frac{\mathrm{d}p}{\mathrm{d}\rho}\right)_s$, the isentropic compressibility can be expressed as $\kappa_s = 1/(\rho_0 c_s^2)$, and the adiabatic equation of state can thus be written in the customary form

$$\mathrm{d}p = c_s^2 \, \mathrm{d}\rho. \tag{2.4}$$

The equation of state Eq. (2.4) allows us to eliminate the pressure field from the governing equations (2.1), by substituting $\boldsymbol{\nabla} p = c_s^2 \boldsymbol{\nabla}\rho$. The Navier—Stokes equation and the continuity equation are now expressed in terms of $\boldsymbol{v}$ and ρ only,

$$\rho \partial_t \boldsymbol{v} + \rho \left(\boldsymbol{v}\cdot\boldsymbol{\nabla}\right)\boldsymbol{v} = -c_s^2 \boldsymbol{\nabla}\rho + \eta \nabla^2 \boldsymbol{v} + \left(\tfrac{1}{3}\eta + \eta^{\mathrm{b}}\right)\boldsymbol{\nabla}\left(\boldsymbol{\nabla}\cdot\boldsymbol{v}\right), \tag{2.5a}$$

$$\partial_t \rho = -\boldsymbol{\nabla}\cdot\left(\rho \boldsymbol{v}\right). \tag{2.5b}$$

These two equations describe the relation between the oscillating density and velocity fields.

[2] The bulk viscosity is sometimes referred to as the second viscosity and represented by the letter ζ [17]. Its value is often incorrectly taken to be zero, however, for water the values of η and η^{b} have the same order of magnitude.

2.2 Perturbation equations

The governing equations (2.5) are non-linear and thus complicated to solved directly. The standard approach within acoustics is to limit the theoretical treatment to cases where the acoustic amplitudes are small, *i.e.* the amplitude of the density oscillations are much smaller than the equilibrium density ρ_0. This is known as the perturbation approach. Each field g is written as

$$g = g_0 + g_1 + g_2, \tag{2.6}$$

for which $|g_2| \ll |g_1| \ll |g_0|$. The perturbation approach transforms the pair of coupled nonlinear governing equations into pairs of coupled linear equations for each order of the perturbation expansion. The homogeneous, isotropic quiescent state at thermal equilibrium is taken to be the zeroth-order state of the fluid, and thus $\boldsymbol{v}_0 = \boldsymbol{0}$,

$$\boldsymbol{v} = \boldsymbol{v}_1 + \boldsymbol{v}_2 \tag{2.7a}$$

$$\rho = \rho_0 + \rho_1 + \rho_2 \tag{2.7b}$$

2.2.1 First-order equations

Inserting the expansions Eq. (2.7) for ρ and $\boldsymbol{v}$ in the governing equations (2.5) and keeping only first-order terms yields

$$\rho_0 \partial_t \boldsymbol{v}_1 = -c_s^2 \boldsymbol{\nabla} \rho_1 + \eta \nabla^2 \boldsymbol{v}_1 + \left(\tfrac{1}{3}\eta + \eta^{\mathrm{b}}\right) \boldsymbol{\nabla} \left(\boldsymbol{\nabla} \cdot \boldsymbol{v}_1\right), \tag{2.8a}$$

$$\partial_t \rho_1 = -\rho_0 \boldsymbol{\nabla} \cdot \boldsymbol{v}_1. \tag{2.8b}$$

Usually, the acoustic fields are excited by a single-frequency vibration of the boundaries. When the system has stabilized in a steady oscillatory state, the first-order fields can be described by pure harmonics, oscillating with the excitation frequency ω. The solution can then be expressed in the frequency domain instead of the time domain, and we use the complex notation

$$g_1(\boldsymbol{r}, t) = \mathrm{Re}\left[g_1(\boldsymbol{r}) \mathrm{e}^{-\mathrm{i}\omega t}\right], \tag{2.9a}$$

$$\partial_t g_1 = -\mathrm{i}\omega g_1. \tag{2.9b}$$

Considering only the steady-state solution, the first-order equations (2.8) can be transformed from the time-domain to the frequency domain,

$$-\mathrm{i}\omega \rho_0 \boldsymbol{v}_1 = -c_s^2 \boldsymbol{\nabla} \rho_1 + \eta \nabla^2 \boldsymbol{v}_1 + \left(\tfrac{1}{3}\eta + \eta^{\mathrm{b}}\right) \boldsymbol{\nabla} \left(\boldsymbol{\nabla} \cdot \boldsymbol{v}_1\right), \tag{2.10a}$$

$$-\mathrm{i}\omega \rho_1 = -\rho_0 \boldsymbol{\nabla} \cdot \boldsymbol{v}_1. \tag{2.10b}$$

Equation (2.10) together with a set of boundary conditions constitute a steady-state first-order acoustic problem under the assumptions of adiabatic thermodynamics and single frequency vibrations of the boundaries.

2.2.2 Second-order equations

Inserting the expansions Eq. (2.7) for ρ and $\boldsymbol{v}$ in the governing equations (2.5) and keeping only second-order terms, *i.e.* second-order perturbations of single variables or products of two first-order perturbations, yields

$$\rho_0\partial_t\boldsymbol{v}_2 + \rho_1\partial_t\boldsymbol{v}_1 + \rho_0\left(\boldsymbol{v}_1\cdot\boldsymbol{\nabla}\right)\boldsymbol{v}_1 = -c_s^2\boldsymbol{\nabla}\rho_2 + \eta\nabla^2\boldsymbol{v}_2 + \left(\tfrac{1}{3}\eta+\eta^{\mathrm{b}}\right)\boldsymbol{\nabla}\left(\boldsymbol{\nabla}\cdot\boldsymbol{v}_2\right), \tag{2.11a}$$

$$\partial_t\rho_2 = -\rho_0\boldsymbol{\nabla}\cdot\boldsymbol{v}_2 - \boldsymbol{\nabla}\cdot(\rho_1\boldsymbol{v}_1). \tag{2.11b}$$

These equations for the second-order velocity and density can be further split into two sets of equation. In steady state the second-order variables consist of a steady component and an oscillatory component oscillating at 2ω, similar to the product of two sines, $\sin(\omega t)\sin(\omega t) = \frac{1}{2} - \frac{1}{2}\cos(2\omega t)$. The steady component is denoted by superscript "0" and the oscillatory second-order component is denoted by superscript "2ω",

$$g_2(\boldsymbol{r},t) = \Big(g_2(\boldsymbol{r},t)\Big)^0 + \Big(g_2(\boldsymbol{r},t)\Big)^{2\omega} = \big\langle g_2(\boldsymbol{r},t)\big\rangle + \mathrm{Re}\left(g_2^{2\omega}(\boldsymbol{r})\,\mathrm{e}^{-\mathrm{i}2\omega t}\right). \tag{2.12}$$

This decomposition is valid only when considering a steady periodic state, and it is essentially a temporal Fourier decomposition of the second-order fields. In the transient regime a continues distribution of frequency components exist, and this is treated in Ref. [30] Appendix E. $\langle g_2\rangle$ denotes time-averaging over one oscillation period $t_0 = \frac{2\pi}{\omega}$ and in steady state it equals the zero-order temporal Fourier component of the field

$$\Big(g_2(\boldsymbol{r},t)\Big)^0 = \big\langle g_2(\boldsymbol{r},t)\big\rangle = \frac{1}{t_0}\int_{t-t_0/2}^{t+t_0/2} g_2(\boldsymbol{r},t')\,\mathrm{d}t'. \tag{2.13}$$

$g_2^{2\omega}(\boldsymbol{r})$ is the complex amplitude of the secondary oscillatory mode, equivalent to $g_1(\boldsymbol{r})$ in Eq. (2.9a), and is given by the second-order Fourier component

$$g_2^{2\omega}(\boldsymbol{r}) = \frac{1}{t_0}\int_{t-t_0/2}^{t+t_0/2} g_2(\boldsymbol{r},t')\mathrm{e}^{-i2\omega t'}\,\mathrm{d}t'. \tag{2.14}$$

The real part of any complex number Z can be written as $\mathrm{Re}[Z] = \frac{1}{2}(Z+Z^*)$, where the asterisk denotes complex conjugation. The product $A(\boldsymbol{r},t)B(\boldsymbol{r},t)$ of two oscillating fields $A(\boldsymbol{r},t) = \mathrm{Re}\left[A\mathrm{e}^{-\mathrm{i}\omega t}\right]$ and $B(\boldsymbol{r},t) = \mathrm{Re}\left[B\mathrm{e}^{-\mathrm{i}\omega t}\right]$ can be decomposed into a steady component and an oscillatory component,

$$A(t)B(t) = \tfrac{1}{2}\Big(A\mathrm{e}^{-\mathrm{i}\omega t} + A^*\mathrm{e}^{\mathrm{i}\omega t}\Big)\tfrac{1}{2}\Big(B\mathrm{e}^{-\mathrm{i}\omega t} + B^*\mathrm{e}^{\mathrm{i}\omega t}\Big) = \tfrac{1}{2}\,\mathrm{Re}\left[A^*B\right] + \tfrac{1}{2}\,\mathrm{Re}\left[AB\mathrm{e}^{-\mathrm{i}2\omega t}\right], \tag{2.15}$$

from which we introduce the following notation

$$\big\langle AB\big\rangle \equiv \tfrac{1}{2}\,\mathrm{Re}\left[A^*B\right], \tag{2.16}$$

$$\big(AB\big)^{2\omega} \equiv \tfrac{1}{2}AB, \tag{2.17}$$

where A and B could be any first-order fields. This can be used to decompose the second-order equations into one set of equations governing the steady component and one set of equations governing the oscillatory component of the second-order fields. The second-order continuity equation (2.11b) is thus in steady-state separated into

$$0 = -\rho_0 \boldsymbol{\nabla} \cdot \langle \boldsymbol{v}_2 \rangle - \boldsymbol{\nabla} \cdot \langle \rho_1 \boldsymbol{v}_1 \rangle, \tag{2.18a}$$

$$-\mathrm{i}2\omega\rho_2^{2\omega} = -\rho_0 \boldsymbol{\nabla} \cdot \boldsymbol{v}_2^{2\omega} - \boldsymbol{\nabla} \cdot \left(\rho_1 \boldsymbol{v}_1\right)^{2\omega}, \tag{2.18b}$$

where we have utilized that $\langle \partial_t g_2 \rangle = 0$ for any steady-state second-order field, and $\partial_t g_2^{2\omega} = -\mathrm{i}2\omega g_2^{2\omega}$. Similarly, the second-order momentum equation (2.11a) separates into

$$\begin{aligned} \langle \rho_1(-\mathrm{i}\omega\boldsymbol{v}_1) \rangle + \rho_0 \langle \left(\boldsymbol{v}_1 \cdot \boldsymbol{\nabla}\right) \boldsymbol{v}_1 \rangle &= -c_s^2 \boldsymbol{\nabla} \langle \rho_2 \rangle + \eta \nabla^2 \langle \boldsymbol{v}_2 \rangle \\ &\quad + \left(\tfrac{1}{3}\eta + \eta^{\mathrm{b}}\right) \boldsymbol{\nabla} \left(\boldsymbol{\nabla} \cdot \langle \boldsymbol{v}_2 \rangle\right), \end{aligned} \tag{2.19a}$$

$$\begin{aligned} -\mathrm{i}2\omega\rho_0 \boldsymbol{v}_2^{2\omega} + \left(\rho_1(-\mathrm{i}\omega\boldsymbol{v}_1)\right)^{2\omega} + \rho_0 \left(\left(\boldsymbol{v}_1 \cdot \boldsymbol{\nabla}\right) \boldsymbol{v}_1\right)^{2\omega} &= -c_s^2 \boldsymbol{\nabla} \rho_2^{2\omega} + \eta \nabla^2 \boldsymbol{v}_2^{2\omega} \\ &\quad + \left(\tfrac{1}{3}\eta + \eta^{\mathrm{b}}\right) \boldsymbol{\nabla} \left(\boldsymbol{\nabla} \cdot \boldsymbol{v}_2^{2\omega}\right). \end{aligned} \tag{2.19b}$$

Equations (2.18) and (2.19) together with a set of boundary conditions constitute a steady-state second-order acoustic problem, under the assumptions of adiabatic thermodynamics and single frequency vibrations of the boundaries.

2.2.3 Summary

Following the perturbation approach we have transformed the two coupled nonlinear equations (2.5) governing ρ and $\boldsymbol{v}$ into six partially coupled equations, governing the primary oscillatory modes ρ_1 and $\boldsymbol{v}_1$ Eq. (2.10), the secondary oscillatory modes $\rho_2^{2\omega}$ and $\boldsymbol{v}_2^{2\omega}$ Eqs. (2.18b) and (2.19b), and the non-oscillatory modes $\langle \rho_2 \rangle$ and $\langle \boldsymbol{v}_2 \rangle$ Eqs. (2.18a) and (2.19a). In the next section, these equations will be solved in the case of two orthogonally oscillating plates.

2.3 Example: orthogonally oscillating plates

In this section we study a system consisting of two infinite parallel plates separated by a distance w and oscillating in the direction of their normal vectors. This is one of the most simple, yet still meaningful examples of an acoustic cavity. This section is inspired by the similar example in Ref. [41], which treats the first-order problem for the two plates oscillating in anti-phase. We will treat both the first-order and second-order problem for the two plates oscillating in phase. The system is sketched in Fig. 2.1. The boundary conditions for the primary oscillatory velocity are

$$\boldsymbol{v}_1\left(y = \pm\frac{w}{2}\right) = v_{\mathrm{bc}} \cos(\omega t) = \mathrm{Re}\left[v_{\mathrm{bc}} \mathrm{e}^{-\mathrm{i}\omega t}\right], \tag{2.20}$$

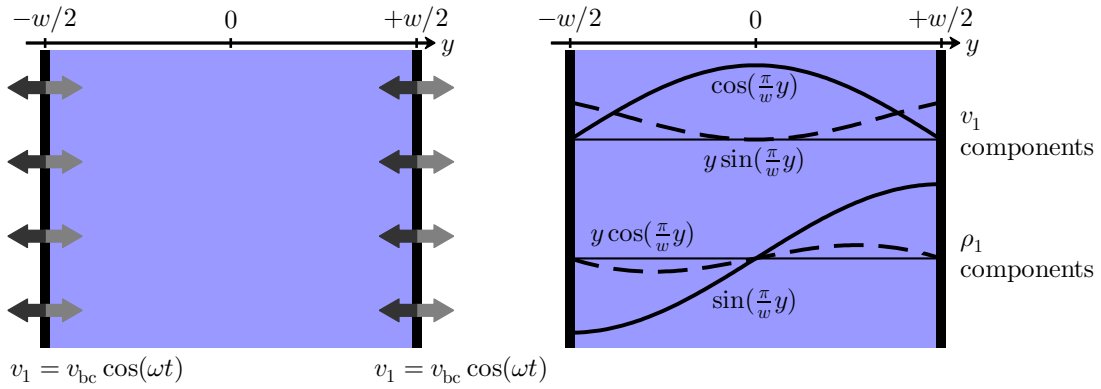

Figure 2.1: (a) Sketch of two parallel plates oscillation in phase in the direction of their surface normal vectors. The one-dimensional domain is defined by $-\frac{w}{2} \le y \le \frac{w}{2}$ and the boundary condition for the fluid velocity field is $v_1(\pm\frac{w}{2}) = v_{\rm bc}\cos(\omega t)$. (b) Graphs showing the structure of the first-order velocity v_1 and density ρ_1 fields, for actuation frequency matched to the fundamental resonance frequency of the parallel plate system, $\omega = \pi c_s/w$. The full lines show the spatial structure of the primary components of the resonant fields Eq. (2.31), whereas the dashed lines show the structure of the small component of order $\mathcal{O}(\Gamma)$ in Eq. (2.31).

which represents the in-phase oscillations of the two plates. The boundary conditions for the secondary oscillatory velocity $\boldsymbol{v}_2^{2\omega}$ and the steady non-oscillatory velocity $\langle \boldsymbol{v}_2 \rangle$ are determined by conservation of mass, *i.e.* there should be no oscillatory mass-current and no steady mass current through the walls,

$$\boldsymbol{v}_2^{2\omega}\Big(y = \pm\frac{w}{2}\Big) = -\frac{1}{\rho_0}\Big(\rho_1 \boldsymbol{v}_1\Big)^{2\omega}_{y=\pm w/2}\,, \tag{2.21}$$

$$\big\langle \boldsymbol{v}_2 \big\rangle\Big(y = \pm\frac{w}{2}\Big) = -\frac{1}{\rho_0}\big\langle \rho_1 \boldsymbol{v}_1 \big\rangle_{y=\pm w/2}\,. \tag{2.22}$$

2.3.1 First-order fields

We consider a velocity field in one dimension oscillating in steady state

$$\boldsymbol{v}_1(\boldsymbol{r}, t) = \mathrm{Re}\left[v_1(y)\mathrm{e}^{-\mathrm{i}\omega t}\right] \tag{2.23}$$

The first-order equations (2.10) in one dimension becomes

$$-\mathrm{i}\omega\rho_0 v_1 = -c_s^2\partial_y\rho_1 + \left(\tfrac{4}{3}\eta + \eta^{\rm b}\right)\partial_y^2 v_1, \tag{2.24a}$$

$$-\mathrm{i}\omega\rho_1 = -\rho_0\partial_y v_1. \tag{2.24b}$$

Inserting Eq. (2.24b) in Eq. (2.24a) yields

$$v_1 + \frac{c_s^2}{\omega^2}\Big[1 - \mathrm{i}\frac{\omega}{\rho_0 c_s^2}\left(\tfrac{4}{3}\eta + \eta^{\rm b}\right)\Big]\partial_y^2 v_1 = 0. \tag{2.25}$$

We then define the damping factor Γ and the complex wavenumber k as

$$\Gamma = \frac{\omega}{2\rho_0 c_s^2}\left(\tfrac{4}{3}\eta + \eta^{\mathrm{b}}\right) \approx 10^{-6}, \tag{2.26a}$$

$$k = (1 + \mathrm{i}\Gamma)\frac{\omega}{c_s} = (1 + \mathrm{i}\Gamma)k_0, \tag{2.26b}$$

where the value of Γ is for a typical water-filled channel exited at 2 MHz. Utilizing the smallness of Γ, Eq. (2.25) can to first order in Γ be expressed as

$$\partial_y^2 v_1 + k^2 v_1 = 0. \tag{2.27}$$

The solution to the governing equation (2.27) and the boundary conditions Eq. (2.20) is

$$v_1(y) = v_{\mathrm{bc}}\frac{\cos(ky)}{\cos(k\frac{w}{2})}, \tag{2.28a}$$

$$\rho_1(y) = \mathrm{i}\rho_0 v_{\mathrm{bc}}\frac{k}{\omega}\frac{\sin(ky)}{\cos(k\frac{w}{2})}, \tag{2.28b}$$

where the solution for ρ_1 is given by Eq. (2.24b). Expanding the trigonometric functions to first order in Γ, the velocity and density becomes

$$v_1(y) = v_{\mathrm{bc}}\frac{\cos(k_0 y) - \mathrm{i}\Gamma k_0 y\sin(k_0 y)}{\cos(k_0\frac{w}{2}) - \mathrm{i}\Gamma k_0\frac{w}{2}\sin(k_0\frac{w}{2})} + \mathcal{O}\big(\Gamma^2\big), \tag{2.29a}$$

$$\rho_1(y) = \mathrm{i}\rho_0\frac{v_{\mathrm{bc}}}{c_s}(1 + \mathrm{i}\Gamma)\frac{\sin(k_0 y) + \mathrm{i}\Gamma k_0 y\cos(k_0 y)}{\cos(k_0\frac{w}{2}) - \mathrm{i}\Gamma k_0\frac{w}{2}\sin(k_0\frac{w}{2})} + \mathcal{O}\big(\Gamma^2\big), \tag{2.29b}$$

where $\mathcal{O}\big(\Gamma^2\big)$ indicates that the terms left out are smaller by a factor of Γ^2 with respect to the leading order term in the expression. The system is at resonance when v_1 and ρ_1 have their maximum amplitudes. This occurs when the denominators in Eq. (2.29) are minimized, which is approximately determined by

$$k_0\frac{w}{2} = (n - \tfrac{1}{2})\pi, \qquad n = 1, 2, 3, \ldots \tag{2.30}$$

The various values of n describe the higher order resonances, but only those for which the main component of v_1 is even in y, due to the choice of in-phase boundary conditions Eq. (2.20). To obtain the odd v_1-resonances, we would need to apply an anti-phase boundary condition $v_1(\pm\frac{w}{2}) = \pm v_{\mathrm{bc}}$, as done in Ref. [41]. At the fundamental resonance $n = 1$ the velocity and density fields become

$$v_1(y) = \mathrm{i}\frac{2}{\pi}\frac{v_{\mathrm{bc}}}{\Gamma}\Big[\cos(k_0 y) - \mathrm{i}\Gamma k_0 y\sin(k_0 y)\Big] + \mathcal{O}\big(\Gamma^2\big), \tag{2.31a}$$

$$\rho_1(y) = -\frac{2}{\pi}\frac{v_{\mathrm{bc}}}{\Gamma c_s}\rho_0\Big[\sin(k_0 y) + \mathrm{i}\Gamma\big(\sin(k_0 y) + k_0 y\cos(k_0 y)\big)\Big] + \mathcal{O}\big(\Gamma^2\big), \tag{2.31b}$$

where $k_0 = \frac{\pi}{w}$. The spatial dependences of the terms in the solution Eq. (2.31) are sketched in Fig. 2.1(b). The perturbation expansion of the governing equations is valid only if

$|\rho_1| \ll \rho_0$, and from the solution Eq. (2.31), we see that this is equivalent to the criterion $|v_1| \ll c_s$, which is often used in the literature. For this specific solution, the perturbation criterion demands

$$\frac{v_{\mathrm{bc}}}{c_s} \ll \frac{\pi\Gamma}{2}. \tag{2.32}$$

The loss factor Γ and the quality factor Q of the system is related by $Q = 1/(2\Gamma)$, so in terms of Q the perturbation criteria Eq. (2.32) becomes

$$\frac{v_{\mathrm{bc}}}{c_s} \ll \frac{\pi}{4Q}. \tag{2.33}$$

This sets a maximum amplitude of the wall oscillations for which the perturbation expansion is valid. While this theoretical parallel plates example has a high $Q \sim 10^5$, determined only by bulk damping, typical water-filled rectangular microchannels driven at 2 MHz has $Q \sim 400$ [24, 29], which is determined mainly by dissipation within the acoustic boundary layers, discussed in Section 2.4.

2.3.2 Second-order time-averaged fields

The time-averaged second-order equations for the one-dimensional parallel plates system becomes

$$\langle \rho_1(-\mathrm{i}\omega v_1)\rangle + \rho_0\langle v_1\partial_y v_1\rangle = -c_s^2\partial_y\langle\rho_2\rangle + \eta\partial_y^2\langle v_2\rangle + \left(\tfrac{1}{3}\eta + \eta^{\mathrm{b}}\right)\partial_y^2\langle v_2\rangle, \tag{2.34a}$$

$$0 = -\rho_0\partial_y\langle v_2\rangle - \partial_y\langle\rho_1 v_1\rangle. \tag{2.34b}$$

Inserting Eqs. (2.34b) and (2.24b) in Eq. (2.34a), and integrating Eq. (2.34b) with the boundary conditions Eq. (2.22), yields

$$\partial_y\langle\rho_2\rangle = \frac{2k_0^2}{\omega}\langle\rho_1(\mathrm{i}v_1)\rangle - \frac{2\Gamma}{\omega}\partial_y^2\langle\rho_1 v_1\rangle, \tag{2.35a}$$

$$\langle v_2\rangle = -\frac{1}{\rho_0}\langle\rho_1 v_1\rangle. \tag{2.35b}$$

Following the rule Eq. (2.16) for the time-average of products of first-order fields, we obtain the following solutions for v_2 and $\partial_y\rho_2$,

$$\partial_y\langle\rho_2\rangle = \frac{k_0^2}{\omega}\,\mathrm{Re}\left(\rho_1^*\mathrm{i}v_1\right) - \frac{\Gamma}{\omega}\partial_y^2\,\mathrm{Re}\left(\rho_1^* v_1\right), \tag{2.36a}$$

$$\langle v_2\rangle = -\frac{1}{2\rho_0}\,\mathrm{Re}\left(\rho_1^* v_1\right). \tag{2.36b}$$

Inserting the first-order solutions Eq. (2.28), the source term $\mathrm{Re}\left(\rho_1^* v_1\right)$ becomes

$$\mathrm{Re}\left(\rho_1^* v_1\right) = -\rho_0\frac{v_{\mathrm{bc}}^2}{c_s}\,\mathrm{Re}\left[\mathrm{i}(1-\mathrm{i}\Gamma)\frac{\sin(k^* y)\cos(ky)}{\cos(k^*\frac{w}{2})\cos(k\frac{w}{2})}\right], \tag{2.37}$$

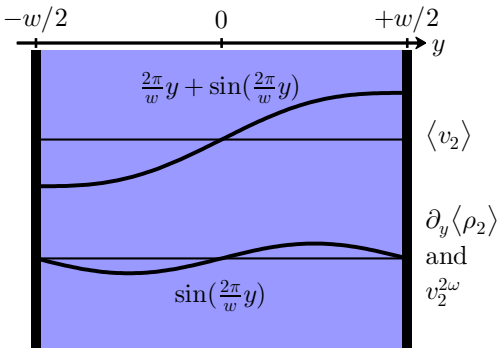

Figure 2.2: Graphs showing the structure of the solutions for the second-order time-averaged velocity $\langle v_2 \rangle$ (top graph) and density $\langle \rho_2 \rangle$ (bottom graph), and the second-order harmonic velocity $v_2^{2\omega}$ (bottom graph), for actuation frequency matched to the fundamental resonance frequency of the parallel plate system.

and assuming the system is at the fundamental resonance $k_0 \frac{w}{2} = \frac{\pi}{2}$, $n = 1$ Eq. (2.30), the solutions (2.36) becomes

$$\partial_y \langle \rho_2 \rangle = \frac{2}{\pi^2} \rho_0 k_0 \frac{v_{\mathrm{bc}}^2}{\Gamma^2 c_s^2} \sin(2k_0 y) + \mathcal{O}(\Gamma), \tag{2.38a}$$

$$\langle v_2 \rangle = \frac{1}{\pi^2} \frac{v_{\mathrm{bc}}^2}{\Gamma c_s} \big[2k_0 y + \sin(2k_0 y) \big] + \mathcal{O}(\Gamma). \tag{2.38b}$$

This concludes our treatment of the time-averaged second-order fields. The spatial dependences of the solutions Eq. (2.38) are shown in Fig. 2.2. Since only the gradient of the time-averaged density $\partial_y \langle \rho_2 \rangle$ enters the governing equations (2.34), there is no extra information gained from integrating Eq. (2.38a).

It may seem contradictory to have a steady velocity in this one-dimensional system. However, the conserved quantities are mass and momentum, not velocity. The mass is indeed conserved because the steady mass current $\langle \rho_1 \boldsymbol{v}_1 \rangle$, from the walls towards the center, is balanced by the steady mass current $\rho_0 \langle \boldsymbol{v}_2 \rangle$, from the center towards the walls. There is thus zero net steady mass current in the system.

The leading-order components of ρ_1 and $\boldsymbol{v}_1$, Eq. (2.31), are oscillating out of phase, and thus we find that $\langle \rho_1 \boldsymbol{v}_1 \rangle \sim \Gamma |\rho_1| |v_1|$, which is an order of Γ smaller than one would expect from dimensional analysis.

2.3.3 Second-order oscillatory fields

The governing equations for the socond-order oscillatory component $\rho_2^{2\omega}$ and $v_2^{2\omega}$, Eqs. (2.18b) and (2.19b), respectively, in one dimension become

$$-\mathrm{i}2\omega \rho_2^{2\omega} = -\rho_0 \partial_y v_2^{2\omega} - \partial_y \big(\rho_1 v_1 \big)^{2\omega}, \tag{2.39a}$$

$$-\mathrm{i}2\omega \rho_0 v_2^{2\omega} + \big(\rho_1 (-\mathrm{i}\omega v_1) \big)^{2\omega} + \rho_0 \big(v_1 \partial_y v_1 \big)^{2\omega} = -c_s^2 \partial_y \rho_2^{2\omega} + \Big(\tfrac{4}{3}\eta + \eta^{\mathrm{b}} \Big) \partial_y^2 v_2^{2\omega}. \tag{2.39b}$$

Since the derivation of the second-order oscillatory components is more extensive, we will only go through the calculation of $v_2^{2\omega}$. The second and third term on the left hand side of Eq. (2.39b) cancel due to first-order continuity Eq. (2.24b) and the rule Eq. (2.17) for the 2ω-component of products of first-order fields, as shown here

$$\rho_0\big(v_1\partial_y v_1\big)^{2\omega} = \tfrac{1}{2}\rho_0 v_1 \partial_y v_1 = \tfrac{1}{2}\rho_0 v_1 \mathrm{i}\omega\frac{\rho_1}{\rho_0} = -\big(\rho_1(-\mathrm{i}\omega v_1)\big)^{2\omega}. \tag{2.40}$$

Inserting Eq. (2.39a) in Eq. (2.39b) and applying the 2ω-rule Eq. (2.17) yields

$$4k_0^2 v_2^{2\omega} + (1-\mathrm{i}4\Gamma)\partial_y^2 v_2^{2\omega} + \frac{1}{2\rho_0}\partial_y^2(\rho_1 v_1) = 0. \tag{2.41}$$

Inserting the first-order solution Eq. (2.28) the source term becomes

$$\frac{1}{2\rho_0}\partial_y^2(\rho_1 v_1) = \frac{1}{2\rho_0}\partial_y^2\left(\mathrm{i}\rho_0\frac{k}{\omega}\frac{v_{\mathrm{bc}}^2}{\cos^2(k\frac{w}{2})}\cos(ky)\sin(ky)\right) = -\mathrm{i}\frac{k^3}{\omega}\frac{v_{\mathrm{bc}}^2}{\cos^2(k\frac{w}{2})}\sin(2ky), \tag{2.42}$$

The governing equation (2.41) for $v_2^{2\omega}$ thus becomes

$$4k_0^2 v_2^{2\omega} + (1-\mathrm{i}4\Gamma)\partial_y^2 v_2^{2\omega} - \mathrm{i}\frac{k^3}{\omega}\frac{v_{\mathrm{bc}}^2}{\cos^2(k\frac{w}{2})}\sin(2ky) = 0. \tag{2.43}$$

The solution to the homogeneous equation is

$$v_2^{2\omega,\mathrm{hom}} = A\cos(2qy) + B\sin(2qy), \tag{2.44}$$

$$q = k_0(1+\mathrm{i}2\Gamma), \tag{2.45}$$

whereas the guess for the inhomogeneous solution is

$$v_2^{2\omega,\mathrm{inhom}} = C\sin(2ky). \tag{2.46}$$

Inserting the inhomogeneous solution Eq. (2.46) into the governing equation (2.43) yields

$$4k_0^2 C - C(1-\mathrm{i}4\Gamma)4k^2 - \mathrm{i}\frac{k^3}{\omega}\frac{v_{\mathrm{bc}}^2}{\cos^2(k\frac{w}{2})} = 0, \tag{2.47}$$

which to first order in Γ becomes

$$\mathrm{i}8\Gamma C k_0^2 - \mathrm{i}(1+\mathrm{i}3\Gamma)\frac{k_0^3}{\omega}\frac{v_{\mathrm{bc}}^2}{\cos^2(k\frac{w}{2})} = 0 \quad \Rightarrow$$

$$C = \frac{1+\mathrm{i}3\Gamma}{8\Gamma}\frac{k_0}{\omega}\frac{v_{\mathrm{bc}}^2}{\cos^2(k\frac{w}{2})} = \frac{1}{8}\frac{1}{\Gamma c_s}\frac{v_{\mathrm{bc}}^2}{\cos^2(k\frac{w}{2})} + \mathcal{O}(\Gamma). \tag{2.48}$$

The A and B coefficients of the homogeneous solution is determined by the boundary conditions Eq. (2.21), which to lowest order in Γ becomes

$$\begin{aligned} v_2^{2\omega}(\pm w/2) = -\frac{1}{\rho_0}\Big(\rho_1 \boldsymbol{v}_1\Big)_{y=\pm w/2}^{2\omega} &= -\mathrm{i}\frac{1}{4c_s}\frac{v_{\mathrm{bc}}^2}{\cos^2(k\frac{w}{2})}\sin(2k(\pm w/2)) \;\Rightarrow \\ A\cos(\pm 2q\tfrac{w}{2}) + B\sin(\pm 2q\tfrac{w}{2}) + C\sin(\pm 2k\tfrac{w}{2}) &= -\mathrm{i}\frac{1}{4c_s}\frac{v_{\mathrm{bc}}^2}{\cos^2(k\frac{w}{2})}\sin(2k(\pm w/2)) \;\Rightarrow \\ A\cos(qw) \pm \Big[B\sin(qw) + C\sin(kw)\Big] &= \mp\mathrm{i}\frac{1}{4c_s}\frac{v_{\mathrm{bc}}^2}{\cos^2(k\frac{w}{2})}\sin(kw), \end{aligned} \tag{2.49}$$

which has the solution

$$A = 0 \;\wedge\; B = -\left[\Big(\frac{1}{8\Gamma} + \mathrm{i}\frac{1}{4}\Big)\frac{1}{c_s}\frac{v_{\mathrm{bc}}^2}{\cos^2(k\frac{w}{2})}\right]\frac{\sin(2k\frac{w}{2})}{\sin(2q\frac{w}{2})} = -\frac{1}{8\Gamma c_s}\frac{v_{\mathrm{bc}}^2}{\cos^2(k\frac{w}{2})}\frac{\sin(2k\frac{w}{2})}{\sin(2q\frac{w}{2})} + \mathcal{O}\big(\Gamma\big). \tag{2.50}$$

Since we are only interested in the solution to $v_2^{2\omega}$ to leading order in Γ and the boundary value, right hand side of Eq. (2.49), is an order of Γ smaller than the amplitude C of the inhomogeneous solution Eq. (2.48), the boundary value turns out to have no influence on the solution to leading order in Γ, expressed in Eq. (2.50). The solution for the second-order oscillatory velocity thus becomes

$$v_2^{2\omega} = \frac{1}{8}\frac{1}{\Gamma c_s}\frac{v_{\mathrm{bc}}^2}{\cos^2(k\frac{w}{2})}\left[\sin(2ky) - \frac{\sin(2k\frac{w}{2})}{\sin(2q\frac{w}{2})}\sin(2qy)\right]. \tag{2.51}$$

With the expansion of the trigonometric function to first order in Γ and applying the resonance condition $k_0\frac{w}{2} = \frac{\pi}{2}$, $n = 1$ Eq. (2.30), we obtain

$$\cos^2(k\tfrac{w}{2}) \approx \Big[\cos(k_0\tfrac{w}{2}) - \mathrm{i}\Gamma k_0\tfrac{w}{2}\sin(k_0\tfrac{w}{2})\Big]^2 = (-\mathrm{i}\Gamma\tfrac{\pi}{2})^2 = -\frac{\pi^2}{4}\Gamma^2, \tag{2.52a}$$

$$\frac{\sin(2k\frac{w}{2})}{\sin(2q\frac{w}{2})} \approx \frac{\sin(2k_0\frac{w}{2}) + \mathrm{i}\Gamma 2k_0\frac{w}{2}\cos(2k_0\frac{w}{2})}{\sin(2k_0\frac{w}{2}) + \mathrm{i}2\Gamma 2k_0\frac{w}{2}\cos(2k_0\frac{w}{2})} = \frac{-\mathrm{i}\pi\Gamma}{-\mathrm{i}2\pi\Gamma} = \frac{1}{2}, \tag{2.52b}$$

$$\begin{aligned} \sin(2ky) - \tfrac{1}{2}\sin(2qy) &\approx \sin(2k_0y) + \mathrm{i}\Gamma 2k_0y\cos(2k_0y) - \tfrac{1}{2}\Big[\sin(2k_0y) + \mathrm{i}2\Gamma 2k_0y\cos(2k_0y)\Big] \\ &= \tfrac{1}{2}\sin(2k_0y) \end{aligned} \tag{2.52c}$$

and $v_2^{2\omega}$ thus becomes

$$v_2^{2\omega} = -\frac{1}{4\pi^2}\frac{1}{\Gamma^3}\frac{v_{\mathrm{bc}}^2}{c_s}\sin(2k_0y) + \mathcal{O}\big(\Gamma\big). \tag{2.53}$$

The spatial dependences of the solution Eq. (2.53) are shown in Fig. 2.2. In order for the perturbation expansion to be valid, we need to check that the amplitude of $v_2^{2\omega}$ is much smaller than the amplitude of v_1,

$$\begin{aligned} \frac{|v_2^{2\omega}|}{|v_1|} = \frac{\frac{1}{4\pi^2}\frac{1}{\Gamma^3}\frac{v_{\mathrm{bc}}^2}{c_s}}{\frac{2}{\pi}\frac{v_{\mathrm{bc}}}{\Gamma}} &\ll 1 \Rightarrow \\ \frac{v_{\mathrm{bc}}}{c_s} &\ll 8\pi\Gamma^2 \end{aligned} \tag{2.54}$$

In terms of the quality factor Q the perturbation criteria becomes

$$\frac{v_{\mathrm{bc}}}{c_s} \ll \frac{2\pi}{Q^2}. \tag{2.55}$$

The criterion Eq. (2.55) from $|v_2^{2\omega}| \ll |v_1|$ is more restrictive than the criterion Eq. (2.33) from $|v_1| \ll c_s$. This is because the amplitude $|v_2^{2\omega}| \sim \frac{1}{\Gamma}|\rho_1||v_1|$ Eq. (2.53) is a factor of $\frac{1}{\Gamma}$ larger than what is expected from dimensional analysis of the governing equations.

2.3.4 Summary of orthogonally oscillating plates

In summary we have derived the following solution for the velocity field for the case of two infinite parallel plates separate by a distance w and oscillating in-phase in the direction of their normal vectors with a velocity amplitude v_{bc} and frequency matched to the fundamental resonance $f = c_s/2w$,

$$v = \mathrm{Re}\left(v_1 \mathrm{e}^{-\mathrm{i}\omega t}\right) + \langle v_2 \rangle + \mathrm{Re}\left(v_2^{2\omega} \mathrm{e}^{-\mathrm{i}2\omega t}\right), \tag{2.56a}$$

$$v_1 = \mathrm{i}\frac{2}{\pi}\frac{v_{\mathrm{bc}}}{\Gamma}\Big[\cos(k_0 y) - \mathrm{i}\Gamma k_0 y \sin(k_0 y)\Big] + \mathcal{O}(\Gamma^2), \tag{2.56b}$$

$$\langle v_2 \rangle = \frac{1}{\pi^2}\frac{v_{\mathrm{bc}}^2}{\Gamma c_s}\big[2k_0 y + \sin(2k_0 y)\big] + \mathcal{O}(\Gamma), \tag{2.56c}$$

$$v_2^{2\omega} = -\frac{1}{4\pi^2}\frac{1}{\Gamma^3}\frac{v_{\mathrm{bc}}^2}{c_s}\sin(2k_0 y) + \mathcal{O}(\Gamma), \tag{2.56d}$$

originally stated in Eqs. (2.31a), (2.38b), and (2.53), and where $k_0 = \frac{\pi}{w}$. In terms of the Q-factor the magnitude of the three velocity components are

$$v_1 \sim Q v_{\mathrm{bc}}, \quad \langle v_2 \rangle \sim \frac{Q v_{\mathrm{bc}}^2}{c_s}, \quad v_2^{2\omega} \sim \frac{Q^3 v_{\mathrm{bc}}^2}{c_s}. \tag{2.57}$$

The new result of this analysis is that the criterion for the validity of the perturbation expansion is $Q^2 v_{\mathrm{bc}} \ll c_s$, based on the assumption of $|\boldsymbol{v}_2| \ll |\boldsymbol{v}_1|$, and not the criterion $Q v_{\mathrm{bc}} \ll c_s$, based on the assumption of $|\boldsymbol{v}_1| \ll c_s$, which is usually stated in the literature.

In the present case of orthogonally oscillating plates there is no boundary-driven acoustic streaming, and the weak steady velocity $\langle \boldsymbol{v}_2 \rangle$ merely ensures zero net steady mass current, as discussed in Section 2.3.2. In the more physical relevant case of a rectangular channel with vibrating sidewalls, the acoustic streaming flow is driven at the top and bottom walls and its magnitude becomes $\langle v_2 \rangle \sim \frac{Q^2 v_{\mathrm{bc}}^2}{c_s} \sim |\rho_1||v_1|$, as expected from dimensional analysis of the governing equations. This will be discussed in the following section.

2.4 The acoustic boundary layer and acoustic streaming

In Section 2.3 we treated an example of wave propagation orthogonal to a wall, and the only source of damping was the bulk absorption. In this section we study acoustic wave

propagation parallel to a wall, at which the velocity field has to fulfill a no-slip boundary condition,

$$\boldsymbol{v} = \boldsymbol{0}, \qquad \text{at wall.} \tag{2.58}$$

The amplitude of the velocity wave thus have to undergo a transition, in the direction perpendicular to it propagation, from its amplitude v_a in the bulk to zero at the wall. This transition region is called the acoustic boundary layer.

The starting point of the boundary treatment is a standing acoustic wave in the bulk of the fluid, far from the wall, given by an expression much similar to the orthogonally oscillating plates solution Eq. (2.31),

$$v_{y1}^{\mathrm{Bulk}}(y,t) = \mathrm{Re}\left\{\mathrm{i}v_\mathrm{a}\cos(k_0 y)\mathrm{e}^{-\mathrm{i}\omega t}\right\}, \tag{2.59}$$

$$\rho_1^{\mathrm{Bulk}}(y,t) = \mathrm{Re}\left\{-\frac{v_\mathrm{a}}{c_s}\rho_0\sin(k_0 y)\mathrm{e}^{-\mathrm{i}\omega t}\right\}, \tag{2.60}$$

where v_a is the amplitude of the velocity oscillations far from the wall. We note that the complex "i" in the expression for v_{y1}^{Bulk} indicates a phase shift between the velocity and density oscillations. This out of phase oscillation of v_1 and ρ_1 was the reason why the time-averaged product $\langle\rho_1 v_1\rangle \sim \Gamma|\rho_1||v_1|$ was a factor of Γ smaller than expected from dimensional analysis in the orthogonally oscillating plates example Section 2.3.2.

Now we introduce a planar wall at $z = 0$, and to accommodate the no-slip condition $v_{y1}(z=0) = 0$, we make the following ansatz for $v_{y1}(y,z,t)$,

$$v_{y1}(y,z,t) = \mathrm{Re}\left\{\mathrm{i}v_\mathrm{a}\cos(k_0 y)f(z)\mathrm{e}^{-\mathrm{i}\omega t}\right\}, \tag{2.61a}$$

$$f(z) \to 1, \quad \text{for } z \to \infty, \tag{2.61b}$$

$$f(z) \to 0, \quad \text{for } z \to 0. \tag{2.61c}$$

The task in now to determine the function $f(z)$.

The governing equation in the frequency domain for $\boldsymbol{v}_1$ and ρ_1, originally stated in Eq. (2.10), are

$$-\mathrm{i}\omega\rho_0\boldsymbol{v} = -c_s^2\boldsymbol{\nabla}\rho_1 + \eta\nabla^2\boldsymbol{v}_1 + \left(\tfrac{1}{3}\eta + \eta^\mathrm{b}\right)\boldsymbol{\nabla}\left(\boldsymbol{\nabla}\cdot\boldsymbol{v}_1\right), \tag{2.62a}$$

$$-\mathrm{i}\omega\rho_1 = -\rho_0\boldsymbol{\nabla}\cdot\boldsymbol{v}_1. \tag{2.62b}$$

Substituting $\boldsymbol{\nabla}\cdot\boldsymbol{v}_1$ in Eq. (2.62a) with Eq. (2.62b) yields,

$$\frac{2\eta}{\omega\rho_0}\nabla^2\boldsymbol{v}_1 + \mathrm{i}2\boldsymbol{v}_1 - \frac{2\omega}{k_0\rho_0}(1-\mathrm{i}\Gamma')\boldsymbol{\nabla}\rho_1 = \boldsymbol{0}, \qquad \Gamma' = \frac{\omega\eta}{\rho c_s^2}\left(\frac{1}{3} + \frac{\eta^\mathrm{b}}{\eta}\right). \tag{2.63}$$

The prefactor to the Laplace term is of great importance, as it leads to the definition of the viscous acoustic boundary layer thickness δ_s given by

$$\delta_\mathrm{s} = \sqrt{\frac{2\eta}{\omega\rho_0}}. \tag{2.64}$$

The subscript "s" refer to shear, since δ_s is related to the viscous shear at the wall. There is also a thermal boundary layer of thickness δ_t, due to thermal conduction at the wall. δ_s is essentially a momentum diffusion length, describing how far the momentum diffuses within an oscillation period.

The y-component of Eq. (2.63) along with the boundary conditions of Eq. (2.61) are satisfied to zeroth order in Γ' by the following solution,

$$v_{y1}(y,z) = \mathrm{i}v_\mathrm{a}\cos(k_0 y)(1-\mathrm{e}^{-\kappa z}), \qquad \kappa = (1-\mathrm{i})\frac{1}{\delta_\mathrm{s}}, \tag{2.65}$$

$$\rho_1(y,z) = -\frac{v_\mathrm{a}}{c_s}\rho_0\sin(k_0 y), \tag{2.66}$$

In the bulk of the fluid ($z \to \infty$) the complex phases of v_{y1} and ρ_1 are i and -1, respectively, representing out of phase oscillations. However, inside the boundary layer the phase of v_{y1} changes due the complex part of κ,

$$v_{y1}(y,z) = \mathrm{i}v_\mathrm{a}\cos(k_0 y)\left[1-\mathrm{e}^{\mathrm{i}\frac{z}{\delta_\mathrm{s}}}\mathrm{e}^{-\frac{z}{\delta_\mathrm{s}}}\right], \tag{2.67}$$

and the oscillation of v_{y1} and ρ_1 are thus not completely out of phase inside the boundary layer, and the magnitude of the time-averaged product $\langle \rho_1 \boldsymbol{v}_1 \rangle \sim |\rho_1||\boldsymbol{v}_1|$ agrees with the prediction from dimensional analysis.

This phase shift and shear of $\boldsymbol{v}_1$ inside the boundary layer is what leads to the generation of a steady acoustic streaming flow. To calculate the generated streaming flow, the first-order problem needs to be treated more thoroughly, including the orthogonal velocity component v_{z1}, after which the time-averaged second-order equations Eqs. (2.18a) and (2.19a) need to be solved. This is outside the scope of this presentation, and the reader is referred to the Master Thesis by Jonas T. Karlsen Ref. [42] and the study by Rednikov and Sadhal Ref. [8]. The non-linear interactions of the oscillatory first-order fields inside the boundary layers generate a steady rotation of the fluid $\langle \boldsymbol{v}_2 \rangle$ inside the boundary layers, which in turn drives a steady rotational flow in the bulk. This mechanism is sketched in Fig. 2.3 for a standing wave in-between two parallel plates, with the direction of propagation parallel to the walls, in contrast to the example in Section 2.3, where the direction of propagation was orthogonal to the walls. The classical results by Lord Rayleigh Ref. [3] for the steady streaming velocity $\langle \boldsymbol{v}_2 \rangle$ near the wall, in our notation becomes

$$\langle v_{y2} \rangle = \frac{3}{8}\frac{v_\mathrm{a}^2}{c_s}\sin\left(2k_0 y\right), \qquad \text{near wall.} \tag{2.68}$$

2.5 Summary of adiabatic theory

In this chapter we have derived the first- and second-order acoustic equations within the framework of the adiabatic approximation. These equations have been solved for the problem of an acoustic wave between two orthogonally oscillating parallel plates, including derivations of the oscillating first-order velocity component, the time-averaged second-order

velocity component, and the oscillating second-order velocity component. The treatment of the oscillatory second-order velocity component is new, and our analysis shows that its amplitude is a factor of Q larger than what is expected from dimensional analysis of the second-order equations. Furthermore, we have discussed the acoustic boundary layer, the shear stresses and the phase shift of the acoustic velocity oscillations within it, and how this leads to the generation of a steady streaming velocity. In the following chapter the governing equations are derived in a more rigorous way without the adiabatic approximation.

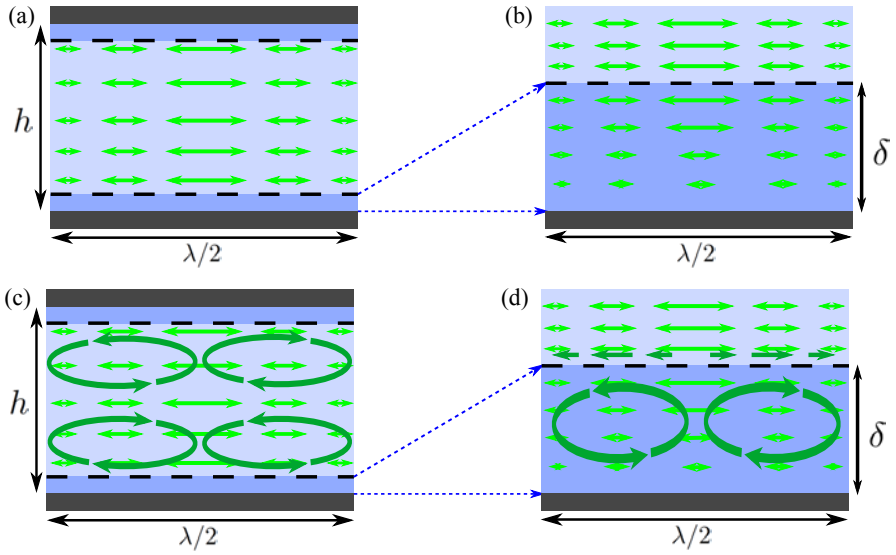

Figure 2.3: Sketch of the boundary layer and the generated acoustic streaming flow between two parallel plates. (a) Standing acoustic wave between two parallel plates, with the direction of propagation parallel to the walls. Light green arrows indicate the oscillating velocity $\boldsymbol{v}_1$. (b) Zoon-in on the boundary layer near the bottom wall. The amplitude of the velocity oscillations decay to fulfill the no-slip condition $\boldsymbol{v} = 0$ at the wall. (c) Dark green arrows indicate the steady rotational streaming flow in the bulk of the fluid, often referred to as Rayleigh streaming, generated by the non-linear interactions of the oscillatory first-order fields inside the boundary layers. (d) Zoom-in on the boundary layer with dark green arrows indicating the rotational motion of the steady streaming flow inside the boundary layer, often referred to as Schlichting streaming. The figure is adapted from Ref. [43].

Chapter 3

Full thermodynamic theory

In this chapter we derive the governing equations for the conservation of mass, momentum and energy in a compressible Newtonian fluid. The governing equations are expanded following standard second-order perturbation theory. The treatment is based on the textbooks *Theoretical Microfludics* by Henrik Bruus [17], *Course of Theoretical Physics* volume 5 *Statistical Physics* and volume 6 *Fluid Mechanics* by Landau and Lifshitz[39, 40]. Part of the theory presented in this chapter is also presented in Refs. [28, 11, 29] Appendixes A, B, and D. Based on dimensional analysis of the perturbation equations, we discuss the orders of magnitude of the first-order fields, the adiabatic approximation, and the magnitude of the acoustic streaming flow. Furthermore, the possible ambiguity of the combination of linear thermodynamic relations and second-order perturbation theory is discussed.

3.1 Thermodynamics

In this treatment we describe changes to the thermodynamic state of a fluid particle[1] by changes in the following five variables, the temperature T, the pressure p, the mass density ρ, the internal energy ε per mass unit, and the entropy s per mass unit, outlined in Table 3.1. These five variables are interdependent and small changes to the state of the fluid can be described by changes in just two variables [39]. We choose T and p to be our

[1] A fluid particle is a collection of fluid molecules large enough to have well-defined average values with small fluctuations, thus fulfilling the continuum hypothesis. The minimum dimension for a liquid particle is approximately 10 nm [17].

Table 3.1: Thermodynamic variables and the chosen hierarchy of independent and dependent variables.

Name	symbol	unit	hierarchy
Temperatur	T	K	Independent
Pressure	p	Pa	Independent
Density	ρ	$\mathrm{kg\,m^{-3}}$	Dependent
Internal energy	ε	$\mathrm{J\,kg^{-1}}$	Dependent
Entropy	s	$\mathrm{J\,K^{-1}\,kg^{-1}}$	Dependent

independent variables, and the objective of this section is to express changes in the three dependent variables ρ, ε, and s in terms of changes in T and p.

The first law of thermodynamics is usually given with s and ρ as the independent variables,

$$\mathrm{d}\varepsilon = T\,\mathrm{d}s - p\,\mathrm{d}\left(\frac{1}{\rho}\right) = T\,\mathrm{d}s + \frac{p}{\rho^2}\,\mathrm{d}\rho. \tag{3.1a}$$

By a standard Legendre transformation of ε to the Gibbs free energy g per unit mass, $g = \varepsilon - Ts + p\,\frac{1}{\rho}$, we obtain the first law with T and p as the independent variables,

$$\mathrm{d}g = -s\,\mathrm{d}T + \frac{1}{\rho}\,\mathrm{d}p. \tag{3.1b}$$

We furthermore introduce the following three thermodynamics coefficients: the isobaric heat capacity per unit mass c_p, the isobaric thermal expansion coefficient α_p, and the isothermal compressibility κ_T, as

$$c_p = T\left(\frac{\partial s}{\partial T}\right)_p, \tag{3.2a}$$

$$\alpha_p = -\frac{1}{\rho}\left(\frac{\partial \rho}{\partial T}\right)_p, \tag{3.2b}$$

$$\kappa_T = \frac{1}{\rho}\left(\frac{\partial \rho}{\partial p}\right)_T. \tag{3.2c}$$

The subscript p or T refers to evaluating the partial derivative while keeping p, respectively, T constant, *e.g.* $(\partial g/\partial T)_p = -s$, Eq. (3.1b). Moreover, as a standard step towards getting rid of explicit references to the entropy, we derive from Eqs. (3.1b) and (3.2b) the following Maxwell relation based on Schwarz' theorem, which states that the order of differentiation is irrelevant,

$$\left(\frac{\partial s}{\partial p}\right)_T = \left\{\frac{\partial}{\partial p}\left[-\left(\frac{\partial g}{\partial T}\right)_p\right]\right\}_T = -\left\{\frac{\partial}{\partial T}\left[\left(\frac{\partial g}{\partial p}\right)_T\right]\right\}_p = -\left[\frac{\partial}{\partial T}\left(\frac{1}{\rho}\right)\right]_p = -\frac{1}{\rho}\,\alpha_p. \tag{3.3}$$

Using Eqs. (3.2) and (3.3) we express $\mathrm{d}s$ and $\mathrm{d}\rho$ in terms of $\mathrm{d}T$ and $\mathrm{d}p$

$$T\mathrm{d}s = c_p\,\mathrm{d}T - \frac{\alpha_p T}{\rho}\,\mathrm{d}p, \tag{3.4a}$$

$$\frac{1}{\rho}\,\mathrm{d}\rho = \kappa_T\,\mathrm{d}p - \alpha_p\,\mathrm{d}T. \tag{3.4b}$$

Substituting $\mathrm{d}s$ in Eq. (3.1a) by Eq. (3.4a), $\mathrm{d}\varepsilon$ is written in terms of $\mathrm{d}T$, $\mathrm{d}p$, and $\mathrm{d}\rho$,

$$\rho\,\mathrm{d}\varepsilon = \rho c_p\,\mathrm{d}T - \alpha_p T\,\mathrm{d}p + \frac{p}{\rho}\mathrm{d}\rho, \tag{3.5a}$$

which will become useful later. Substituting $\mathrm{d}\rho$ by Eq. (3.4b), $\mathrm{d}\varepsilon$ is expressed only in terms of $\mathrm{d}T$ and $\mathrm{d}p$,

$$\rho\,\mathrm{d}\varepsilon = \left(\rho c_p - \alpha_p p\right)\mathrm{d}T + \left(\kappa_T p - \alpha_p T\right)\mathrm{d}p\,. \tag{3.5b}$$

Using Eqs. (3.4) and (3.5b), small changes in the dependent thermodynamic variables s, ρ, and ε can be expressed in terms of changes in the independent thermodynamic variables T and p. The default unperturbed equilibrium state used in this thesis is water at ambient temperature $T_0 = 25.0$ °C and ambient pressure $p_0 = 0.1013$ MPa.

For future reference we also define the isochoric heat capacity c_V per unit mass and the ratio of specific heat capacities γ,

$$c_V = T\left(\frac{\partial s}{\partial T}\right)_V, \tag{3.6a}$$

$$\gamma = \frac{c_p}{c_V}, \tag{3.6b}$$

from which the following two identities can be derived

$$\kappa_T = \gamma\kappa_s, \tag{3.7a}$$

$$\gamma - 1 = \frac{\alpha_p^2 T_0}{\rho_0 c_p \kappa_s}\,. \tag{3.7b}$$

3.2 Governing equations for momentum, mass and energy

Besides the thermodynamic variables, the governing equations of thermoviscous acoustics requires the introduction of the velocity field $\boldsymbol{v}$ of the fluid as well as the stress tensor $\boldsymbol{\sigma}$, which for a Newtonian fluid is given as [17]

$$\boldsymbol{\sigma} = -p\,\mathbf{1} + \boldsymbol{\tau}, \tag{3.8a}$$

$$\boldsymbol{\tau} = \eta\left[\boldsymbol{\nabla v} + (\boldsymbol{\nabla v})^{\mathrm{T}}\right] + \left[\eta^{\mathrm{b}} - \frac{2}{3}\eta\right](\boldsymbol{\nabla}\cdot\boldsymbol{v})\,\mathbf{1}, \tag{3.8b}$$

where τ is denoted the viscous stress tensor, $\mathbf{1}$ is the unit tensor and the superscript "T" indicates tensor transposition.

Mass conservation implies that the rate of change $\partial_t\rho$ of the density in a test volume with surface normal vector $\boldsymbol{n}$ is given by the influx (direction $-\boldsymbol{n}$) of the mass current density $\rho\boldsymbol{v}$. In differential form by Gauss's theorem it is

$$\partial_t\rho = \boldsymbol{\nabla}\cdot\big[-\rho\boldsymbol{v}\big], \tag{3.9a}$$

which is sometimes referred to as the continuity equation. In order to express changes in the thermodynamical state by the chosen independent variables p and T, we substitute $\partial_t\rho$ and $\boldsymbol{\nabla}\rho$ using Eq. (3.4b) and divide by ρ to obtain

$$\kappa_T\,\partial_t p - \alpha_p\,\partial_t T = -\boldsymbol{\nabla}\cdot\boldsymbol{v} - \boldsymbol{v}\cdot(\kappa_T\,\boldsymbol{\nabla}p - \alpha_p\,\boldsymbol{\nabla}T). \tag{3.9b}$$

Similarly, momentum conservation implies that the rate of change $\partial_t(\rho\boldsymbol{v})$ of the momentum density in the same test volume is given by the stress forces $\boldsymbol{\sigma}$ acting on the surface (with normal $\boldsymbol{n}$), and the influx (direction $-\boldsymbol{n}$) of the momentum current density $\rho\boldsymbol{v}\boldsymbol{v}$. In differential form, neglecting body forces, this becomes

$$\partial_t(\rho\boldsymbol{v}) = \boldsymbol{\nabla}\cdot\big[\boldsymbol{\tau} - p\,\mathbf{1} - \rho\boldsymbol{v}\boldsymbol{v}\big]. \tag{3.10a}$$

Applying the expansion $\boldsymbol{\nabla}\cdot(\rho\boldsymbol{v}\boldsymbol{v}) = \rho(\boldsymbol{v}\cdot\boldsymbol{\nabla})\boldsymbol{v} + \boldsymbol{v}(\boldsymbol{\nabla}\cdot(\rho\boldsymbol{v}))$ and the continuity equation (3.9a), the momentum conservation equation (3.10a) can be written in Lagrangian form,

$$\rho(\partial_t + \boldsymbol{v}\cdot\boldsymbol{\nabla})\boldsymbol{v} = \boldsymbol{\nabla}\cdot\big[\boldsymbol{\tau} - p\,\mathbf{1}\big], \tag{3.10b}$$

known as the Navier–Stokes equation, which was treated adiabatically in Chapter 2. When devided by the density ρ, this equation states that the material derivative $\partial_t + (\boldsymbol{v}\cdot\boldsymbol{\nabla})$ of the velocity equals the force per mass due to viscous stresses and pressure, and it is thus the analogous to Newtons second law for fluids.

Finally, energy conservation implies that the rate of change $\partial_t\big(\rho\varepsilon + \frac{1}{2}\rho v^2\big)$ of the energy density (internal plus kinetic), is given by the power of the stress forces $\boldsymbol{v}\cdot\boldsymbol{\sigma}$ on the surface (direction $\boldsymbol{n}$), and the influx (direction $-\boldsymbol{n}$) of both heat conduction power $-k^{\mathrm{th}}\boldsymbol{\nabla}T$ and energy current density $(\rho\varepsilon + \frac{1}{2}\rho v^2)\boldsymbol{v}$. In differential form, neglecting heat sources in the volume, this becomes

$$\partial_t\big(\rho\varepsilon + \tfrac{1}{2}\rho v^2\big) = \boldsymbol{\nabla}\cdot\big[\boldsymbol{v}\cdot\boldsymbol{\tau} - p\,\boldsymbol{v} + k^{\mathrm{th}}\boldsymbol{\nabla}T - \rho(\varepsilon + \tfrac{1}{2}v^2)\boldsymbol{v}\big]. \tag{3.11a}$$

The following rewrite of the energy conservation equation to substitute terms involving ε by terms involving T and p is quite extensive. To make the rewrite less cumbersome, we initially leave out the terms $\partial_t(\frac{1}{2}\rho v^2)$, $\boldsymbol{\nabla}\cdot(\boldsymbol{v}\cdot\boldsymbol{\tau})$, $\boldsymbol{\nabla}\cdot(k^{\mathrm{th}}\boldsymbol{\nabla}T)$, and $\boldsymbol{\nabla}\cdot(\frac{1}{2}\rho v^2)\boldsymbol{v}$ as they are not rewritten, and then reintroduce them in the end. In the meanwhile they are represented by $X = -\partial_t(\frac{1}{2}\rho v^2) + \boldsymbol{\nabla}\cdot\big[\boldsymbol{v}\cdot\boldsymbol{\tau} + k^{\mathrm{th}}\boldsymbol{\nabla}T - (\frac{1}{2}\rho v^2)\boldsymbol{v}\big]$. Letting the time-derivative and divergence operators work on the product terms leads to

$$\varepsilon\partial_t\rho + \rho\partial_t\varepsilon = -p\boldsymbol{\nabla}\cdot\boldsymbol{v} - \boldsymbol{v}\cdot\boldsymbol{\nabla}p - \varepsilon\boldsymbol{\nabla}\cdot(\rho\boldsymbol{v}) - \rho\boldsymbol{v}\cdot\boldsymbol{\nabla}\varepsilon + X. \tag{3.11b}$$

The first term on the left and third term on the right cancel due to continuity Eq. (3.9a). Next, $\partial_t\varepsilon$ and $\boldsymbol{\nabla}\varepsilon$ is substituted by Eq. (3.5a), leading to

$$\rho c_p\partial_t T - \alpha_p T\partial_t p + \tfrac{p}{\rho}\partial_t\rho = -p\boldsymbol{\nabla}\cdot\boldsymbol{v} - (\boldsymbol{v}\cdot\boldsymbol{\nabla})p - \boldsymbol{v}\cdot\Big(\rho c_p\boldsymbol{\nabla}T - \alpha_p T\boldsymbol{\nabla}p + \tfrac{p}{\rho}\boldsymbol{\nabla}\rho\Big) + X. \tag{3.11c}$$

The third term on the left side and the first and fifth terms on the right side cancel due to continuity Eq. (3.9a). Resubstituting X, the energy conservation equation becomes

$$\partial_t\left(\tfrac{1}{2}\rho v^2\right) + \rho c_p\partial_t T - \alpha_p T\partial_t p + \rho c_p(\boldsymbol{v}\cdot\boldsymbol{\nabla})T + (1-\alpha_p T)(\boldsymbol{v}\cdot\boldsymbol{\nabla})p = \boldsymbol{\nabla}\cdot\Big(\boldsymbol{v}\cdot\boldsymbol{\tau} + k^{\mathrm{th}}\boldsymbol{\nabla}T - (\tfrac{1}{2}\rho v^2)\boldsymbol{v}\Big). \tag{3.11d}$$

Equation (3.11d) is the final form of the energy conservation equation, which will be used in the perturbation expansion.

The Energy conservation equation can also be written in Lagrangian form, similar to the Navier—Stokes formulation of momentum conservation. From Eq. (3.11b) we use the continuity equation as before and resubstitute X,

$$\rho\left(\partial_t + (\boldsymbol{v}\cdot\boldsymbol{\nabla})\right)\varepsilon + \partial_t\left(\tfrac{1}{2}\rho v^2\right) = \boldsymbol{\nabla}\cdot\left[\boldsymbol{v}\cdot\boldsymbol{\sigma} + k^{\mathrm{th}}\boldsymbol{\nabla}T\right] - (\boldsymbol{v}\cdot\boldsymbol{\nabla})\left(\tfrac{1}{2}\rho v^2\right) - \left(\tfrac{1}{2}\rho v^2\right)(\boldsymbol{\nabla}\cdot\boldsymbol{v}). \quad (3.12a)$$

Using the continuity equation (3.9a) to rewrite $\boldsymbol{\nabla}\cdot\boldsymbol{v} = -\frac{1}{\rho}(\partial_t\rho + \boldsymbol{v}\cdot\boldsymbol{\nabla}\rho)$, and letting the differential operators work on the product $\frac{1}{2}\rho v^2$, yields

$$\rho\left[\partial_t + (\boldsymbol{v}\cdot\boldsymbol{\nabla})\right](\varepsilon + \tfrac{1}{2}v^2) = \boldsymbol{\nabla}\cdot\left[\boldsymbol{v}\cdot\boldsymbol{\sigma} + k^{\mathrm{th}}\boldsymbol{\nabla}T\right]. \quad (3.12b)$$

When divided by the density ρ, this equation states that the material derivative $\partial_t + (\boldsymbol{v}\cdot\boldsymbol{\nabla})$ of the energy per mass $\varepsilon + \frac{1}{2}v^2$ equals the energy loss per mass due to dissipation and thermal conduction.

This concludes the treatment of the governing equations for the conservation of mass, momentum, and energy in a compressible Newtonian fluid.

3.3 Perturbation theory

The coupled non-linear equations for mass, momentum, and energy conservation can be solved directly using advanced non-linear solvers, and this is indeed necessary in situations with large amplitudes of the acoustic fields, such as shock waves and noise from jet engines. However, for situations where the acoustic field is a small perturbation to the equilibrium state, *i.e.* the amplitude of the acoustic density oscillations is small compared to the equilibrium density, the coupled nonlinear governing equations can be expanded into sets of coupled linear equations. In this thesis and the papers presented, we use the notation of implicit perturbation parameter, and there is no background flow $\boldsymbol{v}_0 = \boldsymbol{0}$. The perturbation expansion to second order becomes

$$\rho = \rho_0 + \rho_1 + \rho_2\ , \qquad \rho_0 \gg |\rho_1| \gg |\rho_2|\ , \quad (3.13a)$$
$$p = p_0 + p_1 + p_2\ , \qquad p_0 \gg |p_1| \gg |p_2|\ , \quad (3.13b)$$
$$T = T_0 + T_1 + T_2\ , \qquad T_0 \gg |T_1| \gg |T_2|\ , \quad (3.13c)$$
$$\boldsymbol{v} = \boldsymbol{0} + \boldsymbol{v}_1 + \boldsymbol{v}_2\ , \qquad c_s \gg |\boldsymbol{v}_1| \gg |\boldsymbol{v}_2|\ , \quad (3.13d)$$

where the subscripts indicate the perturbation order. ρ_0 and T_0 are simply the equilibrium density and temperature of the fluid, both in the case of a gas and a liquid. p_0 is the equilibrium pressure in the case of a gas, however, it is not the ambient equilibrium pressure in the case of a liquid. When treating liquids, as we do in the studies presented in the papers, p_0 should be thought of as an energy density related to the intermolecular bonds in the liquid. p_0 is not discussed in the literature, since only the gradient and time-derivative of the pressure is present in the governing equations, when the energy conservation equation has been reduced to the form Eq. (3.11d). The separation of the nonlinear governing equations into sets of linear equations is achieved by inserting the perturbation expansion Eq. (3.13) into the governing equations (3.9b), (3.10a), and (3.11d), and separating the

equations with respect to perturbation order, which represent a separation with respect to the magnitudes of the terms. The inequalities in Eq. (3.13) are the criteria that have to be fulfilled for the perturbation expansion of the governing equations to be valid. The inequality $c_s \gg \boldsymbol{v}_1$ follow from $\rho_0 \gg \rho_1$, which is explained in Section 2.3.

3.3.1 First-order equations

The first-order equations are obtained by inserting the perturbation expansion Eq. (3.13) into the governing equations (3.9b), (3.10a), and (3.11d) and keeping only first-order terms, which corresponds to a linearization of the governing equations.

$$\alpha_p \, \partial_t T_1 - \kappa_T \, \partial_t p_1 = \boldsymbol{\nabla} \cdot \boldsymbol{v}_1, \tag{3.14a}$$

$$\rho_0 \partial_t \boldsymbol{v}_1 = \boldsymbol{\nabla} \cdot \left[\boldsymbol{\tau}_1 - p_1 \mathbf{1}\right], \tag{3.14b}$$

$$\rho_0 c_p \, \partial_t T_1 - \alpha_p T_0 \, \partial_t p_1 = k_0^{\mathrm{th}} \nabla^2 T_1, \tag{3.14c}$$

where $\boldsymbol{\tau}_1$ is given by

$$\boldsymbol{\tau}_1 = \eta_0 \left[\boldsymbol{\nabla} \boldsymbol{v}_1 + (\boldsymbol{\nabla} \boldsymbol{v}_1)^{\mathrm{T}}\right] + \left[\eta_0^{\mathrm{b}} - \frac{2}{3}\eta_0\right] (\boldsymbol{\nabla} \cdot \boldsymbol{v}_1) \, \mathbf{1}. \tag{3.14d}$$

When considering a steady periodic state, where all first-order fields oscillate with constant amplitude and angular frequency ω, the first-order equations (3.14) can be transformed to frequency domain by describing physical fields through the complex notation

$$g_1(\boldsymbol{r}, t) = \mathrm{Re}\left[g_1(\boldsymbol{r}) \mathrm{e}^{-\mathrm{i}\omega t}\right], \tag{3.15}$$

where g_1 represents any first-order variable, and the value of $g_1(\boldsymbol{r}, t)$ is real, whereas the value of $g_1(\boldsymbol{r})$ is complex. This leads to the substitution $\partial_t \rightarrow -\mathrm{i}\omega$, and the first-order equations in frequency domain become

$$-\mathrm{i}\omega\alpha_p \, T_1 + \mathrm{i}\omega\kappa_T \, p_1 = \boldsymbol{\nabla} \cdot \boldsymbol{v}_1, \tag{3.16a}$$

$$-\mathrm{i}\omega\rho_0 \, \boldsymbol{v}_1 = \boldsymbol{\nabla} \cdot \left[\boldsymbol{\tau}_1 - p_1 \mathbf{1}\right], \tag{3.16b}$$

$$-\mathrm{i}\omega\rho_0 c_p \, T_1 + \mathrm{i}\omega\alpha_p T_0 \, p_1 = k_0^{\mathrm{th}} \nabla^2 T_1. \tag{3.16c}$$

From the first-order energy equation (3.16c), we define the thermal boundary layer thickness δ_{t}, similarly to how we defined δ_{s} in Eq. (2.64) from the first-order momentum equation (3.16b),

$$\delta_{\mathrm{t}} = \sqrt{\frac{2k_0^{\mathrm{th}}}{\rho_0 c_p \omega}} \, . \tag{3.17}$$

3.3.2 Time-dependent second-order equations

The second-order equations are obtained by inserting the perturbation expansion Eq. (3.13) into the governing equations (3.9b), (3.10a), and (3.11d) and keeping only second-order

terms, *i.e.* terms containing only one second-order variable g_2, or terms containing a product of two first-order variables, such as g_1^2,

$$0 = \kappa_T\,\partial_t p_2 - \alpha_p\,\partial_t T_2 + \boldsymbol{\nabla}\cdot\boldsymbol{v}_2 + \boldsymbol{v}_1\cdot(\kappa_T\boldsymbol{\nabla}p_1 - \alpha_p\boldsymbol{\nabla}T_1), \tag{3.18a}$$

$$\begin{aligned}\mathbf{0} = {}& \rho_0\partial_t\boldsymbol{v}_2 + \rho_0(\kappa_T\partial_t p_1 - \alpha_p\partial_t T_1)\boldsymbol{v}_1 + \rho_0(\kappa_T p_1 - \alpha_p T_1)\partial_t\boldsymbol{v}_1 \\ & - \boldsymbol{\nabla}\cdot\big[\boldsymbol{\tau}_2 - p_2\,\mathbf{1} - \rho_0\boldsymbol{v}_1\boldsymbol{v}_1\big],\end{aligned} \tag{3.18b}$$

$$\begin{aligned}0 = {}& \rho_0\boldsymbol{v}_1\partial_t\boldsymbol{v}_1 + \rho_0 c_p\big[\partial_t T_2 + \kappa_T p_1\partial_t T_1 - \alpha_p T_1\partial_t T_1\big] \\ & - \alpha_p\big[T_0\partial_t p_2 + T_1\partial_t p_1\big] + \rho_0 c_p(\boldsymbol{v}_1\cdot\boldsymbol{\nabla})T_1 + (1-\alpha_p T_0)(\boldsymbol{v}_1\cdot\boldsymbol{\nabla})p_1 \\ & - \boldsymbol{\nabla}\cdot\Big[\boldsymbol{v}_1\cdot\boldsymbol{\tau}_1 + k_0^{\mathrm{th}}\boldsymbol{\nabla}T_2 + k_1^{\mathrm{th}}\boldsymbol{\nabla}T_1\Big],\end{aligned} \tag{3.18c}$$

where $\boldsymbol{\tau}_2$ is given by

$$\begin{aligned}\boldsymbol{\tau}_2 = {}& \eta_0\Big[\boldsymbol{\nabla}\boldsymbol{v}_2 + (\boldsymbol{\nabla}\boldsymbol{v}_2)^{\mathrm{T}}\Big] + \Big[\eta_0^{\mathrm{b}} - \frac{2}{3}\eta_0\Big](\boldsymbol{\nabla}\cdot\boldsymbol{v}_2)\,\mathbf{1} \\ & + \eta_1\Big[\boldsymbol{\nabla}\boldsymbol{v}_1 + (\boldsymbol{\nabla}\boldsymbol{v}_1)^{\mathrm{T}}\Big] + \Big[\eta_1^{\mathrm{b}} - \frac{2}{3}\eta_1\Big](\boldsymbol{\nabla}\cdot\boldsymbol{v}_1)\,\mathbf{1}.\end{aligned} \tag{3.18d}$$

In Eqs. (3.18b) and (3.18c) we have applied the substitution $\rho_1 = \rho_0(\kappa_T p_1 - \alpha_p T_1)$, according to Eq. (3.4b), and we have included perturbations in the transport coefficients due to their temperature and density dependences, as introduced in Ref. [29] Appendix D,

$$\eta(T,\rho) = \eta_0(T_0,\rho_0) + \eta_1(T_0,T_1,\rho_0,\rho_1), \tag{3.19a}$$

$$\eta_1 = \left(\frac{\partial\eta}{\partial T}\right)_{T=T_0} T_1 + \left(\frac{\partial\eta}{\partial\rho}\right)_{\rho=\rho_0}\rho_1, \tag{3.19b}$$

$$\eta^{\mathrm{b}}(T,\rho) = \eta_0^{\mathrm{b}}(T_0,\rho_0) + \eta_1^{\mathrm{b}}(T_0,T_1,\rho_0,\rho_1), \tag{3.19c}$$

$$\eta_1^{\mathrm{b}} = \left(\frac{\partial\eta^{\mathrm{b}}}{\partial T}\right)_{T=T_0} T_1 + \left(\frac{\partial\eta^{\mathrm{b}}}{\partial\rho}\right)_{\rho=\rho_0}\rho_1, \tag{3.19d}$$

$$k^{\mathrm{th}}(T,\rho) = k_0^{\mathrm{th}}(T_0,\rho_0) + k_1^{\mathrm{th}}(T_0,T_1,\rho_0,\rho_1), \tag{3.19e}$$

$$k_1^{\mathrm{th}} = \left(\frac{\partial k^{\mathrm{th}}}{\partial T}\right)_{T=T_0} T_1 + \left(\frac{\partial k^{\mathrm{th}}}{\partial\rho}\right)_{\rho=\rho_0}\rho_1. \tag{3.19f}$$

The full thermoviscous second-order acoustic equations (3.18) are quite elaborate and it is not straight forward to understand the physical meaning of each term. That is why we limited the treatment in Chapter 2 to the adiabatic case, which greatly simplifies the equations. Moving on to the treatment of a steady periodic state, we will not treat the secondary oscillatory components $\boldsymbol{v}_2^{2\omega}$, $p_2^{2\omega}$, and $T_2^{2\omega}$ in the general thermodynamic case, but limit the presentation to the time-averaged components $\langle\boldsymbol{v}_2\rangle$, $\langle p_2\rangle$, and $\langle T_2\rangle$.

3.3.3 Time-averaged second-order equations

We now considering a steady oscillatory state and apply the time-averaging over one oscillation period $\langle ... \rangle$ to the equations to treat only the steady components of the density, velocity, and temperature. Since the time average of a time derivative of a steady periodic field is zero by definition, $\langle \partial_t(...) \rangle = 0$, it is advantages not to take the time average of the second-order time-dependent equation Eq. (3.18), but instead take the time average of the governing equations (3.9a), (3.10a), and Eq. (3.11a), and then use the thermodynamic relations Eqs. (3.4b) and (3.5b) to end up with the following second-order time-averaged equations,

$$\boldsymbol{\nabla} \cdot \langle \boldsymbol{v}_2 \rangle + \kappa_T \langle (\boldsymbol{v}_1 \cdot \boldsymbol{\nabla}) p_1 \rangle - \alpha_p \langle (\boldsymbol{v}_1 \cdot \boldsymbol{\nabla}) T_1 \rangle = 0, \tag{3.20a}$$

$$\boldsymbol{\nabla} \cdot \left[\langle \boldsymbol{\tau}_2 \rangle - \langle p_2 \rangle \mathbf{1} - \rho_0 \langle \boldsymbol{v}_1 \boldsymbol{v}_1 \rangle \right] = \mathbf{0}, \tag{3.20b}$$

$$\boldsymbol{\nabla} \cdot \left[k_0^{\text{th}} \boldsymbol{\nabla} \langle T_2 \rangle + \langle k_1^{\text{th}} \boldsymbol{\nabla} T_1 \rangle + \langle \boldsymbol{v}_1 \cdot \boldsymbol{\tau}_1 \rangle - (1 - \alpha_p T_0) \langle p_1 \boldsymbol{v}_1 \rangle - \rho_0 c_p \langle T_1 \boldsymbol{v}_1 \rangle \right] = 0, \tag{3.20c}$$

where $\langle \boldsymbol{\tau}_2 \rangle$ is given by

$$\begin{aligned} \langle \boldsymbol{\tau}_2 \rangle = {} & \eta_0 \left[\boldsymbol{\nabla} \langle \boldsymbol{v}_2 \rangle + \left(\boldsymbol{\nabla} \langle \boldsymbol{v}_2 \rangle \right)^{\mathrm{T}} \right] + \left[\eta_0^{\mathrm{b}} - \frac{2}{3} \eta_0 \right] \left(\boldsymbol{\nabla} \cdot \langle \boldsymbol{v}_2 \rangle \right) \mathbf{1} \\ & + \left\langle \eta_1 \left[\boldsymbol{\nabla} \boldsymbol{v}_1 + (\boldsymbol{\nabla} \boldsymbol{v}_1)^{\mathrm{T}} \right] \right\rangle + \left\langle \left[\eta_1^{\mathrm{b}} - \frac{2}{3} \eta_1 \right] (\boldsymbol{\nabla} \cdot \boldsymbol{v}_1) \, \mathbf{1} \right\rangle. \end{aligned} \tag{3.20d}$$

Solving the time-averaged second-order governing equations (3.20) together with a set of boundary conditions, we are able to predict the steady streaming flow $\langle \boldsymbol{v}_2 \rangle$ in the general thermodynamic case and the steady temperature perturbation $\langle T_2 \rangle$, which are both studied in Ref. [29] Appendix D.

3.4 Discussion of thermodynamic theory

In this section we discuss some aspects of the thermoviscous acoustic theory presented in this chapter. Based on dimensional analysis of the perturbation equations, we discuss the orders of magnitude of the first-order fields, the adiabatic approximation, and the magnitude of the acoustic streaming flow. Furthermore, the possible ambiguity of the combination of linear thermodynamic relations and second-order perturbation theory is discussed.

3.4.1 Magnitudes of first-order fields

We want to examine the validity of the adiabatic approximation used in Chapter 2, but first we need to determine the order of magnitude of the first-order fields in the steady periodic state. Considering the first-order momentum equation in frequency domain Eq. (3.16b) we

get the following relation for the orders of magnitude of the terms,

$$-\mathrm{i}\omega\rho_0\,\boldsymbol{v}_1 = \boldsymbol{\nabla}\cdot\left\{\eta_0\left[\boldsymbol{\nabla}\boldsymbol{v}_1 + (\boldsymbol{\nabla}\boldsymbol{v}_1)^{\mathrm{T}}\right] + \left[\eta_0^{\mathrm{b}} - \frac{2}{3}\eta_0\right](\boldsymbol{\nabla}\cdot\boldsymbol{v}_1)\,\mathbf{1} - p_1\mathbf{1}\right\} \quad \Rightarrow \tag{3.21a}$$

$$\omega\rho_0|\boldsymbol{v}_1| \sim \eta_0|\nabla^2\boldsymbol{v}_1| + |\boldsymbol{\nabla}p_1|, \tag{3.21b}$$

where "$\sim$" indicates same order of magnitude, which implies removal of numeric prefactors, disregarding signs, and assuming $\eta^{\mathrm{b}} \sim \eta$. If we evaluate $|\nabla^2\boldsymbol{v}_1|$ and $|\boldsymbol{\nabla}p_1|$ far from boundaries we obtain $|\boldsymbol{\nabla}| \sim k = \omega/c_s$. If we furthermore substitute $\kappa_s = 1/(\rho_0 c_s^2)$ Eq. (2.3) and $\delta_{\mathrm{s}}^2 = \frac{2\eta_0}{\rho_0\omega}$ Eq. (2.64), we can rewrite Eq. (3.21b) into

$$\frac{|\boldsymbol{v}_1|}{c_s} \sim \kappa_s|p_1| + \delta_{\mathrm{s}}^2 k^2\frac{|\boldsymbol{v}_1|}{c_s} \quad \Rightarrow \tag{3.21c}$$

$$\kappa_s|p_1| \sim \frac{|\boldsymbol{v}_1|}{c_s} + \mathcal{O}\big(\delta_{\mathrm{s}}^2 k^2\big), \tag{3.21d}$$

where we have utilized that the viscous diffusion length δ_{s} is much shorter than the acoustic wavelength $\lambda = 2\pi/k$. Equation (3.21d) relates the scale of the pressure field p_1 to the scale of the velocity field $\boldsymbol{v}_1$.

We can do a similar analysis of the first-order energy equation in the frequency domain Eq. (3.16c). Substituting the thermal diffusion length $\delta_{\mathrm{t}}^2 = \frac{2k_0^{\mathrm{th}}}{\rho_0 c_p\omega}$ Eq. (3.17) and the thermodynamic identity $\gamma - 1 = \frac{\alpha_p^2 t_0}{\kappa_s\rho_0 c_p}$ Eq. (3.7b), the dimensional analysis of Eq. (3.16c) becomes

$$-\mathrm{i}\omega\rho_0 c_p\,T_1 + \mathrm{i}\omega\alpha_p T_0\,p_1 = k_0^{\mathrm{th}}\nabla^2 T_1 \quad \Rightarrow \tag{3.22a}$$

$$|T_1| \sim \frac{\alpha_p T_0}{\rho_0 c_p}|p_1| + \frac{k_0^{\mathrm{th}}}{\omega\rho_0 c_p}|\nabla^2 T_1| \quad \Rightarrow \tag{3.22b}$$

$$|T_1| \sim \frac{\gamma-1}{\alpha_p}\kappa_s|p_1| + \delta_{\mathrm{t}}^2 k^2|T_1| \quad \Rightarrow \tag{3.22c}$$

$$\frac{\alpha_p|T_1|}{\gamma-1} \sim \kappa_s|p_1| \sim \frac{|\boldsymbol{v}_1|}{c_s}, \tag{3.22d}$$

where we have utilized that $\delta_{\mathrm{t}} \ll \lambda$. This relates the scale of the temperature field T_1 to the scales of the pressure field p_1 and the velocity field $\boldsymbol{v}_1$.

3.4.2 The adiabatic approximation

To discuss the validity of the adiabatic approximation, we first consider a standing bulk acoustic wave with the first-order temperature field $T_1 = T_{\mathrm{a}}\sin(k_0 y)$, far from any boundaries. The Laplace term in the first-order frequency-domain energy equation (3.16c) can

thus be rewritten as $\nabla^2 T_1 = -k_0^2 T_1$, and (3.16c) becomes

$$-\mathrm{i}\omega\rho_0 c_p\, T_1 + \mathrm{i}\omega\alpha_p T_0\, p_1 = k_0^{\mathrm{th}}\nabla^2 T_1 \qquad \Rightarrow \tag{3.23a}$$

$$\Big[1 - \mathrm{i}\frac{k_0^{\mathrm{th}}}{\rho_0 c_p \omega}(-k_0^2)\Big] T_1 = \frac{\alpha_p T_0}{\rho_0 c_p} p_1 \qquad \Rightarrow \tag{3.23b}$$

$$\Big[1 + \mathrm{i}\Gamma_{\mathrm{t}}\Big]\frac{\alpha_p T_1}{\gamma - 1} = \kappa_s p_1, \qquad \Gamma_{\mathrm{t}} = \frac{1}{2}k_0^2\delta_{\mathrm{t}}^2, \tag{3.23c}$$

where we have substituted δ_{t} and γ–1 defined in Eq. (3.17) and Eq. (3.7b), respectively. For MHz acoustics in water the thermal damping factor $\Gamma_{\mathrm{t}} \sim 10^{-6}$. From the thermodynamic relation Eq. (3.4b), using the identity $\kappa_T = \gamma\kappa_s$ Eq. (3.7a), we can now express ρ_1 in terms of p_1,

$$\frac{1}{\rho_0}\rho_1 = \kappa_T p_1 - \alpha_p T_1 \qquad \Rightarrow \tag{3.24a}$$

$$\frac{1}{\rho_0}\rho_1 = \gamma\kappa_s p_1 - \Big[1 - \mathrm{i}\Gamma_{\mathrm{t}}\Big](\gamma - 1)\kappa_s p_1 \qquad \Rightarrow \tag{3.24b}$$

$$\frac{1}{\rho_0}\rho_1 = \Big[1 + \mathrm{i}(\gamma - 1)\Gamma_{\mathrm{t}}\Big]\kappa_s p_1. \tag{3.24c}$$

The adiabatic approximation Eq. (2.2) is thus a good approximation for the bulk acoustic wave when $(\gamma - 1)\Gamma_{\mathrm{t}} \ll 1$, which is case for the fluids and operating conditions treated in this theses. However, near walls of high thermal conductivity relative to the fluid, where thermal boundary layers are present, the Laplace term $\nabla^2 T_1$ becomes much larger, such that $|\delta_{\mathrm{t}}^2 \nabla^2 T_1| \sim |T_1|$. Consequently, the adiabatic approximation is only valid inside the thermal boundary layer if $\gamma - 1 \ll 1$, which is still a fairly good approximation for water at 25 °C for which $\gamma = 1.01$.

3.4.3 Magnitude of the acoustic streaming flow

The order of magnitude of the steady streaming flow can be estimated from dimensional analysis of the governing equations. We first consider the time-averaged second-order momentum equation (3.20b) without perturbation of the viscosity, $\eta_1 = 0$,

$$\boldsymbol{\nabla} \cdot \big[\langle \boldsymbol{\tau}_2 \rangle - \langle p_2 \rangle \mathbf{1} - \rho_0 \langle \boldsymbol{v}_1 \boldsymbol{v}_1 \rangle\big] = \mathbf{0} \quad \Rightarrow \tag{3.25a}$$

$$\eta_0 |\nabla^2 \langle \boldsymbol{v}_2 \rangle| \sim |\boldsymbol{\nabla}\langle p_2 \rangle| + \rho_0 |\boldsymbol{\nabla} \cdot \langle \boldsymbol{v}_1 \boldsymbol{v}_1 \rangle|, \tag{3.25b}$$

where we have only included the larger component of $\boldsymbol{\nabla} \cdot \langle \boldsymbol{\tau}_2 \rangle$. $\boldsymbol{\nabla}\langle p_2 \rangle$ is a reaction to the gradient component of the source term $\rho_0 \boldsymbol{\nabla} \cdot \langle \boldsymbol{v}_1 \boldsymbol{v}_1 \rangle$ and can be disregarded in our determination of the order of magnitude of $\langle \boldsymbol{v}_2 \rangle$. Assuming the acoustic propagation to be parallel to a wall, the leading order of $|\nabla^2 \langle \boldsymbol{v}_2 \rangle|$ near the wall is $|\nabla^2 \langle \boldsymbol{v}_2 \rangle| \sim \frac{1}{\delta_{\mathrm{s}}^2}|\boldsymbol{v}_2|$. On the other hand $|\boldsymbol{\nabla} \cdot \langle \boldsymbol{v}_1 \boldsymbol{v}_1 \rangle| \sim k|\boldsymbol{v}_1|^2$, because the leading order component of $\boldsymbol{v}_1$ is parallel to the wall and thus $|\boldsymbol{\nabla} \cdot \boldsymbol{v}_1| \sim k|\boldsymbol{v}_1|$. With these orders of magnitude and the definition

$\delta_s = \sqrt{\frac{\eta_0}{\rho_0 \omega}}$ Eq. (2.64), Eq. (3.25b) becomes

$$\eta_0 \frac{1}{\delta_s^2} |\boldsymbol{v}_2| \sim \rho_0 k |\boldsymbol{v}_1|^2 \quad \Rightarrow \tag{3.25c}$$

$$|\boldsymbol{v}_2| \sim \frac{|\boldsymbol{v}_1|^2}{c_s}, \tag{3.25d}$$

which is consistent with Lord Rayleigh's result of $|\boldsymbol{v}_2| = \frac{3}{8}\frac{|\boldsymbol{v}_1|^2}{c_s}$ in Ref. [3].

We now include the perturbation of the viscosity Eq. (3.19a), and the equivalent of Eq. (3.25c) now becomes

$$\eta_0 \frac{1}{\delta_s^2} |\boldsymbol{v}_2| \sim |\eta_1| \frac{1}{\delta_s^2} |\boldsymbol{v}_1| + \rho_0 k |\boldsymbol{v}_1|^2 \quad \Rightarrow \tag{3.26a}$$

$$|\boldsymbol{v}_2| \sim \frac{|\eta_1|}{\eta_0} |\boldsymbol{v}_1| + \frac{|\boldsymbol{v}_1|^2}{c_s} \quad \Rightarrow \tag{3.26b}$$

$$|\boldsymbol{v}_2| \sim \frac{1}{\eta_0} \left[\left| \frac{\partial \eta}{\partial T} T_1 \right| + \left| \frac{\partial \eta}{\partial \rho} \rho_1 \right| \right] |\boldsymbol{v}_1| + \frac{|\boldsymbol{v}_1|^2}{c_s} \quad \Rightarrow \tag{3.26c}$$

$$|\boldsymbol{v}_2| \sim \frac{1}{\eta_0} \left[\left| \frac{\partial \eta}{\partial T} \right| \frac{\gamma - 1}{\alpha_p} \frac{|\boldsymbol{v}_1|}{c_s} + \left| \frac{\partial \eta}{\partial \rho} \right| \rho_0 \frac{|\boldsymbol{v}_1|}{c_s} \right] |\boldsymbol{v}_1| + \frac{|\boldsymbol{v}_1|^2}{c_s} \quad \Rightarrow \tag{3.26d}$$

$$|\boldsymbol{v}_2| \sim \left\{ 1 + \left| \frac{\partial \eta}{\partial T} \right| \frac{\gamma - 1}{\eta_0 \alpha_p} + \left| \frac{\partial \eta}{\partial \rho} \right| \frac{\rho_0}{\eta_0} \right\} \frac{|\boldsymbol{v}_1|^2}{c_s}. \tag{3.26e}$$

The estimated order of magnitude of $|\boldsymbol{v}_2|$ Eq. (3.26e) is as far as we can get with only dimensional analysis. The magnitude of the acoustic streaming near a planar wall, including effects of viscosity perturbations, have been solved analytically by Rednikov and Sadhal Ref. [8], which in our notation becomes

$$|\boldsymbol{v}_2| = \left\{ 1 + \frac{\frac{2}{3}\sqrt{\frac{c_p \eta_0}{k_0^{\text{th}}}}}{1 + \frac{c_p \eta_0}{k_0^{\text{th}}}} \left[(\gamma - 1) - \frac{\gamma - 1}{\eta_0 \alpha_p} \left(\frac{\partial \eta_1}{\partial T} \right)_p \right] \right\} \frac{3}{8} \frac{|\boldsymbol{v}_1|^2}{c_s}. \tag{3.27}$$

The fraction $\frac{c_p \eta_0}{k_0^{\text{th}}}$ is known as the Prandtl number and is the ratio of momentum diffusivity and thermal diffusivity, and it can also be expressed in terms of the viscous and thermal boundary layers thicknesses as $\frac{\delta_s^2}{\delta_t^2}$. For water at room temperature the Prandl number is approximately 4. The term $\frac{\gamma - 1}{\eta_0 \alpha_p} \left(\frac{\partial \eta_1}{\partial T} \right)_p$ in Eq. (3.27) agrees with the second term in the result from the dimensional analysis Eq. (3.26e). In the analytical calculation of Ref. [8], they show that the pressure dependency of the viscosity has no influence in the case of a planar wall, and thus the only viscosity derivative that enters the final expression Eq. (3.27) is $\left(\frac{\partial \eta_1}{\partial T} \right)_p$. Furthermore, the exact numerical result includes another term, scaling by $\gamma - 1$ in Eq. (3.27), which enters due to non-adiabatic compressibility, and which is not predicted by the dimensional analysis Eq. (3.26e).

In conclusion, the magnitude of the acoustic streaming velocity predicted by the dimensional analysis Eq. (3.26e) is in agreement with the order of magnitude of the exact analytical result Eq. (3.27). The corrections to the magnitude of the acoustic streaming, due to perturbation in the viscosity, is treated numerically in Ref. [29] Appendix D and is on the order of 20% at room temperature.

3.4.4 Thermodynamics and perturbation theory

In this section the possible ambiguity of the combination of linear thermodynamic relations and second-order perturbation theory is discussed. This topic is outside the scope of the studies presented in this thesis, and the considerations presented here are meant as an outlook on the further development of the theory of second-order perturbation theory applied in acoustics.

Comparing the unperturbed governing equations (3.9b), (3.10a), and (3.11d), and the second-order perturbation equations (3.18), it may seem inconsistent that we introduce perturbations in the coefficients η, η^{b}, and k^{th}, but not in the thermodynamic coefficients κ_T, α_p, and c_p. The explanation of this is grounded on how we treat the thermodynamics.

The thermodynamic relations in Section 3.1 are based on a linear Taylor expansions of the equation of state about a thermodynamic equilibrium state, such as

$$\mathrm{d}\rho = \left(\frac{\partial\rho}{\partial T}\right)_p \mathrm{d}T + \left(\frac{\partial\rho}{\partial p}\right)_T \mathrm{d}p. \tag{3.28}$$

The parameters κ_T, α_p, and c_p are some of the coefficients that arise in these linear expansions and are by definition evaluated at the equilibrium state. They are thus properties of the equilibrium state, independent of the perturbed state of the fluid.

The coefficients η, η^{b}, and k^{th} are also coefficients in linear constitutive relation, *e.g.* the definition of the dynamic viscosity η from the linear relation between shear stress and shear velocity in a Couette flow. However, since they are not defined from thermodynamic constitutive relations, but rather related to transport phenomena, such as viscous and thermal diffusion, they depend on the perturbed state of the fluid, and not just the equilibrium state.

This explains why we introduce perturbations in the transport coefficients η, η^{b}, and k^{th}, but not in the thermodynamic coefficients κ_T, α_p, and c_p. However, it may still seem inconsistent that we only apply linear relations between the thermodynamic variables, while we are treating second-order perturbations of the independent thermodynamic variables. To avoid this inconsistency we need a new set of thermodynamic relations based on second-order Taylor expansions, such as

$$\mathrm{d}\rho = \left(\frac{\partial\rho}{\partial T}\right)_p \mathrm{d}T + \left(\frac{\partial\rho}{\partial p}\right)_T \mathrm{d}p + \frac{1}{2}\left(\frac{\partial^2\rho}{\partial T^2}\right)_p (\mathrm{d}T)^2 + \frac{1}{2}\left(\frac{\partial^2\rho}{\partial p^2}\right)_T (\mathrm{d}p)^2 \,. \tag{3.29}$$

This would introduce new expansion coefficients, such as $\left(\frac{\partial^2\rho}{\partial p^2}\right)_T$, which are also properties of the equilibrium state, independent of the perturbed state of the fluid. The values of the

new second-order thermodynamic coefficients for water could be obtained from the complex fit of the equation of state provided by the International Association of the Properties of Water and Steam (IAPWS) in Ref. [44].

Finally, it is difficult say how the second-order thermodynamic relations, such as Eq. (3.29), would impact our theoretical results of the second-order acoustic phenomena, such as the radiation force and streaming flow. In experiments the energy density in the channel is calibrated through observations of particle motion due to the radiation force and streaming-induced drag force. Consequently, it is not possible to make a comparison of theory and experiments for the magnitude of one of these forces independent of the other. To give a specific example, the comparison of the drag-force-dominated particle motion in Ref. [11] Appendix B rely on the assumption that the theoretical expression for the radiation force is correct, as this is used for the calibration of the energy density based on radiation-force-dominated particle motion.

This ends the discussion of the possible inconsistency in the combination of first-order thermodynamics and second-order acoustics. The use of second-order thermodynamic relations are left as a suggestion for future work, or at least to explain why this is not necessary.

3.5 Summary of thermodynamic theory

In this chapter we have derived the governing equations for the conservation of mass, momentum and energy in a compressible Newtonian fluid. The governing equations were rewritten using linear thermodynamic relations and expanded using second-order perturbation theory. Through dimensional analysis, we discussed the relative orders of magnitude of the first-order acoustic fields, the adiabatic approximation, and the magnitude of the acoustic streaming. As an outlook for future work, the possible ambiguity of the combination of linear thermodynamic relations and second-order perturbation theory was discussed.

Chapter 4

Acoustofluidic forces on particles

In this chapter we describe the forces acting on a particle suspended in a water-filled microchannel and in the presence of an acoustic field. The treatment is partly based on the analytical study of the acoustic radiation force presented by Karlsen and Bruus Ref. [16]. The particle is defined by its volume $\Omega(t)$, its surface $\partial\Omega(t)$, the outward-pointing surface normal vector $\boldsymbol{n}(\boldsymbol{r},t)$, and the velocity of its center of mass $\boldsymbol{u}(t)$, which all depend on time due to the acoustic oscillations of the particle. The total force on the particle is given by the stress on the particle surface, exerted by the surrounding fluid, and the body force densities $\boldsymbol{f}$ acting on the particle volume,

$$m\frac{\mathrm{d}\boldsymbol{u}}{\mathrm{d}t} = \oint_{\partial\Omega(t)} \boldsymbol{\sigma}\cdot\boldsymbol{n}\,\mathrm{d}A + \int_{\Omega(t)} \boldsymbol{f}\,\mathrm{d}V. \tag{4.1}$$

In the following, we neglect the gravitational body force on the particle and the buoyancy contribution to the surface stress from the hydrostatic pressure. This is reasonable for most studies of microparticles in water, as the sedimentation time is much longer than other relevant timescales, such as focusing time. It is customary to further separate the surface force into two parts: the radiation force $\boldsymbol{F}^{\mathrm{rad}}$ originating from the stress exerted directly by the acoustic wave, and the drag force $\boldsymbol{F}^{\mathrm{drag}}$ originating from the stress exerted by an external flow,

$$m\frac{\mathrm{d}\boldsymbol{u}}{\mathrm{d}t} = \boldsymbol{F}^{\mathrm{drag}} + \boldsymbol{F}^{\mathrm{rad}}. \tag{4.2}$$

$\boldsymbol{F}^{\mathrm{rad}}$ represents the force from scattering of an acoustic wave on a particle in an infinite, initially quiescent fluid domain, thus also including the effects of streaming flow generated at the particle surface. $\boldsymbol{F}^{\mathrm{drag}}$ represents the effects of a finite domain, and assuming an initially quiescent state of the fluid, $\boldsymbol{F}^{\mathrm{drag}}$ is given by the Stokes drag force induced by the acoustic streaming flow generated at the boundaries of the finite water domain.

We define the acoustic radiation force by

$$\boldsymbol{F}^{\mathrm{rad}} = \oint_{\partial\Omega(t)} \left(\boldsymbol{\sigma} - \boldsymbol{\sigma}^{\mathrm{ext}}\right)\cdot\boldsymbol{n}\,\mathrm{d}A, \tag{4.3}$$

where $\boldsymbol{\sigma}^{\text{ext}}$ is the stress exerted by the external flow. The radiation force is usually defined by the time-average of Eq. (4.3) for a periodic state, where all transients have diminished [16]. In the limit where the particle radius a is much smaller than the acoustic wavelength $a \ll \lambda$, relevant for microparticle acoustophoresis, the time-averaged radiation force can be expressed in terms of the incoming acoustic fields p_{in} and $\boldsymbol{v}_{\text{in}}$ and the scattering coefficients f_0 and f_1 [15],

$$\left\langle \boldsymbol{F}^{\text{rad}} \right\rangle = -\pi a^3 \left[\frac{2\kappa_s}{3} \operatorname{Re}\left\{ f_0^* p_{\text{in}}^* \boldsymbol{\nabla} p_{\text{in}} \right\} - \rho_0 \operatorname{Re}\left\{ f_1^* \boldsymbol{v}_{\text{in}}^* \cdot \boldsymbol{\nabla} \boldsymbol{v}_{\text{in}} \right\} \right]. \tag{4.4}$$

The scattering coefficients f_0 and f_1 depend on the thermodynamic and transport properties of the fluid and the particle. For a thorough study of this, including effects of both viscous and thermal boundary layers, the reader is referred to Karlsen and Bruus Ref. [16]. In the limit where the particle radius is much larger than the thicknesses of the viscous and thermal boundary layers, $a \ll \delta_{\text{s}}$ and $a \ll \delta_{\text{t}}$, the scattering coefficients become

$$f_0 = 1 - \tilde{\kappa}_s, \qquad \tilde{\kappa}_s = \frac{\kappa_s^{\text{p}}}{\kappa_s}, \tag{4.5a}$$

$$f_1 = \frac{2(\tilde{\rho} - 1)}{2\tilde{\rho} + 1}, \qquad \tilde{\rho}_0 = \frac{\rho_0^{\text{p}}}{\rho_0}, \tag{4.5b}$$

where superscript "p" refers to the properties of the particle. For a one-dimensional standing acoustic wave of pressure $p_1(\boldsymbol{r}, t) = \operatorname{Re}\left\{ -p_{\text{a}} \sin(k_0 y) \mathrm{e}^{-\mathrm{i}\omega t} \right\}$, velocity $\boldsymbol{v}_1(\boldsymbol{r}, t) = \operatorname{Re}\left\{ \mathrm{i} v_{\text{a}} \cos(k_0 y) \mathrm{e}^{-\mathrm{i}\omega t} \mathbf{e}_y \right\}$ and acoustic energy density $E_{\text{ac}} = \frac{1}{4}\kappa_s p_{\text{a}}^2 = \frac{1}{4}\rho_0 v_{\text{a}}^2$, the acoustic radiation force $\left\langle \boldsymbol{F}_{\text{1D}}^{\text{rad}} \right\rangle$ becomes

$$\left\langle \boldsymbol{F}_{\text{1D}}^{\text{rad}} \right\rangle = -4\pi \Phi a^3 k_0 E_{\text{ac}} \sin(2k_0 y) \mathbf{e}_y, \tag{4.6a}$$

$$\Phi = \frac{1}{3} \operatorname{Re}\left\{ f_0 \right\} + \frac{1}{2} \operatorname{Re}\left\{ f_1 \right\}, \tag{4.6b}$$

where Φ is referred to as the contrast factor. When Φ is positive, the radiation force is directed towards the pressure nodes, and the particles are referred to as "acoustically hard", which is the case for particles with low compressibility and high mass density. All particles treated in this thesis are acoustically hard.

The Stokes drag force induced by the external velocity field $\boldsymbol{v}^{\text{ext}}$ is given by

$$\boldsymbol{F}^{\text{drag}} = \oint_{\partial\Omega(t)} \boldsymbol{\sigma}^{\text{ext}} \cdot \boldsymbol{n} \, \mathrm{d}A = 6\pi\eta a \Big(\boldsymbol{v}^{\text{ext}} - \boldsymbol{u} \Big). \tag{4.7}$$

Assuming periodic acoustic fields and an initially quiescent state of the fluid, the time-averaged drag force becomes

$$\left\langle \boldsymbol{F}^{\text{drag}} \right\rangle = 6\pi\eta a \Big(\left\langle \boldsymbol{v}_2^{\text{ext}} \right\rangle - \left\langle \boldsymbol{u} \right\rangle \Big), \tag{4.8}$$

where $\left\langle \boldsymbol{v}_2^{\text{ext}} \right\rangle$ is the steady external streaming velocity and $\left\langle \boldsymbol{u} \right\rangle$ is the velocity of the particle averaged over one oscillation period of the acoustic wave.

4.1 Critical particle size

The motion of the suspended particles are determined by the interplay between $\boldsymbol{F}^{\text{rad}}$ and $\boldsymbol{F}^{\text{drag}}$ Eq. (4.2). Due to the difference in the dependence on the particle size of the two forces, the motion of suspended particles is largely determined by their size. The magnitude of the acoustic streaming Eq. (3.27) can be expressed as $\left|\langle \boldsymbol{v}_2 \rangle\right| = \Psi \frac{v_{\text{a}}^2}{c_s} = 4\Psi \frac{E_{\text{ac}}}{\rho_0 c_s}$, where Ψ is a factor of order unity, that depends primarily on the position of the particle in the channel and also the thermodynamic state of the fluid. Balancing the magnitude of the two forces $\left|\langle \boldsymbol{F}^{\text{rad}} \rangle\right| = \left|\langle \boldsymbol{F}^{\text{drag}} \rangle\right|$ for a fixed particle, $\langle \boldsymbol{u} \rangle = \boldsymbol{0}$, yields

$$
\begin{aligned}
4a_{\text{c}}^2 &= 24 \frac{\Psi}{\Phi} \frac{\eta}{\rho_0 \omega} \Rightarrow \\
2a_{\text{c}} &= \sqrt{24 \frac{\Psi}{\Phi} \frac{\eta}{\rho_0 \omega}} = \sqrt{12 \frac{\Psi}{\Phi}}\, \delta_{\text{s}},
\end{aligned}
\tag{4.9}
$$

where a_{c} is the critical particle radius at which the magnitude of the two forces are equal. In Eq. (4.9) the channel geometry enters through Ψ, particle and liquid material parameters enters through Φ, and liquid parameters and frequency through δ_{s}. For polystyrene particles in water at 2 MHz, the critical particle size a_{c} is around 2 µm. Larger particles are dominated by the acoustic radiation force and focused at the pressure nodes, whereas smaller particles are dominated by the streaming-induced drag force and follow the rotational motion of the fluid. The transition in particle motion from radiation domination to streaming domination is studied in Ref. [28] Appendix A.

This concludes the treatment of the forces acting on suspended particles in acoustofluidic systems. The acoustic streaming flow counteracts acoustophoretic focusing of particles below the critical particle limit, such as bacteria or proteins. One of the main goals of this thesis work has been to find ways to overcome this limitation. This was achieved in Ref. [31] Appendix C by utilizing overlapping resonances of a nearly-square channel to create a single roll streaming flow, that did not counteract the acoustophoretic focusing by the weak radiation force.

Chapter 5

Numerical model

The numerical work presented in this thesis is based on the Finite Element Method (FEM) numerical scheme. The equations are implemented and solved in the commercially available FEM software Comsol Multiphysics (version 4.2a-4.4b). This work presents no improvements of numerical solvers, but focuses on how to use existing numerical tools to enlighten and solve physics problems. The quality control of our numerical work is based on the following two principles. Firstly, we check the converge of the numerical solution with respect to parameters such as spatial and temporal resolution, which can be considered an internal consistency check of the numerical model. Secondly, we compare the numerical results to analytical results and experimental measurements, to test the physical assumptions of both analytics and numerics. Awareness of the limitation of the physical assumptions that goes into the theoretical models are the key to developing models that can accurately predict the outcome of associated experiments, which requires a great deal of both theoretical and experimental insight.

In this chapter a very brief introduction to the FEM scheme is given, along with a practical example of how an equation is rewritten and implemented in Comsol. Furthermore, examples of spatial and temporal convergence analysis are given. For a more thorough introduction to FEM the reader is referred to Refs. [45, 46].

5.1 The Finite Element Method

The basic principle of the Finite Element Method is to expand the physical fields on a set of basis function, also referred to as test functions, similar to Fourier analysis where a signal is expanded in terms of harmonic functions. In FEM the spatial domain is divided by a grid (mesh), and each basis function is associated to a node point, where it takes the value of one, while it is zero at neighboring nodes.

We now consider a stationary inhomogeneous boundary value problem defined by a set of boundary condition and a bulk partial differential equation (PDE),

$$\mathcal{L}\{g(\boldsymbol{r})\} = F(\boldsymbol{r}), \tag{5.1}$$

where $\mathcal{L}$ is a differential operator, g is a physical field, $\boldsymbol{r}$ is the spatial coordinate, and F

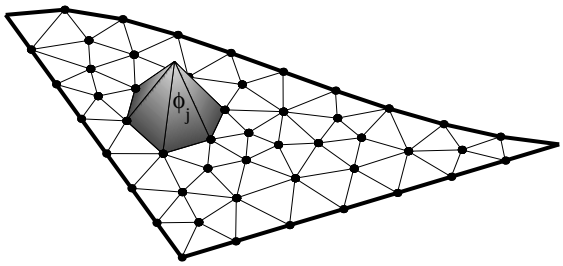

Figure 5.1: Sketch of a triangular computational mesh for the finite element method (FEM). The domain Ω is divided into triangular regions and a basis function ϕ_j (in text ψ_n) is associated to each nodal point. The basis function is depicted as a piecewise linear function, but in general, it can have a higher-order spatial dependence. Figure adapted from Ref. [45].

is a forcing term. We now expand $g(\boldsymbol{r})$ on a set of basis functions ψ_n,

$$g(\boldsymbol{r}) = \sum_n c_n \psi_n(\boldsymbol{r}), \tag{5.2}$$

where c_n are the expansion coefficients. Defining the defect $d(\boldsymbol{r})$,

$$d(\boldsymbol{r}) = \mathcal{L}\{g(\boldsymbol{r})\} - F(\boldsymbol{r}), \tag{5.3}$$

the expansion of $g(\boldsymbol{r})$ Eq. (5.2) will provide an approximative solution to the strong form equation (5.1), if the inner product of each basis function and the defect $d(\boldsymbol{r})$ vanishes

$$\int_\Omega \left[\psi_m(\boldsymbol{r})\, d(\boldsymbol{r})\right] \mathrm{d}\boldsymbol{r} = \left\langle \psi_m(\boldsymbol{r}), d(\boldsymbol{r}) \right\rangle = \left\langle \psi_m(\boldsymbol{r}), \left[\mathcal{L}\left\{ \sum_n c_n \psi_n(\boldsymbol{r}) \right\} - F(\boldsymbol{r}) \right] \right\rangle = 0, \qquad \text{for all } m. \tag{5.4}$$

This is a formalized way of saying that the values of the coefficients c_n is chosen such as to obtain the best approximative solution to the governing equation (5.1). A solution fulfilling Eq. (5.4) is called a weak solution, whereas a solution fulfilling Eq. (5.1) is called a strong solution.

If the differential operator $\mathcal{L}$ is linear, Eq. (5.4) becomes

$$\sum_n c_n \left\langle \psi_m(\boldsymbol{r}), \mathcal{L}\psi_n(\boldsymbol{r}) \right\rangle = \left\langle \psi_m(\boldsymbol{r}), F(\boldsymbol{r}) \right\rangle, \qquad \text{for all } m, \tag{5.5}$$

which can be written as a matrix equation

$$\boldsymbol{K}\boldsymbol{c} = \boldsymbol{f}, \tag{5.6}$$

where $\boldsymbol{K}$ is refereed to as the stiffness matrix and its elements are given by $K_{m,n} = \langle \psi_m, \mathcal{L}\psi_n \rangle$, $\boldsymbol{c}$ is a vector with the expansion coefficient c_n, and f is the force vector with elements $f_m = \langle \psi_m, F \rangle$. In order to find a weak solution to the governing equation (5.1), we thus need to solve the matrix equation (5.6) for the unknown expansion coefficients in $\boldsymbol{c}$.

In the following we consider an inhomogeneous PDE on the general divergence form

$$\boldsymbol{\nabla} \cdot \boldsymbol{J} + F = 0, \tag{5.7}$$

where $\boldsymbol{J}$ is a vector and F a scalar, but $\boldsymbol{J}$ could as well be a tensor and F a vector. A physical interpretation of Eq. (5.7) is that the divergence of a current density $\boldsymbol{J}$ is equal to a source density $-F$. Most of the equations encountered in physics originate from conservation laws and can be written on the form Eq. (5.7). To find a weak solution we insert the defect $d(\boldsymbol{r}) = \boldsymbol{\nabla} \cdot \boldsymbol{J} + F$ from Eq. (5.7) in Eq. (5.4),

$$\int_\Omega \Big[\psi_m \left(\boldsymbol{\nabla} \cdot \boldsymbol{J} + F\right)\Big] \, \mathrm{d}\boldsymbol{r} = 0, \qquad \text{for all } m. \tag{5.8}$$

Utilizing $\boldsymbol{\nabla} \cdot (\psi_m \boldsymbol{J}) = \psi_m \boldsymbol{\nabla} \cdot \boldsymbol{J} + \boldsymbol{J} \cdot \boldsymbol{\nabla} \psi_m$ and Gauss's theorem, we can rewrite Eq. (5.8) into

$$\int_{\partial\Omega} \Big[\psi_m \boldsymbol{J} \cdot \boldsymbol{n}\Big] \, \mathrm{d}\boldsymbol{r} + \int_\Omega \Big[- \boldsymbol{\nabla} \psi_m \cdot \boldsymbol{J} + \psi_m F\Big] \, \mathrm{d}\boldsymbol{r} = 0, \qquad \text{for all } m, \tag{5.9}$$

where $\boldsymbol{n}$ is the outwards pointing surface normal. Equation (5.9) is the theoretical equation we should have in mind when implementing bulk equation in Comsol, as exemplified in Section 5.2.

Boundary conditions can be implemented either as Neumann conditions or Dirichlet conditions. For Neumann conditions the current density $\boldsymbol{J}$ is assigned a fixed value $\boldsymbol{J}_{\mathrm{bd}}$ at the boundary by altering the boundary integral in Eq. (5.9),

$$\int_{\partial\Omega} \Big[\psi_m (\boldsymbol{J} - \boldsymbol{J}_{\mathrm{bd}}) \cdot \boldsymbol{n}\Big] \, \mathrm{d}\boldsymbol{r} = 0, \qquad \text{for all } m. \tag{5.10}$$

For Dirichlet conditions a function M, depending on both the physical fields and the spatial coordinates, is forced to be zero at the boundary

$$M(g(\boldsymbol{r}), \boldsymbol{r}) = 0. \tag{5.11}$$

The Dirichlet condition is implemented by use of a Lagrange multiplier, which is a field that lives only at the boundary where the Dirichlet condition is applied. For an explanation on how this boundary condition is coupled to the governing equation (5.9), the reader is referred to Refs. [45, 46].

5.2 Implementation of equations in Comsol Multiphysics

In this section a practical example is given of how to implement an equation in Comsol, following the theoretical expression Eq. (5.9). We treat the first-order frequency-domain equation (3.14c) governing the temperature field T_1, which is rewritten as

$$-\mathrm{i}\omega\rho_0 c_p T_1 + \mathrm{i}\omega\alpha_p T_0 p_1 = k_0^{\mathrm{th}} \nabla^2 T_1 \quad \Rightarrow \tag{5.12}$$

$$\boldsymbol{\nabla} \cdot (k_0^{\mathrm{th}} \boldsymbol{\nabla} T_1) + \mathrm{i}\omega(\rho_0 c_p T_1 - \alpha_p T_0 p_1) = 0. \tag{5.13}$$

Following the general divergence equation (5.7), we define

$$\boldsymbol{J} = k_0^{\mathrm{th}} \boldsymbol{\nabla} T_1, \quad F = \mathrm{i}\omega(\rho_0 c_p T_1 - \alpha_p T_0 p_1). \tag{5.14}$$

Considering a Comsol model based on a two-dimensional domain in the (y,z)-plane, in which we have defined the geometry, material parameters and created the necessary "Physics", using the "Weak Form PDE", we define the following three variables in Comsol

$$\texttt{Jy} = \texttt{kth0}^*\texttt{T1y} \tag{5.15}$$

$$\texttt{Jz} = \texttt{kth0}^*\texttt{T1z} \tag{5.16}$$

$$\texttt{F} = \texttt{i}^*\texttt{omega}^*(\texttt{rho0}^*\texttt{cp}^*\texttt{T1} - \texttt{alpp}^*\texttt{T0}^*\texttt{p1}) \ , \tag{5.17}$$

where `T1y` and `T1z` are the build-in spatial derivatives of the variable `T1`. In the "Weak Form PDE" we would then implement the bulk equation (5.13) as the bulk integral in Eq. (5.9),

$$-\texttt{test(T1y)}^*\texttt{Jy} - \texttt{test(T1z)}^*\texttt{Jz} + \texttt{test(T1)}^*\texttt{F} \ , \tag{5.18}$$

where `test(T1)`, `test(T1y)`, and `test(T1y)` are the Comsol notations for ψ, $\partial_y\psi$, and $\partial_z\psi$, respectively. This provides a consistent way to implement all equations in the model, and this helps to avoid typographical errors in the code. Furthermore, this makes it easy to understand the meaning of the default "zero flux" boundary condition in Comsol, which simply implies that $\boldsymbol{J}\cdot\boldsymbol{n} = 0$, as stated by the surface integral in Eq. (5.9). For a model example of this method of implementation, the reader is referred to the Comsol model provided in the supplemental material to Ref. [30] Appendix E.

5.3 Spatial resolution

The physical fields are expanded by basis function that are defined on a spatial mesh of elements that can have different shapes, such as triangular, rectangular, or free quadrilateral shape. Examples of a triangular and a rectangular mesh are shown in Fig. 5.2(a) and (b), reprinted from Ref. [29] Appendix D. A triangular mesh is advantages because it has no favorable direction and it can smoothly resolve small features of the domain. The rectangular mesh is advantages because it allows for high aspect ratio elements and thus typically requires fewer elements in comparison to the triangular mesh, resulting in increased computational efficiency. The choice of elements is often determined by the geometry of the problem, for curved boundaries the triangular elements are most efficient, while for planar boundaries the square elements offer the best flexibility. During the studies presented in this thesis, the meshing of the rectangular channel cross section has been continuously improved, with the culmination of the customized largely-inhomogeneous rectangular mesh used in Ref. [30] Appendix E, consisting of elements ranging in size from 0.16-µm-by-0.16-µm in the corners of the domain, 0.16-µm-by-24-µm along the sides, and 24-µm-by-24-µm in the bulk of the domain.

The numerical convergence with respect to the spatial resolution is considered through the relative convergence parameter $C(g)$ defined in Ref. [28] Appendix A by

$$C(g) = \sqrt{\frac{\int \left(g - g_{\mathrm{ref}}\right)^2 \,\mathrm{d}y\,\mathrm{d}z}{\int \left(g_{\mathrm{ref}}\right)^2 \,\mathrm{d}y\,\mathrm{d}z}}, \tag{5.19}$$

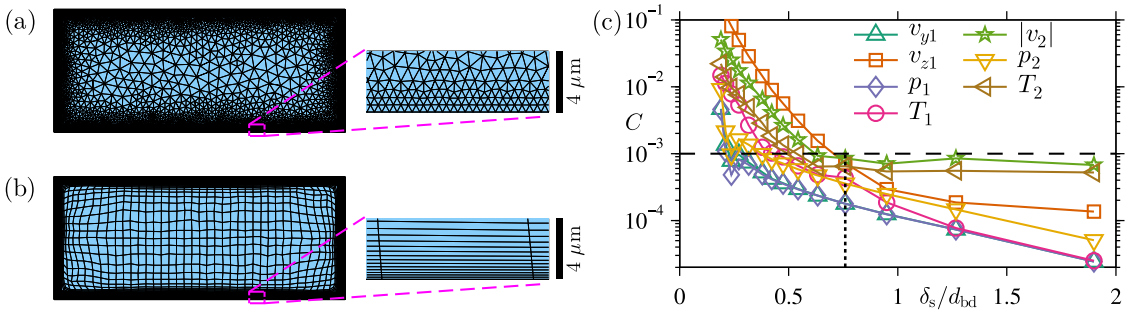

Figure 5.2: Spatial mesh and numerical convergence analysis. (a) Triangular mesh with a gradually increasing element size from 0.5 µm at the boundaries to 20 µm in the bulk, consisting of 30246 elements. (b) Rectangular mesh with thin elongated 0.1-µm-by-10-µm elements at the boundaries and gradually changing to nearly square 10-µm-by-10-µm elements in the bulk, consisting of 3308 elements. (c) The convergence parameter C (semilog scale) of Eq. (5.19) for all first-order steady harmonic fields and second-order time-averaged fields versus the numerical resolution defined by δ_s/d_{bd}, where δ_s is the viscous boundary layer thickness Eq. (2.64) and d_{bd} is the mesh-element size at the boundary. The fields are solved on triangular meshes with different boundary element sizes, but all with fixed bulk element size $d_{bk} = 20$ µm and growth rate $\alpha = 1.3$, while the reference solution is calculated for $d_{bd} = 0.15$ µm, $d_{bk} = 2$ µm, and $\alpha = 1.3$. The vertical dotted line indicates the solution for $d_{bd} = 0.5$ µm which was chosen as the default value for the simulations in Ref. [29] Appendix D. Figure adapted from Ref. [29] Appendix D.

where $C(g)$ is the relative convergence of a solution g with respect to a reference solution g_{ref}. The reference solution should be calculated for a spatial resolution that is better than what is expected to be necessary. Figure 5.2(c) shows an example of the numerical convergence with respect to the spatial resolution δ_s/d_{bd}, where δ_s is the viscous boundary layer thickness Eq. (2.64) and d_{bd} is the mesh-element size at the boundary. The convergence parameter C is shown on a logarithmic scale and the graphs show how C initially decays exponentially, until a point where no further improvement is seen for the second-order velocity and temperature. This demonstrates internal consistency for the numerical results and provides insight to choose the most efficient mesh sizes.

5.4 Temporal resolution

When solving the governing equations in time domain, compared to solving the periodic state, the solution is obtained by a time-marching scheme that estimates the time-derivatives and steps forward in time with a given time step Δt. The necessary temporal resolution for the time-marching scheme can be determined by the Courant–Friedrichs–Lewy (CFL) condition, also referred to as just the Courant number

$$\mathrm{CFL} = \frac{c_s \, \Delta t}{\Delta r} \leq \mathrm{CFL}_{\max}, \tag{5.20}$$

where Δt is the temporal discretization and Δr is the spatial discretization. This means that the length over which a disturbance travels within a time step Δt should be some fraction of the mesh element size, ultimately ensuring that disturbances do not travel through a mesh element in one time step. A more accurate interpretation of the CFL-

condition is that it ensures that the error on the approximation of the time-derivative is smaller than the error on the approximation of the spatial-derivatives. Consequently, the value of $\mathrm{CFL}_{\max}$ depends on the specific solver and on the order of the basis functions. For fourth-order basis functions and the generalized alpha solver [47], Ref. [48] reports a value of $\mathrm{CFL}_{\max}^{4\mathrm{th}} = 0.05$, which is an empirical result for a specific model.

To determine a reasonable trade-off between numerical accuracy and computational time, we study the convergence of the transient solution towards the steady solution for different values of the temporal resolution $t_0/\Delta t$. The acoustic energy $E_{\mathrm{ac}}(t)$ is shown in Fig. 5.3(a) for different values of Δt and normalized by the steady time-averaged energy $\langle E_{\mathrm{ac}}^{\mathrm{fd}}(\infty)\rangle$ of the frequency-domain calculation, and it is thus expected to converge to the unity for long times. In Fig. 5.3(b), $E_{\mathrm{ac}}(1000t_0)/\langle E_{\mathrm{ac}}^{\mathrm{fd}}(\infty)\rangle$ is plotted versus the temporal resolution $t_0/\Delta t$, which shows how the accuracy of the time-domain solution increases as the temporal resolution is increased. In Ref. [30] Appendix E the time step of $\Delta t = t_0/256$, the circled point in Fig. 5.3(b), was chosen as a reasonable trade-off, for which the time-domain energy converge to 99.4% of the energy of the steady calculation.

In Ref. [30] Appendix E it was further noted that the fastest convergence was obtained when actuating the system at its (numerically determined) resonance frequency f_{res}. When shifting the actuation frequency half the resonance width $\frac{1}{2}\Delta f$ away from f_{res}, the energy $E_{\mathrm{ac}}(t)$ for $\Delta t = t_0/256$ converged to only 95% of the steady value $\langle E_{\mathrm{ac}}^{\mathrm{fd}}(\infty)\rangle$ (calculated in the frequency domain), thus necessitating smaller time steps to obtain reasonable convergence.

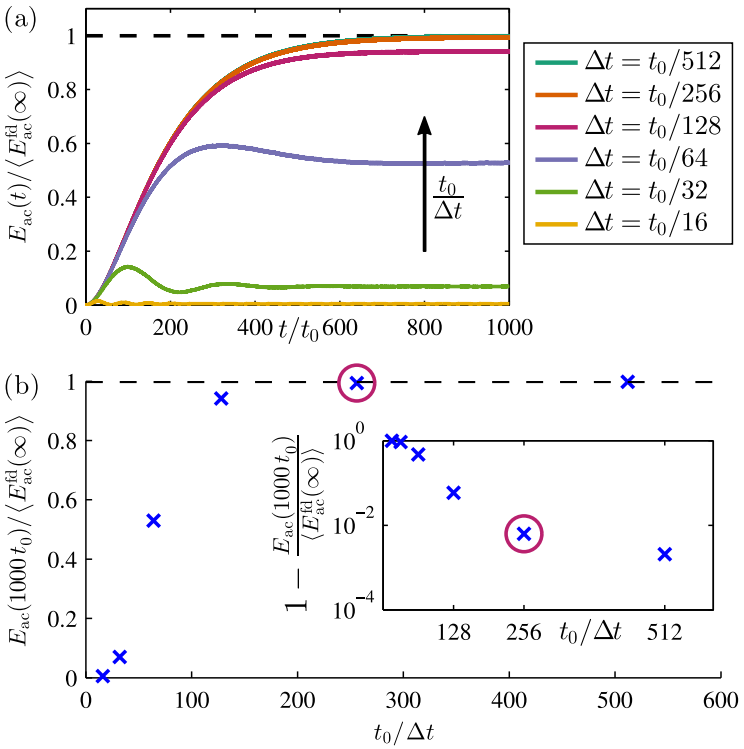

Figure 5.3: Numerical convergence and temporal resolution. (a) Graphs of the build-up of acoustic energy $E_{ac}(t)$ in the time-domain simulations calculated with different fixed time steps Δt. The energy of the time-domain simulations is normalized with respect to the energy $\langle E_{ac}^{fd}(\infty)\rangle$ of the steady solution in the frequency domain, and should thus converge towards unity. In all simulations the actuation frequency equals the numerically determined resonance frequency. (b) Acoustic energy $E_{ac}(1000\,t_0)$ at $t = 1000\,t_0$, normalized by $\langle E_{ac}^{fd}(\infty)\rangle$, and plotted versus the temporal resolution $t_0/\Delta t$ of the oscillation. The inset is a semilog plot of the relative deviation of $E_{ac}(1000\,t_0)$ from $\langle E_{ac}^{fd}(\infty)\rangle$. The circled point in each graph indicates the time step $\Delta t = t_0/256$ used in all subsequent simulations. Figure adapted from Ref. [30] Appendix E.

Chapter 6

Streaming studies

This chapter presents an extended conclusion on this thesis work by summarizing the main results of the five journal papers and discussing their relations to each other and to the field of acoustofluidics. The studies are not treated chronologically but rather in a way to address relevant topics, for which some are addressed in more than one of the papers.

6.1 Analytical streaming calculations

As mentioned in Chapter 1 there have been many analytical studies of acoustic streaming through out the last hundred years. However, there was a gap between the analytical studies and the experimental systems that were used in the acoustofluidic community. Most theoretical studies treat very thin channel cross sections, i.e. low aspect ratio $h/w \ll 1$, because it is theoretically easier and it is relevant for applications within the field of thermoacoustic engines. In acoustofluidic applications, the aspect ratio is typically in the range from 0.2 to 1. This issue was addressed in ref. [11] Appendix B, in which an analytical calculation of the acoustic streaming is presented, valid for arbitrarily large aspect ratios. Furthermore, the effects of the sidewalls on the streaming flow was taking into account by introducing a no-slip condition on the sides, that resulted in a retardation of the streaming flow. This was in contrast to previous analytical studies, which treated the channel cross section as infinite parallel plates, thus not taken into account the effect of the sidewalls, which is only a good approximation for low aspect ratio channels. These extensions brought the analytical model closer to the experimental systems and enabled direct comparison between theoretical predictions and experimental measurements of acoustofluidic systems, which was not possible before.

In acoustofluidic experiments the most convenient way to measure the magnitude of the acoustic streaming flow is to measure the velocity of small particles in the horizontal center plane of the channel, $z = 0$ in Fig. 6.1. The streaming flow rolls are generated at the top and bottom walls and have a finite extend in the vertical direction. Thus for a tall channel the magnitude of the streaming flow decays towards the center of the channel, as shown in Fig. 6.1(a). The streaming flow for higher-order resonance have a higher spatial frequency in the horizontal direction and thus also a faster decay from the top and bottom

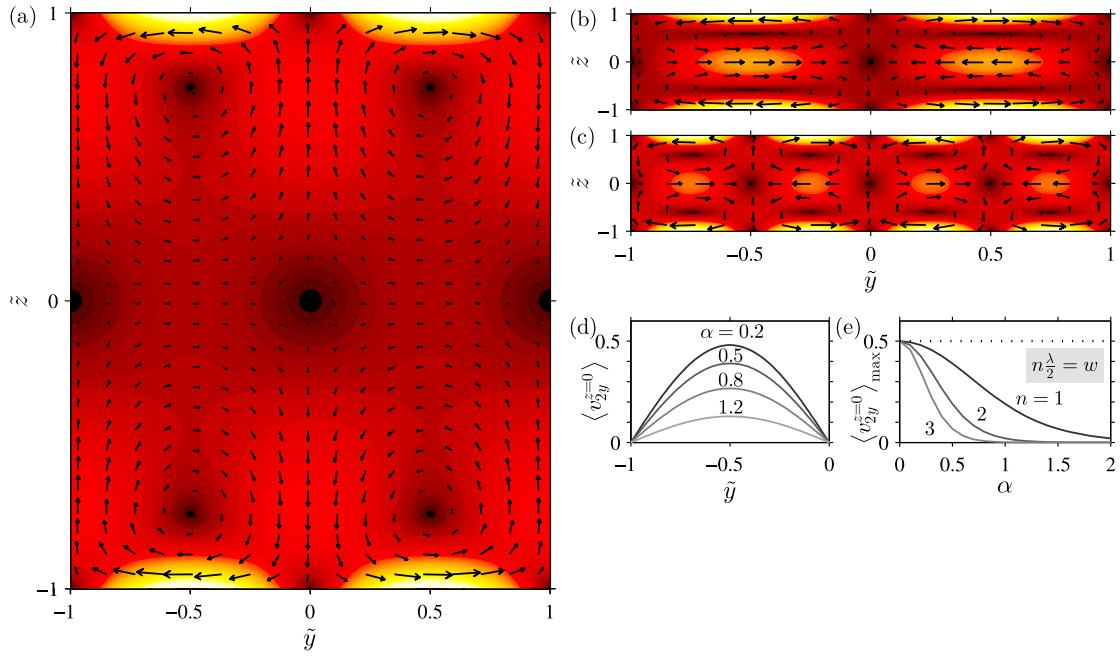

Figure 6.1: Analytical solution for the steady streaming velocity field $\langle \boldsymbol{v}_2 \rangle$ in parallel-plate channels. (a) $\langle \boldsymbol{v}_2 \rangle$ (arrows) and its magnitude [color plot from 0 (black) to maximum v_{str} (white)] in the vertical y-z-cross section of a parallel-plate channel with $\lambda/2 = w$ and aspect ratio $\alpha = h/w = 1.2$. The normalized spatial coordinates are $\tilde{y} = y/(\frac{w}{2})$ and $\tilde{z} = z/(\frac{h}{2})$. (b) The same as (a), but for $\alpha = 0.2$. (c) The same as (b) but for a standing full wave $\lambda = w$. (d) Line plot of the horizontal streaming velocity along the horizontal centerline $z = 0$, $\langle v_{y2}(y,0) \rangle$, divided by the maximum streaming velocity v_{str}, for $\lambda/2 = w$ and aspect ratios $\alpha = 0.2$, 0.5, 0.8, and 1.2. (e) Line plot of the maximum $\langle v_{y2}(y,0) \rangle_{\text{max}}$ of the center-axis streaming velocity, divided by the maximum streaming velocity v_{str}, as function of aspect ratio, and for the resonances $n\lambda/2 = w$, with n = 1, 2, and 3, respectively. Figure adapted from ref. [11] Appendix B.

towards the center, resulting in a lower streaming magnitude in the center plane. Figure 6.1(e) shows the analytical prediction of the maximum streaming velocity in the horizontal center plane $z = 0$ as a function of the aspect ratio $\alpha = \frac{h}{w}$ of the channel cross section, with curves for the first-, second-, and third-order resonances, $n = 1, 2, 3$. The graphs show how the streaming velocity in the center plane is significantly smaller for larger aspect ratios and higher-order resonances. The effect of the no-slip condition on the sidewalls is not included in Fig. 6.1, and for a visual interpretation of this effect the reader is referred to Ref. [11] Appendix B.

6.2 Numerical modeling of acoustic streaming

The field of acoustofluidics was, and still is, very experimentally driven, and in many cases it had become clear that a better understanding of the underlying physics was necessary to progress even further. This need was addressed by the numerical model presented in Ref. [28] Appendix A. The purposed of the model was to give a better insight into the physical mechanisms of the acoustic resonance and the generation of the acoustic streaming flow. The model solved the nonlinear acoustics using a perturbation expansion in the small amplitude of the acoustic field. The resonant acoustic field was generated directly by an oscillating velocity boundary condition, and the model resolved the thin acoustic boundary layer at the walls. Consequently, the model was a very flexible tool to investigate the physics of acoustic streaming generation and it avoided the use of the analytical effective slip velocity approximation. The resolution of the boundary layers enabled accurate estimations of loss factors and detailed information about how the streaming flow was generated inside these thin layers. However, the model was computationally heavy and further optimization of the numerical scheme was needed.

This was addressed in Ref. [29] Appendix D, where the numerical scheme was optimized for computational efficiency. Furthermore, perturbations in the dynamic viscosity of the fluid, due to the oscillating perturbations of the temperature and the density, was included, to provide even better comparison between the numerical model and experimental studies. The model in Ref. [29] Appendix D also incorporated an automatic calculation of the material parameters of water and their temperature and density derivatives. These parameter values where based on the studies made by the International Association for the Properties of Water and Steam (IAPWS). The IAPWS data is a collection of many experimental studies, based on which the equation of state for water is fitted using a function with 56 parameters and covering the range $T \leq 1273.15$ K and $p \leq 1000$ MPa. The formulation of this massive result is very complex, and we wanted to transform this into something that was easy to implement in a numerical model. Ref. [29] Appendix D presented polynomial fits, based on the IAPWS data, of all parameters and their derivatives relevant for acoustofluidic applications in the temperature range from 10 ℃ to 50 ℃. This was an important part of making the numerical model flexible towards predicting outcomes of acoustofluidic experiments with various operating conditions. Furthermore, it ensured high precision on all input parameters, which is necessary for quantitative comparison between theory and experiment.

The main purpose of the numerical model was to enable comparison to experimental measurements and to analytical calculations, however, it resulted in several other advantages. Because the model gave direct access to the generating mechanism of the acoustic streaming, it strengthened the understanding and intuition of the physics of acoustic streaming. Furthermore, it was a tool to create a visual interpretation of the physics of acoustic resonances and acoustic streaming, which was missing in many previous theoretical studies, and which was necessary to reach out to an experimentally driven community.

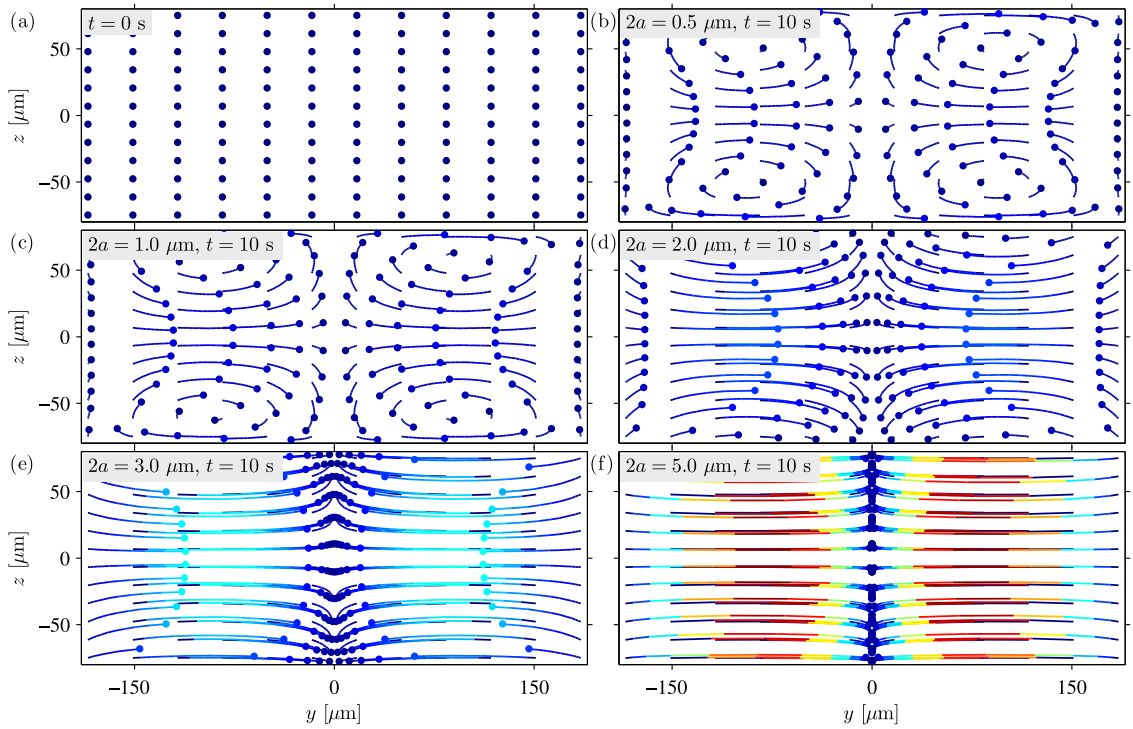

Figure 6.2: Particle trajectories illustrating the cross-over from streaming-induced drag force dominated motion to radiation force dominated motion as a result of increasing particle size. (a) The starting positions (dots) of 144 evenly distributed particles at t = 0 s. The following five panels show the trajectories (colored lines) and positions (dots) that the particles have reached by acoustophoresis at t = 10 s for five different particle diameters: (b) 0.5 µm, (c) 1 µm, (d) 2 µm, (e) 3 µm, and (f) 5 µm. The colors indicate the instantaneous particle speed u ranging from 0 µm/s (dark blue) to 44 µm/s (dark red). The lengths of the trajectories indicate the distance covered by the particles in 10 s. Streaming-induced drag dominates the motion of the smallest particles, which consequently are being advected along the acoustic streaming rolls. In contrast, the acoustic radiation force dominates the motion of the larger particles, which therefore are forced to the vertical nodal plane at $y = 0$ of the first-order pressure p_1. Figure adapted from Ref. [28] Appendix A.

6.3 Numerical modeling of acoustophoretic particle motion

Even with the improved analytical analysis and numerical model of acoustic streaming, there was still a gab between the theoretical predictions of fluid velocities and the experimental measurements of particle velocities, as the drag force from the acoustic streaming flow is not the only force acting on the suspended particles. This gab was closed by the numerical particle tracking scheme presented in Ref. [28] Appendix A. Previously, experimental studies of radiation force dominated particle motion was often neglecting the small contribution from the streaming-induced drag force, and studies of drag force dominated particle motion was neglecting the small contribution from the radiation force. In Ref. [28] Appendix A this interplay between the radiation force and the streaming-induced drag force was treated, and the particle motion was visualized, see Fig. 6.2. This provided an intuitive understanding of the critical particle size and how the transition from radia-

tion force dominated motion to streaming-induced drag force dominated motion should be interpreted. Furthermore, the dependence of the critical particle size on the fluid medium and frequency, which is often not illuminated due to the main focus on the particle size, was emphasize by visualizations of particle motion in a high viscosity medium and for a higher-order resonance.

The transition from streaming velocities to predicted particle trajectories converted complex theoretical calculations into something that was easy to relate to. This strengthened the intuition of particle motion in acoustophoresis systems and was one of the most important steps in reaching out to an experimentally driven community.

6.4 Quantitative comparison of acoustophoretic particle motion

The ultimate validation of both analytical and numerical models is a direct quantitative comparison, with no free parameters, to experimental measurements. This was achieved in Ref. [11] Appendix B. The streaming studied throughout this thesis is in the vertical cross section of a microchannel, which makes it challenging to experimentally measure the particle motion in this plane, as it is parallel to the optical axis. This can however be achieved using defocussing techniques, such as Astigmatism Particle Tracking Velocimetry (APTV), which derives the position of the particle along the optical axis by its defocused image. This enabled measurements of streaming dominated particles in the vertical channel cross section. In order to avoid a free scaling parameter in the theoretical prediction of the streaming velocity field, the motion of large radiation force dominated particles was measured at the same position in the channel, from which the acoustic energy density in the channel could be derived. With the indirectly measured acoustic energy density, there was no free parameters left in the theoretical prediction of the motion of the small streaming-dominated particles. This enabled a quantitative comparison between theory and experiment of the two-dimensional acoustic streaming velocity field, which had not been done before. With reasonable statistics on the experimental measurements, the measurements and predictions agreed with differences around 20%, which was a low deviation given state-of-the-art in the field. The reconstructed three-dimensional trajectories and two-dimensional comparison are shown in Fig. 6.3. This was a very satisfying validation of both the analytical and numerical models, the culmination of all our efforts, and presumably that which have received the least attention by others.

6.5 Focusing of sub-micrometer particles

The interest in acoustic streaming within the acoustofluidic community is mainly due to the fact that it is an obstruction when trying to focus small particles by use of the acoustic radiation force. One example of such a particle is the E. coli bacteria, which is about 1 μm in size and responsible for fresh water contamination. It is present in such small concentrations that an up-concentration step is necessary in order to detect it, and acoustophoresis is a candidate for this task. To up-concentrate such small particles with

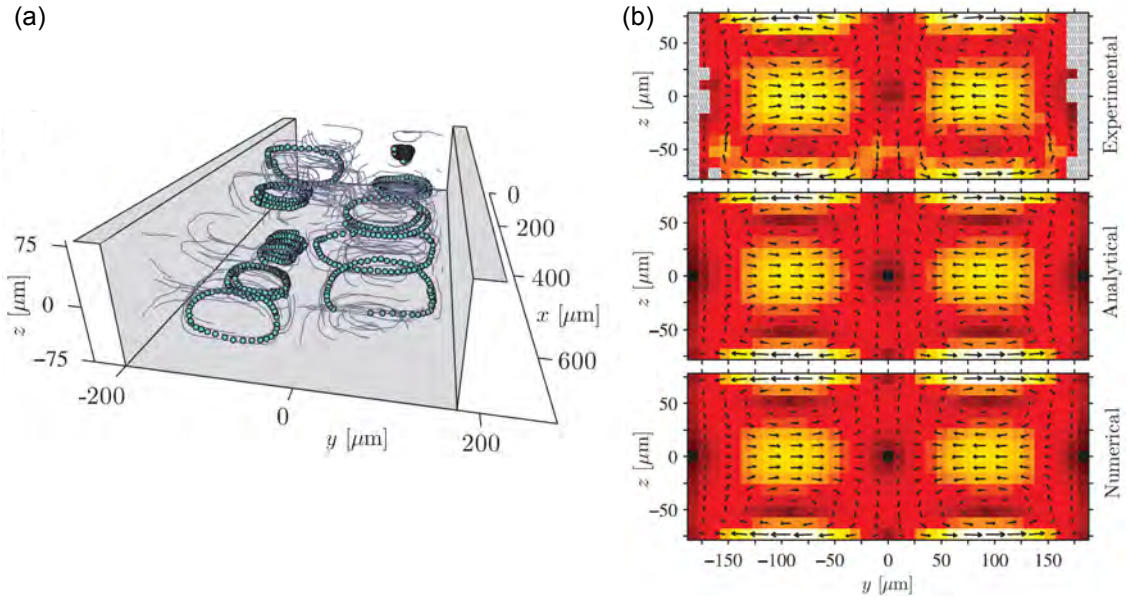

Figure 6.3: (a) Measured trajectories (thin black lines) of 0.5-μm-diameter particles obtained using the 3D-APTV technique in the microchannel (gray walls) actuated at its horizontal half-wave resonance. For selected trajectories, the particle positions are represented by dots. The particle motion is dominated by the streaming-induced drag and follow circular trajectories. (b) Comparison between experimental, analytical, and numerical studies of the acoustophoretic particle velocities of 0.5-μm-diameter polystyrene particles in water. The particle velocities (vectors) and their magnitude [color plot ranging from 0 μm/s (black) to 63 μm/s (white) in all three plots] are shown in the vertical cross section of the microchannel, divided into a pixel array consisting of 37×15 square bins of side length 10 μm. The axes of the plot coincide with the position of the channel walls. There are no free parameters in the theoretical predictions, as the acoustic energy density was calibrated *in situ* based on measurements of large 5-μm-diameter particles. Figure adapted from Ref. [11] Appendix B.

acoustophoresis, the streaming flow needs to be either diminished or altered in such a way that it does not counteract the focusing. An example of the latter is presented in Ref. [31] Appendix C, which demonstrates a single flow roll streaming pattern in a nearly-square channel cross section. The numerical model for the square channel streaming flow was based on the studies of the fundamental one-dimensional half-wavelength resonance in the rectangular channel Ref. [28] Appendix A. By using actuation of all four channel boundaries in the model, we could engineer a streaming flow consisting of a single flow roll. The drag force induced by the single roll streaming flow does not counteract the focusing by the weak radiation force on the small particles. The single roll streaming flow was also observed experimentally, resulting in a spiraling focusing of particles smaller than the usual critical particle size of about 2 µm in standard half-wavelength acoustophoresis devices.

The single roll streaming flow was obtained by utilizing the two closely-spaced resonance peaks of the fundamental half-wavelength resonances along the width and the height of the nearly-square channel. Figure 6.4 shows the numerical predictions of the particle trajectories for three actuation frequencies around the two resonance peaks. It was not possible to make a detailed comparisons of theory and experiments because the numerical results depended largely on the choice of boundary conditions, and the observed small-particle trajectories varied along the length of the channel. However, the nearly-square channel did on average along the channel length enable two-dimensional focusing of E. coli bacteria and 0.6 µm polystyrene particles with recoveries above 95%, whereas for the standard one-dimensional focusing in a rectangular channel, the recoveries were below 50%.

6.6 Numerical modeling of time-dependent streaming

All previous studies of acoustic streaming treats the steady fluid flow, which can be observed in various acoustic systems. In acoustofluidic applications this is reasonable because the streaming flow reaches steady state on a timescale of a few milliseconds, which is typically much shorter than other relevant timescales, such as focusing time of suspended particles. The initial purpose of studying the build-up of the acoustic streaming and its response to a pulsed actuation, Ref. [30] Appendix E, was to diminish the magnitude of the streaming flow. This was motivated by an experimental study of a similar system by Hoyos and Castro [49], which indicated that a pulsation of the ultrasound actuation could reduce the streaming flow relative to the radiation force, and thus allow for radiation force dominated manipulation of sub-micrometer particles. Furthermore, scaling analysis indicated that the timescale for the build-up of the acoustic resonance was approximately ten times faster than the timescale for the build-up of the streaming flow. The more fundamental purpose of the study in Ref. [30] Appendix E was to understand the physical mechanisms involved in the build-up of the acoustic resonance and the streaming flow.

The study showed that the build-up of acoustic energy in the microfluidic channel Fig. 6.5(b) could be accurately described by the analytical solution for a sinusoidally-driven under-damped harmonic oscillator Fig. 6.5(a). A distinct feature of the underdamped harmonic oscillator is that it may transiently overshoot its steady energy, as shown in

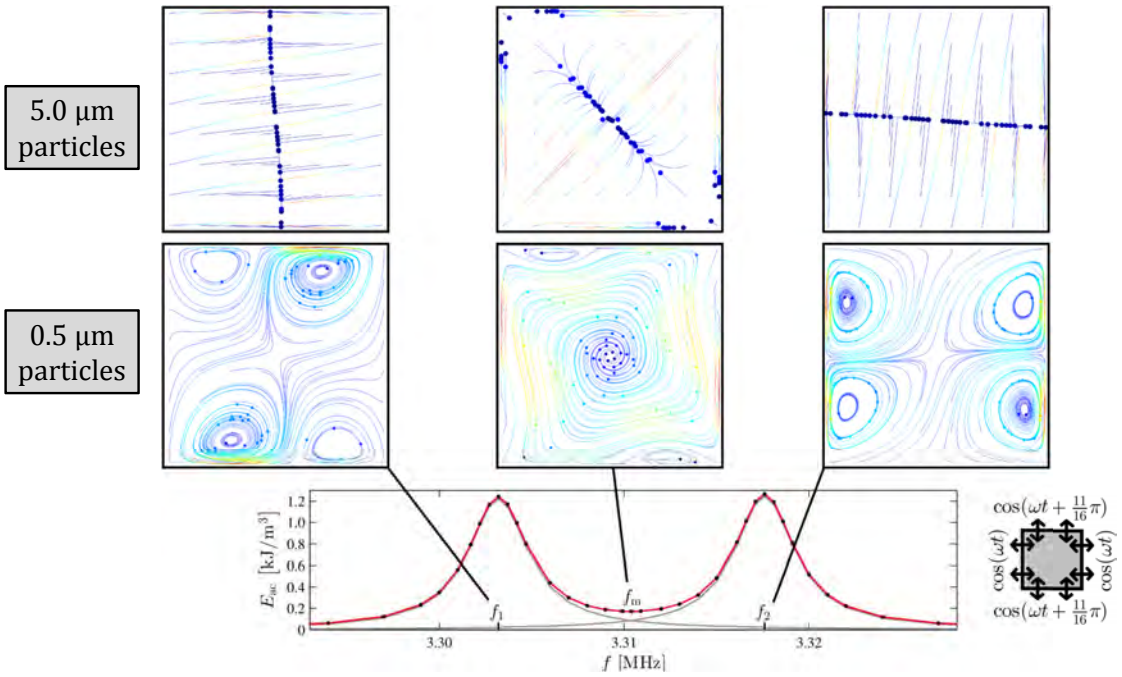

Figure 6.4: Numerical particle trajectories of 5-µm-diameter particles (top row) and 0.5-µm-diameter particles (middle row) in a nearly-square channel for three different actuation frequencies $\omega = 2\pi f$. The bottom graph shows the acoustic energy in the channel as function of the actuation frequency of the velocity boundary conditions sketched to the bottom right. The trajectories correspond to actuation at the horizontal half-wavelength resonance frequency f_1 (left column), the frequency f_m in between the two resonance peaks (center column), and the vertical half-wavelength resonance frequency f_2 (right column). The phase shift of the velocity boundary conditions sketched to the bottom right has been chosen such as to achieve a single roll streaming flow. The results presented in the figure is based on the simulations described in Ref. [31] Appendix C.

Fig. 6.5(d) for both the analytical solution for the oscillator and the numerical solution for the channel. The transient overshoot is a result of the mismatch between the phase of the forcing and the phase of the oscillation. For the channel resonance, the overshoot thus occurs when the frequency f of the boundary oscillations does not match the resonance frequency f_{res}, which can be determined numerically from the resonance curves shown in Fig. 6.5(c). For the channel this may seem counter-intuitive, since the most basic understanding of the acoustic resonance is that energy is gradually pumped into the acoustic resonance field until the viscous loss equals the power input, resulting in a monotonic build-up of the energy. However, due to the oscillator behavior of the channel resonance, the monotonic build-up of the energy only occurs when $f = f_{\text{res}}$, which is also shown in Fig. 6.5(d).

The numerical analysis in Ref. [30] Appendix E showed that the acoustic energy builds up approximately five times faster than the streaming flow. Since the radiation force scales by the acoustic energy, this makes the radiation force more dominant in the transient regime of approximately one millisecond compared to the steady-state. Applying a pulsed actuation did not improve the ratio of radiation force and streaming-induced drag force. On the contrary, the conclusion was that it would never be advantages to turn off the actuation, since this causes the energy and thus the radiation force to decay fast, while the magnitude of the streaming flow decays much slower.

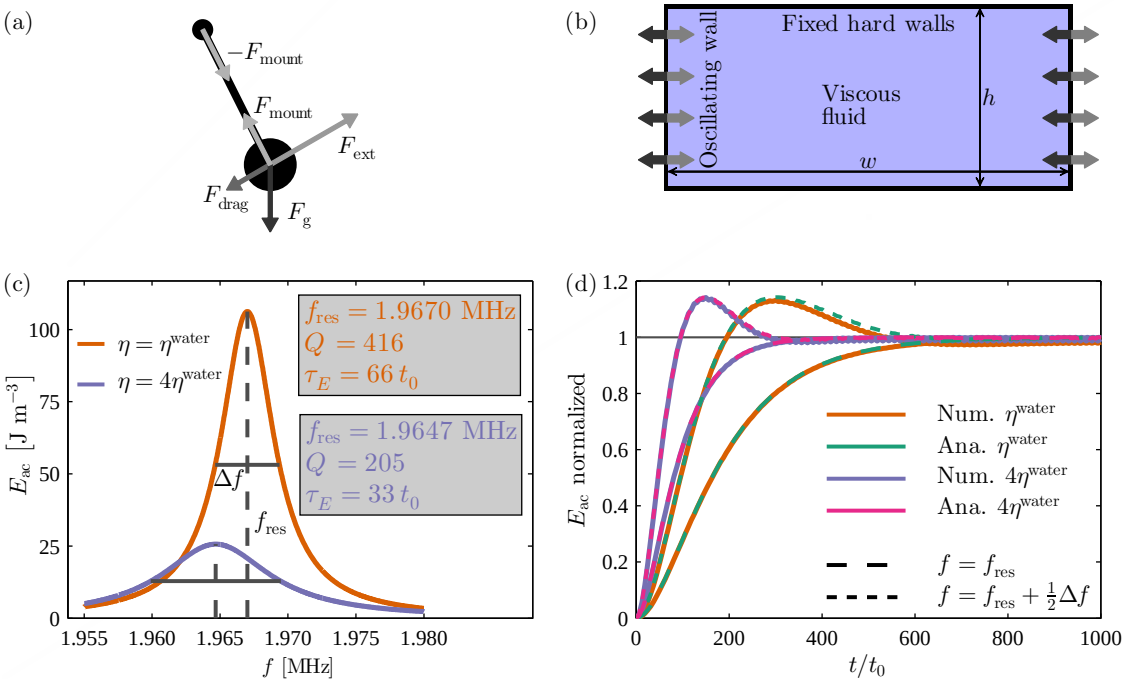

Figure 6.5: Resonance curves and energy build-up in an acoustic cavity, and a comparison to the analytical solution for a sinusoidally-driven damped harmonic oscillator. (a) Sketch of a pendulum, which for small amplitudes can be considered a damped harmonic oscillator. The forces acting on the pendulum are the gravitational force F_{g}, the drag force from the surrounding fluid F_{drag}, the force from the mounting F_{mount} balancing the radial component of F_{g}, and the external oscillating force F_{ext}. Here F_{ext} is depicted as a body force on the pendulum mass, but it could as well be a torque on the rotation axis. (b) Sketch of the numerical model of the channel cross section, with arrows indicating the in-phase oscillations of the left and right boundaries. (c) Resonance curves showing the steady acoustic energy density E_{ac} versus the actuation frequency f for the numerical model of the water-filled channel, with viscosity $\eta = \eta^{\text{water}}$ (brown) and artificially increased viscosity $\eta = 4\eta^{\text{water}}$ (purple). The inset exhibits the fitted resonance frequency f_{res}, the quality factor $Q = f_{\text{res}}/\Delta f$, where Δf is the full width at half maximum, and the resonance relaxation time $\tau_E = Q/(2\pi f_{\text{res}})$. The maximum energy scales by η, while the cavity quality factor Q scales by $\eta^{\frac{1}{2}}$. (d) Build-up of the time-dependent energy $E_{\text{ac}}(t)$ versus time t for constant actuation amplitude. Graphs for $\eta = \eta^{\text{water}}$, numerical (brown) and analytical (green), and for $\eta = 4\eta^{\text{water}}$, numerical (purple) and analytical (pink), all four cases for actuation at resonance $f = f_{\text{res}}$ (long dashes) and for actuation off resonance $f = f_{\text{res}} + \frac{\Delta f}{2}$ (short dashes). The figure is an extended version of similar figures presented in Ref. [30] Appendix E.

Chapter 7

Outlook

The studies presented in this thesis have brought us several steps further in the progress of understanding the physics of acoustic resonances and acoustic streaming flows. The numerical model, which we have developed and refined throughout the past three years, is publicly available as supplemental material to Ref. [30] Appendix E, and it will hopefully inspire others to make further progress along the path of the present studies.

The challenge of acoustophoretic focusing of sub-micrometer particles has been a main topic throughout this thesis work. It has been addressed through studies of the basic physics of the acoustic streaming flow and through engineering of a new single roll streaming flow, that did not counteract the acoustophoretic focusing. The future progress in meeting this challenge may follow two paths: (i) Continuing work on the single roll streaming flow of the nearly-square channel to experimentally achieve better control of the streaming flow, resulting in a more reliable focusing and focusing of even smaller particles. (ii) Theoretical and experimental studies of the streaming flows and particle trajectories obtained when switching between resonances with opposing streaming patterns, on a time-scale much shorter than the build-up time of the acoustic streaming, thus fighting streaming with streaming.

When studying the motion of suspended particles in the transient case, such as when switching between resonances as described above, new challenges arise. Firstly, the force on a particle due to the scattering of the now transient acoustic field needs to be derived analytically, since the usual time-averaged radiation force is valid only for the purely periodic state. Secondly, the forces on the particles need to be integrated with a time step of a fraction of the oscillation period, which makes the solution of particle trajectories over several seconds a very demanding task using brute-force integration of the equations of motion. Consequently, a new numerical method for prediction of acoustophoretic particle trajectories in a transient acoustic field needs to be developed.

The studies of this thesis all treat the two-dimensional fluid domain of the channel cross section, neglecting the vibrations of the surrounding solid material and assuming invariance along the length of the channel. Modeling the vibrations in the solid, including the electromechanical couplings in the piezo-electric transducer, and going from a two-dimensional domain to a three-dimensional full chip model present a wide range of challenges in making

a reliable and efficient numerical model. Addressing these challenges will enable a more extensive comparison between theoretical predictions and experimental observations.

Appendix A

Paper published in Lab on a Chip, July 2012

A numerical study of microparticle acoustophoresis driven by acoustic radiation forces and streaming-induced drag forces

Peter Barkholt Muller, Rune Barnkob, Mads Jakob Herring Jensen and Henrik Bruus

Abstract: We present a numerical study of the transient acoustophoretic motion of microparticles suspended in a liquid-filled microchannel and driven by the acoustic forces arising from an imposed standing ultrasound wave: the acoustic radiation force from the scattering of sound waves on the particles and the Stokes drag force from the induced acoustic streaming flow. These forces are calculated numerically in two steps. First, the thermoacoustic equations are solved to first order in the imposed ultrasound field taking into account the micrometer-thin but crucial thermoviscous boundary layer near the rigid walls. Second, the products of the resulting first-order fields are used as source terms in the time-averaged second-order equations, from which the net acoustic forces acting on the particles are determined. The resulting acoustophoretic particle velocities are quantified for experimentally relevant parameters using a numerical particle-tracking scheme. The model shows the transition in the acoustophoretic particle motion from being dominated by streaming-induced drag to being dominated by radiation forces as a function of particle size, channel geometry, and material properties.

http://dx.doi.org/10.1039/c2lc40612h

Lab on a Chip

Cite this: *Lab Chip*, 2012, **12**, 4617–4627

www.rsc.org/loc

PAPER

A numerical study of microparticle acoustophoresis driven by acoustic radiation forces and streaming-induced drag forces

Peter Barkholt Muller,[a] Rune Barnkob,[b] Mads Jakob Herring Jensen[c] and Henrik Bruus*[a]

Received 28th May 2012, Accepted 18th July 2012
DOI: 10.1039/c2lc40612h

We present a numerical study of the transient acoustophoretic motion of microparticles suspended in a liquid-filled microchannel and driven by the acoustic forces arising from an imposed standing ultrasound wave: the acoustic radiation force from the scattering of sound waves on the particles and the Stokes drag force from the induced acoustic streaming flow. These forces are calculated numerically in two steps. First, the thermoacoustic equations are solved to first order in the imposed ultrasound field taking into account the micrometer-thin but crucial thermoviscous boundary layer near the rigid walls. Second, the products of the resulting first-order fields are used as source terms in the time-averaged second-order equations, from which the net acoustic forces acting on the particles are determined. The resulting acoustophoretic particle velocities are quantified for experimentally relevant parameters using a numerical particle-tracking scheme. The model shows the transition in the acoustophoretic particle motion from being dominated by streaming-induced drag to being dominated by radiation forces as a function of particle size, channel geometry, and material properties.

I Introduction

In the past decade there has been a markedly increasing interest in applying ultrasound acoustofluidics as a tool for purely mechanical and label-free manipulation of particle and cell suspensions in MEMS and biologically oriented lab-on-a-chip systems. Recent extended reviews of acoustofluidics can be found in *Review of Modern Physics*[1] and the tutorial series in *Lab on a Chip*[2] which, among other topics, treats the application of ultrasound bulk[3] and surface[4] acoustic waves as well as acoustic forces on particles from acoustic radiation[5] and from streaming-induced drag.[6]

When a standing ultrasound wave is established in a microchannel containing a microparticle suspension, the particles are subject to two acoustic forces: the acoustic radiation force from the scattering of sound waves on the particles, and the Stokes drag force from the induced acoustic streaming flow. The resulting motion of a given particle is termed acoustophoresis, migration by sound. Experimental work on acoustophoresis has mainly dealt with the radiation force, primarily because this force dominates over the streaming-induced drag force for the studied aqueous suspensions of polymer particles or biological cells with diameters larger than 2 μm. Detailed measurements of the acoustophoretic motion of large 5 μm diameter polystyrene particles in water[7,8] have shown good agreement with the theoretical predictions[9,10] for the radiation force on compressible particles with a radius a much smaller than the acoustic wavelength λ and neglecting the viscosity of the suspending fluid.

However, as the particle diameter $2a$ is reduced below 2 μm, viscous effects are expected to become significant, because this length corresponds to a few times the viscous penetration depth or boundary-layer thickness δ. Analytical expressions for the viscous corrections to the radiation force valid in the experimentally relevant limit of long wavelength λ, characterized by $a \ll \lambda$ and $\delta \ll \lambda$, have been given recently,[11] but have not yet been tested experimentally. In addition to these modifications of the radiation force, the acoustic streaming flow induced by viscous stresses in the boundary layers near rigid walls, and depending critically on the detailed geometry and boundary conditions, also significantly influences the acoustophoretic particle motion as the size of the particle or the confining microchannel is reduced.[12,13] The cross-over from radiation-dominated to streaming-dominated motion has been observed in experiments,[14,15] and a scaling analysis of the critical particle diameter for this cross-over has been provided in the literature[16] and will be restated in Section IV D.

Although acoustic streaming is a well-known phenomenon in acoustics, it is pointed out in a recent review[6] that streaming is often misunderstood outside the relatively small circles of acoustics experts due to the many forms in which it may arise in, *e.g.*, acoustofluidic microsystems. Not only is acoustic streaming difficult to predict quantitatively due to its sensitivity

[a]*Department of Physics, Technical University of Denmark, DTU Physics Building 309, DK-2800 Kongens Lyngby, Denmark. E-mail: bruus@fysik.dtu.dk*
[b]*Department of Micro- and Nanotechnology, Technical University of Denmark, DTU Nanotech Building 345 East, DK-2800 Kongens Lyngby, Denmark*
[c]*COMSOL A/S, Diplomvej 373, DK-2800 Kongens Lyngby, Denmark*

to the detailed geometry and boundary conditions, but part of the more conceptual difficulties with acoustic streaming in acoustofluidics may be related to the lack of theoretical analysis in the experimental relevant limit where the microchannel height h is equal to one or a few times half the acoustic wavelength λ, *i.e.* $h \simeq \lambda$. The classical Rayleigh–Schlichting boundary-layer theory for acoustic streaming,[17–20] see Fig. 1, is valid in the limit of thin boundary layers in medium-sized channels, $\delta \ll h \ll \lambda$, and a later extension[13] is valid in the limit of thin boundary layers in shallow channels, $\delta \simeq h \ll \lambda$. Moreover, in contrast to rectangular channel cross sections of experimental relevance, the classical analysis of the parallel-plate channel and recent numerical studies of it[21] do not include the effects of the vertical side walls. One exception is the special case of gases in shallow, low-aspect-ratio channels studied by Aktas and Farouk.[22]

The push within contemporary acoustofluidics for handling smaller particles like bacteria, viruses, and large biomolecules, and for doing so with better accuracy, emphasizes the urgency of performing a numerical analysis of microparticle acoustophoresis including acoustic radiation forces, streaming flows, and boundary layers. Based directly on the governing equations, we provide such an analysis in this paper for a simple, yet experimentally relevant microsystem. In Section II we present the governing thermoacoustic equations to first and second order in the external ultrasound actuation. In Section III we describe the model system, the numerical implementation of it, as well as mesh-convergence analysis. In Section IV this is followed by the results for first-order fields, time-averaged second-order fields, and microparticle acoustophoresis as function of particle size and material properties. We end with a concluding discussion in Section V.

II Governing equations

The governing perturbation equations for the thermoacoustic fields are well-known textbook material.[23–25] The full acoustic problem in a fluid, which before the presence of any acoustic wave is quiescent with constant temperature T_0, density ρ_0, and pressure p_0, is described by the four scalar fields pressure p, temperature T, density ρ, and entropy s per mass unit as well as the velocity vector field $\boldsymbol{v}$. Changes in ρ and s are given by the two thermodynamic relations

$$\mathrm{d}\rho = \gamma\kappa\,\rho\,\mathrm{d}p - \alpha\,\rho\,\mathrm{d}T, \tag{1a}$$

$$\mathrm{d}s = \frac{C_p}{T}\,\mathrm{d}T - \frac{\alpha}{\rho}\mathrm{d}p, \tag{1b}$$

which, besides the specific heat capacity C_p at constant pressure, also contain the specific heat capacity ratio γ, the isentropic compressibility κ, and the isobaric thermal expansion coefficient α given by

$$\gamma = \frac{C_p}{C_V}, \tag{2a}$$

$$\kappa = \frac{1}{\rho}\left(\frac{\partial\rho}{\partial p}\right)_s, \tag{2b}$$

$$\alpha = -\frac{1}{\rho}\left(\frac{\partial\rho}{\partial T}\right)_p. \tag{2c}$$

Eqn (1) can be used to eliminate ρ and s, so that we only need to deal with the acoustic perturbations in temperature T, pressure p, and velocity $\boldsymbol{v}$. Taking first and second order (subscript 1 and 2, respectively) into account, we write the perturbation series

$$T = T_0 + T_1 + T_2, \tag{3a}$$

$$p = p_0 + p_1 + p_2, \tag{3b}$$

$$\boldsymbol{v} = \boldsymbol{v}_1 + \boldsymbol{v}_2. \tag{3c}$$

We model the external ultrasound actuation through boundary conditions on the first-order velocity $\boldsymbol{v}_1$ while keeping the temperature constant,

$$T = T_0, \text{ on all walls,} \tag{4a}$$

$$\boldsymbol{v} = \boldsymbol{0}, \text{ on all walls,} \tag{4b}$$

$$\boldsymbol{n}\cdot\boldsymbol{v}_1 = v_{\mathrm{bc}}(y,z)\mathrm{e}^{-\mathrm{i}\omega t}, \text{ added to actuated walls.} \tag{4c}$$

Here $\boldsymbol{n}$ is the outward pointing surface normal vector, and ω is the angular frequency characterizing the harmonic time dependence.

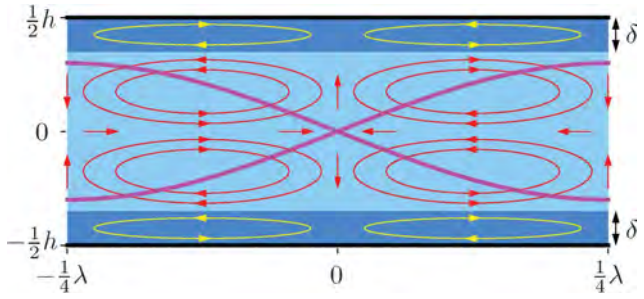

Fig. 1 A sketch of the classical Rayleigh-Schlichting streaming pattern in a liquid-filled gap of height h between two infinite, parallel rigid walls (black lines). The bulk liquid (light blue) supports a horizontal standing sinusoidal pressure wave (magenta line) of wavelength λ in the horizontal direction parallel to the walls. In the viscous boundary layers (dark blue) of sub-micrometer thickness δ, large shear stresses appear, which generate the boundary-layer (Schlichting) streaming rolls (yellow). These then drive the bulk (Rayleigh) streaming rolls (red). The streaming pattern is periodic in the horizontal direction with periodicity $\lambda/2$, and thus only the top and bottom walls are subject to the no-slip boundary condition.

A First-order equations

To first order in the amplitude of the imposed ultrasound field, the thermodynamic heat transfer equation for T_1, the kinematic continuity equation expressed in terms of p_1, and the dynamic Navier–Stokes equation for $\boldsymbol{v}_1$, become

$$\partial_t T_1 = D_{\mathrm{th}}\nabla^2 T_1 + \frac{\alpha T_0}{\rho_0 C_p}\,\partial_t p_1, \tag{5a}$$

$$\partial_t p_1 = \frac{1}{\gamma\kappa}\left[\alpha\partial_t T_1 - \nabla\cdot\boldsymbol{v}_1\right], \tag{5b}$$

$$\rho_0\partial_t\boldsymbol{v}_1 = -\nabla p_1 + \eta\nabla^2\boldsymbol{v}_1 + \beta\eta\nabla(\nabla\cdot\boldsymbol{v}_1). \tag{5c}$$

Here, D_{th} is the thermal diffusivity, η is the dynamic viscosity, and β is the viscosity ratio, which has the value 1/3 for simple liquids.[23] A further simplification can be obtained when assuming that all first-order fields have a harmonic time dependence $e^{-i\omega t}$ inherited from the imposed ultrasound field (eqn (4c)), because then p_1 is eliminated by inserting eqn (5b) with $\partial_t p_1 = -i\omega p_1$ into eqn (5a) and (c). After using the thermodynamic identity[26] $T_0\alpha^2/(\rho_0 C_p\kappa) = \gamma - 1$, we arrive at

$$i\omega T_1 + \gamma D_{\mathrm{th}}\nabla^2 T_1 = \frac{\gamma-1}{\alpha}\nabla\cdot\boldsymbol{v}_1, \tag{6a}$$

$$i\omega\boldsymbol{v}_1 + \nu\nabla^2\boldsymbol{v}_1 + \nu\left[\beta + i\frac{1}{\gamma\rho_0\kappa\nu\omega}\right]\nabla(\nabla\cdot\boldsymbol{v}_1) = \frac{\alpha}{\gamma\rho_0\kappa}\nabla T_1, \tag{6b}$$

where $\nu = \eta/\rho_0$. From eqn (6) arise the thermal and the viscous penetration depth δ_{th} and δ, respectively (values for ultrasound waves at 2 MHz in water at 25 °C),

$$\delta_{\mathrm{th}} = \sqrt{\frac{2D_{\mathrm{th}}}{\omega}} = 0.15\ \mu\mathrm{m}, \quad \text{and} \quad \delta = \sqrt{\frac{2\nu}{\omega}} = 0.38\ \mu\mathrm{m}. \tag{7}$$

These are the length scales over which the thermoacoustic fields change from their bulk values to the boundary conditions of the rigid walls stated in eqn (4).

B Second-order, time-averaged equations

For water and most other liquids, the thermal effects in the above first-order equations are minute because of the smallness of the pre-factor $\gamma - 1 \approx 10^{-2}$ and $\delta_{\mathrm{th}}/\delta \approx 0.3$. To simplify the following treatment, we therefore neglect the coupling in the second-order equations between the temperature field T_2 and the mechanical variables $\boldsymbol{v}_2$ and p_2. Furthermore, the values of η and β are kept fixed at the ones given at $T = T_0$. The second-order continuity equation and Navier–Stokes equation are

$$\partial_t\rho_2 = -\rho_0\nabla\cdot\boldsymbol{v}_2 - \nabla\cdot(\rho_1\boldsymbol{v}_1), \tag{8a}$$

$$\rho_0\partial_t\boldsymbol{v}_2 = -\nabla p_2 + \eta\nabla^2\boldsymbol{v}_2 + \beta\eta\nabla(\nabla\cdot\boldsymbol{v}_2) - \rho_1\partial_t\boldsymbol{v}_1 - \rho_0(\boldsymbol{v}_1\cdot\nabla)\boldsymbol{v}_1, \tag{8b}$$

and consequently, thermal effects enter solely through the temperature-dependent first-order fields ρ_1 and $\boldsymbol{v}_1$.

In a typical experiment on microparticle acoustophoresis, the microsecond timescale of the ultrasound oscillations is not resolved. It therefore suffices to treat only the time-averaged equations. The time average over a full oscillation period, denoted by the angled brackets $\langle\ldots\rangle$, of the second-order continuity equation and Navier–Stokes equation becomes[27]

$$\rho_0\nabla\cdot\langle\boldsymbol{v}_2\rangle = -\nabla\cdot\langle\rho_1\boldsymbol{v}_1\rangle, \tag{9a}$$

$$\eta\nabla^2\langle\boldsymbol{v}_2\rangle + \beta\eta\nabla(\nabla\cdot\langle\boldsymbol{v}_2\rangle) - \langle\nabla p_2\rangle = \langle\rho_1\partial_t\boldsymbol{v}_1\rangle + \rho_0\langle(\boldsymbol{v}_1\cdot\nabla)\boldsymbol{v}_1\rangle. \tag{9b}$$

It is seen that products of first-order fields act as source terms (at the right-hand sides) for the second-order fields (at the left-hand sides). We note that for complex-valued fields $A(t)$ and $B(t)$ with harmonic time-dependence $e^{-i\omega t}$, the time average is given by the real-part rule $\langle A(t)B(t)\rangle = \frac{1}{2}Re[A(0)^* B(0)]$, where the asterisk represents complex conjugation.

The second-order problem was solved in the case of the infinite parallel-plate channel by Rayleigh,[17,20] see Fig. 1. Assuming a first-order bulk velocity field with only the horizontal y-component v_{1y} being non-zero and of the form $v_{1y} = U_1\cos(2\pi y/\lambda)e^{-i\omega t}$, the resulting y-component $\langle v_{2y}^{\mathrm{bnd}}\rangle$ of $\langle\boldsymbol{v}_2\rangle$ just outside the boundary layers (in our notation at $z \approx \pm[h/2 - 3\delta]$), becomes

$$\langle v_{2y}^{\mathrm{bnd}}\rangle = \frac{3}{8}\frac{U_1^2}{c_0}\sin\left(4\pi\frac{y}{\lambda}\right), \tag{10}$$

Relative to the first-order bulk velocity v_{1y}, the second-order field $\langle v_{2y}^{\mathrm{bnd}}\rangle$ is phase shifted by $\pi/2$, period doubled in space, and smaller by a factor of U_1/c_0, where c_0 is the speed of sound of the liquid.

C Time-averaged acoustic forces on a single suspended microparticle

Once the first- and second-order acoustic fields have been calculated, it is possible to determine the time-averaged acoustic forces on a single suspended particle. These are the acoustic radiation force $\boldsymbol{F}^{\mathrm{rad}}$ due to the scattering of acoustic waves on the particle and the Stokes drag force $\boldsymbol{F}^{\mathrm{drag}}$ from the acoustic streaming.

The time-average acoustic radiation force $\boldsymbol{F}^{\mathrm{rad}}$ on a single small spherical particle of radius a, density ρ_{p}, and compressibility κ_{p} in a viscous fluid is given by[11]

$$\boldsymbol{F}^{\mathrm{rad}} = -\pi a^3\left[\frac{2\kappa_0}{3}Re[f_1^*\,p_1^*\nabla p_1] - \rho_0 Re[f_2^*\,\boldsymbol{v}_1^{*}\cdot\nabla\boldsymbol{v}_1]\right], \tag{11}$$

where $\kappa_0 = 1/(\rho_0 c_0^2)$ is the compressibility of the fluid, and where the pre-factors f_1 and f_2 are given by

$$f_1(\tilde{\kappa}) = 1 - \tilde{\kappa}, \qquad \text{with } \tilde{\kappa} = \frac{\kappa_{\mathrm{p}}}{\kappa_0}, \tag{12a}$$

$$f_2\left(\tilde{\rho},\tilde{\delta}\right) = \frac{2\left[1-\Gamma\left(\tilde{\delta}\right)\right](\tilde{\rho}-1)}{2\tilde{\rho}+1-3\Gamma\left(\tilde{\delta}\right)}, \quad \text{with } \tilde{\rho} = \frac{\rho_{\mathrm{p}}}{\rho_0}, \tag{12b}$$

$$\Gamma\left(\tilde{\delta}\right) = -\frac{3}{2}\left[1+i\left(1+\tilde{\delta}\right)\right]\tilde{\delta}, \quad \text{with } \tilde{\delta} = \frac{\delta}{a}, \tag{12c}$$

For the special case of the horizontal pressure half-wave resonance, $p_1 = p_a\sin(qy)$, with channel width w and wavenumber $q = \pi/w$, the acoustic energy density is $E_{\mathrm{ac}} = \frac{1}{4}\kappa_0 p_a^2 = \frac{1}{4}\rho_0 U_1^2$. The expression for the radiation force then simplifies to

$$F_{1D}^{rad} = 4\pi\Phi(\tilde{\kappa},\tilde{\rho},\tilde{\delta})a^3 qE_{ac}\sin(2qy), \quad (13a)$$

$$\Phi\left(\tilde{\kappa},\tilde{\rho},\tilde{\delta}\right) = \frac{1}{3}f_1(\tilde{\kappa}) + \frac{1}{2}\,\mathrm{Re}\left[f_2\left(\tilde{\rho},\tilde{\delta}\right)\right], \quad (13b)$$

where Φ is the so-called acoustic contrast factor.

The time-averaged Stokes drag force $\boldsymbol{F}^{drag}$ on a spherical particle of radius a moving with velocity $\boldsymbol{u}$ in a fluid having the streaming velocity $\langle \boldsymbol{v}_2 \rangle$ is given by the usual expression

$$\boldsymbol{F}^{drag} = 6\pi\eta a(\langle \boldsymbol{v}_2 \rangle - \boldsymbol{u}), \quad (14)$$

valid for particles sufficiently far from the channel walls.[28]

III Numerical model

In the following we present the idealized numerical model, and how we implement and solve the governing equations for this model using the finite element software COMSOL Multiphysics 4.2a, see ref. 29.

A Model system and computational domain

Given the detailed measurements of the acoustophoretic motion and the successful comparison with theoretical predictions presented in ref. 7 and 8, it is natural to use an idealization of their straight microchannel of length 35 mm and rectangular cross section as a model system in our numerical study. We neglect the chip structure and simply represent the silicon–glass chip as hard-wall boundary conditions. We further neglect any axial dynamics in the long straight channel, and thus restrict our analysis to the rectangular cross section Ω of width w = 0.38 mm and height h = 0.16 mm in the vertical yz-plane, see Fig. 2. Finally, we represent the ultrasonic piezo transducer by the velocity boundary condition eqn (4). The particle suspensions are modeled as being monodisperse and containing non-interacting, spherical polystyrene particles with diameters of 0.5, 1.0, 2.0, 3.0, or 5.0 μm, respectively.

The model system has a horizontal half-wave resonance across the width w given by the frequency $f = \omega/(2\pi) = c_0/(2w)$, equal to 1.97 MHz for water. To excite this resonance, we let all external acoustic excitations have a harmonic time dependence of frequency f = 1.97 MHz. All relevant material parameters are listed in Table 1 .

B Particle tracing model

In order to study the acoustophoretic motion of N particles suspended in the microchannel, we apply the COMSOL Particle Tracing Module, which closely mimics experimental particle tracing and velocimetry.[7,8] This module provides a Lagrangian description of the motion of the particles, each of which is treated as a point particle governed by Newton's law of motion, and thus involving one ordinary differential equation (ODE) for each spatial direction. Consequently, in total $2N$ ODEs are solved for the particle suspension. The input are the particle masses m_j and all forces $\mathrm{F}_i(\boldsymbol{r}_j)$ acting on each particle at position $\boldsymbol{r}_j$. The ODE for the jth particle with velocity $\boldsymbol{v}_j = \mathrm{d}\boldsymbol{r}_j/\mathrm{d}t$ is

$$m_j \frac{\mathrm{d}\boldsymbol{v}_j}{\mathrm{d}t} = \sum_i \boldsymbol{F}_i(\boldsymbol{r}_j). \quad (15)$$

Neglecting gravitational effects, the forces acting on a particle in our model are the radiation force $\boldsymbol{F}^{rad}$, eqn (11) , and the Stokes drag force $\boldsymbol{F}^{drag}$, eqn (14). These forces are calculated numerically as described in the following sub-section.

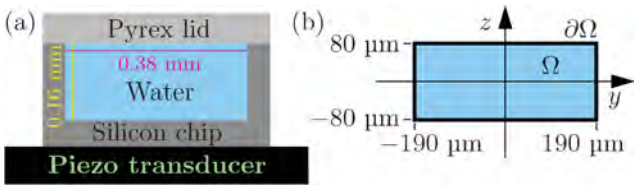

Fig. 2 (a) End-view sketch of the acoustophoresis microchip with a fluidic channel of width w = 0.38 mm and height h = 0.16 mm used in experiments.[7,8] It consists of a silicon chip (dark gray), a pyrex lid (light gray), water (blue), and a piezo transducer (black). (b) The corresponding two-dimensional computational domain Ω (blue) surrounded by rigid walls ∂Ω (black) implemented in our numerical model.

Table 1 Model parameters. The parameters are given at temperature T = 25° and taken from the COMSOL Material Library unless explicit stated otherwise.

Polystyrene			
Density[30]	ρ_{ps}	1050	kg m^{-3}
Speed of sound[31] (at 20 °C)	c_{ps}	2350	m s^{-1}
Poisson's ratio[32]	σ_{ps}	0.35	
Compressibility[a]	κ_{ps}	249	TPa^{-1}
Water			
Density	ρ_0	998	kg m^{-3}
Speed of sound	c_0	1495	m s^{-1}
Compressibility[b]	κ_0	448	TPa^{-1}
Viscosity	η	0.893	mPa s
Visc. boundary layer, 1.97 MHz	δ	0.38	μm
Thermal conductivity	k_{th}	0.603	W m^{-1} K^{-1}
Specific heat capacity	C_p	4183	Jkg^{-1}K^{-1}
Specific heat capacity ratio[c]	γ	1.014	
Thermal diffusivity[d]	D_{th}	1.43 × 10^{-7}	m^2 s^{-1}
Thermal expansion coeff.[e]	α	2.97 × 10^{-4}	K^{-1}
50% glycerol-in-water mixture			
Density[34]	ρ_0	1129	kg m^{-3}
Speed of sound[35]	c_0	1725	m s^{-1}
Compressibility[b]	κ_0	298	TPa^{-1}
Viscosity[34]	η	5.00	mPa s
Visc. boundary layer, 2.27 MHz	δ	0.79	μm
Thermal cond.[36] (at 20 °C)	k_{th}	0.416	W m^{-1} K^{-1}
Specific heat cap.[37] (at 1.7 °C)	C_p	3360	J kg^{-1} K^{-1}
Specific heat capacity ratio[c]	γ	1.043	
Thermal diffusivity[d]	D_{th}	1.10 × 10^{-7}	m^2 s^{-1}
Thermal expansion coeff.[e]	α	4.03 × 10^{-4}	K^{-1}

[a] Calculated as $\kappa_{ps} = \frac{3(1-\sigma_{ps})}{1+\sigma_{ps}}\frac{1}{(\rho_{ps}c_{ps}^2)}$ from ref. 33.
[b] Calculated as $\kappa_0 = 1/(\rho_0 c_0^2)$ from eqn (2b).
[c] Calculated from $T_0\alpha^2/(\rho_0 C_p \kappa) = \gamma - 1$.
[d] Calculated as $D_{th} = k_{th}/(\rho_0 C_p)$.
[e] Calculated from eqn (2c).

C Numerical procedure

We have used the following sequential procedure to solve the problem numerically in COMSOL:

(*i*) The first-order acoustic fields of eqn (5), subject to the boundary conditions of eqn (4), are calculated using the predefined Thermoacoustic Physics Interface.

(*ii*) The time-averaged second-order flow $\langle \boldsymbol{v}_2 \rangle$ is calculated by implementing eqn (9) in the Laminar Flow Physics Interface, modified to include the addition of the time-averaged first-order products from step (*i*) on the right-hand sides: the right-hand side of eqn (9a) is included as a mass source term by adding a so-called weak contribution to the governing equations, $-\frac{1}{2}\int_\Omega [\partial_x Re(\rho_1 v_{1x}^*) + \partial_y Re(\rho_1 v_{1y}^*)]\tilde{p}_2 \, \mathrm{d}V$ ($\tilde{p}_2$ being the pressure test function), while the right-hand side of eqn (9b) is added straightforwardly as a body force term. Furthermore, the fourth-order non-linear term $\rho_0(\langle \boldsymbol{v}_2 \rangle \cdot \nabla)\langle \boldsymbol{v}_2 \rangle$ is kept in the laminar flow equations in COMSOL to enhance numerical stability.

(*iii*) The acoustic radiation forces are determined using eqn (11) with the first-order fields of step (*i*).

(*iv*) Finally, the time-dependent motion of the particles is determined using the COMSOL Particle Tracing Module only taking into account the radiation force of step (*iii*) and the drag force of eqn (14).

The solution strategy was carried out on a computational mesh large enough for all dependent variables to reach convergence, while taking special care to properly resolve the acoustic boundary layer with an adequate computational mesh, see Section III E. This fine mesh was used when determining the first-order fields and the time-averaged second-order fields. In the subsequent simulation of the time-dependent particle motion, the flow field and radiation forces were interpolated to a coarser mesh to speed up the transient solving procedure substantially.

D Computer hardware requirements

The computation was performed on a DELL Precision 7500 workstation running Windows 7 (64-bit) equipped with 48 GB RAM (1333 MHz) and two hexa-core Intel Xeon X5650 processors of clock frequency 2.66 GHz and 12 MB cache.

When calculating the first-order acoustic fields in step (*i*), we used the mesh found by the mesh-convergence analysis described in the following subsection, and this resulted in about 3×10^6 degrees of freedom, a calculation time of 4.5 min, and a peak RAM usage of 64% or 31 GB. The calculation of the second-order acoustic fields in step (*ii*) required around 5×10^5 degrees of freedom and took 2 min, while having a peak RAM usage of 19% or 9 GB. The computation time for steps (*iii*) and (*iv*) was less than 15 s for calculation of 144 particle trajectories of 100 time steps and solved on a coarser mesh resulting in about 9×10^4 degrees of freedom.

E Mesh convergence

The computational mesh is generated from a maximum element size length d_{mesh} at the domain boundaries $\partial\Omega$ and a maximum element size in the bulk of the domain Ω given by $10d_{\mathrm{mesh}}$. For illustrative purposes, the computational mesh shown in Fig. 3(a) is a coarse mesh with 1204 elements and $d_{\mathrm{mesh}} = 20\delta$, or $\delta/d_{\mathrm{mesh}} = 0.05$, where δ is the boundary layer thickness defined in eqn (7). In order to verify the correctness of the solution, a mesh-convergence analysis is required. The solutions are compared for decreasing mesh element size d_{mesh} to determine the point at which the solution becomes independent of any further decrease of d_{mesh}. We define a relative convergence parameter $C(g)$ for a solution g with respect to a reference solution g_{ref} taken to be the

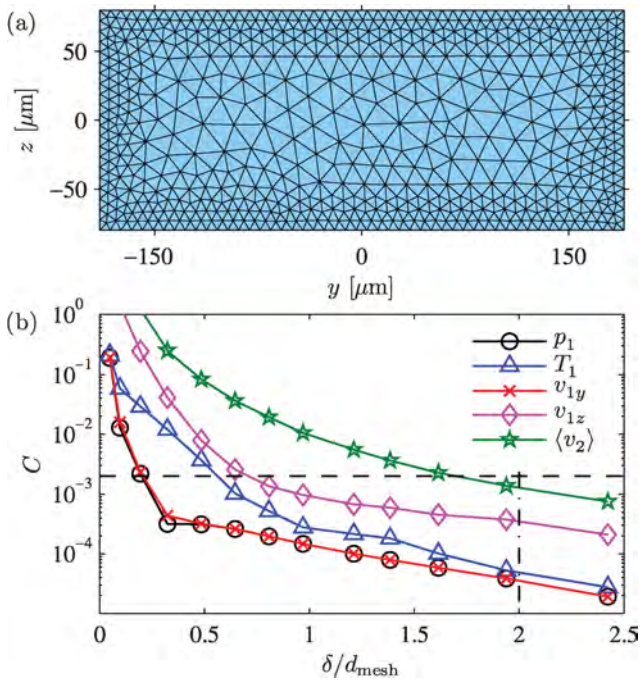

Fig. 3 (a) The computational mesh for a maximum element size of $d_{\mathrm{mesh}} = 20\delta$ at the boundaries, resulting in a coarse mesh with only 1204 triangular elements. (b) Semi-logarithmic plot of the relative convergence parameter C, eqn (16), for the physical fields as the size of the mesh elements is decreased. The dashed line indicates a threshold of $C = 0.002$, chosen as a trade off between accuracy and computational time. For the second-order velocity field to get below this convergence threshold, a maximum element size of $d_{\mathrm{mesh}} = 0.5\delta$ or $\delta/d_{\mathrm{mesh}} = 2.0$ is needed at the boundaries of the domain (dash-dotted line).

solution for the smallest value of d_{mesh},

$$C(g) = \sqrt{\frac{\int (g - g_{\mathrm{ref}})^2 \, \mathrm{d}y \, \mathrm{d}z}{\int (g_{\mathrm{ref}})^2 \, \mathrm{d}y \, \mathrm{d}z}}. \qquad (16)$$

For g_{ref} we have chosen $d_{\mathrm{mesh}} = 0.3\delta$ or $\delta/d_{\mathrm{mesh}} = 3.3$, which resulted in 2.6×10^5 triangular mesh elements.

The exponential convergence of both first- and second-order fields for $d_{\mathrm{mesh}} < \delta$ shows up as straight lines in the semi-logarithmic plots of Fig. 3(b). The time-averaged second-order velocity field $\langle \boldsymbol{v}_2 \rangle$ converges considerably slower than the first-order fields, as it depends on the gradients of the first-order fields, and thus demands better resolution. In order to obtain a relative convergence of the second-order velocity field below 0.002 (dashed line), a maximum element size of $d_{\mathrm{mesh}} = 0.5\delta$ or $\delta/d_{\mathrm{mesh}} = 2.0$ is needed at the boundaries. This mesh size, which results in 1.2×10^5 triangular elements, is used for the results presented in this paper.

IV Results

The following results are aimed at showing the insensitivity of the horizontal half-wave resonance to the specific form of the ultrasound actuation, at characterizing the first- and second-order acoustic fields, and at investigating the dependence of the acoustophoretic microparticle motion on system geometry and material parameters.

A Actuation

The ultrasound actuation is modeled using the velocity boundary condition in eqn (4c) at the frequency 1.97 MHz to excite the horizontal half-wave resonance in our model system Fig. 2(b). Using the following three actuation modes for the velocity boundary condition v_{bc} in eqn (4c),

$$v_{bc}^{A}(\pm w/2,z) = \pm v_{bc,0}^{A}, \tag{17a}$$

$$v_{bc}^{B}(y,-h/2) = v_{bc,0}^{B} \sin\left(2\pi\frac{y}{w}\right), \tag{17b}$$

$$v_{bc}^{C}(y,-h/2) = v_{bc,0}^{C}\left(\frac{1}{2}-\frac{y}{w}\right)\left(\frac{1}{2}+\frac{y}{w}\right)^{2}, \tag{17c}$$

we show the expected result that this resonance is indeed excited regardless of the detailed spatial dependence of v_{bc} as long as the oscillation frequency equals the resonance frequency.

For all three actuation modes, the amplitude of the velocity boundary conditions is chosen in such a way that the line integral of the absolute value $|v_{bc}|$ of the velocity along the perimeter $\partial\Omega$ of the domain Ω is given in terms of the angular frequency ω and a characteristic value d_0 of the displacement of an actuated boundary,

$$\oint_{\partial\Omega} |v_{bc}^{X}|\,d\ell = 2h\omega d_0, \quad X = A,B,C. \tag{18}$$

In particular, the normalization constant $2h$ is chosen so that $v_{bc,0}^{A} = \omega d_0$, with d_0 = 0.1 nm, a typical value of displacements,[38] which results in resonance amplitudes in the range of those measured in typical experiments.[7,39–41]

The first-order pressure fields resulting from the three different actuation modes are shown in Fig. 4. It is seen that all of the actuation modes excite the horizontal half-wave 1.97-MHz resonance. Although the velocity boundary conditions have been normalized, the amplitude of the resonance is different for each of the three actuation modes, *i.e.* each actuation mode couples to the resonance mode with its own strength. In the studies presented in the rest of this paper, we have used the velocity boundary condition eqn (17a), shown in Fig. 4(a), due to its simplicity and strong coupling to the resonance mode.

B First-order fields

We now turn to a study of the first-order fields resulting from the velocity boundary condition eqn (17a) and Fig. 4(a). In Fig. 5, color plots of the pressure p_1, temperature T_1, horizontal velocity

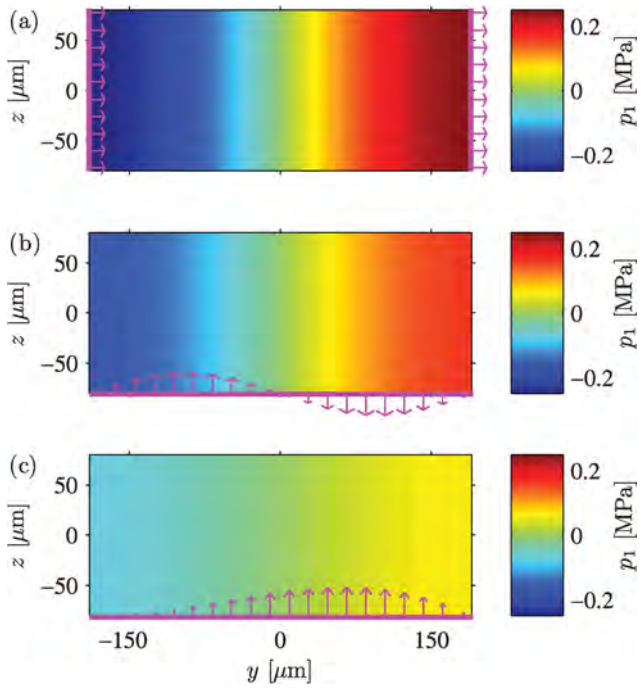

Fig. 4 Three different actuation modes v_{bc} (magenta arrows) of the water-filled cavity. Color plot of the first-order pressure field p_1 resulting from the actuation, eqn (17). In all cases the actuation frequency is 1.97 MHz, corresponding to the lowest resonance frequency of the cavity, and it is seen that all three actuation modes excite the horizontal half-wave resonance. The pressure amplitude of the resonance mode is (a) 0.24 MPa with side-wall actuation, (b) 0.16 MPa with anti-symmetric bottom-wall actuation, and (c) 0.06 MPa with non-symmetric bottom-wall actuation.

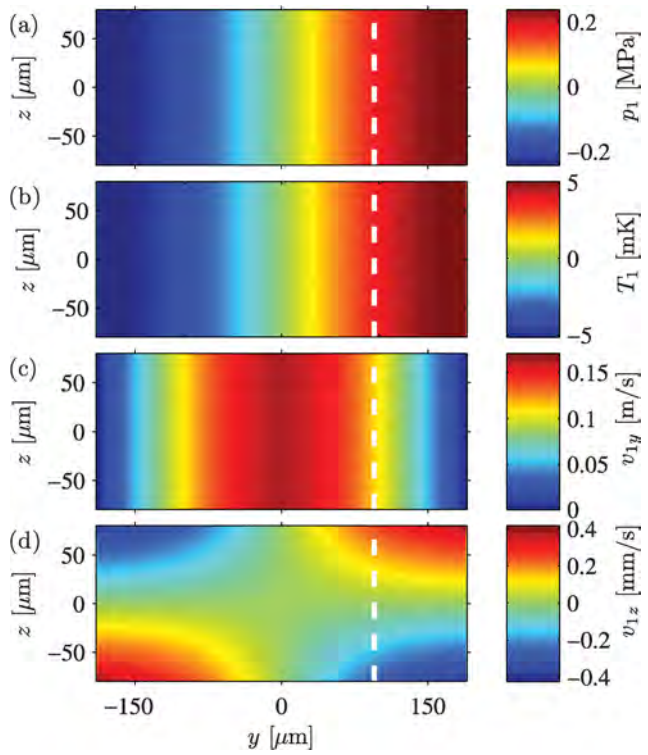

Fig. 5 Color plots of the amplitudes of the oscillating first-order fields in the water-filled channel at the horizontal standing half-wave 1.97-MHz resonance excited by velocity boundary condition eqn (17a): (a) pressure p_1, identical to panel (a) in Fig. 4, (b) temperature T_1, (c) horizontal velocity v_{1y}, and (d) vertical velocity v_{1z}. The horizontal velocity is much larger than the vertical velocity, arising because of the interaction of the acoustic resonance with the bottom and top walls. The sub-micrometer thin viscous boundary cannot be seen on the 100-μm scale of the plot. The dashed white lines indicate the domain for the line plots in Fig. 6.

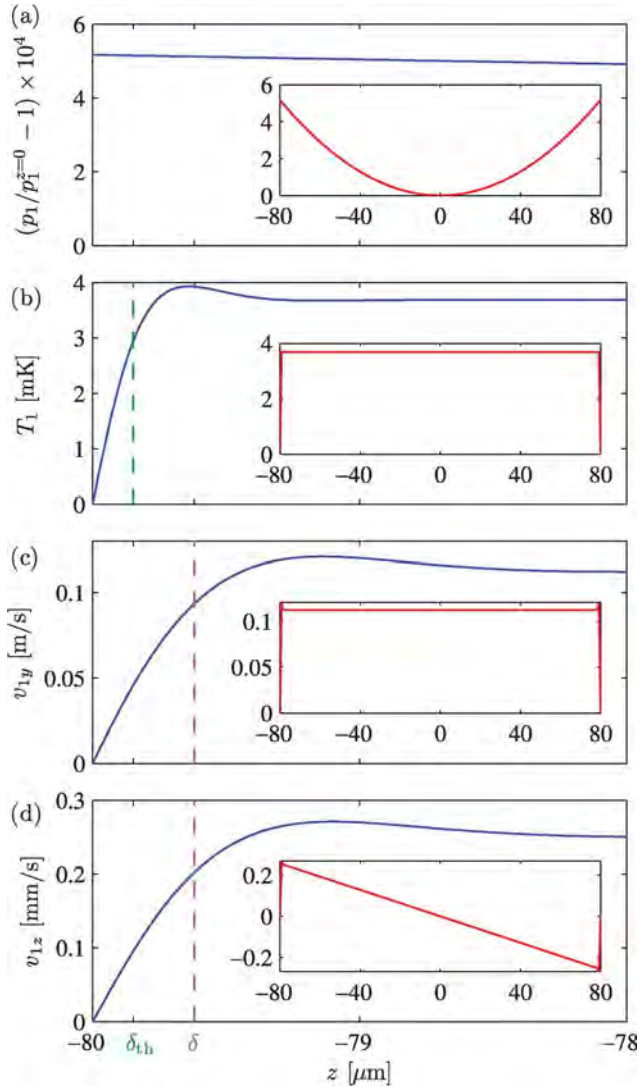

Fig. 6 Line plots, along the dashed white lines at $y = w/4$ shown in Fig. 5, of the amplitudes of the oscillating first-order fields: (a) relative pressure change $p_1/p_1^{z=0} - 1$, (b) temperature T_1, (c) horizontal velocity v_{1y}, and (d) vertical velocity v_{1z}. The main plots (blue curves) show the field amplitudes close to the bottom wall, while the insets (red curves) show the field amplitudes along the entire height of the channel. The characteristic length scales of the thermal and viscous boundary layers, δ_{th} and δ, are indicated by the green and magenta dashed lines, respectively. T_1, v_{1y}, and v_{1z} all show marked variations on the length scale of the boundary layer, while p_1 and v_{1z} only show variations across the full height of the domain.

v_{1y}, and vertical velocity v_{1z} are shown. The amplitudes and structures of p_1, T_1, and v_{1y} relate to the acoustic resonance, while v_{1z} arises due to the viscous interaction of the horizontal half-wave resonance in the bulk with the bottom and top walls. Consequently, the magnitude of v_{1z} is insignificant compared to the magnitude of v_{1y}. The amplitudes of p_1 and T_1 have the same spatial structure, shifted horizontally by $\lambda/4$ with respect to the spatial structure of v_{1y}.

In Fig. 6 the amplitudes of the first-order fields are plotted along the dashed white lines at $y = w/4$ shown in Fig. 5. In Fig. 6(a) we have plotted the relative pressure change, $p_1/p_1^{z=0} - 1$, with respect to the pressure amplitude at the center $(y,z) = (w/4,0)$. This relative change is in the order of 10^{-4}, implying that p_1 is nearly independent of z. In particular, p_1 shows no marked variation on the length scale of the boundary layer thickness δ as opposed to the velocity v_{1y} and temperature T_1 of Fig. 6(b)–(c). To fulfill the boundary conditions in eqn (4), the latter two decrease from their bulk values to zero at the wall over a few times δ_{th} and δ, respectively, which defines the thicknesses of the thermal and viscous boundary layers, respectively (dashed lines in Fig. 6). Further, also v_{1z} increases from zero at the wall, but then it exhibits a slow linear decrease outside the boundary layer, Fig. 6(d). T_1, v_{1y}, and v_{1z} all overshoot slightly before settling at their respective bulk values, an effect similar to that observed in the classical problem of a planar wall executing in-plane oscillations.[20] While T_1 and v_{1y} show no variations in the height of the channel outside the boundary layers, p_1 and v_{1z} do so, with p_1 being symmetric (nearly parabolic) and v_{1z} being anti-symmetric (nearly linear). These variations of p_1 and v_{1z} result from the viscous interaction between the horizontal acoustic resonance and the bottom and top wall, bounding the acoustic resonance fields.

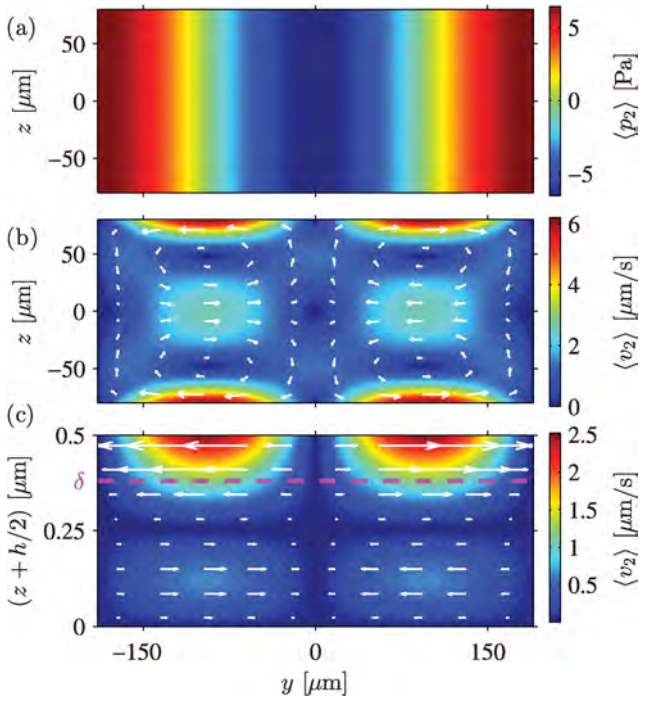

Fig. 7 Time-averaged second-order fields in the water-filled channel excited in the horizontal half-wave 1.97-MHz resonance by the side-wall actuation shown in Fig. 4(a) and driven by the first-order fields plotted in Fig. 5. (a) Color plot of the time-averaged second-order pressure $\langle p_2 \rangle$ with a magnitude approximately 2.5×10^{-5} times smaller than the amplitude of the oscillating first-order pressure p_1 in Fig. 5(a). (b) Vector plot (white arrows) of the time-averaged second-order streaming velocity $\langle \boldsymbol{v}_2 \rangle$ and color plot of its magnitude $\langle v_2 \rangle$. Four bulk (Rayleigh) streaming rolls are clearly seen having the maximum speed near the top and bottom walls. (c) Zoom-in on the 0.4-μm-thick boundary layer near the bottom wall exhibiting the two boundary (Schlichting) streaming rolls that drive the bulk (Rayleigh) streaming rolls.

C Second-order fields and acoustic streaming

As described by eqn (9) the non-linear interactions of the first-order fields give rise to time-averaged second-order fields, resulting in a static pressure field and a steady velocity field as shown in Fig. 7 . The time-averaged second-order fields exhibit a spatial oscillation in the horizontal y-direction of wave length $\lambda/2$. This is reminiscent of the spatial period doubling for the classical infinite parallel-plate system of Fig. 1 .

The magnitude of the time-averaged second-order pressure $\langle p_2 \rangle$ in Fig. 7(a) is approximately 2.5×10^{-5} times smaller than the amplitude of the oscillating first-order pressure in Fig. 5(a). The time-averaged velocity field $\langle \boldsymbol{v}_2 \rangle$ in Fig. 7(b) contains four bulk (Rayleigh) streaming rolls. The streaming velocity is maximum close to the top and bottom wall and has two local maxima on the horizontal center axis $z = 0$, where opposite pairs of bulk rolls meet. The solution in Fig. 7(b) is similar to Rayleigh's analytical solution[17,20] sketched in Fig. 1, but it deviates on the following two points: (*i*) as we consider a rectangular geometry and not parallel plates, the velocity is forced to be zero at the side walls, which slightly slows down the rotational flow of the streaming rolls, and (*ii*) as we are not in the limit $h \ll \lambda$, the strength of the streaming rolls decreases slightly before meeting in the center of the channel, which results in a lower magnitude of the streaming velocity in the horizontal center plane than predicted by Rayleigh.

Fig. 7(c) shows a zoom-in on the 0.4-μm-thick viscous boundary layer close to the bottom wall containing two boundary (Schlicting) streaming rolls. These boundary rolls are very elongated in the horizontal direction; the z-axis in Fig. 7(c) is stretched nearly a factor 10^3 relative to the y-axis. It is important to mention that the boundary streaming rolls are generated by the non-linear interactions of the first-order fields inside the boundary layer, whereas the bulk streaming rolls are driven by the boundary streaming rolls and not by the non-linear interaction of the first-order fields in the bulk. The time-averaged second-order velocity $\langle \boldsymbol{v}_2 \rangle$ is zero at the bottom wall, thus fulfilling the boundary conditions eqn (4b), while the maximum of its horizontal component $v_{2y}{}^{\mathrm{bnd}} = 6.42\ \mu\mathrm{m\ s}^{-1}$ is reached at a distance of approximately 3δ from the wall. The maximum bulk amplitude $U_1 = 0.162\ \mathrm{m\ s}^{-1}$ of the horizontal first-order velocity component, v_{1y} shown in Fig. 5(c), is reached at the channel center $y = 0$. From this we calculate the characteristic velocity ratio $\Psi = c_0\, v_{2y}^{\mathrm{bnd}}/U_1{}^2 = 0.367$, which deviates less than 3% from the value $\Psi = 3/8 = 0.375$ of the parallel-plate model eqn (10).

D Particle tracing simulations

In most experimental microfluidic flow visualization techniques, tracer particles are employed.[42] To mimic this and to ease comparison with experiment, we have performed particle tracing simulations using the technique described in Section III B. In all simulations, we have studied the motion of 144 polystyrene microparticles suspended in water and distributed evenly at the initial time $t = 0$ as shown in Fig. 8(a).

In Fig. 8(b)–(f), the particle trajectories after 10 s of acoustophoretic motion of the 144 microparticles are shown. Within each panel, all particles have the same diameter $2a$, but the particle size is progressively enlarged from one panel to the next: (b) $2a = 0.5$ μm, (c) 1 μm, (d) 2 μm, (e) 3 μm, and (f) 5 μm. For the smallest particles, panels (b) and (c), the drag force from the acoustic streaming dominates the particle motion, and the characteristic streaming flow rolls are clearly visualized. For the larger particles, panels (e) and (f), the acoustic radiation force dominates the particle motion, and the particle velocity $\boldsymbol{u}$ is nearly horizontal with the sinusoidal spatial dependence given by $u_y(y) = F_{1\mathrm{D}}^{\mathrm{rad}}(y)/(6\pi\eta a)$ found from eqn (13a). This results in a focusing motion of the particles towards the vertical pressure nodal plane at $y = 0$. Panels (d) and (e) show an intermediate regime where drag and radiation forces are of the same order of magnitude.

At the nodal plane $y = 0$ the radiation forces are zero, and consequently for times t larger than 10 s all particles in panel (f) that have reached $y = 0$ end up at $(y,z) = (0, \pm h/2)$ due to the weak but non-zero streaming-induced drag forces.

The cross-over from one acoustophoretic behavior to the other as a function of particle size, with a critical particle diameter of 2 μm found in Fig. 8(d), is in agreement with the following scaling argument:[16] If we assume a force balance between the radiation force and the drag force from acoustic streaming, $\boldsymbol{F}^{\mathrm{rad}} = -\boldsymbol{F}^{\mathrm{drag}}$, keeping a given particle fixed ($\boldsymbol{u} = \boldsymbol{0}$), and if we estimate the magnitude of the streaming velocity to be given by eqn (10) as $\langle v_2 \rangle = \Psi U_1{}^2/c_0$, where Ψ is a geometry-dependent factor of order unity, then eqn (13) and (14) lead to

$$\pi a_c^3 q\, \rho_0 U_1^2 \Phi \approx 6\pi\eta a_c\, \Psi\, \frac{U_1^2}{c_0}, \tag{19}$$

where a_c is the critical particle radius. Thus, as found in eqn (16), the critical particle diameter $2a_c$ becomes

$$2a_c = \sqrt{12\,\frac{\Psi}{\Phi}}\,\delta \approx 2.0\ \mu\mathrm{m}. \tag{20}$$

The value is calculated using $\Psi = 0.375$, valid for a planar wall (eqn (10)), and $\Phi = 0.165$, obtained for polystyrene particles with diameters between 0.5 μm and 5 μm in water obtained from eqn (13b) using the parameter values from Table 1. The relation eqn (20) for the critical cross-over particle diameter is important for designing experiments relying on specific acoustophoretic behaviors as function of particle size. Channel geometry enters through the factor Ψ, particle and liquid material parameters through Φ, and liquid parameters and frequency through the boundary layer thickness δ.

E Streaming for an increased aspect ratio

As an example of how geometry affects the acoustophoretic motion of polystyrene microparticles, we study here the consequences of increasing the aspect ratio of the channel cross-section from $h/w = 0.42$ to 2 keeping all other parameters fixed. As illustrated in Fig. 9(a), the streaming velocity field is only significant close to the top and bottom of the channel for the large aspect ratio $h/w = 2$. This happens because given enough vertical space, the vertical extension Δ of the streaming roll is identical to the horizontal one, which is $\Delta = \lambda/4$. For the horizontal half-wave resonance in a channel of aspect ratio $h/w = 2$ we have $\lambda = 2w = h$, which implies $\Delta = h/4$, and we therefore expect a streaming-free region with a vertical extent of $h - 2(h/4) = h/2$ around the center of the channel, which indeed is seen in Fig. 9(a).

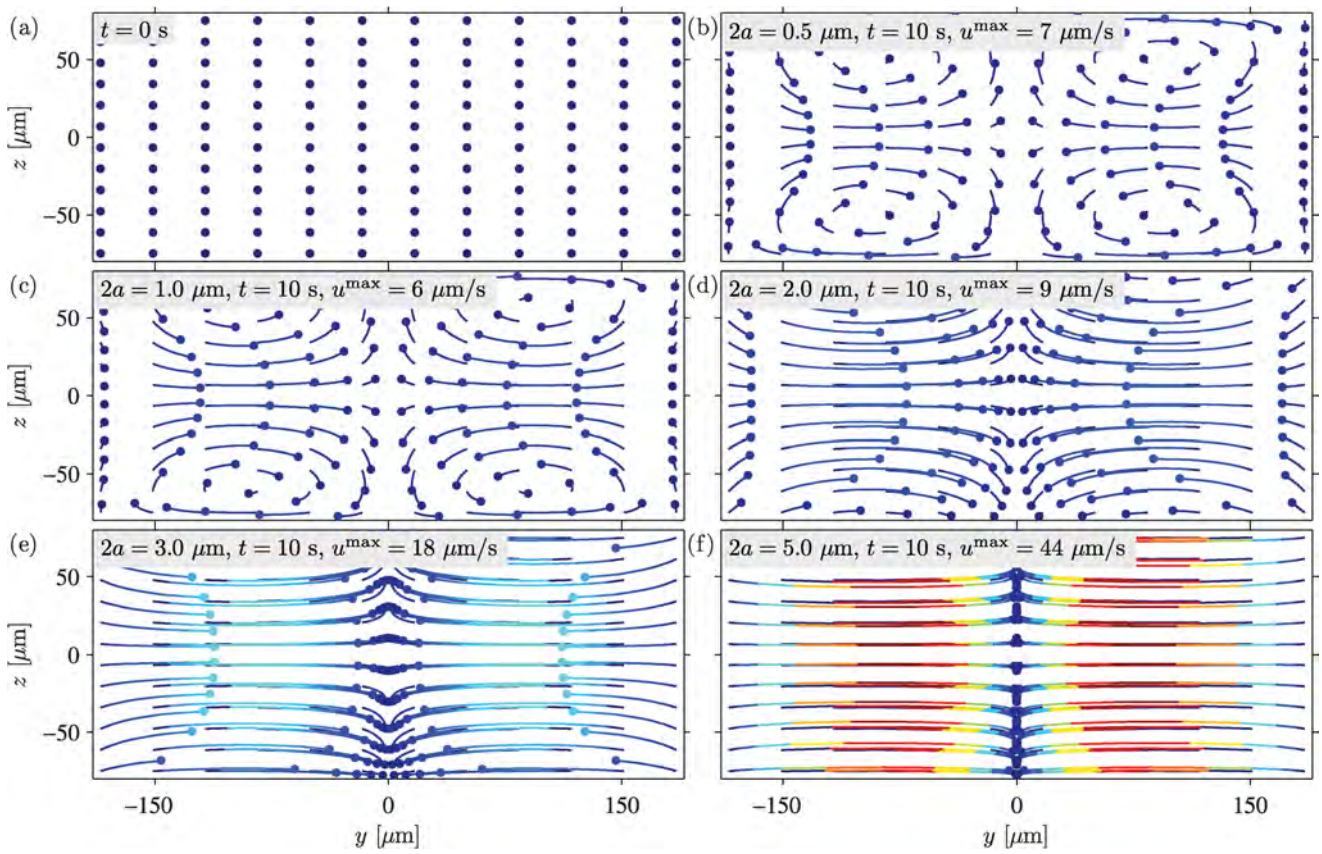

Fig. 8 (a) The starting positions (dots) of 144 evenly distributed particles at $t = 0$ s in the computational domain at the onset of the horizontal half-wave 1.97-MHz resonance shown in Fig. 5 and 7. The following five panels show the trajectories (colored lines) and positions (dots) that the particles have reached by acoustophoresis at $t = 10$ s for five different particle diameters: (b) 0.5 μm, (c) 1 μm, (d) 2 μm, (e) 3 μm, and (f) 5 μm. The colors indicate the instantaneous particle velocity u ranging from 0 μm s^{-1} (dark blue) to 44 μm s^{-1} (dark red). The lengths of the trajectories indicate the distance covered by the particles in 10 s. Streaming-induced drag dominates the motion of the smallest particles, which consequently are being advected along the acoustic streaming rolls of Fig. 7(b). In contrast, the acoustic radiation force dominates the motion of the larger particles, which therefore are forced to the vertical nodal plane at $y = 0$ of the first-order pressure p_1 shown in Fig. 5(a).

As a consequence, the acoustophoretic motion of particles in the center region is controlled by the radiation force. This is illustrated in Fig. 9(b), where trajectories of small 1-μm-diameter particles are shown. For $-h/4 < z < h/4$ their motion is similar to the radiation-force dominated motion of the larger 5-μm-diameter particles moving in the shallow channel with $h/w = 0.42$ as shown in Fig. 8(f). Near the top and bottom walls, the 1 μm diameter particles exhibit the usual small-particle streaming-induced motion.

Clearly, geometry can be used to obtain more control of the acoustophoretic motion of suspended particles in microchannels.

F Streaming in a high-viscosity buffer

According to eqn (20), the critical particle diameter for cross-over between radiation-dominated and streaming-dominated acoustophoretic motion is proportional to the boundary layer thickness $\delta = \sqrt{2\eta/(\rho_0\omega)}$. Obviously, viscosity can also be used to control acoustophoresis. We therefore studied the effects of replacing water (η = 1 mPa s) with glycerol mixtures, in particular the 50% glycerol-in-water mixture (η = 5 mPa s), for which the relevant material parameters are listed in Table 1.

First, to ensure comparable conditions, we wanted to excite the horizontal half-wave resonance in the glycerol-in-water system. As the speed of sound of the glycerol mixture is 15% larger than that of water, we found the resonance frequency to be $f = c_0/(2w) = 2.27$ MHz. This frequency was used in the velocity boundary condition eqn (17a) to calculate the results shown in Fig. 10 for the first-order pressure field, the time-averaged second-order streaming velocity field, and particle trajectories for 5-μm-diameter polystyrene particles.

The glycerol-in-water and the water system are actuated with the same boundary velocity given in eqn (18) , but the difference in viscosity of the two liquids leads to different acoustic responses. The amplitude of the induced first-order resonance pressure is reduced by a factor of 2.6 from 0.243 MPa in the low-viscosity water of Fig. 5(a) to 0.094 MPa in the high-viscosity glycerol mixture of Fig. 10(a). Likewise, the induced streaming velocity $\langle v_{2y}^{bnd} \rangle$ near the boundary is reduced by a factor of 15 from 6.42 μm s^{-1} in water, Fig. 7(b), to 0.43 μm s^{-1} in glycerol-in-water, Fig. 10(b). In contrast, given the validity of Rayleigh's streaming theory, the velocity ratio $\Psi = c_0\langle v_{2y}^{bnd} \rangle / U_1^2$ should be independent of viscosity. For the glycerol-in-water mixture it is 0.336 deviating 8% from the value in water, see Section IV C, and 10% from the Rayleigh value 3/8 of eqn (10) . The significant difference in the numerically determined values of Ψ for water and glycerol-in-water points to the inadequacy of the Rayleigh

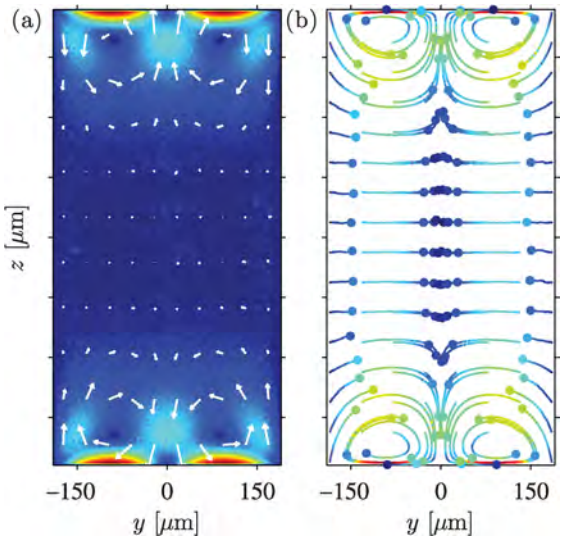

Fig. 9 Acoustophoresis in a high-aspect-ratio channel. The setup is identical to Fig. 4(a) except that for the fixed width w = 0.38 mm the channel height h has been increased from 0.16 mm (aspect ratio h/w = 0.42) to 0.76 mm (aspect ratio h/w = 2). (a) Vector plot (white arrows), similar to Fig. 7(b), of the time-averaged second-order streaming velocity $\langle \boldsymbol{v}_2 \rangle$ and color plot [from 0 μm s^{-1} (dark blue) to 4.2 μm s^{-1} (dark red)] of its magnitude. (b) Particle tracing plot for 1-μm-diameter polystyrene particles corresponding to Fig. 8(c) but for time t = 100 s, aspect ratio h/w = 2, and velocity ranging from 0 μm s^{-1} (dark blue) to 3.3 μm s^{-1} (dark red). In this high aspect-ratio geometry the acoustic streaming flow rolls are located near the top and bottom walls leaving the center region nearly streaming free.

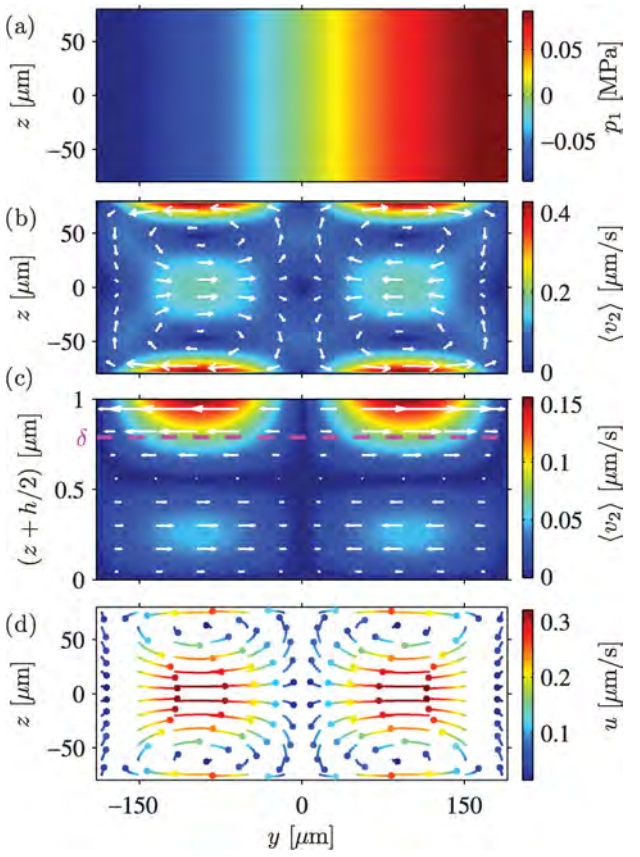

Fig. 10 Acoustophoresis in a 50% glycerol-in-water mixture. The setup is identical to Fig. 4(a) except that the resonance frequency is increased to $f = c_0/(2w)$ = 2.27 MHz. (a) Color plot of the pressure p_1 showing the horizontal half-wave resonance. (b) Vector plot (white arrows) of the time-averaged second-order streaming velocity $\langle \boldsymbol{v}_2 \rangle$ and color plot of its magnitude corresponding to Fig. 7(b). (c) Zoom-in on the 0.4-μm-thick boundary layer near the bottom wall corresponding to Fig. 7(c). (d) Particle tracing plot for 5-μm-diameter polystyrene particles corresponding to Fig. 8(f) but for 150 s. Contrary to the water-filled channel in Fig. 8(f), the motion of the 5-μm-particles in the more viscous glycerol-in-water mixture are dominated by the streaming-induced drag, whereby the particle trajectories end up looking more like those of the smaller 1-μm-diameter particles Fig. 8(c).

theory in a rectangular channel. This is perhaps not a surprise, as this theory is derived for an infinite parallel-plate channel.

In Fig. 10(c) is shown that the viscous boundary-layer thickness in the glycerol-in-water mixture at 2.27 MHz is δ = 0.79 μm, a factor 2.1 larger than the value δ = 0.38 μm in water at 1.97 MHz shown in Fig. 7(c). As the two resonance frequencies only differ by 10%, the change in the boundary-layer thickness is mainly due to the viscosity ratio, $\sqrt{5\ \text{mPa s}}/\sqrt{1\ \text{mPa s}} \approx 2.2$.

Finally, from eqn (10) using $\Psi = 3/8$ and $\Phi = 0.031$, we calculated the critical particle diameter to be $2a_c$ = 9.5 μm for the cross-over from radiation-dominated to streaming-dominated acoustophoretic motion in the glycerol-in-water system. This value explains why the particle trajectories for the 5-μm-diameter polystyrene particles in Fig. 10(d) appear to be much more influenced by the acoustic streaming rolls, compared to the same-sized particles in water, Fig. 8(f). Instead, Fig. 10(d) resembles more the motion of the 1-μm-diameter particles in water, Fig. 8(c). This resemblance can be quantified by the ratio a/a_c: for 5-μm-diameter particles in the glycerol-in-water mixture it is 0.52, while for 1-μm-diameter particles in pure water it is 0.50, only 4% lower. Note that because of the reduction in streaming velocity by the above-mentioned factor of 15, we have chosen to follow the particles in the glycerol-in-water mixture for 150 s and in water only for 10 s.

V Concluding discussion

The finite element method was successfully used to model the acoustophoretic motion of microparticles inside a microchannel subject to a transverse horizontal half-wave ultrasound resonance. The motion is due to the combined effect of Stokes drag from the time-averaged second-order streaming flow and the acoustic radiation forces. To achieve this, the first-order acoustic field of a standing wave was determined inside a microchannel cavity by solving the linearized compressional Navier–Stokes equation, the continuity equation, and the heat equation, while resolving the boundary layers near rigid walls. The first-order field was then used to determine the streaming flow and the acoustic radiation forces, and from this the time-dependent trajectories of an ensemble of non-interacting microparticles was calculated.

A main result is the characterization of the cross over from streaming-dominated to radiation-dominated acoustophoretic microparticle motion as a function of particle diameter, geometry, and viscosity. Using a water-filled shallow microchannel as the base example, we demonstrated how to get rid of streaming effects in the center region of a microchannel by

increasing the height-to-width ratio. In contrast, by replacing water by a 50% glycerol-in-water mixture, we demonstrated how to enhance the streaming effects. The former study may form a good starting point for designing streaming-free devices for handling of sub-micrometer particles, such as small cells, bacteria, and viruses, and thus supporting concurrent experimental efforts to suppress streaming, *e.g.*, through averaging over alternating actuation frequencies.[43] The latter study is pointing in the direction of developing devices with improved mixing capabilities by enhancing streaming.[44,45] We have thus shown that our simulation tool has a great potential for enabling improved design of acoustofluidic devices.

An important next step is to obtain a direct experimental verification of our numerical simulation. As the relative uncertainty of measured acoustophoretic particle velocities in current experimental acoustofluidics is 5% or better,[8] it is within reach to obtain such an experimental verification. A problem is of course that the streaming fields calculated in this work are in the vertical plane, which is perpendicular to the usual horizontal viewing plane, and thus specialized 3-dimensional visualization techniques are required such as stereoscopic micro particle–image velocimetry[42,46] or astigmatism particle tracking velocimetry.[47] But even if such 3D-methods are complex to carry out, it would be worth the effort given the great use of having a well-verified numerical model of acoustophoretic particle motion.

Given a successful experimental verification, it would clearly be valuable to extend the numerical model. One obvious step, which is not conceptually difficult, but which would require significant computational resources, would be to make a full 3D-model taking the elastic properties of the chip surrounding the microchannel into account. The relevance of such an extension lies in the sensitivity of the acoustic streaming on the boundary conditions. Only a full acousto-elastic theory would supply realistic and accurate boundary conditions. Another class of obvious model extensions deals with the modeling of the particle suspension. A trivial extension would be to include gravity and buoyancy, but more importantly and much more difficult would be the inclusion of particle–particle and particle–wall interactions that are neglected in the present work. These many-particle effects include, *e.g.*, the generation of streaming flow in the boundary layer of each particle[48] and not just the boundary layer of the wall. After such an extension, our model could be used together with high-precision experiments as a new and better research tool to study and clarify the many yet unsolved problems with particle–particle and particle–wall interactions in acoustofluidics.

The above-mentioned applications all demonstrate that our numerical model is both timely and has a huge potential within device design and studies of basic physical aspects of acoustophoresis.

Acknowledgements

This research was supported by the Danish Council for Independent Research, Technology and Production Sciences, Grants No. 274-09-0342 and No. 11-107021.

References

1 J. Friend and L. Y. Yeo, *Rev. Mod. Phys.*, 2011, **83**, 647–704.
2 H. Bruus, J. Dual, J. Hawkes, M. Hill, T. Laurell, J. Nilsson, S. Radel, S. Sadhal and M. Wiklund, *Lab Chip*, 2011, **11**, 3579–3580.
3 A. Lenshof, C. Magnusson and T. Laurell, *Lab Chip*, 2012, **12**, 1210–1223.
4 M. Gedge and M. Hill, *Lab Chip*, 2012, **12**, 2998–3007.
5 H. Bruus, *Lab Chip*, 2012, **12**, 1014–1021.
6 M. Wiklund, R. Green and M. Ohlin, *Lab Chip*, 2012, **12**, 2438–2451.
7 R. Barnkob, P. Augustsson, T. Laurell and H. Bruus, *Lab Chip*, 2010, **10**, 563–570.
8 P. Augustsson, R. Barnkob, S. T. Wereley, H. Bruus and T. Laurell, *Lab Chip*, 2011, **11**, 4152–4164.
9 K. Yosioka and Y. Kawasima, *Acustica*, 1955, **5**, 167–173.
10 L. P. Gorkov, *Soviet Physics – Doklady*, 1962, **6**, 773–775.
11 M. Settnes and H. Bruus, *Phys. Rev. E*, 2012, **85**, 016327.
12 K. Frampton, S. Martin and K. Minor, *Appl. Acoust.*, 2003, **64**, 681–692.
13 M. Hamilton, Y. Ilinskii and E. Zabolotskaya, *J. Acoust. Soc. Am.*, 2003, **113**, 153–160.
14 J. F. Spengler, W. T. Coakley and K. T. Christensen, *AIChE J.*, 2003, **49**, 2773–2782.
15 S. M. Hagsäter, T. G. Jensen, H. Bruus and J. P. Kutter, *Lab Chip*, 2007, **7**, 1336–1344.
16 H. Bruus, *Lab Chip*, 2012, **12**, 1578–1586.
17 L. Rayleigh, *Philos. Trans. R. Soc. London*, 1884, **175**, 1–21.
18 H. Schlichting, *Physik Z*, 1932, **33**, 327–335.
19 J. Lighthill, *J. Sound Vib.*, 1978, **61**, 391–418.
20 L. D. Landau and E. M. Lifshitz, *Fluid Mechanics*, Pergamon Press, Oxford, 2nd edn, 1993, **vol. 6**, Course of Theoretical Physics.
21 H. Lei, D. Henry and H. BenHadid, *Appl. Acoust.*, 2011, **72**, 754–759.
22 M. K. Aktas and B. Farouk, *J. Acoust. Soc. Am.*, 2004, **116**, 2822–2831.
23 P. M. Morse and K. U. Ingard, *Theoretical Acoustics*, Princeton University Press, Princeton NJ, 1986.
24 A. D. Pierce, *Acoustics*, Acoustical Society of America, Woodbury, 1991.
25 D. T. Blackstock, *Physical acoustics*, John Wiley and Sons, Hoboken NJ, 2000.
26 L. D. Landau and E. M. Lifshitz, *Statistical physics, Part 1*, Butterworth-Heinemann, Oxford, 3rd edn, 1980, **vol. 5**.
27 W. L. Nyborg, *J. Acoust. Soc. Am.*, 1953, **25**, 68–75.
28 M. Koklu, A. C. Sabuncu and A. Beskok, *J. Colloid Interface Sci.*, 2010, **351**, 407–414.
29 COMSOL Multiphysics 4.2a, www.comsol.com, 2012.
30 CRCnetBASE Product, *CRC Handbook of Chemistry and Physics*, Taylor and Francis Group, www.hbcpnetbase.com/, 92nd edn, 2012.
31 L. Bergmann, *Der Ultraschall und seine Anwendung in Wissenschaft und Technik*, S. Hirzel Verlag, Stuttgart, 6th edn, 1954.
32 P. H. Mott, J. R. Dorgan and C. M. Roland, *J. Sound Vib.*, 2008, **312**, 572–575.
33 L. D. Landau and E. M. Lifshitz, *Theory of Elasticity. Course of Theoretical Physics*, Pergamon Press, Oxford, 3rd edn, 1986, **vol. 7**.
34 N.-S. Cheng, *Ind. Eng. Chem. Res.*, 2008, **47**, 3285–3288.
35 F. Fergusson, E. Guptill and A. MacDonald, *J. Acoust. Soc. Am.*, 1954, **26**, 67–69.
36 O. Bates, *Ind. Eng. Chem.*, 1936, **28**, 494–498.
37 F. Gucker and G. Marsh, *Ind. Eng. Chem.*, 1948, **40**, 908–915.
38 J. Dual and T. Schwarz, *Lab Chip*, 2012, **12**, 244–252.
39 M. Wiklund, P. Spégel, S. Nilsson and H. M. Hertz, *Ultrasonics*, 2003, **41**, 329–333.
40 J. Hultström, O. Manneberg, K. Dopf, H. M. Hertz, H. Brismar and M. Wiklund, *Ultrasound Med. Biol.*, 2007, **33**, 145–151.
41 R. Barnkob, I. Iranmanesh, M. Wiklund and H. Bruus, *Lab Chip*, 2012, **12**, 2337–2344.
42 M. Raffel, C. E. Willert, S. T. Wereley and J. Kompenhans, *Particle Image Velocimetry*, Springer, New York, 2007.
43 M. Ohlin, A. Christakou, T. Frisk, B. Önfelt and M. Wiklund, Proc. 15th MicroTAS, 2 - 6 October 2011, Seattle (WA), USA, 2011, pp. 1612–1614.
44 K. Sritharan, C. Strobl, M. Schneider, A. Wixforth and Z. Guttenberg, *Appl. Phys. Lett.*, 2006, **88**, 054102.
45 T. Frommelt, M. Kostur, M. Wenzel-Schaefer, P. Talkner, P. Haenggi and A. Wixforth, *Phys. Rev. Lett.*, 2008, **100**, 034502.
46 R. Lindken, M. Rossi, S. Grosse and J. Westerweel, *Lab Chip*, 2009, **9**, 2551–2567.
47 C. Cierpka, M. Rossi, R. Segura and C. J. Kaehler, *Meas. Sci. Technol.*, 2011, **22**, 015401.
48 S. Sadhal, *Lab Chip*, 2012, **12**, 2600–2611.

Appendix B

Paper published in Physical Review E, August 2013

Ultrasound-induced acoustophoretic motion of microparticles in three dimensions

P. B. Muller, M. Rossi, A. G. Marin, R. Barnkob, P. Augustsson, T. Laurell, C. J. Kähler, and H. Bruus

Abstract: We derive analytical expressions for the three-dimensional (3D) acoustophoretic motion of spherical microparticles in rectangular microchannels. The motion is generated by the acoustic radiation force and the acoustic streaming-induced drag force. In contrast to the classical theory of Rayleigh streaming in shallow, infinite, parallel-plate channels, our theory does include the effect of the microchannel sidewalls. The resulting predictions agree well with numerics and experimental measurements of the acoustophoretic motion of polystyrene spheres with nominal diameters of 0.537 and 5.33 μm. The 3D particle motion was recorded using astigmatism particle tracking velocimetry under controlled thermal and acoustic conditions in a long, straight, rectangular microchannel actuated in one of its transverse standing ultrasound-wave resonance modes with one or two half-wavelengths. The acoustic energy density is calibrated in situ based on measurements of the radiation dominated motion of large 5-μm-diameter particles, allowing for quantitative comparison between theoretical predictions and measurements of the streaming-induced motion of small 0.5-μm-diameter particles.

http://dx.doi.org/10.1103/PhysRevE.88.023006

Ultrasound-induced acoustophoretic motion of microparticles in three dimensions

P. B. Muller,[1] M. Rossi,[2] Á. G. Marín,[2] R. Barnkob,[1] P. Augustsson,[3] T. Laurell,[3,4] C. J. Kähler,[2] and H. Bruus[1,*]

[1]*Department of Physics, Technical University of Denmark, DTU Physics Building 309, DK-2800 Kongens Lyngby, Denmark*

[2]*Universität der Bundeswehr München, Werner-Heisenberg-Weg 39, 85579 Neubiberg, Germany*

[3]*Department of Measurement Technology and Industrial Electrical Engineering, Lund University, PO-Box 118, S-221 00 Lund, Sweden*

[4]*Department of Biomedical Engineering, Dongguk University, Seoul, South Korea*

(Received 1 March 2013; published 8 August 2013)

We derive analytical expressions for the three-dimensional (3D) acoustophoretic motion of spherical microparticles in rectangular microchannels. The motion is generated by the acoustic radiation force and the acoustic streaming-induced drag force. In contrast to the classical theory of Rayleigh streaming in shallow, infinite, parallel-plate channels, our theory does include the effect of the microchannel side walls. The resulting predictions agree well with numerics and experimental measurements of the acoustophoretic motion of polystyrene spheres with nominal diameters of 0.537 and 5.33 μm. The 3D particle motion was recorded using astigmatism particle tracking velocimetry under controlled thermal and acoustic conditions in a long, straight, rectangular microchannel actuated in one of its transverse standing ultrasound-wave resonance modes with one or two half-wavelengths. The acoustic energy density is calibrated *in situ* based on measurements of the radiation dominated motion of large 5-μm-diameter particles, allowing for quantitative comparison between theoretical predictions and measurements of the streaming-induced motion of small 0.5-μm-diameter particles.

DOI: 10.1103/PhysRevE.88.023006 PACS number(s): 47.15.−x, 43.25.Nm, 43.25.Qp, 43.20.Ks

I. INTRODUCTION

Acoustofluidics is gaining increasing interest in lab-on-a-chip and microfluidics applications. Techniques based on acoustofluidic forces permit us to perform a large variety of different tasks such as trapping, separation and sorting of cells, particle manipulation, and generation of fluid motion in a non-intrusive way [1,2]. Acoustic forces allow for nondestructive and label-free particle handling based on size, density, and compressibility. Experimentally, the acoustophoretic motion of particles is driven by an ultrasonic standing wave that generates acoustic radiation forces on the particles and acoustic streaming in the fluid, which exerts a Stokes drag force on the particles. Theoretically, such phenomena are described by complex, nonlinear governing equations sensitive to the boundary conditions and are thereby difficult to predict. Therefore, the development of analytical and numerical methods that are able to accurately predict the acoustophoretic motion of different particle or cell types is currently a major challenge in the design of acoustofluidic systems.

Regarding the acoustic radiation force on microparticles, recent theoretical studies by Doinikov [3], Danilov and Mironov [4], as well as Settnes and Bruus [5] have advanced the theoretical treatment, beyond the seminal contributions by King [6], Yosioka and Kawasima [7], and Gorkov [8]. We use these models without any new contributions. However, so far theoretical treatments of the acoustic streaming generated by standing acoustic waves have not included an analysis of the effect of the vertical sidewall in rectangular microchannels, instead the focus has been on the idealized parallel-plate geometry [9–14] or single-wall systems [15–18]. Also, in most theoretical work either the radiation force or the streaming effects have been studied separately, but not combined with wall effects to obtain a complete description of microparticle acoustophoresis. Recently, a number of numerical studies of acoustic streaming [19–21] and acoustophoresis [22,23] have appeared in the literature. In this work, we present a theoretical analysis of acoustic streaming, taking the effect of the vertical sidewalls into account, and apply it to a theoretical study of microparticle acoustophoresis in rectangular microchannels. Our results (both with and without vertical sidewalls) are valid for channel heights and acoustic wavelengths much larger than the acoustic boundary layer thickness, thus extending previous results for parallel-plate systems that are only valid for heights much smaller than the acoustic wavelength [9,10].

To guide and control the theoretical developments, precise experimental measurements of the acoustophoretic motion of microparticles are necessary, and particle-based velocimetry techniques are among the best methods available. The work of Hagsäter *et al.* [24] was one of the first to use microparticle image velocimetry (μPIV) in resonant microfluidic chips. In their case, the measurements were employed to visualize the resonance modes in the microchip, using the radiation-dominated horizontal motion of 5-μm-diameter particles and the associated horizontal acoustic streaming pattern using 1-μm-diameter particles. Using a similar μPIV technique, Manneberg *et al.* [25] characterized multiple localized ultrasonic manipulation functions in a single microchip. Barnkob *et al.* [26] and Koklu *et al.* [27] also studied acoustophoretic motion of large particles (5- and 4-μm-diameter, respectively), but instead used particle tracking velocimetry (PTV) to obtain particle paths, which were compared with theoretical results. Later, Augustsson *et al.* [28] employed both PTV and μPIV to make high-accuracy measurements of the acoustic energy density as well as the temperature and frequency dependence of acoustic resonances in microchannels filled with 5-μm-diameter particles dominated by the radiation force. Such approaches have successfully been applied to the two-dimensional (2D) motion of particles in the optical focal plane in simple geometries and resonances. Recently, Dron *et al.* [29] used defocusing of particle images to measure

*bruus@fysik.dtu.dk

the magnitude of radiation-dominated acoustophoretic particle velocities parallel to the optical axis in similar simple half-wave resonance systems. However, in more complex configurations, or in the case of small particles dragged along by acoustic streaming rolls, more advanced techniques are necessary, which are able to resolve three-dimensional (3D) particle positions and three-component (3C) motion. Among these techniques, those based on μPIV have issues regarding the depth of correlation between adjacent planes [30,31], while classical 3D particle tracking techniques require either stereomicroscopes with tedious calibration protocols, or fast confocal microscopes with great losses in light intensity due to the use of pinholes [32].

In this work, an analytical and experimental analysis is presented with the aim to improve the understanding of the full 3D character of ultrasound-induced acoustophoretic motion of microparticles. In particular, analytical expressions for this motion are obtained by extending the classical results for Rayleigh streaming in shallow parallel-plate channels to also cover rectangular channels of experimental relevance. The analytical results are compared with measurements of the 3D motion of particles in an acoustofluidic microchip performed by use of astigmatism particle tracking velocimetry (APTV) [33–35]. APTV is a very precise single-camera tracking method which allows a time-resolved, reconstruction in 3D of the trajectories of microparticles in acoustophoretic motion. The technique is applicable to general 3D acoustophoretic motion of microparticles influenced by both the acoustic radiation force and the Stokes drag from acoustic streaming.

The paper is organized as follows. In Sec. II we derive an analytical expression of acoustic streaming in long, straight channels with rectangular cross section, and we analyze the implications of this streaming for acoustophoretic motion of suspended microparticles. This is followed in Sec. III by a description of the experimental methods, in particular the astigmatism particle tracking velocimetry technique. In Sec. IV we compare the theoretical and experimental results for the acoustophoretic microparticle motion, and finally in Secs. V and VI we discuss the results and state our conclusions.

II. THEORY

The governing perturbation equations for the thermoacoustic fields are standard textbook material [36–38]. The full acoustic problem in a fluid, which before the presence of any acoustic wave is quiescent with constant temperature T_0, density ρ_0, and pressure p_0, is described by the four scalar fields temperature T, density ρ, pressure p, and entropy s per mass unit as well as the velocity vector field $\boldsymbol{v}$. Changes in ρ and s are given by the two thermodynamic relations

$$d\rho = \gamma\kappa_s\,\rho\,dp - \alpha_p\,\rho\,dT, \tag{1a}$$

$$ds = \frac{c_p}{T}\,dT - \frac{\alpha_p}{\rho}\,dp, \tag{1b}$$

which besides the specific heat capacity c_p at constant pressure also contain the specific heat capacity ratio γ, the isentropic compressibility κ_s, and the isobaric thermal expansion coefficient α_p given by

$$\gamma = \frac{c_p}{c_v} = 1 + \frac{\alpha_p^2 T_0}{\rho_0 c_p \kappa_s}, \tag{2a}$$

$$\kappa_s = \frac{1}{\rho}\left(\frac{\partial\rho}{\partial p}\right)_s, \tag{2b}$$

$$\alpha_p = -\frac{1}{\rho}\left(\frac{\partial\rho}{\partial T}\right)_p. \tag{2c}$$

The energy (heat), mass (continuity), and momentum (Navier-Stokes) equations take the form

$$\rho T[\partial_t + (\boldsymbol{v}\cdot\nabla)]s = \sigma' : \nabla\boldsymbol{v} + \nabla\cdot(k_{\mathrm{th}}\nabla T), \tag{3a}$$

$$\partial_t\rho = -\nabla\cdot(\rho\boldsymbol{v}), \tag{3b}$$

$$\rho[\partial_t + \boldsymbol{v}\cdot\nabla]\boldsymbol{v} = -\nabla p + \nabla\cdot[\eta\{\nabla\boldsymbol{v} + (\nabla\boldsymbol{v})^{\mathrm{T}}\}] + (\beta - 1)\nabla(\eta\nabla\cdot\boldsymbol{v}), \tag{3c}$$

where η is the dynamic viscosity, β is the viscosity ratio, which has the value $\frac{1}{3}$ for simple liquids [36], k_{th} is the thermal conductivity, and σ' is the viscous stress tensor. As in Ref. [22], we model the external ultrasound actuation through boundary conditions of amplitude v_{bc} on the first-order velocity $\boldsymbol{v}_1$ while keeping T constant,

$$T = T_0 \quad \text{on all walls,} \tag{4a}$$

$$\boldsymbol{v} = \boldsymbol{0} \quad \text{on all walls,} \tag{4b}$$

$$\boldsymbol{n}\cdot\boldsymbol{v}_1 = v_{\mathrm{bc}}(y,z)\,e^{-i\omega t} \quad \text{added to actuated walls.} \tag{4c}$$

Here, $\boldsymbol{n}$ is the outward pointing surface normal vector, and ω is the angular frequency characterizing the harmonic time dependence written using complex notation.

A. First-order fields in the bulk

To first order in the amplitude v_{bc} of the imposed ultrasound field we can substitute the first-order fields ρ_1 and s_1 in the governing equation (3) using Eq. (1). The heat transfer equation for T_1, the kinematic continuity equation expressed in terms of p_1, and the dynamic Navier-Stokes equation for $\boldsymbol{v}_1$ then become

$$\partial_t T_1 = D_{\mathrm{th}}\nabla^2 T_1 + \frac{\alpha_p T_0}{\rho_0 c_p}\,\partial_t p_1, \tag{5a}$$

$$\partial_t p_1 = \frac{1}{\gamma\kappa_s}[\alpha_p\partial_t T_1 - \nabla\cdot\boldsymbol{v}_1], \tag{5b}$$

$$\partial_t \boldsymbol{v}_1 = -\frac{1}{\rho_0}\nabla p_1 + \nu\nabla^2\boldsymbol{v}_1 + \beta\nu\,\nabla(\nabla\cdot\boldsymbol{v}_1). \tag{5c}$$

Here, $D_{\mathrm{th}} = k_{\mathrm{th}}/(\rho_0 c_{\mathrm{p}})$ is the thermal diffusivity, and $\nu = \eta_0/\rho_0$ is the kinematic viscosity. A further simplification can be obtained when assuming that all first-order fields have a harmonic time dependence $e^{-i\omega t}$ inherited from the imposed ultrasound field (4c). Then, p_1 can be eliminated by inserting Eq. (5b), substituting $\partial_t p_1 = -i\omega p_1$, into Eqs. (5a) and (5c). Solutions of Eq. (5) describe the formation of thin thermoviscous boundary layers at rigid walls. In the viscous boundary layer of thickness

$$\delta = \sqrt{\frac{2\nu}{\omega}}, \tag{6}$$

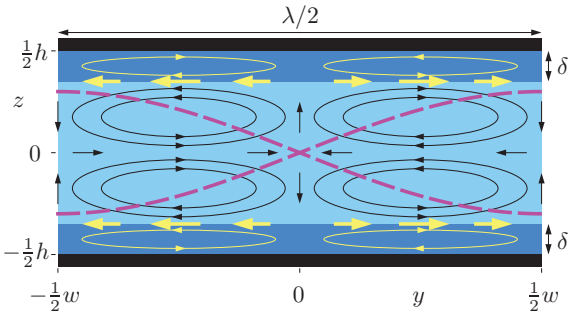

FIG. 1. (Color online) A cross-sectional sketch in the yz plane of the classical Rayleigh-Schlichting streaming pattern in the liquid-filled gap of height h between two infinite, parallel rigid walls (black) in the xy plane. The bulk liquid (light shade) supports a horizontal standing sinusoidal pressure half-wave p_1 (dashed lines) of wavelength λ in the horizontal direction parallel to the walls. In the viscous boundary layers (dark shade) of submicrometer thickness δ, large shear stresses appear, which generate the boundary-layer (Schlichting) streaming rolls (light thin lines). These result in an effective boundary condition $\langle v_{2y}^{\mathrm{bnd}}\rangle$ (thick light arrows) with periodicity $\lambda/2$ driving the bulk (Rayleigh) streaming rolls (black thin lines). Only the top and bottom walls are subject to this effective slip boundary condition.

the velocity gradients are large because the velocity field changes from its bulk value to zero at the walls across this layer [36–38]. In water at $\omega/(2\pi) = 2$ MHz it becomes $\delta \approx 0.4\ \mu$m.

We focus on the transverse standing-wave resonance sketched in Fig. 1, which is established by tuning of ω in the time-harmonic boundary condition (4c) to achieve one of the resonance conditions $n\lambda_n/2 = w$, $n = 1,2,3,\ldots$, where $\lambda_n = 2\pi c_0/\omega_n$ is the acoustic wavelength of the nth horizontal resonance. The associated first-order fields $\boldsymbol{v}_1$, p_1, and T_1 in the bulk of the channel take the form

$$\boldsymbol{v}_1 = v_{\mathrm{a}} \sin(k_n y + n\pi/2)\, e^{-i\omega_n t}\boldsymbol{e}_y, \tag{7a}$$

$$p_1 = p_{\mathrm{a}} \cos(k_n y + n\pi/2)\, e^{-i\omega_n t}, \tag{7b}$$

$$T_1 = T_{\mathrm{a}} \cos(k_n y + n\pi/2)\, e^{-i\omega_n t}, \tag{7c}$$

where $k_n = 2\pi/\lambda_n = n\pi/w$ is the wave number of the nth horizontal resonance, and the oscillation amplitudes of the first-order fields, indicated by subscript "a", are related through $|v_{\mathrm{a}}/c_0| \sim |p_{\mathrm{a}}/p_0| \sim |T_{\mathrm{a}}/T_0| \ll 1$, with c_0 being the isentropic speed of sound in water. The spatial form of the standing-wave resonance is determined entirely by the resonance frequency and the geometry of the resonator, while its amplitude (here $v_{\mathrm{a}} \approx 10^4\, v_{\mathrm{bc}}$ [22]) is governed by the specific form of v_{bc} and of the Q factor of the resonance cavity. The acoustic energy density E_{ac} is constant throughout the cavity and given by

$$E_{\mathrm{ac}} = \tfrac{1}{4}\rho_0 v_{\mathrm{a}}^2 = \tfrac{1}{4}\kappa_0 p_{\mathrm{a}}^2. \tag{8}$$

B. Second-order governing equations for $\langle \boldsymbol{v}_2\rangle$

In a typical experiment on microparticle acoustophoresis, the microsecond time scale of the ultrasound oscillations is not resolved. It therefore suffices to treat only the time-averaged equations. The time average over a full oscillation period, denoted by the angled brackets $\langle\ldots\rangle$, of the second-order continuity equation and Navier-Stokes equation becomes

$$\rho_0 \nabla\cdot\langle\boldsymbol{v}_2\rangle = -\nabla\cdot\langle\rho_1\boldsymbol{v}_1\rangle, \tag{9a}$$

$$\begin{aligned}\eta_0\nabla^2\langle\boldsymbol{v}_2\rangle + \beta\eta_0\nabla(\nabla\cdot\langle\boldsymbol{v}_2\rangle) - \nabla\langle p_2\rangle \\ = \langle\rho_1\partial_t\boldsymbol{v}_1\rangle + \rho_0\langle(\boldsymbol{v}_1\cdot\nabla)\boldsymbol{v}_1\rangle \\ - \langle\eta_1\nabla^2\boldsymbol{v}_1\rangle - \langle\beta\eta_1\nabla(\nabla\cdot\boldsymbol{v}_1)\rangle \\ - \langle\nabla\eta_1\cdot[\nabla\boldsymbol{v}_1 + (\nabla\boldsymbol{v}_1)^{\mathrm{T}}]\rangle \\ - \langle(\beta-1)(\nabla\cdot\boldsymbol{v}_1)\nabla\eta_1\rangle.\end{aligned} \tag{9b}$$

Here, η_1 is the perturbation of the dynamic viscosity due to temperature, $\eta = \eta_0 + \eta_1 = \eta(T_0) + [\partial_T\eta(T_0)]\,T_1$. From Eq. (9) we notice that second-order temperature effects enter only through products of first-order fields. Dimensional analysis leads to a natural velocity scale u_0 for second-order phenomena given by

$$u_0 = \frac{4E_{\mathrm{ac}}}{\rho_0 c_0} = \frac{v_{\mathrm{a}}^2}{c_0}. \tag{10}$$

C. Boundary condition for bulk streaming flow

The second-order problem (9) was solved analytically by Lord Rayleigh [9,39] in the isothermal case ($T = T_0$) for the infinite parallel-plate channel in the yz plane with the imposed first-order bulk velocity $\boldsymbol{v}_1$ [Eq. (7a)]. The resulting y component $\langle v_{2y}^{\mathrm{bnd}}\rangle$ of $\langle\boldsymbol{v}_2\rangle$ just outside the boundary layers at the top and bottom walls becomes

$$\langle v_{2y}^{\mathrm{bnd}}\rangle = -v_{\mathrm{str}}\ \sin\left[n\pi\left(\frac{2y}{w}+1\right)\right], \tag{11}$$

as sketched in 1 for the half-wave $k_1 = \pi/w$. In Rayleigh's isothermal derivation, the amplitude v_{str} of the streaming velocity boundary condition $\langle v_{2y}^{\mathrm{bnd}}\rangle$ becomes

$$v_{\mathrm{str}}^0 = \frac{3}{8}\frac{v_{\mathrm{a}}^2}{c_0} = \frac{3}{8}u_0, \tag{12}$$

where the superscript "0" refers to isothermal conditions. Recently, Rednikov and Sadhal [18] extended this analysis by including the oscillating thermal field T_1 as well as the temperature dependence $\eta_1(T)$ of the viscosity. They found that the amplitude of the streaming velocity boundary condition v_{str}^T then becomes

$$v_{\mathrm{str}}^T = \frac{8}{3}K^T v_{\mathrm{str}}^0 = K^T u_0, \tag{13a}$$

$$K^T = \frac{3}{8} + \frac{\gamma-1}{4}\left[1 - \frac{(\partial_T\eta)_p}{\eta_0\alpha_p}\right]\frac{\sqrt{\nu/D_{\mathrm{th}}}}{1+\nu/D_{\mathrm{th}}}, \tag{13b}$$

where the superscript "T" refers to inclusion of thermoviscous effects leading to a temperature-dependent pre-factor multiplying the temperature-independent result. For water at 25 °C we find $v_{\mathrm{str}}^T = 1.26\, v_{\mathrm{str}}^0$ using the material parameter values of Table I, and in all calculations below we use this thermoviscous value for v_{str}.

D. Second-order governing equations for bulk $\langle \boldsymbol{v}_2\rangle$

In the bulk of the fluid the oscillating velocity and density fields $\boldsymbol{v}_1$ and ρ_1 are out of phase by $\pi/2$. Consequently

TABLE I. Model parameters for water and polystyrene given at temperature $T = 25\,^{\circ}\mathrm{C}$ and taken from the literature as indicated or derived based on these.

Parameter	Symbol	Value	Unit
Water			
Density[a]	ρ_0	998	kg m^{-3}
Speed of sound[a]	c_0	1495	m s^{-1}
Viscosity[a]	η	0.893	mPa s
Specific heat capacity[a]	c_p	4183	J kg^{-1} K^{-1}
Heat capacity ratio	γ	1.014	
Thermal conductivity[a]	k_{th}	0.603	W m^{-1} K^{-1}
Thermal diffusivity	D_{th}	1.44×10^{-7}	m^2 s^{-1}
Compressibility	κ_s	448	TPa^{-1}
Thermal expansion coeff.	α_p	2.97×10^{-4}	K^{-1}
Thermal viscosity coeff.[a]	$\frac{(\partial_T \eta)_p}{\eta_0}$	-0.024	K^{-1}
Polystyrene			
Density[b]	ρ_{ps}	1050	kg m^{-3}
Speed of sound[c]	c_{ps}	2350	m s^{-1}
Poisson's ratio[d]	σ_{ps}	0.35	
Compressibility[e]	κ_{ps}	249	TPa^{-1}

[a]COMSOL Multiphysics Material Library [40].
[b]Reference [41].
[c]Reference [42].
[d]Reference [43].
[e]Calculated as $\kappa_{\mathrm{ps}} = \frac{3(1-\sigma_{\mathrm{ps}})}{1+\sigma_{\mathrm{ps}}} \frac{1}{\rho_{\mathrm{ps}} c_{\mathrm{ps}}^2}$ (see Ref. [44]).

$\langle \rho_1 \boldsymbol{v}_1 \rangle = 0$, and the source term in the second-order continuity equation (9a) vanishes. As a result, the time-averaged second-order velocity field $\langle \boldsymbol{v}_2 \rangle$ is divergence free or incompressible in the bulk. Hence, the continuity equation and the Navier-Stokes equation for the bulk streaming velocity field reduce to

$$\nabla \cdot \langle \boldsymbol{v}_2 \rangle = 0, \tag{14a}$$

$$\begin{aligned} \eta_0 \nabla^2 \langle \boldsymbol{v}_2 \rangle - \nabla \langle p_2 \rangle = {} & \langle \rho_1 \partial_t \boldsymbol{v}_1 \rangle + \rho_0 \langle (\boldsymbol{v}_1 \cdot \nabla) \boldsymbol{v}_1 \rangle \\ & - \langle \eta_1 \nabla^2 \boldsymbol{v}_1 \rangle - \langle \beta \eta_1 \nabla (\nabla \cdot \boldsymbol{v}_1) \rangle \\ & - \langle \nabla \eta_1 \cdot [\nabla \boldsymbol{v}_1 + (\nabla \boldsymbol{v}_1)^{\mathrm{T}}] \rangle \\ & - \langle (\beta - 1)(\nabla \cdot \boldsymbol{v}_1) \nabla \eta_1 \rangle. \end{aligned} \tag{14b}$$

Only the y component of the source terms on the right-hand side of Eq. (14b) is nonzero in the bulk, and it depends only on y and not on z. Consequently, their rotation is zero, and they can be reformulated as a gradient term absorbed together with $\nabla \langle p_2 \rangle$ into an effective pressure gradient $\nabla \chi$ given by

$$\begin{aligned} \nabla \chi = {} & \nabla \langle p_2 \rangle + \langle \rho_1 \partial_t \boldsymbol{v}_1 \rangle + \rho_0 \langle (\boldsymbol{v}_1 \cdot \nabla) \boldsymbol{v}_1 \rangle \\ & - \langle \eta_1 \nabla^2 \boldsymbol{v}_1 \rangle - \langle \beta \eta_1 \nabla (\nabla \cdot \boldsymbol{v}_1) \rangle \\ & - \langle \nabla \eta_1 \cdot [\nabla \boldsymbol{v}_1 + (\nabla \boldsymbol{v}_1)^{\mathrm{T}}] \rangle \\ & - \langle (\beta - 1)(\nabla \cdot \boldsymbol{v}_1) \nabla \eta_1 \rangle. \end{aligned} \tag{15}$$

Using this, the system of bulk equations reduces to the standard equation of incompressible creeping flow

$$\nabla \cdot \langle \boldsymbol{v}_2 \rangle = 0, \tag{16a}$$

$$\eta_0 \nabla^2 \langle \boldsymbol{v}_2 \rangle = \nabla \chi. \tag{16b}$$

These equations together with appropriate boundary conditions, to be discussed below, govern the steady bulk streaming velocity field $\langle \boldsymbol{v}_2 \rangle$ in the microchannel.

E. Streaming in a parallel-plate channel

Based on Rayleigh's analysis, we first study the analytical solution for $\langle \boldsymbol{v}_2 \rangle$ in the special case of a standing half-wave ($n = 1$) in the parallel-plate channel shown in 1. We choose the symmetric coordinate system such that $-w/2 < y < w/2$ and $-h/2 < z < h/2$, and introduce nondimensionalized coordinates $\tilde{y}$ and $\tilde{z}$ by

$$\tilde{y} = \frac{2y}{w} \quad \text{with} \quad -1 < \tilde{y} < 1, \tag{17a}$$

$$\tilde{z} = \frac{2z}{h} \quad \text{with} \quad -1 < \tilde{z} < 1, \tag{17b}$$

$$\alpha = \frac{h}{w} \quad \text{the aspect ratio.} \tag{17c}$$

In this case, using Eq. (11), the boundary conditions for $\langle \boldsymbol{v}_2(\tilde{y},\tilde{z}) \rangle$ are

$$\langle v_{2y} \rangle = v_{\mathrm{str}} \sin(\pi \tilde{y}) \quad \text{for} \quad \tilde{z} = \pm 1, \tag{18a}$$

$$\langle v_{2z} \rangle = 0 \quad \text{for} \quad \tilde{z} = \pm 1, \tag{18b}$$

$$\langle v_{2y} \rangle = 0 \quad \text{for} \quad \tilde{y} = \pm 1, \tag{18c}$$

$$\partial_y \langle v_{2z} \rangle = 0 \quad \text{for} \quad \tilde{y} = \pm 1, \tag{18d}$$

where Eqs. (18c) and (18d) express the symmetry condition at the wall-less vertical planes at $\tilde{y} = \pm 1$. Rayleigh focused his analysis of the parallel plate geometry on shallow channels for which $\alpha \ll 1$. Here, $\alpha = 0.4$, derived from the aspect ratio of the microchannel described in Sec. III and in Refs. [26,28,45], and consequently we need to solve the case of arbitrary α. We find

$$\langle v_{2y}(\tilde{y},\tilde{z}) \rangle = v_{\mathrm{str}} \sin(\pi \tilde{y})\, A^{\parallel}(\alpha,\tilde{z}), \tag{19a}$$

$$\langle v_{2z}(\tilde{y},\tilde{z}) \rangle = v_{\mathrm{str}} \cos(\pi \tilde{y})\, A^{\perp}(\alpha,\tilde{z}), \tag{19b}$$

where the α- and z-dependent amplitude functions $A^{\parallel}$ and $A^{\perp}$ for the velocity component parallel and perpendicular to the first-order wave, respectively, are given by

$$\begin{aligned} A^{\parallel}(\alpha,\tilde{z}) = {} & B(\alpha)\{[1 - \pi\alpha \coth(\pi\alpha)] \cosh(\pi\alpha\tilde{z}) \\ & + \pi\alpha\tilde{z} \sinh(\pi\alpha\tilde{z})\}, \end{aligned} \tag{20a}$$

$$\begin{aligned} A^{\perp}(\alpha,\tilde{z}) = {} & \pi\alpha B(\alpha)\{\coth(\pi\alpha) \sinh(\pi\alpha\tilde{z}) \\ & - \tilde{z} \cosh(\pi\alpha\tilde{z})\}, \end{aligned} \tag{20b}$$

$$B(\alpha) = \frac{\sinh(\pi\alpha)}{\sinh(\pi\alpha)\cosh(\pi\alpha) - \pi\alpha}, \tag{20c}$$

with $A^{\parallel}(\alpha,\pm 1) = 1$ and $A^{\perp}(\alpha,\pm 1) = 0$. In Rayleigh's well-cited shallow-channel limit $\alpha \ll 1$, the amplitude functions reduce to

$$A^{\parallel}(\alpha,\tilde{z}) \approx \frac{3}{2}\tilde{z}^2 - \frac{1}{2} \quad \text{for} \quad \alpha \ll 1, \tag{21a}$$

$$A^{\perp}(\alpha,\tilde{z}) \approx \frac{\pi\alpha}{2}(\tilde{z} - \tilde{z}^3) \quad \text{for} \quad \alpha \ll 1. \tag{21b}$$

The analytical solution of $\langle \boldsymbol{v}_2 \rangle$ for $\lambda/2 = w$ is illustrated in Figs. 2(a) and 2(b) for channel aspect ratios $\alpha = 1.2$ and 0.2. We note that the maximum streaming velocity is near the top and bottom walls. For the shallow channel [Fig. 2(b)], there is furthermore a significant streaming velocity along the

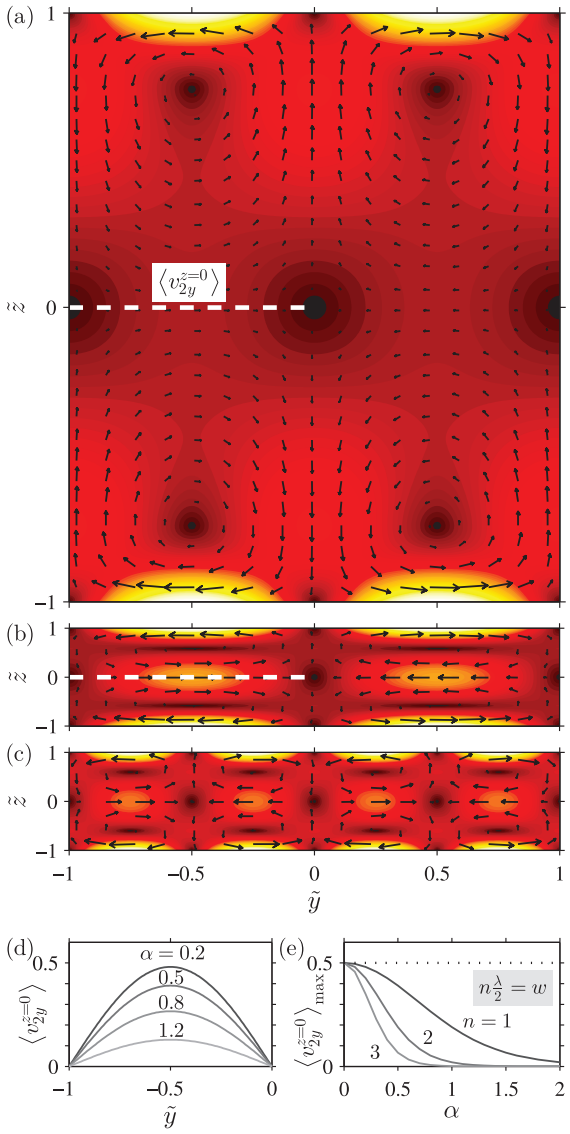

FIG. 2. (Color online) Analytical results for the streaming velocity $\langle \boldsymbol{v}_2 \rangle$ in parallel-plate channels. (a) Plot of the analytical expressions (19) and (20) for $\langle \boldsymbol{v}_2 \rangle$ (arrows) and its magnitude [color plot from 0 (black) to v_{str} (white)] in the vertical yz cross section of a parallel-plate channel (Fig. 1) with $\lambda/2 = w$ ($n = 1$) and aspect ratio $\alpha = 1.2$. (b) The same as (a), but for $\alpha = 0.2$. (c) The same as (b) but for a standing full wave $\lambda = w$ ($n = 2$). (d) Line plot of the amplitude $\langle v_{2y}(\tilde{y},0)\rangle$ of the streaming velocity, in units of v_{str}, along the first half of the center axis [white dashed lines in (a) and (b)] with $\lambda/2 = w$ for aspect ratios $\alpha = 0.2$, 0.5, 0.8, and 1.2. (e) Line plot of the maximum $\langle v_{2y}(\tilde{y},0)\rangle_{\max}$ of the center-axis streaming velocity, in units of v_{str}, as function of aspect ratio for the resonances $n\lambda/2 = w$, with $n = 1$, 2, and 3, respectively.

horizontal center line $\tilde{z} = 0$. However, the amplitude of this velocity decreases for increasing aspect ratio α as shown in Fig. 2(d).

This special case of the pure sinusoidal horizontal boundary condition (18a) can readily be generalized to any horizontal boundary condition by a Fourier expansion in wave number $k_m = 2\pi/\lambda_m = m\pi/w$, where m is a positive integer,

$$\langle v_{2y} \rangle = v_{\text{str}}\, f(\tilde{y}) \quad \text{for} \quad \tilde{z} = \pm 1, \tag{22a}$$

$$f(\tilde{y}) = \sum_{m=1}^{\infty} a_m \sin(m\pi\tilde{y}). \tag{22b}$$

As the governing equations (16) for the second-order bulk flow are linear, we can make a straightforward generalization of Eq. (19), and the two velocity components of the superposed solution for $\langle \boldsymbol{v}_2 \rangle$ become

$$\langle v_{2y}(\tilde{y},\tilde{z}) \rangle = v_{\text{str}} \sum_{m=1}^{\infty} a_m \sin(m\pi\tilde{y})\, A^{\parallel}(m\alpha,\tilde{z}), \tag{23a}$$

$$\langle v_{2z}(\tilde{y},\tilde{z}) \rangle = v_{\text{str}} \sum_{m=1}^{\infty} a_m \cos(m\pi\tilde{y})\, A^{\perp}(m\alpha,\tilde{z}), \tag{23b}$$

where the wave index m multiplies both the horizontal coordinate $\tilde{y}$ and the aspect ratio α. Note that $A^{\parallel}(m\alpha,\pm 1) = 1$ and $A^{\perp}(m\alpha,\pm 1) = 0$. The resulting steady effective pressure χ is just the weighted sum of the partial pressures χ_m of each Fourier component $\chi = \sum_{m=1}^{\infty} a_m \chi_m$.

In Fig. 2(c) is shown the streaming velocity field for the higher harmonic boundary condition $f(\tilde{y}) = \sin(n\pi\tilde{y})$ with $n = 2$. Furthermore, Fig. 2(e) shows how the maximum $\langle v_{2y}(\tilde{y},0)\rangle_{\max}$ of the center-axis streaming velocity decays as function of aspect ratio α for $n = 1$, 2, and 3. Given sufficient room, the flow rolls decay in the vertical direction on the length scale of $\lambda_n/4$. Since n is the number of half wavelengths of the first-order resonance pressure across the channel, we conclude that the streaming amplitude in the center of the channel decreases for higher harmonic resonances.

F. Streaming in a rectangular channel

Moving on to the rectangular channel cross section, we note that the only change in the problem formulation is to substitute the symmetry boundary conditions (18c) and (18d) by no-slip boundary conditions, while keeping the top-bottom slip boundary conditions (18a) and (18b) unaltered:

$$\langle v_{2y} \rangle = v_{\text{str}} \sin(\pi\tilde{y}) \quad \text{for} \quad \tilde{z} = \pm 1, \tag{24a}$$

$$\langle v_{2z} \rangle = 0 \quad \text{for} \quad \tilde{z} = \pm 1, \tag{24b}$$

$$\langle v_{2y} \rangle = 0 \quad \text{for} \quad \tilde{y} = \pm 1, \tag{24c}$$

$$\langle v_{2z} \rangle = 0 \quad \text{for} \quad \tilde{y} = \pm 1. \tag{24d}$$

If we want to use the solution obtained for the parallel-plate channel, we need to cancel the vertical velocity component $\langle v_{2z} \rangle$ on the vertical walls at $\tilde{y} = \pm 1$. This leads us to consider the problem rotated 90°, where the first-order velocity field is parallel to the vertical walls (interchanging y and z), and the fundamental wavelength is $\lambda/2 = h$, and the aspect ratio is $w/h = \alpha^{-1}$. As the governing equations for the bulk flow (16) are linear, we simply add this kind of solution to the former solution and determine the Fourier expansion coefficients such that the boundary conditions (24) are fulfilled. Given this, (23)

generalizes to

$$\langle v_{2y}(\tilde{y},\tilde{z})\rangle = v_{\rm str}\sum_{m=1}^{\infty}[a_m \sin(m\pi\tilde{y})\, A^{\parallel}(m\alpha,\tilde{z}) + b_m A^{\perp}(m\alpha^{-1},\tilde{y})\, \cos(m\pi\tilde{z})], \quad (25a)$$

$$\langle v_{2z}(\tilde{y},\tilde{z})\rangle = v_{\rm str}\sum_{m=1}^{\infty}[a_m \cos(m\pi\tilde{y})\, A^{\perp}(m\alpha,\tilde{z}) + b_m A^{\parallel}(m\alpha^{-1},\tilde{y})\, \sin(m\pi\tilde{z})]. \quad (25b)$$

The two perpendicular-to-the-wall velocity conditions (24b) and (24c) are automatically fulfilled as they by construction are inherited from the original conditions (18b) and (18c). The unknown coefficients a_m and b_m are thus to be determined by the parallel-to-the-wall conditions (24a) and (24d).

Using $\langle v_{2y}\rangle$ in the form of Eq. (25a), boundary condition (24a) becomes

$$\sin(\pi\tilde{y}) = \sum_{m=1}^{\infty}[a_m \sin(m\pi\tilde{y}) + (-1)^m b_m A^{\perp}(m\alpha^{-1},\tilde{y})]. \quad (26)$$

The discrete Fourier transform of this equation, i.e., multiplying by $\sin(j\pi\tilde{y})$, where j is an arbitrary integer, and integrating over $\tilde{y}$ from -1 to 1, becomes

$$\delta_{j,1} = \sum_{m=1}^{\infty}[\delta_{j,m}\, a_m + \mathsf{A}^{\perp}_{j,m}(\alpha^{-1})\, b_m], \quad j = 1,2,3,\ldots, \quad (27)$$

where the (j,m)th element $\mathsf{A}^{\perp}_{j,m}$ of the α-dependent matrix $\mathbf{A}^{\perp}$ is given by

$$\mathsf{A}^{\perp}_{j,m}(\alpha^{-1}) = (-1)^m \int_{-1}^{1} d\tilde{y}\, A^{\perp}(m\alpha^{-1},\tilde{y})\, \sin(j\pi\tilde{y}). \quad (28)$$

Introducing the coefficient vectors $\boldsymbol{a}$ and $\boldsymbol{b}$ and the first unit vector $\boldsymbol{e}_1$ with mth components a_m, b_m, and $\delta_{1,m}$, respectively, we can write Eq. (27) as the matrix equation

$$\boldsymbol{e}_1 = \boldsymbol{a} + \mathbf{A}^{\perp}(\alpha^{-1})\cdot\boldsymbol{b}. \quad (29)$$

Likewise, using Eq. (25b) and multiplying it by $\sin(j\pi\tilde{z})$, where j is an arbitrary integer, and integrating over $\tilde{z}$ from -1 to 1, the zero-parallel-component boundary condition (24d) can be written as the matrix equation

$$\mathbf{0} = \mathbf{A}^{\perp}(\alpha)\cdot\boldsymbol{a} + \boldsymbol{b}. \quad (30)$$

Solving the equation systems (29) and (30), the coefficient vectors $\boldsymbol{a}$ and $\boldsymbol{b}$ become

$$\boldsymbol{a} = [\mathbf{I} - \mathbf{A}^{\perp}(\alpha^{-1})\mathbf{A}^{\perp}(\alpha)]^{-1}\cdot\boldsymbol{e}_1, \quad (31a)$$

$$\boldsymbol{b} = -\mathbf{A}^{\perp}(\alpha)\cdot\boldsymbol{a}. \quad (31b)$$

A comparison between results for the classical parallel-plate geometry and the new results for the rectangular geometry is shown in Fig. 3. It is seen how the velocity profile of the rectangular channel solution [Eq. (25)] is suppressed close to the wall in comparison to the parallel-plate channel solution [Eq. (19)]. Note that for the nth resonance $k_n = n\pi/w$, the unit vector $\boldsymbol{e}_1$ in Eq. (31a) is replaced by $(-1)^{n-1}\,\boldsymbol{e}_n$, with the sign originating from the n-dependent phase shift in the streaming boundary condition (11).

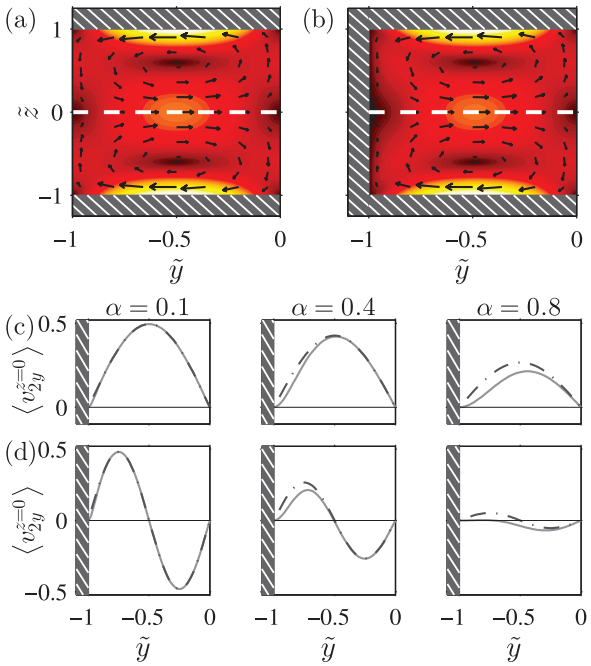

FIG. 3. (Color online) Analytical results comparing the streaming velocity field $\langle \boldsymbol{v}_2\rangle$ in the parallel plate and the rectangular channel. (a) Color plot from 0 (black) to $v_{\rm str}$ (white) of the analytical expression for $\langle v_2\rangle$ [Eqs. (19) and (20)] in the classical parallel-plate geometry with a half-wave resonance $\lambda/2 = w$ ($n = 1$). Due to symmetry, only the left half ($-1 < \tilde{y} < 0$) of the vertical channel cross section is shown. (b) As in (a) but for $\langle v_2\rangle$ in the rectangular channel [Eqs. (25) and (31)], including the first 20 terms of the Fourier series. (c) Line plots of $\langle v_{2y}(\tilde{y},0)\rangle$ in units of $v_{\rm str}$ along the left half of the center line for the parallel-plate channel (dashed lines) and the rectangular channel (full lines) for aspect ratios $\alpha = 0.1$, 0.4, and 0.8 and the half-wave resonance $\lambda/2 = w$. (d) As in (c) but for the full-wave resonance $\lambda = w$ ($n = 2$).

G. Acoustophoretic particle velocity

The forces of acoustic origin acting on a single microparticle of radius a, density $\rho_{\rm p}$, and compressibility $\kappa_{\rm p}$ undergoing acoustophoresis with velocity $\boldsymbol{u}^{\rm p}$ in a liquid of density ρ_0, compressibility κ_s, and viscosity η_0 are the Stokes drag force $\boldsymbol{F}^{\rm drag} = 6\pi\eta_0 a[\langle \boldsymbol{v}_2\rangle - \boldsymbol{u}^{\rm p}]$ from the acoustic streaming $\langle \boldsymbol{v}_2\rangle$ and the acoustic radiation force $\boldsymbol{F}^{\rm rad}$. Given an observed maximum acoustophoretic velocity of $u^{\rm p} \lesssim 1$ mm/s for the largest particles of diameter $2a = 5.0$ μm, the Reynolds number for the flow around the particle becomes $\rho_0 2au^{\rm p}/\eta \lesssim 6\times10^{-3}$, and the time scale for acceleration of the particle becomes $\tau_{\rm acc} = [(4/3)\pi a^3\rho_{\rm p}]/[6\pi\eta a] \approx 2$ μs. Since the acceleration time is much smaller than the time scale for the translation of the particles $\tau_{\rm trans} = w/(2u^{\rm p}) \gtrsim 0.1$ s, the inertia of the particle can be neglected, and the quasi-steady-state equation of motion $\boldsymbol{F}^{\rm drag} = -\boldsymbol{F}^{\rm rad}$ for a spherical particle of velocity $\boldsymbol{u}^{\rm p}$ then becomes

$$\boldsymbol{u}^{\rm p} = \frac{\boldsymbol{F}^{\rm rad}}{6\pi\eta_0 a} + \langle \boldsymbol{v}_2\rangle = \boldsymbol{u}^{\rm rad} + \langle \boldsymbol{v}_2\rangle, \quad (32)$$

where $\boldsymbol{u}^{\rm rad}$ is the contribution to the particle velocity from the acoustic radiation force. The streaming velocity $\langle \boldsymbol{v}_2\rangle$ is given in the previous sections, while an analytical expression for

the viscosity-dependent time-averaged radiation force $\boldsymbol{F}^{\mathrm{rad}}$ in the experimentally relevant limit of the wavelength λ being much larger than both the particle radius a and the boundary layer thickness δ was given recently by Settnes and Bruus [5]. For the case of a 1D transverse pressure resonance [Eq. (7b)], the viscosity-dependent acoustic radiation force on a particle reduces to the x- and z-independent expression

$$\boldsymbol{F}^{\mathrm{rad}}(\tilde{y}) = 4\pi a^3 k_n E_{\mathrm{ac}}\, \Phi(\tilde{\kappa},\tilde{\rho},\tilde{\delta})\, \sin[n\pi(\tilde{y}+1)]\boldsymbol{e}_y. \quad (33)$$

The acoustic contrast factor Φ is given in terms of the material parameters as

$$\Phi(\tilde{\kappa},\tilde{\rho},\tilde{\delta}) = \frac{1}{3} f_1(\tilde{\kappa}) + \frac{1}{2}\,\mathrm{Re}[f_2(\tilde{\rho},\tilde{\delta})], \quad (34a)$$

$$f_1(\tilde{\kappa}) = 1 - \tilde{\kappa}, \quad (34b)$$

$$f_2(\tilde{\rho},\tilde{\delta}) = \frac{2[1-\Gamma(\tilde{\delta})](\tilde{\rho}-1)}{2\tilde{\rho}+1-3\Gamma(\tilde{\delta})}, \quad (34c)$$

$$\Gamma(\tilde{\delta}) = -\frac{3}{2}[1+i(1+\tilde{\delta})]\tilde{\delta}, \quad (34d)$$

where $\tilde{\kappa} = \kappa_{\mathrm{p}}/\kappa_s$, $\tilde{\rho} = \rho_{\mathrm{p}}/\rho_0$, and $\tilde{\delta} = \delta/a$. Using Eq. (33) for the transverse resonance, $\boldsymbol{u}^{\mathrm{rad}}$ only has a horizontal component u_y^{rad}:

$$u_y^{\mathrm{rad}} = u_0 \frac{a^2}{a_0^2}\, \sin[n\pi(\tilde{y}+1)], \quad n = 1,2,3,\ldots, \quad (35a)$$

where the characteristic particle radius a_0 is given by

$$a_0 = \delta\sqrt{\frac{3}{\Phi}}, \quad (35b)$$

with δ given by Eq. (6). The acoustophoretic particle velocity $\boldsymbol{u}^{\mathrm{p}}$ will in general have nonzero z components, due to the contribution from the acoustic streaming $\langle \boldsymbol{v}_2 \rangle$. However, for the special case of particles in the horizontal center plane $\tilde{z} = 0$ of a parallel-plate or rectangular channel, the vertical streaming velocity component vanishes, $\langle v_{2z}(\tilde{y},0)\rangle = 0$. From Eqs. (19a) and (35a), we find that the horizontal particle velocity component $u_y^{\mathrm{p}}(\tilde{y},0)$ in a parallel-plate channel is given by the sinusoidal expression

$$u_y^{\mathrm{p}}(\tilde{y},0) = u_0\left[\frac{a^2}{a_0^2} - K^T A^{\parallel}(n\alpha,0)\right]\sin[n\pi(\tilde{y}+1)]. \quad (36)$$

Since by Eq. (20a) $A^{\parallel}(n\alpha,0)$ is always negative, it follows that the streaming-induced drag and the radiation force have the same direction in the horizontal center plane of the channel. For the rectangular channel using Eq. (25a), the expression for $u_y^{\mathrm{p}}(\tilde{y},0)$ becomes

$$u_y^{\mathrm{p}}(\tilde{y},0) = u_0\Bigg\{\frac{a^2}{a_0^2}\, \sin[n\pi(\tilde{y}+1)] + K^T \sum_{m=1}^{\infty}[a_m \sin(m\pi\tilde{y})\, A^{\parallel}(m\alpha,0) + b_m A^{\perp}(m\alpha^{-1},\tilde{y})]\Bigg\}, \quad (37)$$

which is not sinusoidal in $\tilde{y}$ but still proportional to u_0. This particular motion in the ultrasound symmetry plane is studied in detail in Ref. [45].

III. EXPERIMENTS

We have validated experimentally the analytical expressions derived above by measuring trajectories of micrometer-sized polystyrene particles displaced by acoustophoresis in a long, straight silicon-glass microchannel with rectangular cross section. A fully three-dimensional evaluation of the particle trajectories and velocities was performed by means of the astigmatism particle tracking velocimetry (APTV) technique [33,34] coupled to the temperature-controlled and automated setup presented in Ref. [28]. APTV is a single-camera particle tracking method in which an astigmatic aberration is introduced in the optical system by means of a cylindrical lens placed in front of the camera sensor. Consequently, an image of a spherical particle obtained in such a system shows a characteristic elliptical shape unequivocally related to its depth position z. More details about calibration and uncertainty of this technique, as well as comparison with other whole-field velocimetry methods for microflows, can be found in Refs. [34,35].

A. Acoustophoresis microchip

The acoustophoresis microchip used for the experiment was the one previously presented in Refs. [26,28,45]. In Ref. [28] the microchip and the experimental setup are described in details; here, we give a brief description. A rectangular cross section channel ($L = 35$ mm, $w = 377$ μm, and $h = 157$ μm) was etched in silicon. A Pyrex lid was anodically bonded to seal the channel and provided the optical access for the microscope. The outer dimensions of the chip are $L = 35$ mm, $W = 2.52$ mm, and $H = 1.48$ mm. Horizontal fluidic connections were made at the ends of the microchip. From top and down, glued together using ethyl-2-cyanoacrylat (ExpressLim, Akzo Nobel Bygglim AB, Sweden), the chip was placed on top of a piezoceramic transducer (piezo) (35 mm $\times$ 5 mm $\times$ 1 mm, PZT26, Ferroperm Piezo-ceramics, Denmark), an aluminum slab to distribute heat evenly along the piezo, and a Peltier element (standard 40 mm $\times$ 40 mm, Supercool AB, Sweden) to enable temperature control. The temperature was kept constant at 25 °C, based on readings from a temperature sensor placed near the chip on top of the piezo. This chip stack was mounted on a computer-controlled xyz stage. Ultrasound vibrations propagating in the microchip were generated in the piezo by applying an amplified sinusoidal voltage from a function generator, and the resulting piezo voltage U_{pp} was monitored using an oscilloscope.

B. APTV setup and method

The images of the particles in the microfluidic chip were taken using an epifluorescent microscope (DM2500 M, Leica Microsystems CMS GmbH, Wetzlar, Germany) in combination with a 12-bit, 1376 $\times$ 1040 pixels, interline transfer CCD camera (Sensicam QE, PCO GmbH). The optical arrangement consisted of a principal objective lens with 20$\times$ magnification and 0.4 numerical aperture and a cylindrical lens with focal length $f_{\mathrm{cyl}} = 150$ mm placed in front of the CCD sensor of the camera. This configuration provided a measurement volume of 900 $\times$ 600 $\times$ 120 μm^3 with an estimated uncertainty in the particle position determination of ± 1 μm in the z direction

and less than $\pm 0.1\ \mu$m in the x and y directions. Two scan positions along the z direction were used to cover the whole cross-sectional area of the channel.

Monodisperse spherical polystyrene particles with nominal diameters of 5.33 μm (SD 0.09) and 0.537 μm (PDI 0.005) were used for the experiments ($\rho_{ps} = 1050\ \mathrm{kgm}^{-3}$ and $\kappa_{ps} = 249\ \mathrm{TPa}^{-1}$). For simplicity we will refer to them as 5-μm-diameter and 0.5-μm-diameter particles, respectively. The particles were fabricated and labeled with a proprietary fluorescent dye by Microparticles GmbH to be visualized with an epifluorescent microscopy system. The illumination was provided by a continuous diode-pumped laser with 2 W at 532 nm wavelength.

Once the particle 3D positions had been detected using the APTV technique, their trajectories and velocities were calculated. Due to the low seeding density in the experiments, the particle interdistance was large enough to employ a simple nearest-neighbor approach in which the particle in one frame is identified with the closest particle in the next frame. The method was compared with more sophisticated ones as predictors and probabilistic algorithms with identical results. Trajectories composed by less than five particle positions were rejected. From the obtained trajectories the velocities could be calculated given the capture rate of the camera. Different approaches have been followed depending on the type of trajectories expected. For particles following almost straight paths as those dominated by radiation force, a simple two-position approach was used and the velocities were calculated based on the frame-to-frame particle displacement. For particles with highly curved paths, like those present in streaming-dominated flows, a more sophisticated multiframe approach has been followed, as those reported already by Hain and Kähler [46] for μPIV. In our case, each velocity data point was calculated from a trajectory segment composed by four consecutive points. Such a multiframe approach applied for PTV has been shown to better solve the velocity vector positions and values when the trajectories present large curvatures and for high-shear flows [47].

IV. RESULTS

A. APTV measurements

Examples of the measured 3D trajectories of the 5-μm-diameter particles are shown in Fig. 4(a). The data were collected from 10 consecutive experiments with the piezo operated at 1.94 MHz and peak-to-peak voltage of $U_{pp} = 0.91$ V. An overall number of 111 trajectories were determined. The 5-μm-diameter particles are affected mainly by the acoustic radiation force F_y^{rad} that quickly pushes them to the center of the channel with a horizontal velocity u_y^p [24,45]. At the vertical pressure nodal plane $y = 0$, $\boldsymbol{F}_{rad}$ vanishes and the hitherto negligible drag force from the acoustic streaming, shown in Fig. 2(b), slowly drags the particles towards the top and bottom of the channel.

Examples of the measured 3D trajectories of the 0.5-μm-diameter particles are shown in Fig. 4(b). The data were collected from four consecutive experiments with the piezo operated at 1.94 MHz and peak-to-peak voltage of $U_{pp} = 1.62$ V. An overall number of 731 trajectories were determined.

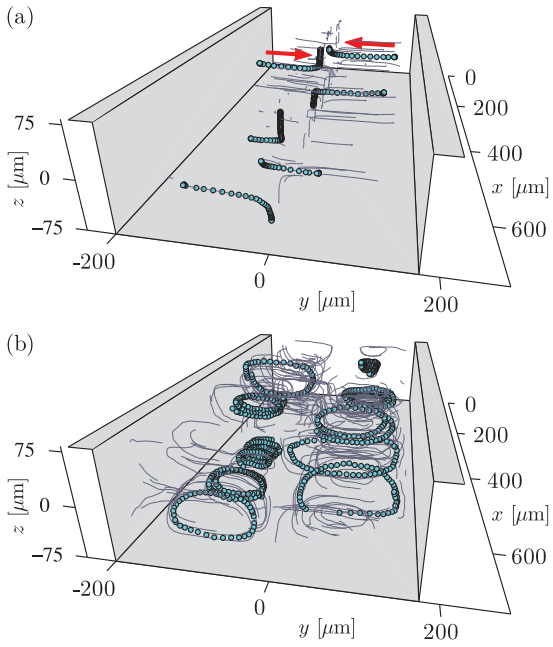

FIG. 4. (Color online) Measured particle trajectories (thin black lines) obtained using the 3D-APTV technique in the microchannel (gray walls) actuated at the 1.94-MHz horizontal half-wave resonance. For selected trajectories, the particle positions are represented by dots. (a) 5-μm-diameter particles moving (thick arrows) to the vertical center plane $y = 0$, and (b) 0.5-μm-diameter particles exhibiting circular motion as in Fig. 2(b).

The acoustic radiation force F_y^{rad} is in this case minute and the particles are primarily transported by the acoustic streaming $\langle \boldsymbol{v}_2 \rangle$ of the fluid resulting in particle trajectories following the four vertical vortices in the bulk, shown in Fig. 2(b). The setup and results are illustrated in the entry for the APS-DFD 2012 Video Gallery [48].

B. Comparison of theory and experiments

Theoretically, the acoustophoretic particle velocity $\boldsymbol{u}^p$ is given by Eq. (32) combined with the expressions for the streaming velocity of the liquid [Eqs. (25) and (31)] and the expression for the radiation force on the particles [Eq. (33)]. The amplitudes of both the acoustic streaming and the radiation force depend linearly on the acoustic energy density E_{ac} through Eqs. (12) and (33). To make a theoretical prediction of the motion of the 0.5-μm-diameter particles, we need to determine the acoustic energy density $E_{ac}^{0.5\,\mu m}$. This calibration was done *in situ* based on the measurements of the 5-μm-diameter particles, by the following three-step procedure.

First, we determined the acoustic energy density $E_{ac}^{5\,\mu m}$ for the experiment with the 5-μm-diameter particles. This was done by fitting the $\sin(\pi\tilde{y})$-dependent expression (36) for $u_y^p(\tilde{y},0)$ to the measured instantaneous velocities, using the amplitude as the only fitting parameter [26,45]. The small contribution from the acoustic streaming to the 5-μm-diameter-particle velocity was taken into account although it constituted only 6% of the total particle velocity. The fit showed good agreement between theory and experiment, and

after correcting for a wall-enhanced drag coefficient of 1.032 at the horizontal center plane (see Refs. [27,45,49,50]), we extracted the acoustic energy density $E_{\mathrm{ac}}^{5\,\mu\mathrm{m}} = (20.6 \pm 0.7)\,\mathrm{J/m^3}$, where the 1σ standard error of the estimated value is stated. Since both the wall-enhanced drag coefficient and the drag force from the acoustic streaming fluid velocity are height dependent, only five trajectories of 5-μm-diameter particles close to the horizontal center line ($z = 0$) qualified for use in the fit, based on a criterion of $|z_0| \leqslant 6\ \mu\mathrm{m}$. The starting positions (x_0, y_0, z_0) of the five tracks were (34 μm, -115 μm, 6 μm), (310 μm, -66 μm, -6 μm), (482 μm, -35 μm, -5 μm), (74 μm, 115 μm, 2 μm), and (350 μm, 128 μm, 0 μm), and they all reached the vertical center plane $y = 0$.

Second, the acoustic energy density $E_{\mathrm{ac}}^{0.5\,\mu\mathrm{m}}$ for the experiment with the 0.5-μm-diameter particles was determined, using the result for $E_{\mathrm{ac}}^{5\,\mu\mathrm{m}}$ combined with the fact that E_{ac} scales as the square of the applied voltage U_{pp} [26]. The measured voltages for the two experiments are $U_{\mathrm{pp}}^{0.5\,\mu\mathrm{m}} = (1.62 \pm 0.01)$ V and $U_{\mathrm{pp}}^{5\,\mu\mathrm{m}} = (0.91 \pm 0.01)$ V, where the stated error corresponds to the standard deviation of a series of voltage measurements, with the power turned off in-between each measurement. The derived value for $E_{\mathrm{ac}}^{0.5\,\mu\mathrm{m}}$, taking into account the errors of $U_{\mathrm{pp}}^{0.5\,\mu\mathrm{m}}$, $U_{\mathrm{pp}}^{5\,\mu\mathrm{m}}$, and $E_{\mathrm{ac}}^{5\,\mu\mathrm{m}}$, becomes $E_{\mathrm{ac}}^{0.5\,\mu\mathrm{m}} = (U_{\mathrm{pp}}^{0.5\,\mu\mathrm{m}}/U_{\mathrm{pp}}^{5\,\mu\mathrm{m}})^2 E_{\mathrm{ac}}^{5\,\mu\mathrm{m}} = (65 \pm 2)\ \mathrm{J/m^3}$, with the contribution from the error of the measured voltages being negligible.

Third, based on Eq. (10), the derived value for the energy density $E_{\mathrm{ac}}^{0.5\,\mu\mathrm{m}}$ is used in the analytical expression for the particle velocities (32). The radiation force is given by Eq. (33) and the acoustic streaming velocity is given by Eqs. (25) and (31), using the thermoviscous-corrected amplitude v_{str}^{T} [Eq. (13)]. The contribution from the acoustic radiation force to the 0.5-μm-diameter particle velocity was small and constituted only 12% of the total particle velocity in the horizontal center plane $z = 0$. The contribution from the radiation force to the 0.5-μm-diameter-particle velocity was not corrected for the wall-enhanced drag coefficient since this was minute for these small particles.

To compare the experimental results and the analytical prediction, we consider the 0.5-μm-diameter particle velocities in the vertical cross section, yz plane, of the channel as in Figs. 1, 2, and 3. In Fig. 5 are shown color plots of (a) the experimentally measured acoustophoretic velocities for the 0.5-μm-diameter particles, (b) the analytical prediction of the same, and (c) the numerical validation of the analytical result using the methods of Muller *et al.* [22]. The three data sets are shown on the same 37×15 bin array and with the same color scale. The experimental and the analytical velocities agree well both qualitatively and quantitatively, although the experimental velocities are approximately 20% higher on average. The experimental results for the particle velocities [Fig. 5(a)] are found as the mean of several measurements of the particle velocity in each bin. The number of measurements performed in each bin is shown in Fig. 6(a), while the standard error of the mean (SEM) particle velocity is shown in Fig. 6(b). These plots show that we typically have between 20 and 70 measurements in each bin and the experimental error is on average only 1 μm/s, while the relative experimental error

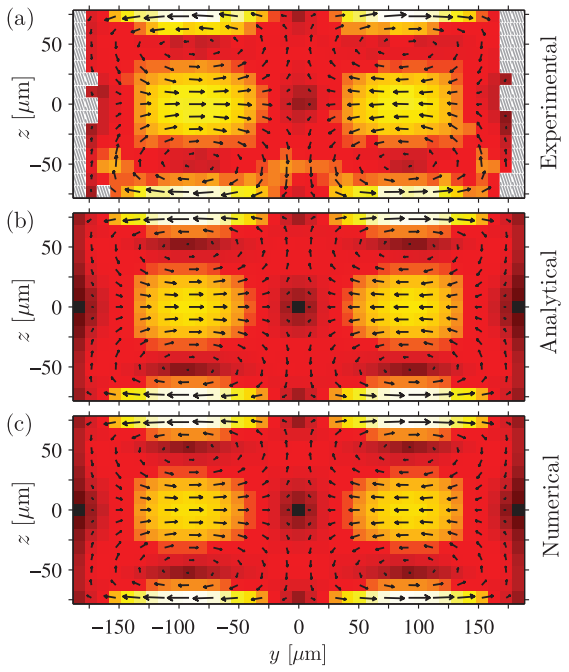

FIG. 5. (Color online) Comparison between experimental, analytical, and numerical studies of the acoustophoretic particle velocities $\boldsymbol{u}^{\mathrm{p}}$ of 0.5-μm-diameter polystyrene particles in water. The particle velocities $\boldsymbol{u}^{\mathrm{p}}$ (vectors) and their magnitude [color plot ranging from 0 μm/s (black) to 63 μm/s (white) in all three plots] are shown in the vertical cross section of the microchannel, divided into a pixel array consisting of 37×15 square bins of side length 10 μm. The axes of the plot coincide with the position of the channel walls. (a) The APTV measurements of the 0.5-μm-diameter particles, shown in Fig. 4(b), projected onto the vertical cross section. The maximum velocity is 63 μm/s. Close to the side walls, experimental data could not be obtained, which is represented by hatched bins. (b) Analytical prediction of $\boldsymbol{u}^{\mathrm{p}}$ based on Eq. (32), taking both the radiation force and the streaming-induced drag force into account. The first 20 terms of the Fourier series for $\langle \boldsymbol{v}_2 \rangle$ [Eq. (25)] have been included in the calculation. The maximum velocity is 59 μm/s. There are no free parameters in this prediction as the acoustic energy density was calibrated *in situ* based on measurements of large 5-μm-diameter particles, shown in Fig. 4(a). (c) Numerical validation of the analytical result for $\boldsymbol{u}^{\mathrm{p}}$ using the method described in Muller *et al.* [22]. The numerical solution has been scaled by the thermoviscous prefactor to the streaming amplitude (13). The maximum velocity is 59 μm/s.

is on average 4%. The error of the theoretical prediction is given by the relative error of 4% on the estimated value for the energy density $E_{\mathrm{ac}}^{0.5\,\mu\mathrm{m}}$.

The quantitative differences between the experimental particle velocities [Fig. 5(a)] and the analytical prediction [Fig. 5(b)] are emphasized in Fig. 7, showing the difference Δu^{p} between the experimental and analytical acoustophoretic particle speeds

$$\Delta u^{\mathrm{p}} = \left|\boldsymbol{u}_{\mathrm{exp}}^{\mathrm{p}}\right| - \left|\boldsymbol{u}_{\mathrm{anl}}^{\mathrm{p}}\right|. \tag{38}$$

We have chosen to consider the difference of the absolute velocity values $|\boldsymbol{u}_{\mathrm{exp}}^{\mathrm{p}}| - |\boldsymbol{u}_{\mathrm{anl}}^{\mathrm{p}}|$ instead of the absolute value of the difference $|\boldsymbol{u}_{\mathrm{exp}}^{\mathrm{p}} - \boldsymbol{u}_{\mathrm{anl}}^{\mathrm{p}}|$ because the former allows us to

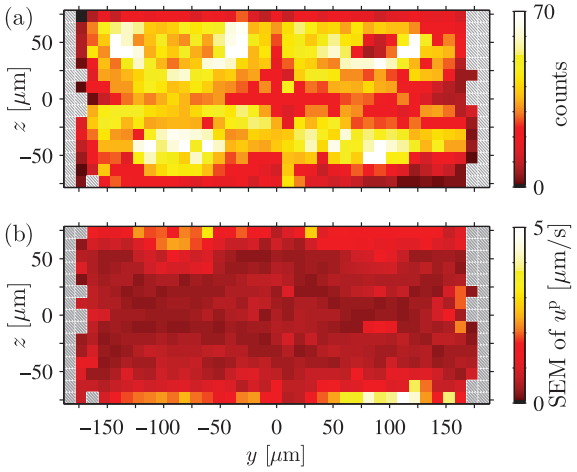

FIG. 6. (Color online) (a) Color plot of the number of times the velocity has been measured in each square bin. (b) Color plot of standard error of the mean (SEM) particle velocity in each square bin.

see when the experimental velocity respectively overshoots and undershoots the analytical prediction. Figure 7(a) shows a color plot of Δu^{p} in the channel cross section, while Fig. 7(b)

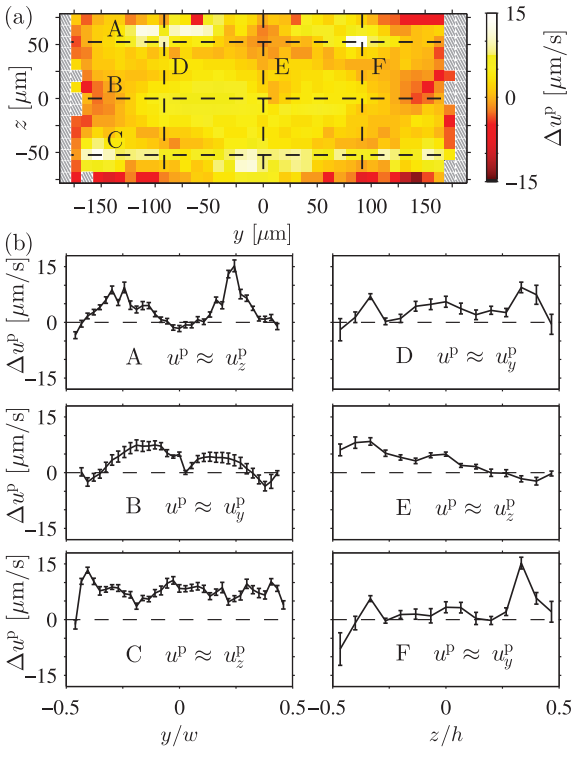

FIG. 7. (Color online) (a) Color plot of the difference between the experimental and analytical acoustophoretic particle speeds Δu^{p} [Eq. (38)]. (b) Line plots of Δu^{p} along the dashed lines in (a), marked A, B, C, D, E, and F, with error bars indicating the 1σ error of Δu^{p}. The lines are positioned at $y = 0$ μm, $y = \pm 91.7$ μm, $z = 0$ μm, and $z = \pm 52.3$ μm. The off-center lines go through the rotation centers of the flow rolls, and consequently $\boldsymbol{u}^{\mathrm{p}} \approx u_y^{\mathrm{p}} \boldsymbol{e}_y$ in B, D, and F, while $\boldsymbol{u}^{\mathrm{p}} \approx u_z^{\mathrm{p}} \boldsymbol{e}_z$ in A, C, and E.

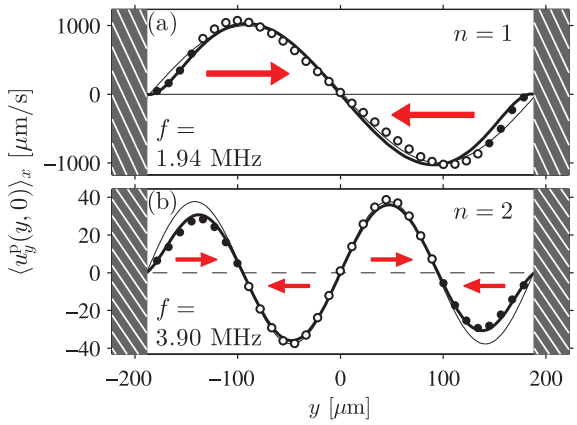

FIG. 8. (Color online) Experimental data from Ref. [45] compared with the theoretical predictions of Eqs. (36) and (37). μPIV measurements, in the center plane $z = 0$, of the y component of the acoustophoretic velocity $\langle u_y^{\mathrm{p}}(y,0)\rangle_x$ (open and closed dots) for 0.6-μm-diameter polystyrene particles in water, small enough that streaming dominates and $\boldsymbol{u}^{\mathrm{p}} \approx \langle \boldsymbol{v}_2 \rangle$. The observed motion (thick arrows) in (a) and (b) resembles the analytical results shown in Figs. 2(b) and 2(c), respectively. For each value of y, the measured velocity u_y^{p} is averaged along the x coordinate, with resulting SEM smaller than the size of the dots. The sinusoidal parallel-plate prediction (thin line) [Eq. (36)] is fitted to the data points far from the side walls (open dots), while the rectangular-channel prediction (thick line) [Eq. (37)] is fitted to all data points (open and closed dots). In both fits the acoustic energy E_{ac} is treated as a free parameter. (a) The half-wave resonance $\lambda/2 = w$ ($n = 1$) with $f = 1.940$ MHz and $U_{\mathrm{pp}} = 1$ V. (b) The full-wave resonance $\lambda = w$ ($n = 2$) with $f = 3.900$ MHz and $U_{\mathrm{pp}} = 1$ V.

shows line plots of Δu^{p} along the dashed lines in Fig. 7(a), allowing for a more detailed study of the spatial dependence of the difference. These lines are chosen to go through the rotation centers of the flow rolls. The error bars in Fig. 7(b) show the 1σ error of Δu^{p}, taking into account both the SEM for the experimental measurements [Fig. 6(b)] and the error of the analytical prediction (4%) inherited from the derived value for $E_{\mathrm{ac}}^{0.5\,\mu\mathrm{m}}$. The experimental and analytical velocities do not agree within the error of Δu^{p}, moreover, a trend of the experimental velocities being larger than the analytical predictions is seen.

A further comparison between the analytical model presented in this paper and experimental measurements on 0.6-μm-diameter polystyrene particles from Ref. [45] is shown in Fig. 8. These particles are dominated by the drag from the acoustic streaming, and in this comparison we are only interested in studying how the side walls influence the shape of $u_y^{\mathrm{p}}(\tilde{y},0)$ [Eq. (37)]. Consequently, the amplitude of the streaming velocity, and thus the acoustic energy density, was treated as a fitting parameter. The experimental results support our analytical prediction (37) (thick line) for the rectangular channel with side walls, which shows a suppression of u_y^{p} near the walls compared to the sinusoidal form of u_y^{p} in Eq. (36) (thin line) predicted for the parallel-plate channel without side walls. This is particularly clear for the full-wave resonance $\lambda = w$ ($n = 2$) [Fig. 8(b)]. The difference in the amplitude of

u^{p} between Figs. 8(a) and 8(b) is due to differences in the resonance modes, i.e., E_{ac} is not the same even though U_{pp} is.

V. DISCUSSION

The comparison shows good agreement between the experimental measurements and the analytical prediction of the streaming-induced particle velocities. The qualitative agreement is seen in Fig. 5 for the two-dimensional topology of the particle motion, and in Fig. 8 for the effect of the side walls. Quantitatively, the experimental and analytical results agree within a mean relative difference of approximately 20%, a low deviation given state-of-the-art in the field. However, as illustrated by the statistical analysis in Fig. 7, the differences Δu^{p} are larger than the estimated 1σ errors. This could indicate a minor systematic error in the experimental procedure or in the theoretical model, or be due to underestimation of the experimental error involved in the analytical prediction.

In the 5-μm-diameter-particle experiment, the acoustic energy density is determined using only five particle trajectories close to the channel center $z = 0$. This is reasonable as the error of the calculated energy density is relatively low (3%), however, a calculation based on more particle trajectories would be desirable. This can be realized through more experimental repetitions or through implementation of the 2D dependence of the wall-enhanced drag force, allowing for use of off-center particle trajectories. One source of error that has not yet been discussed arises from the assumption made that the acoustic energy density, and thus the acoustic forces, does not depend on the x position in the investigated field of view. In the same setup, Augustsson *et al.* [28] observed negligible field gradients in the x direction in some field of views and significant ones in others. This inhomogeneity was considered here when making the measurements: we made sure to check that the five 5-μm-diameter-particle trajectories sample the x range reasonably well and exhibit only negligible variations in the acoustic energy density as a function of the x position.

In the 0.5-μm-diameter-particle experiment, the statistics and sampling of the x range are good, however, they could still be improved to achieve better statistics close to the walls. The relative positions of the 0.5-μm-diameter particles are accurately determined by use of the APTV technique, whereas the absolute position in the channel, which was used to compare with theory, is difficult to determine precisely and might also be improved. Furthermore, accurate measurements of the channel dimensions are also important, as these are key parameters in the theoretical model.

The analytical model could be improved in several ways. The treatment of the liquid could be extended by including thermal dependence of more material parameters such as the specific heat capacity ratio γ, thermal expansion α_p, compressibility κ_s, and speed of sound c_0. The influence of the surrounding chip material could be included, thereby relaxing the assumptions of infinite acoustic impedance (ideal reflection) and infinite thermal conduction (ideal heat sink) of the channel walls. Solving the full elastic wave problem in the whole chip is beyond analytical solutions, but is, however, possible with numerical models. This might be necessary to achieve accurate quantitative agreement between theoretical predictions and experiments. Furthermore, the analytical and numerical models assume an ideal rectangular channel cross section, which is crucial since the generating mechanism for the acoustic streaming takes place within the μm-thin acoustic boundary layer. Even small defects, such as uneven surfaces on the μm scale, might lead to changes in the acoustic streaming velocity field.

VI. CONCLUSIONS

In this work, we have derived an analytical expression for the acoustophoretic velocity of microparticles resulting from the acoustic radiation force and the acoustic streaming-induced drag force in a rectangular microchannel, and we have successfully compared it with a direct numerical solution of the governing equations. We have also accurately measured 3D trajectories of 0.5-μm-diameter and 5-μm-diameter particles in an acoustically actuated microchannel, with an average relative experimental error of 4% for the 0.5-μm-particle velocities. This allowed us to perform a quantitative comparison in 3D between theory and experiments of streaming-induced particle velocities in a rectangular channel. The analytical derivation successfully predicted the measured streaming-induced 0.5-μm-diameter-particle velocities, with qualitative agreement and quantitative differences around 20%, a low deviation given state-of-the-art in the field. This shows that the time-averaged second-order perturbation model of the governing equations yields an adequate description of the acoustophoretic particle motion.

The differences between the theoretical prediction and the experimental results emphasize the need for further extensions of the analytical model, along with improved numerical simulations [22]. Aiming for more detailed quantitative studies of acoustophoresis, the results also stress the need for improved accuracy of the measurements of the channel dimensions and the absolute positions of the particles in the microchannel. The trinity of analytical, numerical, and experimental studies of the acoustophoretic particle motion enhances the understanding of acoustophoresis and opens up for more elaborate and broader applications.

ACKNOWLEDGMENTS

This work was supported by the Danish Council for Independent Research, Technology and Production Sciences, Grants No. 274-09-0342 and No. 11-107021, the German Research Foundation (DFG), under the individual grants program KA 1808/12-1, the Swedish Governmental Agency for Innovation Systems, VINNOVA, the program Innovations for Future Health, Cell CARE, Grant No. 2009-00236, and the Swedish Research Council, Grant No. 621-2010-4389.

[1] H. Bruus, J. Dual, J. Hawkes, M. Hill, T. Laurell, J. Nilsson, S. Radel, S. Sadhal, and M. Wiklund, Lab Chip **11**, 3579 (2011).

[2] T. Laurell, F. Petersson, and A. Nilsson, Chem. Soc. Rev. **36**, 492 (2007).

[3] A. A. Doinikov, J. Acoust. Soc. Am. **101**, 722 (1997).
[4] S. D. Danilov and M. A. Mironov, J. Acoust. Soc. Am. **107**, 143 (2000).
[5] M. Settnes and H. Bruus, Phys. Rev. E **85**, 016327 (2012).
[6] L. V. King, Proc. R. Soc. London, Ser. A **147**, 212 (1934).
[7] K. Yosioka and Y. Kawasima, Acustica **5**, 167 (1955).
[8] L. P. Gorkov, Sov. Phys.–Dokl. **6**, 773 (1962) [Doklady Akademii Nauk SSSR **140**, 88 (1961)].
[9] L. Rayleigh, Philos. Trans. R. Soc. London **175**, 1 (1884).
[10] M. Hamilton, Y. Ilinskii, and E. Zabolotskaya, J. Acoust. Soc. Am. **113**, 153 (2003).
[11] M. Hamilton, Y. Ilinskii, and E. Zabolotskaya, J. Acoust. Soc. Am. **114**, 3092 (2003).
[12] T. Secomb, J. Fluid Mech. **88**, 273 (1978).
[13] C. Wang and B. Drachman, Appl. Sci. Res. **39**, 55 (1982).
[14] K. Ilin and A. Morgulis, SIAM J. Appl. Math. **72**, 1406 (2012).
[15] H. Schlichting, Phys. Z **33**, 327 (1932).
[16] W. L. Nyborg, J. Acoust. Soc. Am. **30**, 329 (1958).
[17] C. Lee and T. Wang, J. Acoust. Soc. Am. **85**, 1081 (1989).
[18] A. Y. Rednikov and S. S. Sadhal, J. Fluid Mech. **667**, 426 (2011).
[19] H. Lei, D. Henry, and H. BenHadid, Appl. Acoust. **72**, 754 (2011).
[20] M. K. Aktas and B. Farouk, J. Acoust. Soc. Am. **116**, 2822 (2004).
[21] B. Tajik, A. Abbassi, M. Saffar-Avval, A. Abdullah, and H. Mohammad-Abadi, Eng. Applicat. Comput. Fluid Mech. **6**, 366 (2012).
[22] P. B. Muller, R. Barnkob, M. J. H. Jensen, and H. Bruus, Lab Chip **12**, 4617 (2012).
[23] J. Lei, P. Glynne-Jones, and M. Hill, Lab Chip **13**, 2133 (2013).
[24] S. M. Hagsäter, T. G. Jensen, H. Bruus, and J. P. Kutter, Lab Chip **7**, 1336 (2007).
[25] O. Manneberg, S. M. Hagsäter, J. Svennebring, H. M. Hertz, J. P. Kutter, H. Bruus, and M. Wiklund, Ultrasonics **49**, 112 (2009).
[26] R. Barnkob, P. Augustsson, T. Laurell, and H. Bruus, Lab Chip **10**, 563 (2010).
[27] M. Koklu, A. C. Sabuncu, and A. Beskok, J. Colloid Interface Sci. **351**, 407 (2010).
[28] P. Augustsson, R. Barnkob, S. T. Wereley, H. Bruus, and T. Laurell, Lab Chip **11**, 4152 (2011).
[29] O. Dron and J. L. Aider, Europhys. Lett. **97**, 44011 (2012).
[30] M. G. Olsen and R. J. Adrian, Exp Fluids Suppl. **29** S166 (2000).
[31] M. Rossi, R. Segura, C. Cierpka, and C. J. Kähler, Exp. Fluids **52**, 1063 (2012).
[32] M. Raffel, C. E. Willert, S. T. Wereley, and J. Kompenhans, *Particle Image Velocimetry* (Springer, New York, 2007).
[33] C. Cierpka, R. Segura, R. Hain, and C. J. Kähler, Meas. Sci. Technol. **21**, 045401 (2010).
[34] C. Cierpka, M. Rossi, R. Segura, and C. J. Kähler, Meas. Sci. Technol. **22**, 015401 (2011).
[35] C. Cierpka, M. Rossi, R. Segura, F. Mastrangelo, and C. J. Kähler, Exp. Fluids **52**, 605 (2012).
[36] P. M. Morse and K. U. Ingard, *Theoretical Acoustics* (Princeton University Press, Princeton, NJ, 1986).
[37] A. D. Pierce, *Acoustics* (Acoustical Society of America, Woodbury, NY, 1991).
[38] D. T. Blackstock, *Physical Acoustics* (Wiley, Hoboken NJ, 2000).
[39] L. D. Landau and E. M. Lifshitz, *Fluid Mechanics*, 2nd ed., Vol. 6, Course of Theoretical Physics (Pergamon, Oxford, 1993).
[40] COMSOL Multiphysics 4.2a, www.comsol.com
[41] CRCnetBASE Product, *CRC Handbook of Chemistry and Physics*, 92nd ed. (CRS Press, Boca Raton, FL, 2012), www.hbcpnetbase.com
[42] L. Bergmann, *Der Ultraschall und seine Anwendung in Wissenschaft und Technik*, 6th ed. (S. Hirzel Verlag, Stuttgart, 1954).
[43] P. H. Mott, J. R. Dorgan, and C. M. Roland, J. Sound Vib. **312**, 572 (2008).
[44] L. D. Landau and E. M. Lifshitz, *Theory of Elasticity. Course of Theoretical Physics*, 3rd ed. (Pergamon, Oxford, 1986), Vol. 7.
[45] R. Barnkob, P. Augustsson, T. Laurell, and H. Bruus, Phys. Rev. E **86**, 056307 (2012).
[46] R. Hain and C. J. Kähler, Exp. Fluids **42**, 575 (2007).
[47] C. Cierpka, B. Lütke, and C. J. Kähler, Exp Fluids **54**, 1533 (2013).
[48] A. Marin, M. Rossi, R. Barnkob, P. Augustsson, P. Muller, H. Bruus, T. Laurell, and C. Kaehler, arXiv: 1210.3973 [physics.flu-dyn] (see two versions of the video listed under 'Ancillary files'), http://www.aps.org/units/dfd/pressroom/videos/2012.cfm.
[49] R. Barnkob, I. Iranmanesh, M. Wiklund, and H. Bruus, Lab Chip **12**, 2337 (2012).
[50] J. Happel and H. Brenner, *Low Reynolds Number Hydrodynamics with Special Applications to Particulate Media* (Martinus Nijhoff, The Hague, 1983).

Appendix C

Paper published in Lab on a Chip, May 2014

Focusing of sub-micrometer particles and bacteria enabled by two-dimensional acoustophoresis

M. Antfolk, P. B. Muller, P. Augustsson, H. Bruus and T. Laurell

Abstract: Handling of sub-micrometer bioparticles such as bacteria are becoming increasingly important in the biomedical field and in environmental and food analysis. As a result, there is an increased need for less labor-intensive and time-consuming handling methods. Here, an acoustophoresis-based microfluidic chip that uses ultrasound to focus sub-micrometer particles and bacteria, is presented. The ability to focus sub-micrometer bioparticles in a standing one-dimensional acoustic wave is generally limited by the acoustic-streaming-induced drag force, which becomes increasingly significant the smaller the parti- cles are. By using two-dimensional acoustic focusing, *i.e.* focusing of the sub-micrometer particles both horizontally and vertically in the cross section of a microchannel, the acoustic streaming velocity field can be altered to allow focusing. Here, the focusability of E. coli and polystyrene particles as small as 0.5 μm in diameter in microchannels of square or rectangular cross sections, is demonstrated. Numerical analysis was used to determine generic transverse particle trajectories in the channels, which revealed spiral-shaped trajectories of the sub-micrometer particles towards the center of the microchannel; this was also confirmed by experimental observations. The ability to focus and enrich bacteria and other sub-micrometer bioparticles using acoustophoresis opens the research field to new microbiological applications.

http://dx.doi.org/10.1039/c4lc00202d

Lab on a Chip

PAPER

Focusing of sub-micrometer particles and bacteria enabled by two-dimensional acoustophoresis†

Cite this: *Lab Chip*, 2014, **14**, 2791

M. Antfolk,*[a] P. B. Muller,[b] P. Augustsson,[ac] H. Bruus[b] and T. Laurell*[a]

Received 14th February 2014,
Accepted 20th May 2014

DOI: 10.1039/c4lc00202d

www.rsc.org/loc

Handling of sub-micrometer bioparticles such as bacteria are becoming increasingly important in the biomedical field and in environmental and food analysis. As a result, there is an increased need for less labor-intensive and time-consuming handling methods. Here, an acoustophoresis-based microfluidic chip that uses ultrasound to focus sub-micrometer particles and bacteria, is presented. The ability to focus sub-micrometer bioparticles in a standing one-dimensional acoustic wave is generally limited by the acoustic-streaming-induced drag force, which becomes increasingly significant the smaller the particles are. By using two-dimensional acoustic focusing, *i.e.* focusing of the sub-micrometer particles both horizontally and vertically in the cross section of a microchannel, the acoustic streaming velocity field can be altered to allow focusing. Here, the focusability of *E. coli* and polystyrene particles as small as 0.5 μm in diameter in microchannels of square or rectangular cross sections, is demonstrated. Numerical analysis was used to determine generic transverse particle trajectories in the channels, which revealed spiral-shaped trajectories of the sub-micrometer particles towards the center of the microchannel; this was also confirmed by experimental observations. The ability to focus and enrich bacteria and other sub-micrometer bioparticles using acoustophoresis opens the research field to new microbiological applications.

Introduction

The ability to control and process sub-micrometer bioparticles, *e.g.* bacteria and subcellular organelles, is becoming increasingly important in biomedicine and in environmental and food analysis.[1,2] Methods such as blood culture of bacteria[1] and subcellular fractionation[3] are, however, labor-intensive, complicated, and time-consuming, and new technologies are being sought to redress these shortcomings.

Microfluidics offers a means of automated handling and analysis of sub-micrometer bioparticles with the associated advantage of a continuous mode of sample handling. Thus, considerations such as initial sample volume or batch volume are no longer relevant. Previously used methods for handling of sub-micrometer particles included filters,[4,5] dielectrophoresis,[6–8] inertia in combination with hydrodynamic forces,[9] magnetophoresis,[10,11] deterministic lateral displacement,[12] and surface acoustic waves (SAW).[13] These methods have been mainly used for handling of bacteria and particles of around 1 μm in diameter. Recently, SAW were used to separate 0.5 μm polystyrene particles from 0.3 μm particles,[14] Stoneley waves were used to focus 0.5 μm polystyrene particles at flow rates of 200 nL min^{-1},[15] and acoustic trapping has been used to successfully trap 0.1 μm particles using seeding particles.[16] Although acoustic seed trapping gives good recovery of sub-micrometer particles and bacteria, the system operates in batch mode, which is limited by the capacity of the acoustic trap. In spite of these developments, one common need is the ability to process sub-micrometer particles in continuous-flow mode together with the possibility of handling rare species in crude samples with high recovery rates without previous sample preparation.

In this regard, the use of acoustophoresis in microfluidic systems has attracted much attention in recent years as a continuous-flow and non-contact mode method of separating or enriching microparticles or cells while offering a reasonable degree of throughput. The method involves the use of ultrasound standing waves to focus cells or particles in the nodal (or anti-nodal) plane of the standing wave according to their intrinsic properties: size, density, and compressibility.[17] Furthermore, this label-free and gentle[18,19] method—which operates independently of the biochemical and electrical properties of the suspension medium—has been extensively explored to separate, wash, or concentrate various biological

[a] *Department of Biomedical Engineering, Lund University, Box 118, SE-221 00 Lund, Sweden. E-mail: thomas.laurell@bme.lth.se, maria.antfolk@bme.lth.se*
[b] *Department of Physics, Technical University of Denmark, DTU Physics Bldg 309, DK-2800 Kongens Lyngby, Denmark*
[c] *Department of Electrical Engineering and Computer Science, Massachusetts Institute of Technology, Cambridge, MA, USA*

† Electronic supplementary information (ESI) available. See DOI: 10.1039/c4lc00202d

samples including blood,[20–23] raw milk,[24] circulating tumor cells,[25,26] and yeast.[27]

For bulk acoustic waves (BAW) microchannel acoustophoresis is usually carried out in the 1–10 MHz frequency range and particles are focused along a single dimension. For larger particles, the acoustically induced particle motion is dominated by the primary acoustic radiation force, whereas the motion of smaller particles is instead dominated by the acoustic streaming-induced drag force of the suspending liquid.[28,29] Attempts have been made to address the need for bacterial or other sub-micrometer particle manipulation and enrichment in acoustic standing-wave systems. Bacteria have been processed with some success in batch mode using ultrasound to agglomerate them,[30,31] and a quarter-wavelength acoustic device was used to concentrate 1 μm particles in continuous flow.[32] However, no systems have yet emerged that enable continuous flow-based focusing of bacteria or other sub-micrometer particles at recovery rates above 90%, relevant when handling highly dilute suspensions.

This paper presents continuous flow-based sub-micrometer particle focusing using two-dimensional BAW-acoustophoresis. The use of two-dimensional focusing has previously only been explored for particles larger than 5 μm in diameter.[25,26,33–35] In contrast to the case with one-dimensional standing acoustic waves, the simultaneous excitation of two orthogonal resonances generates an acoustic streaming velocity field that does not counteract the primary radiation force. A numerical model that predicts a streaming field with essentially a single large vortex centered in the cross section of the channel, in agreement with experimental data, is also presented.

Theory

Particles in a standing-wave acoustophoresis system are primarily affected by two forces: the acoustic radiation force from scattering of the acoustic wave on the particles, and the drag force from the acoustic streaming velocity field of the fluid generated by viscous stresses in the acoustic boundary layers. The interplay between these two forces and the regimes in which they each dominate the particle motion in acoustophoresis systems have been studied extensively by Barnkob *et al.*[29] Through theoretical derivation and experimental verification, these authors have described how the motion of large particles is dominated by the acoustic radiation force while the motion of small particles is dominated by the drag force from the acoustic streaming.

To theoretically determine the critical particle diameter $2a_c$, where the crossover from radiation force-dominated particle motion to acoustic streaming-induced drag force-dominated particle motion occurs, the magnitudes of the two forces are equated, resulting in the following equation valid for single-particle motion in a half-wavelength resonance:[29]

$$2a_c = \sqrt{\frac{12s}{\pi}\frac{\nu}{\Phi f}} \approx 1.6\ \mu\text{m}, \qquad (1)$$

where s is a factor related to the channel geometry, ν is the kinematic viscosity of the medium, Φ is the acoustic contrast factor, and f is the frequency of the acoustic field. The numerical value is calculated for a polystyrene particle in water and a frequency of f = 3.19 MHz. The geometrical value used is s = 0.47 for a particle near the top or bottom walls, and includes thermal effects.[29] The critical particle size is independent of the applied peak-to-peak voltage U_{pp} driving the piezo-ceramic ultrasound transducer, because both the radiation force and the streaming depend linearly on the energy density of the standing acoustic wave. In contrast, it can be seen in eqn (1) that the critical particle size does depend on the material parameters ν of the fluid and Φ of the fluid and particles, and on the actuation frequency f. Increasing the frequency to achieve radiation force-dominated motion of smaller particles is a relatively straightforward solution, but such an increase often necessitates reduced channel dimensions, which drastically reduces the throughput of the device. In this paper we propose another solution, namely to change the whole acoustic resonance such that the acoustic radiation force and the acoustic streaming-induced drag work together in focusing the particles.

The acoustic streaming and acoustophoretic particle motion in a microchannel cross section have been studied numerically by Muller *et al.*[28] The method is valid for long, straight microchannels of constant rectangular cross section and employs a pertubation approach to the pressure, temperature and velocity fields. Briefly, the numerical scheme is as follows. The first-order acoustic fields are solved in the frequency domain for an oscillating velocity boundary condition on the walls of the rectangular channel domain. From the first-order fields, the acoustic radiation force is calculated from the expression given by Settnes and Bruus,[36] while the steady acoustic streaming velocity field is calculated numerically by solving the time-averaged second-order Navier–Stokes equation and continuity equation.[27] This method only considers actuation at a single frequency, but can readily be extended to consider actuation with two frequencies by superposition of the second-order streaming flows. For this superposition to be valid the separation of the two frequencies should be much larger than the width of the resonances, which is typically on the order of 10 kHz, such that the first-order fields of the two resonances do not couple in the time-averaged second-order source terms for the streaming velocity field.[28] However, if the two resonance frequencies are closely spaced, resulting in overlapping resonance curves, the two resonances can be excited simultaneously at a single frequency. In this case, the first-order fields of the two resonances couple in the time-averaged second-order source terms, and consequently the streaming velocity field cannot be calculated by superposition of second-order streaming flows. This case of close-lying overlapping resonances is the subject of the numerical analysis in the following section, where we show that the relative phases of the wall oscillations control the structure of the streaming flow, and that specific

values can lead to structures qualitatively different from the standard quadrupolar Rayleigh streaming flow observed for the half-wavelength resonance.[37]

Numerical analysis

The following numerical analysis is a generic investigation of the acoustophoretic motion of 0.5 μm-diameter particles in a nearly-square channel cross section. It is not intended to be a direct numerical simulation of the actual experiments presented in this paper; nevertheless, it predicts the existence of two fundamentally different acoustic streaming patterns relevant for the interpretation of the experiments. The numerical analysis employs the method presented by Muller *et al.*[28] and to avoid spurious effects of perfect square symmetry and to imitate the uncertainty in microchannel fabrication, the cross-sectional dimensions of the microchannel in the model was chosen to be 230.5 μm wide and 229.5 μm high. The parameters used in the model correspond to the biologically relevant temperature of 37 °C. The first-order velocity boundary condition applied to the walls was $u_{bc} = u_0 \cos(\omega t)\boldsymbol{e}_y$ on the left and right walls and $u_{bc} = u_0 \cos(\omega t + \phi)\boldsymbol{e}_z$ on the top and bottom walls, where u_0 is the amplitude, $\omega = 2\pi f$ is the angular frequency of the transducer, ϕ is a constant phase shift, and $\boldsymbol{e}_y$ and $\boldsymbol{e}_z$ are the unit vectors in the transverse horizontal and vertical directions, respectively. Because both the acoustic streaming-induced drag force and the acoustic radiation force depend non-linearly on the oscillating velocity boundary conditions, the consequences of changing the phase shift ϕ between the two wall pairs cannot easily be deduced analytically.

To characterize the resonances of the nearly-square channel, the average acoustic energy density,[38] denoted E_{ac}, was calculated numerically for a range of frequencies, shown in Fig. 1. This was done for several different actuations of the nearly-square channel. In each panel an inset shows a sketch of the channel geometry and which walls are actuated and by which phase factor $\cos(\omega t + \phi)$. In Fig. 1(a) the nearly-square channel was actuated in phase on the left/right walls to obtain the usual horizontal half-wavelength resonance, showing up as a Lorentzian peak centered around the resonance frequency $f_1 = 3.3032$ MHz. In Fig. 1(b) the nearly-square channel was actuated in phase on the top/bottom walls resulting in a peak at the slightly higher resonance frequency $f_2 = 3.3176$ MHz corresponding to the vertical half-wavelength resonance. f_2 is slightly higher than f_1 because the height of the nearly-square channel is slightly smaller than the width. In Fig. 1(c) the nearly-square channel was actuated in phase on all four walls ($\phi = 0$). Due to the finite width of the two resonance peaks, this actuation simultaneously excites both the horizontal and the vertical half-wavelength resonances, resulting in a resonance curve with two peaks and a plateau in between, in contrast to the previous single-peak resonance curves. As a guide to the eye, the single-peak resonance curves from Fig. 1(a–b) are included in Fig. 1(c) in grey. The frequency mid-way between the two resonance peaks is

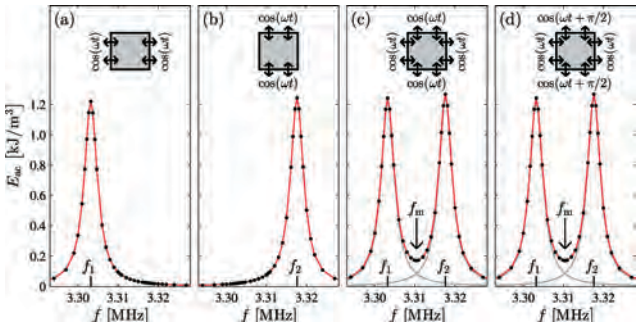

Fig. 1 Resonance curves, obtained by plotting the average acoustic energy density E_{ac} *vs.* the frequency $f = \omega/2\pi$ of the wall actuations. (a) A nearly-square channel, 230.5 μm by 229.5 μm cross section, with the left/right walls vibrating in phase. (b) The nearly-square channel with the top/bottom walls vibrating in phase. (c) The nearly-square channel with all walls vibrating in phase. The resonance curves from (a) and (b) are shown in grey. (d) Same as (c) except that the top/bottom wall pair vibrate with a phase shift of $\phi = \pi/2$ relative to the left/right wall pair. f_1 and f_2 are the two resonance frequencies corresponding to the horizontal and vertical half-wavelength resonance, respectively. f_m indicates the middle frequency between the two resonance peaks. All walls have the same oscillation amplitude u_0.

$f_m = (f_1 + f_2)/2 = 3.3104$ MHz. At this particular frequency, the amplitudes of the horizontal and the vertical resonances are the same, however much reduced relative to the two resonance maxima. In Fig. 1(d) the nearly-square channel was actuated on all four walls, but the phase of the actuation on the top/bottom wall pair was shifted relative to the left/right wall pair by $\phi = \pi/2$. The resulting resonance curve is the same; however, as we will see below, the second-order steady acoustic streaming velocity field changes significantly by introducing this phase shift.

We now study the acoustophoretic motion of 0.5 μm-diameter particles in the nearly-square channel cross section, shown in Fig. 2, for each of the four actuations shown in Fig. 1. This particle motion results from the acoustic radiation force and the streaming-induced drag force, both second-order acoustic effects.[28] Given the small particle diameter, the acoustophoretic motion is dominated by the drag force from the acoustic streaming.[29] Fig. 2 contains four rows (a–d) corresponding to the four cases in Fig. 1. The actuation frequency was f_1 in (a), f_2 in (b), and f_m in (c–d). For each case, column 1 shows the first-order acoustic pressure, column 2 shows the acoustic radiation force together with streamlines of the steady streaming velocity field, and column 3 shows the acoustophoretic trajectories of 0.5 μm-diameter particles.

For the two cases (a–b) the weak radiation force acts to focus the particles towards a center line, but as the particle motion is dominated by the streaming-induced drag force, they follow the quadrupolar streaming flow of the 1D half-wavelength resonance. For the two cases (c–d) both the horizontal and the vertical half-wavelength resonances are exited simultaneously at the single frequency f_m, and the streaming flow is qualitatively different from the usual quadrupolar structure. For $\phi = 0$ (c), the streaming flow consists of two larger

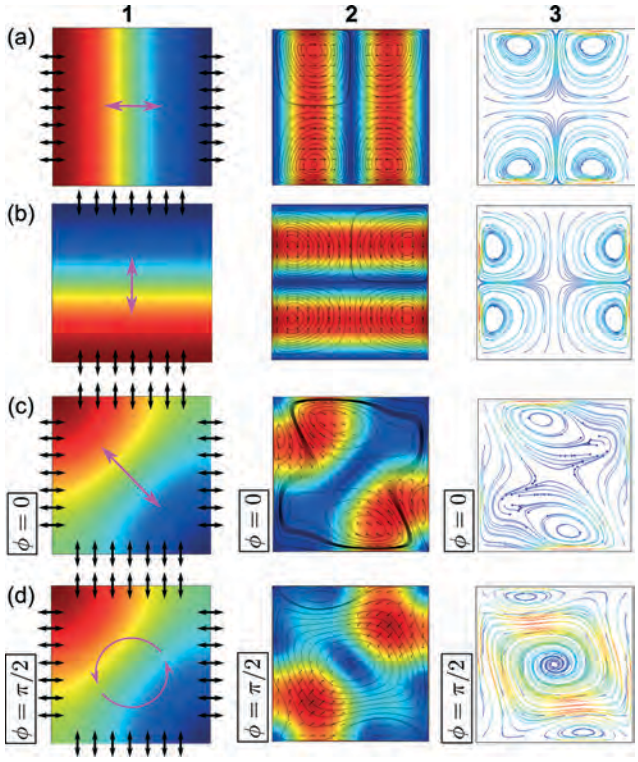

Fig. 2 Acoustophoretic motion of 0.5 μm-diameter particles in the nearly-square microchannel cross section. The rows (a–d) corresponds to the four cases shown in Fig. 1. The actuation frequency was f_1 in (a), f_2 in (b), and f_m in (c–d). For each case, column 1 is a snapshot in time of the amplitude of the oscillating first-order acoustic pressure (color plot where red is positive, green is zero, and blue is negative). Column 2 is the acoustic radiation force (color plot and arrows where red is positive and blue is zero) together with streamlines (black contour lines) of the steady streaming velocity field. Column 3 is the acoustophoretic trajectories (colors indicate the speed where red is positive and blue is zero) of 0.5 μm-diameter particles released from a regular grid in the channel cross section. To best illustrate the qualitative results, the color scale is set by the maximum value in each plot individually. For the color plots 1(a–c) the magenta arrow indicates that the pressure has an almost static nodal line (green) while the amplitude oscillates. For the color plot 1(d) the magenta arrows indicate that the nodal line (green) of the pressure field rotates in time.

flow rolls at the top and bottom walls along with two smaller flow rolls at the side walls. The small particles follow this streaming flow and are not focused in the center. For $\phi = \pi/2$ (d), the streaming flow consists of one large flow roll in the center of the channel and two smaller flow rolls at the top and bottom walls. The combined effect of the weak radiation force towards the centre and the strong streaming-induced drag force acts to focus the particles at the centre of the channel cross section following a spiralling motion. This allows for focusing of sub-micrometer particles, which is not possible in the standard one-dimensional half-wavelength resonance (a–b). By numerically tuning the phase shift ϕ a solution was obtained where the large centred flow roll covered the whole channel cross section without any smaller bulk flow rolls, allowing all particles to be focused at the centre. Changing the phase shift ϕ by π results in a counter-rotating streaming flow. The acoustic radiation force in Fig. 2(c–d) is similar to that reported for acoustic focusing of large particles in cylindrical channels.[39] It should be stressed that the steady streaming is a boundary driven second-order flow, it is not driven by the rotation of the first-order pressure in Fig. 2(d) first column.

This numerical analysis is a generic study not aimed at direct simulation of the following experiments. Experimentally it is very difficult to control, even to measure, the vibration of the channel walls. Moreover, the wall oscillation presumably varies along the length of the channel, by analogy with what has already been verified experimentally for the acoustic field of the half-wavelength resonance.[40] However, the numerical results indicate the existence of a streaming flow that enables focusing of sub-micrometer particles, which is impossible with the well-known quadrupolar Rayleigh streaming. This new streaming flow strongly depends on the relative phase of the vibrations of the walls, *i.e.* the boundary conditions for the first-order acoustic field. Moreover, the spatial variation of the actuation, which has not been investigated, will presumably also influence the streaming flow and thus the focusability. This calls for a more in-depth numerical study of the dependency of the acoustic streaming on the actuation boundary condition which will be included in future work, as for the present work the main emphasis is on the experimental results.

Materials and experimental methods

Design and fabrication of the device

The chips were fabricated from <110> oriented silicon using photolithography and anisotropic wet etching in KOH (400 g L^{-1} H_2O, 80 °C). Inlets and outlets were drilled through the silicon using a diamond drill (Tools Sverige AB, Lund, Sweden) and the chips were sealed by anodic bonding to a glass lid. The two chips had one trifurcation inlet and outlet split each, of which only a single inlet was used and the unused one was sealed (Fig. 3). The square-cross-section channel had a width

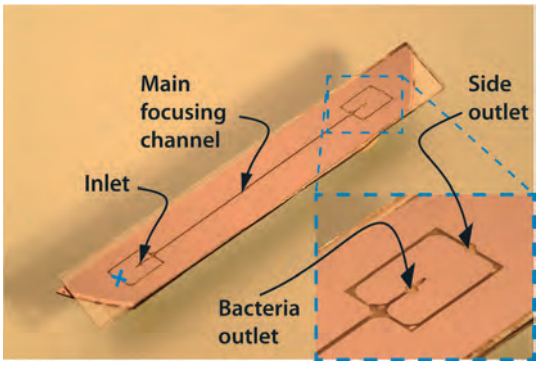

Fig. 3 Photograph of the chip design. The main focusing channel is 35 mm long and 230 μm wide, while its height is either 230 μm (square channel) or 150 μm (flat rectangular channel). After the trifurcation, the side channels are connected to one outlet. The inlet marked with a blue cross is not used.

and height of 230 μm and was operated at 3.19 MHz. The rectangular-cross-section channel had a width of 230 μm and a height of 150 μm, and was operated at 3.24 MHz and 5.09 MHz, respectively. The piezo-ceramic ultrasound transducers (PZ26; Ferroperm piezoceramics, Kvistgaard, Denmark) actuating the chips were glued to the chips with cyanoacrylate glue (Loctite Super Glue, Henkel Norden AB, Stockholm, Sweden). The 3 MHz ultrasound transducer was glued to the silicon and the 5 MHz transducer was glued to the glass lid, both at the middle of the chip. To control the temperature, a Peltier element (Farnell, London, UK) was glued underneath the 3 MHz ultrasound transducer and a Pt100 or Pt1000 resistance temperature detector (Farnell, London, UK) was glued to the glass lid.

Instrument set-up

The transducers were actuated using a dual-channel function generator (AFG 3022B; Tektronix UK Ltd., Bracknell, UK), the signals were amplified using in-house built power amplifiers based on an LT1012 power amplifier (Linear Technology Corp., Milpitas, CA, USA) and the applied voltage was monitored using an oscilloscope (TDS 2120; Tektronix). The temperature was controlled using a Peltier-controller (TC2812; Cooltronic GmbH, Beinwil am See, Switzerland) and the temperature was set to 37 °C throughout all experiments. Fluorescent microscopy images were obtained using a Hamamatsu camera (Hamamatsu Photonics KK, Hamamatsu, Japan) installed on an Olympus microscope (BX51WI; Olympus Corporation, Tokyo, Japan).

Experimental set-up

The flow rates were controlled using syringe pumps (neMESYS; Cetoni GmbH, Korbussen, Germany) mounted with glass syringes (Hamilton Bonaduz AG, Bonaduz, Switzerland) connected to the inlet and the outlet of the side channels. The center outlet was kept open and sample was collected from a short piece of tubing directly into an Eppendorf tube. While the inlet and outlet flow rates were varied, the outlet flow rates were kept at a split ratio of 40 : 60 at the center outlet and the outlet connected to the side channels. To minimize errors caused by sedimentation in the syringes and tubing, which would vary with the flow rate, sample collection with the ultrasound either on or off (for each flow rate) was compared. Particles and bacteria were quantified using a Coulter counter (Multiziser III; Beckman Coulter, Brea, CA, USA). Flow rates and voltage settings are given in Table 1.

Microparticles

Polystyrene microparticles of various sizes were used to characterize the system: 7.11 μm, 4.99 μm, and 3.17 μm diameter particles were obtained from Sigma-Aldrich (Buchs, Switzerland), and 0.992 μm and 0.591 μm particles and 0.49 μm and 0.24 μm fluorescent particles were obtained from Kisker (Kisker Biotech GmbH & Co. KG, Steinfurt, Germany). Fluorescent particles 0.78 μm in diameter were obtained from Bangs Laboratories (Bangs Laboratories, Fishers, IN, USA). Particle concentrations were kept below 10^9 mL^{-1}, to minimize the effect of acoustic and hydrodynamic interaction forces between particles.

Bacteria

For biological evaluation of the system, *Escherichia coli* (*E. coli*) DH5-α (containing a plasmid that carries the ampicillin-resistance gene), a kind gift from Åsa Janfalk Carlsson, was used. *E. coli* was cultured in liquid LB medium or LB plates containing 10 g L^{-1} tryptone (T1332; Saveen & Werner, Limhamn, Sweden), 5 g L^{-1} yeast extract (Hy-Yeast 412; Sigma-Aldrich), 10 g L^{-1} NaCl (Sigma-Aldrich) and 100 mg L^{-1} ampicillin (A9518-5G; Sigma-Aldrich) or agar (bacteriology-grade, A0949; Saveen & Werner).

Experimental results and discussion

In what follows, a system is presented that reduces the lower particle size focusing limit for acoustophoresis to the sub-micrometer range, thus enabling applications in research fields such as microbiology. The experiments were carried out on two variants of an acoustophoresis microfluidic chip, which had a straight square or rectangular channel with a single inlet for particle suspensions and a trifurcation outlet split (Fig. 3). Ideally, with the onset of continuous ultrasonic actuation, particles are focused in the center of the channel and exit through the central outlet—to an extent that depends on the acoustic energy density, the flow rate of the suspension, and the size and material properties of the particles relative to the suspending liquid. In the experiments particles with diameters ranging from 0.6 μm to 7 μm were used and for

Table 1 Nominal flow rates Q as set on the syringe pumps and voltage settings for the different experiments

Particle		Rectangular chip 1D		Rectangular chip 2D		Square chip 2D	
Diameter (μm)	Manufacturer	Voltage U_{pp} (V)	Flow rate Q (μL min^{-1})	Voltage $U_{pp,2}$ (V)	Flow rate Q (μL min^{-1})	Voltage U_{pp} (V)	Flow rate Q (μL min^{-1})
7	Sigma-Aldrich	2.5	50, 70, 90, 110, 130			3.16	50, 70, 90, 110, 130
5	Sigma-Aldrich	3.52	50, 70, 90, 110, 130			4.26	50, 60, 70, 80 90
3	Sigma-Aldrich	5.72	70, 80, 90, 100, 150, 200			5.73	50, 60, 70, 80, 90
1	Kisker	10.4	10, 20, 30, 40, 50, 60	0–4	10	10.6	15, 25, 35, 45, 55
0.6	Kisker	11	3, 5, 10, 15, 20	0–4	3	10.6	5, 10, 15, 20
0.5	Kisker	11	0.5, 0.8, 1.2, 2			10.6	0.5, 0.8, 1.2, 2

each particle size the flow rate was varied while keeping the peak-to-peak voltage applied to the transducer constant.

In the experiments the relative focusability R of the suspended particles, was measured. The relative focusability is defined as the proportion of particles moved by the ultrasound to the center outlet, particles which would otherwise end up in the side outlets if the ultrasound was not turned on. A relative focusability of $R = 1$ therefore corresponds to a recovery of 100% of the particles at the center outlet while a relative focusability of $R = 0$ corresponds to a recovery of $Q_c/(Q_c + Q_s) = 40\%$, where Q_c and Q_s are the flow rates of the center and side outlets, respectively. The 40% recovery corresponds to the fraction of particles that would be obtained at the center outlet when the ultrasound is turned off, depending on the flow split ratio between the center and side outlets.

The transverse focusing velocity u_{rad} due to the acoustic radiation force is proportional to the square of the transducer peak-to-peak voltage U_{pp} and the square of the particle radius a, *i.e.* $u_{rad} \propto {U_{pp}}^2 a^2$.[29] To be able to acquire data for different particle sizes while still maintaining a reasonable flow rate in the system, the applied voltage U_{pp} and therefore the acoustic energy density, was set higher in experiments involving smaller (weakly focusing) particles than in experiments with larger (strongly focusing) particles. To compare the results, the flow rates were normalized with respect to the transverse focusing velocity u_{rad}. The 7 μm particle was used as a normalization reference, as this was the largest particle used in the experiments, and it shows an almost ideal radiation force-dominated motion. The normalized flow rate Q_{norm} in a particular experiments with nominal flow rates Q is thus given by

$$Q_{norm} = Q\frac{(u_{rad})_{7\mu m}}{u_{rad}} = Q\frac{\left({U_{pp}}^2 a^2\right)_{7\mu m}}{{U_{pp}}^2 a^2}. \quad (2)$$

One-dimensional focusing in a channel of rectangular cross-section

The small size of many bioparticles such as bacteria inherently makes them less suitable for acoustic standing wave focusing in microfluidic systems without experiencing severe losses, a problem that is prominent when handling highly dilute species in situations where recoveries of more than 90% are needed.

Fig. 4(a) shows the results of one-dimensional focusing in a rectangular channel (230 μm × 150 μm in cross section) where relatively large polystyrene particles with diameters of 7 μm, 5 μm, and 3 μm (red, purple, and green) could all be focused, with a relative focusability of more than 0.9 ($R = 0.98 \pm 0.10$, 0.93 ± 0.003, and 0.98 ± 0.006, respectively). Throughout the paper, the stated uncertainty in the value of R is the standard deviation of three repeated measurements. The smaller polystyrene particles with diameters of 1 μm and 0.6 μm (blue and turquoise) could not be focused under the given conditions, and the focusability measured was only $R = 0.52 \pm 0.17$ and $R = 0.48 \pm 0.07$, respectively. For these particles, the relative focusability R will not approach unity (*i.e.* improve) as the flow rate is decreased further because of

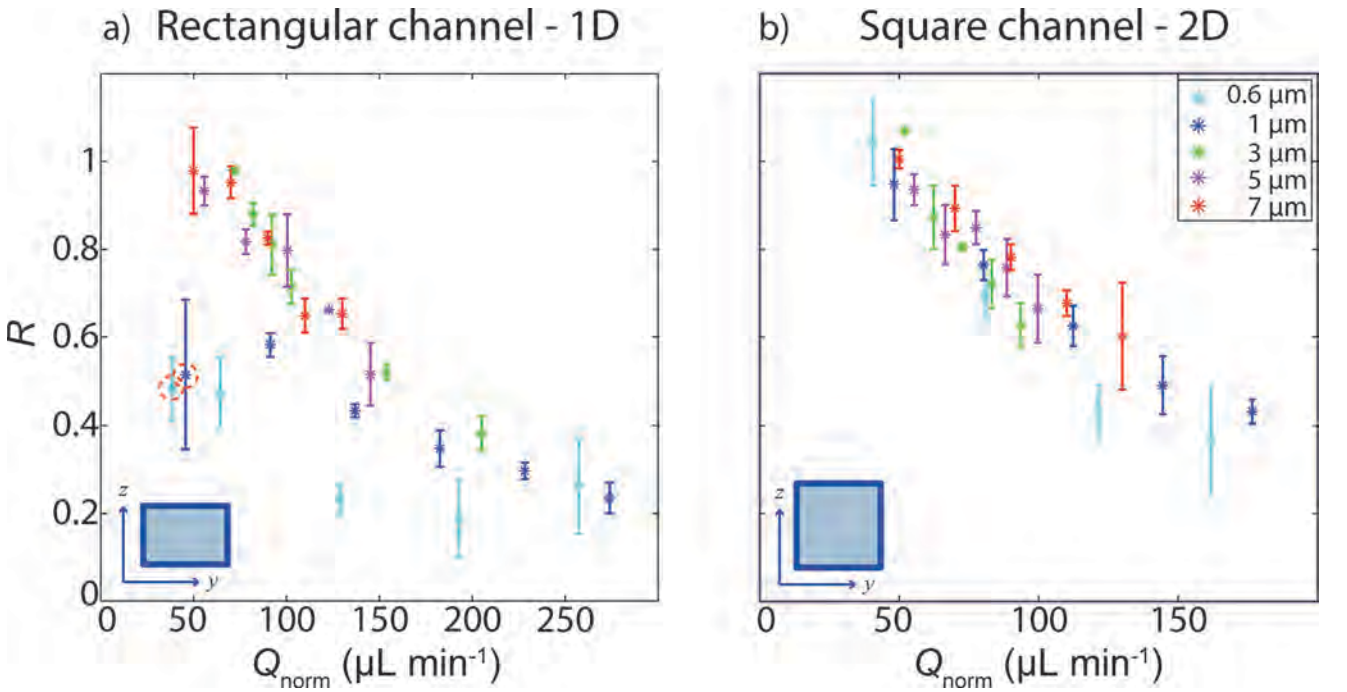

Fig. 4 (a) One-dimensional focusing in the rectangular channel. The relative focusability R plotted against the normalized flow rate Q_{norm}. (b) Two-dimensional single-frequency focusing in the square channel. The relative focusability R plotted against Q_{norm}. All error bars are standard deviations from three repeated measurements. The nominal flow rates for each data point are collected in Table 1.

the acoustic streaming-induced drag force. This is reflected in the saturation of R for the 1 μm and 0.6 μm particles seen for the data points obtained at the two lowest flow rates. The smaller the particle diameter, the more influence the streaming will have in comparison to the primary acoustic radiation force. This is also reflected in the fact that the focusability was generally lower for the 0.6 μm diameter particles than for the 1 μm diameter particles. Increasing the acoustic energy or decreasing the flow rate through the channel will not increase the focusability, since both the acoustic streaming and the acoustic radiation force depend linearly on the acoustic energy density.

For one-dimensional acoustophoretic focusing in this system, the acoustic streaming-induced drag force limits the focusability of particles less than 1.6 μm in diameter. This is caused by the streaming, counteracting the radiation force in the top and bottom regions of the channel, whereby the particles are pushed outwards from the center of the channel instead of inwards.[28] This can be avoided by using two-dimensional focusing, without compromising the channel size or sample throughput, as presented in the following section.

Two-dimensional dual-frequency focusing in a channel of rectangular cross-section

To enable focusing of the particles in the vertical direction as well, a second piezo-ceramic ultrasound transducer was added to the rectangular channel with a half-wavelength matched to the height of the channel. This resulted in a significantly improved focusability of the 1 μm and 0.6 μm particles of $R = 0.87 \pm 0.10$ and $R = 0.92 \pm 0.34$, respectively (Fig. 5). The voltage $U_{pp,2}$ applied to the second transducer was varied at an interval from 0 V to 4 V, while maintaining the settings for the flow rate and voltage of the first transducer in the corresponding one-dimensional focusing experiment at the lowest flow rate, indicated by dashed rings in Fig. 4(a). The relative focusability R increased steadily as the voltage $U_{pp,2}$ approached the maximum achievable in the current system configuration. The increase in the value of R for the small particles demonstrates the benefit of introducing a second orthogonal acoustic standing wave. Increasing the voltage $U_{pp,2}$ above 4 V may result in higher focusability, but it also caused the temperature of the system to rise above the dynamic range of the temperature regulator. An improvement in the focusability of the small particles was seen visually when the flow rate was reduced further.

Two-dimensional single-frequency focusing in a channel of square cross-section

A more straightforward way to generate two-dimensional focusing in an acoustophoresis microchannel is by using a square cross-section geometry. In this way, the same transducer operated at a single frequency can excite both the vertical and horizontal component of the standing waves. Even though the strict square symmetry is broken slightly, *e.g.* due to fabrication inaccuracies, the two resonances can still be

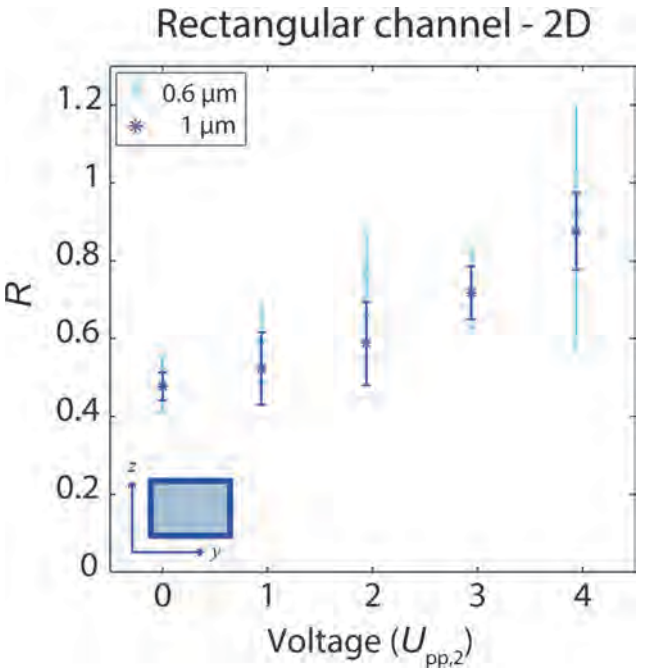

Fig. 5 Two-dimensional dual-frequency focusing in the rectangular channel. The relative focusability R plotted against the voltage $U_{pp,2}$ on the second (5 MHz) piezo transducer focusing the particles vertically in the rectangular channel. The voltage U_{pp} on the first (2 MHz) transducer and the flow rate were kept constant at the same value as used to focus the particles giving the data points surrounded by the dashed red rings in Fig. 4 for the 1 μm (10 μL min^{-1}) and 0.6 μm-particles (3 μL min^{-1}), respectively.

excited simultaneously due to their finite width of approximately 10 kHz.[38]

In the square channel (230 μm × 230 μm in cross section), which supports a two-dimensional resonance, again the large particles with diameters of 7 μm, 5 μm, and 3 μm reached high focusability of $R = 1.01 \pm 0.02$, 0.94 ± 0.04, and 1.07 ± 0.004, respectively (Fig. 4(b)). The smaller particles with diameters of 1 μm and 0.6 μm also reached high focusability ($R = 0.95 \pm 0.08$ and 1.04 ± 0.10, respectively), thus demonstrating improved focusability compared to the one-dimensional focusing experiment. This is evident from the fact that the normalized focusability data for all the different particles now collapsed onto a single line (Fig. 4(b)) as compared to the one-dimensional focusability data (Fig. 4(a)).

The square channel cross section offers a simpler system configuration with only one frequency. In contrast, the rectangular channel required the use of two different piezo-ceramic transducers and therefore of two electronic driving systems (signal generators and power amplifiers), adding both cost and complexity to the system. Also, two transducers complicate the design of the temperature controller and are more likely to cause overheating, leading to a shift in frequency of the acoustic resonance and therefore poor focusing performance.

To investigate the performance of the three systems for particles less than 0.6 μm in diameter, fluorescence

microscopy was employed as these particles were too small to be quantified in the Multisizer 3 Coulter Counter used in this study. Visually, it could be observed that 0.5 μm diameter fluorescent polystyrene particles could be focused in both the square (Fig. 6, Table 2) at 2 μL min^{-1} and the rectangular cross-section channels at 0.5 μL min^{-1} when using two-dimensional focusing (data not shown). When using one-dimensional focusing in the rectangular cross-section channel, the particles could not be completely focused, which is consistent with our previous results. The focusability of 0.24 μm fluorescent particles was also investigated, but these particles could only be seen to stream and they could not be focused in any channel (data not shown), placing the new critical particle diameter somewhere between 0.24 μm and 0.5 μm.

Bacteria focusing

A suspension of *E. coli* was also investigated to evaluate the biological relevance of the systems. The bacteria showed a relative focusability $R = 0.95 \pm 0.35$ in the square channel with two-dimensional focusing, whereas it was only $R = 0.40 \pm 0.13$ in the rectangular channel using one-dimensional focusing (Table 3).

In these experiments, we deliberately kept the concentration of particles and bacteria below 10^9 mL^{-1} to avoid the complication of particle-particle interaction due to hydrodynamic coupling of the particles.[41] Also, in future microbiological applications, the need for bacterial enrichment is most evident in samples with very low concentrations of bacteria. In contrast, previously reported focusing of *E. coli* based on a one-dimensional standing wave used a high sample concentration of 10^{10} mL^{-1}, which caused the bacteria to agglomerate and effectively act as larger particles.[42]

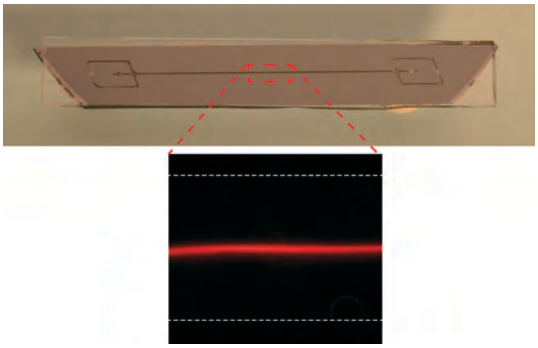

Fig. 6 Fluorescent image of 0.5 μm particles (red) focusing in the square-cross-section channel at a flow rate of 2 μL min^{-1} and at the same voltage as used for the 0.6 μm particles in the square-cross-section channel focusing experiments. The broken gray lines show the edges of the channel.

Table 2 Highest relative focusability achieved for 0.5 μm and 0.6 μm diameter polystyrene particles

Focusing method	Particle	Relative focusability	Flow rate Q
1D rectangle	0.6 μm	0.48 ± 0.07	3 μL min^{-1}
2D rectangle	0.6 μm	0.92 ± 0.34	3 μL min^{-1}
2D square	0.6 μm	1.04 ± 0.1	5 μL min^{-1}
2D square	0.5 μm	1[a]	2 μL min^{-1}
SAW[14,c]	0.5 μm	0.79[b]	1.8 μL min^{-1}
SAW[15]	0.5 μm	1[a]	0.2 μL min^{-1}

[a] No recovery data obtained. Visual focus of particles shown. [b] Recovery, no focusability data available. [c] Device uses a combination of dielectrophoretic and acoustic forces.

Table 3 Highest relative focusability achievable for *E. coli* and 1 μm and 0.6 μm diameter polystyrene particles

Particle	1D rectangular	2D rectangular	2D square
E. coli	0.40 ± 0.13		0.95 ± 0.35
1 μm	0.52 ± 0.17	0.87 ± 0.1	0.95 ± 0.08
0.6 μm	0.48 ± 0.07	0.92 ± 0.34	1.04 ± 0.1

Comparison of the experimental and numerical streaming flow

The experimental data demonstrate that sub-micrometer particles as small as 0.5 μm can be focused using two-dimensional acoustic focusing, which indicates that these systems are dominated by a streaming velocity field similar to that in Fig. 2(d) rather than Fig. 2(c). Importantly, the centred streaming roll derived in Fig. 2(d) has also been observed visually in some parts of the channel (video S1 of ESI†), while other parts appear to be "quieter" (*i.e.* not showing much streaming activity). This is consistent with the assumption that the vibration of the walls most likely changes along the channel. At different positions along the channel, the streaming rolls observed did not all move in the same direction: both clockwise and counter-clockwise streaming rolls were seen. Analogous streaming patterns have also been observed in acoustic resonance cavities with almost square geometry.[43]

Based on the experimental data and the numerical simulation, we hypothesise that the centred streaming roll in combination with two-dimensional focusing is the predominant effect along the full length of the channel, which enables focusing of sub-micrometer particles in the experimental square channel system presented in this paper.

Conclusions

This paper reports the successful use of acoustophoresis to focus sub-micrometer cells and particles. The use of two-dimensional actuation of a square channel was found to enable two-dimensional focusing of *E. coli* and polystyrene particles as small as 0.5 μm in diameter with recovery above 90%, something that could not be achieved using one-dimensional focusing. This sets the experimental limiting particle diameter for continuous-flow half-wavelength resonators operated at about 3 MHz to somewhere between 0.25 μm and 0.5 μm for particles and bacteria with acoustic properties similar to those of polystyrene suspended in water. The focusing of sub-micrometer particles is enabled by a streaming velocity field consisting of a large centered flow roll that does not counteract the weak two-dimensional focusing,

in contrast to the standard quadrupolar flow roll structure generated by a one-dimensional half-wavelength resonance.

The ability to manipulate bacteria and other submicrometer particles in a half-wavelength ultrasound standing wave field opens up the acoustophoresis research field to new applications in microbiology. Future research will concentrate on using the new method to generate systems capable of reducing diagnosis and detection times in the biomedical field, and in environmental and food applications.

Acknowledgements

We thank Åsa Janfalk Carlsson for the kind gift of *E. coli*. The work was supported by the Swedish government agency for innovation systems, Vinnova, CellCARE (grant no. 2009-00236), the Swedish Research Council (grant no. 621-2010-4389 and 2012-6708), the Royal Physiographic Society, the Crafoord Foundation, the Carl Trygger Foundation, and the Danish Council for Independent Research, Technology, and Production Sciences (grant no. 11-107021).

References

1 P. M. Dark, P. Dean and G. Warhurst, *Crit. Care*, 2009, **13**, 217.
2 L. A. Huber, K. Pfaller and I. Vietor, *Circ. Res.*, 2003, **92**, 962–968.
3 C. Pasquali, I. Fialka and L. A. Huber, *J. Chromatogr. B: Biomed. Sci. Appl.*, 1999, **722**, 89–102.
4 C. Lay, C. Y. Teo, L. Zhu, X. L. Peh, H. M. Ji, B.-R. Chew, R. Murthy, H. H. Feng and W.-T. Liu, *Lab Chip*, 2008, **8**, 830–833.
5 L. Zhu, Q. Zhang, H. Feng, S. Ang, F. S. Chau and W.-T. Liu, *Lab Chip*, 2004, **4**, 337–341.
6 D. Chen and H. A. Du, *Microfluid. Nanofluid.*, 2009, **9**, 281–291.
7 B. H. Lapizco-Encinas, B. A. Simmons, E. B. Cummings and Y. Fintschenko, *Anal. Chem.*, 2004, **76**, 1571–1579.
8 S. Bhattacharya, S. Salamat, D. Morisette, P. Banada, D. Akin, Y.-S. Liu, A. K. Bhunia, M. Ladisch and R. Bashir, *Lab Chip*, 2008, **8**, 1130–1136.
9 Z. Wu, B. Willing, J. Bjerketorp, J. K. Jansson and K. Hjort, *Lab Chip*, 2009, **9**, 1193–1199.
10 N. Xia, T. P. Hunt, B. T. Mayers, E. Alsberg, G. M. Whitesides, R. M. Westervelt and D. E. Ingber, *Biomed. Microdevices*, 2006, **8**, 299–308.
11 J. D. Adams, U. Kim and H. T. Soh, *Proc. Natl. Acad. Sci. U. S. A.*, 2008, **105**, 18165–18170.
12 L. R. Huang, E. C. Cox, R. H. Austin and J. C. Sturm, *Science*, 2004, **304**, 987–990.
13 J. Shi, D. Ahmed, X. Mao, S.-C. S. Lin, A. Lawit and T. J. Huang, *Lab Chip*, 2009, **9**, 2890–2895.
14 D. J. Collins, T. Alan and A. Neild, *Lab Chip*, 2014, **14**, 1595–1603.
15 V. Yantchev, J. Enlund, I. Katardjiev and L. A. Johansson, *J. Micromech. Microeng.*, 2010, **20**, 035031.
16 B. Hammarström, T. Laurell and J. Nilsson, *Lab Chip*, 2012, **12**, 4296–4304.
17 T. Laurell, F. Petersson and A. Nilsson, *Chem. Soc. Rev.*, 2007, **36**, 492–506.
18 M. Wiklund, *Lab Chip*, 2012, **12**, 2018–2028.
19 M. A. Burguillos, C. Magnusson, M. Nordin, A. Lenshof, P. Augustsson, M. J. Hansson, E. Elmér, H. Lilja, P. Brundin, T. Laurell and T. Deierborg, *PLoS One*, 2013, **8**, e64233.
20 J. D. Adams, C. L. Ebbesen, R. Barnkob, A. H. J. Yang, H. T. Soh and H. Bruus, *J. Micromech. Microeng.*, 2012, **22**, 075017.
21 A. Ahmad-Tajudin, K. Petersson, A. Lenshof, A.-M. Swärd-Nilsson, L. Åberg, G. Marko-Varga, J. Malm, H. Lilja and T. Laurell, *Lab Chip*, 2013, **13**, 1790–1796.
22 F. Petersson, A. Nilsson, C. Holm, H. Jonsson and T. Laurell, *Analyst*, 2004, **129**, 938–943.
23 A. Lenshof, A. Ahmad-Tajudin, K. Järås, A.-M. K. Swärd-Nilsson, L. Åberg, G. Marko-Varga, J. Malm, H. Lilja and T. Laurell, *Anal. Chem.*, 2009, **81**, 6030–6037.
24 C. Grenvall, P. Augustsson, J. R. Folkenberg and T. Laurell, *Anal. Chem.*, 2009, **81**, 6195–6200.
25 P. Augustsson, C. Magnusson, M. Nordin, H. Lilja and T. Laurell, *Anal. Chem.*, 2012, **84**, 7954–7962.
26 M. Nordin and T. Laurell, *Lab Chip*, 2012, **12**, 4610–4616.
27 S. Radel, A. J. McLoughlin, L. Gherardini, O. Doblhoff-Dier and E. Benes, *Ultrasonics*, 2000, **38**, 633–637.
28 P. B. Muller, R. Barnkob, M. J. H. Jensen and H. Bruus, *Lab Chip*, 2012, **12**, 4617–4627.
29 R. Barnkob, P. Augustsson, T. Laurell and H. Bruus, *Phys. Rev. E: Stat., Nonlinear, Soft Matter Phys.*, 2012, **86**, 056307.
30 M. S. Limaye, J. J. Hawkes and W. T. Coakley, *J. Microbiol. Methods*, 1996, **27**, 211–220.
31 M. Zourob, J. J. Hawkes, W. T. Coakley, B. J. Treves Brown, P. R. Fielden, M. B. McDonnell and N. J. Goddard, *Anal. Chem.*, 2005, **77**, 6163–6168.
32 R. J. Townsend, M. Hill, N. R. Harris and M. B. McDonnell, *Ultrasonics*, 2008, **48**, 515–520.
33 O. Manneberg, J. Svennebring, H. M. Hertz and M. Wiklund, *J. Micromech. Microeng.*, 2008, **18**, 095025.
34 S. Oberti, A. Neild and J. Dual, *J. Acoust. Soc. Am.*, 2007, **121**, 778–785.
35 O. J. E. Jakobsson, C. Grenvall, M. Nordin, M. Evander and T. Laurell, *Lab Chip*, 2014, **14**, 1943–1950.
36 M. Settnes and H. Bruus, *Phys. Rev. E: Stat., Nonlinear, Soft Matter Phys.*, 2012, **85**, 016327.
37 P. B. Muller, M. Rossi, Á. G. Marín, R. Barnkob, P. Augustsson, T. Laurell, C. J. Kähler and H. Bruus, *Phys. Rev. E: Stat., Nonlinear, Soft Matter Phys.*, 2013, **88**, 023006.
38 R. Barnkob, P. Augustsson, T. Laurell and H. Bruus, *Lab Chip*, 2010, **10**, 563–570.
39 G. Gregory and K. Gregory, *J. Acoust. Soc. Am.*, 2005, **117**, 3440–3447.
40 P. Augustsson, R. Barnkob, S. T. Wereley, H. Bruus and T. Laurell, *Lab Chip*, 2011, **11**, 4152–4164.
41 C. Mikkelsen and H. Bruus, *Lab Chip*, 2005, **5**, 1293–1297.
42 J. J. Hawkes, M. S. Limaye and W. T. Coakley, *J. Appl. Microbiol.*, 1997, **82**, 39–47.
43 M. Wiklund, R. Green and M. Ohlin, *Lab Chip*, 2012, **12**, 2438–2451.

Appendix D

Paper published in Physical Review E, October 2014

Numerical study of thermoviscous effects in ultrasound-induced acoustic streaming in microchannels

Peter Barkholt Muller and Henrik Bruus

Abstract: We present a numerical study of thermoviscous effects on the acoustic streaming flow generated by an ultrasound standing-wave resonance in a long straight microfluidic channel containing a Newtonian fluid. These effects enter primarily through the temperature and density dependence of the fluid viscosity. The resulting magnitude of the streaming flow is calculated and characterized numerically, and we find that even for thin acoustic boundary layers, the channel height affects the magnitude of the streaming flow. For the special case of a sufficiently large channel height, we have successfully validated our numerics with analytical results from 2011 by Rednikov and Sadhal for a single planar wall. We analyzed the time-averaged energy transport in the system and the time-averaged second-order temperature perturbation of the fluid. Finally, we have made three main changes in our previously published numerical scheme to improve the numerical performance: (i) The time-averaged products of first-order variables in the time-averaged second-order equations have been recast as flux densities instead of as body forces. (ii) The order of the finite-element basis functions has been increased in an optimal manner. (iii) Based on the International Association for the Properties of Water and Steam (IAPWS 1995, 2008, and 2011), we provide accurate polynomial fits in temperature for all relevant thermodynamic and transport parameters of water in the temperature range from 10 to 50 ℃.

http://dx.doi.org/10.1103/PhysRevE.90.043016

PHYSICAL REVIEW E **90**, 043016 (2014)

Numerical study of thermoviscous effects in ultrasound-induced acoustic streaming in microchannels

Peter Barkholt Muller* and Henrik Bruus†

Department of Physics, Technical University of Denmark, DTU Physics Building 309, DK-2800 Kongens Lyngby, Denmark

(Received 21 August 2014; published 21 October 2014)

We present a numerical study of thermoviscous effects on the acoustic streaming flow generated by an ultrasound standing-wave resonance in a long straight microfluidic channel containing a Newtonian fluid. These effects enter primarily through the temperature and density dependence of the fluid viscosity. The resulting magnitude of the streaming flow is calculated and characterized numerically, and we find that even for thin acoustic boundary layers, the channel height affects the magnitude of the streaming flow. For the special case of a sufficiently large channel height, we have successfully validated our numerics with analytical results from 2011 by Rednikov and Sadhal for a single planar wall. We analyzed the time-averaged energy transport in the system and the time-averaged second-order temperature perturbation of the fluid. Finally, we have made three main changes in our previously published numerical scheme to improve the numerical performance: (i) The time-averaged products of first-order variables in the time-averaged second-order equations have been recast as flux densities instead of as body forces. (ii) The order of the finite-element basis functions has been increased in an optimal manner. (iii) Based on the International Association for the Properties of Water and Steam (IAPWS 1995, 2008, and 2011), we provide accurate polynomial fits in temperature for all relevant thermodynamic and transport parameters of water in the temperature range from 10 to 50 ℃.

DOI: 10.1103/PhysRevE.90.043016 PACS number(s): 47.15.−x, 43.25.Nm, 43.25.+y, 43.35.Ud

I. INTRODUCTION

Ultrasound acoustophoresis has been used to handle particles of a few micrometers to tens of micrometers in microfluidic channels [1], with applications in, e.g., up-concentration of rare samples [2], cell synchronization [3], cell trapping [4], cell patterning [5], cell detachment [6], cell separation [7], and particle rotation [8]. Control and processing of submicrometer bioparticles have many applications in biomedicine and in environmental and food analysis, however acoustophoretic focusing of submicrometer particles by the primary radiation force is hindered by the drag force from the acoustic streaming flow of the suspending liquid. Consequently, there is a need for understanding the acoustic streaming and for developing tools for engineering acoustic streaming patterns that allow for acoustic handling of submicrometer particles.

The theory of acoustic streaming, driven by the time-averaged shear stress near rigid walls in the acoustic boundary layers of a standing wave, was originally described by Lord Rayleigh [9]. It was later extended, among others, by Schlicting [10], Nyborg [11], Hamilton [12,13], and Muller *et al.* [14]. Recently, Rednikov and Sadhal [15] have included the temperature dependence of the dynamic viscosity and shown that this can lead to a significant increase in the magnitude of the streaming velocity. In the present work, we present a numerical study of this and related thermoviscous effects.

A major challenge in numerical modeling of acoustic streaming is the disparate length scales characterizing the bulk of the fluid and the acoustic boundary layer, the latter often being several orders of magnitude smaller than the former in relevant experiments. One way to handle this problem is to determine the first-order oscillatory acoustic field without resolving the acoustic boundary layers, and from this calculate an approximate expression for the time-averaged streaming velocity at the boundary, acting as a boundary condition for the steady bulk streaming [16,17]. This method has the advantage of being computationally less demanding. For example, Lei *et al.* [18,19] used it to model streaming flow in microfluidic channels in three dimensions, and they were able to qualitatively explain several experimental observations of streaming flow in microchannels and flat microfluidics chambers. Another method is the direct numerical solution of the full thermoviscous acoustic equations both in the bulk and in the thin boundary layers, demanding a fine spatial resolution close to rigid surfaces as developed by, e.g., Muller *et al.* [20]. They obtained a quantitative description of the physics of the thermoviscous boundary layers and the acoustic resonance. The same model was later employed in a quantitative comparison between numerics, analytics, and experiments of microparticle acoustophoresis, demonstrating good agreement [14]. In a more recent study, the numerical scheme was further used to demonstrate how simultaneous actuation of the two overlapping half-wavelength resonances of a nearly square channel can generate a single vortex streaming flow that allows for focusing of submicrometer particles, an effect demonstrated experimentally by focusing 0.5-μm − diam particles and *E. coli* bacteria [21].

In this paper, we extend our numerical model for a rectangular microchannel [20] to include the thermoviscous effects, which were treated analytically in the special case of a single planar infinite rigid wall by Rednikov and Sadhal [15]. The extension is done by including the dependence on the oscillatory first-order temperature and density fields

*peter.b.muller@fysik.dtu.dk
†bruus@fysik.dtu.dk

in the dynamic shear viscosity, previously taken to be constant. This has a significant influence on the shear stresses in the thermoviscous boundary layers responsible for generating the steady acoustic streaming. Furthermore, we study the steady temperature rise and energy current densities resulting from solving the time-averaged second-order energy transport equation. Finally, we improve the convergence properties of our previous numerical scheme [20] by implementing the governing equations in a source-free flux formulation and optimizing the order of the basis functions of the finite-element scheme.

II. BASIC THEORY

In this section, we derive the governing equations for the first- and second-order perturbations to the thermoviscous acoustic fields in a compressible Newtonian fluid. We only consider the acoustics in the fluid, and we treat the surrounding walls as ideal hard walls. Our treatment is based on textbook thermodynamics [22] and thermoviscous acoustics [23], but in a source-free flux formulation suitable for our specific numerical implementation. As water is our model fluid of choice, we carefully implement the best available experimental data for the thermodynamic and transport parameters provided by the International Association for the Properties of Water and Steam (IAPWS).

A. Thermodynamics

The independent thermodynamic variables of the compressible Newtonian fluid are taken to be the temperature T and the pressure p [22]. The dependent variables are the mass density ρ, the internal energy ε per mass unit, and the entropy s per mass unit. The first law of thermodynamics is usually stated with s and ρ as the independent variables,

$$d\varepsilon = T\,ds - pd\left(\frac{1}{\rho}\right) = T\,ds + \frac{p}{\rho^2}d\rho. \tag{1a}$$

By a standard Legendre transformation of ε to the Gibbs free energy g per unit mass, $g = \varepsilon - Ts + p\frac{1}{\rho}$, we obtain the first law with T and p as the independent variables,

$$dg = -s\,dT + \frac{1}{\rho}dp. \tag{1b}$$

Due to their importance in thermoacoustics, we furthermore introduce the following three thermodynamics coefficients: the isobaric heat capacity c_p per unit mass, the isobaric thermal expansion coefficient α_p, and the isothermal compressibility κ_T, as

$$c_p = T\left(\frac{\partial s}{\partial T}\right)_p, \tag{2a}$$

$$\alpha_p = -\frac{1}{\rho}\left(\frac{\partial \rho}{\partial T}\right)_p, \tag{2b}$$

$$\kappa_T = \frac{1}{\rho}\left(\frac{\partial \rho}{\partial p}\right)_T. \tag{2c}$$

Moreover, as a standard step toward getting rid of explicit references to the entropy, we derive from Eqs. (1b) and (2b) the following Maxwell relation:

$$\left(\frac{\partial s}{\partial p}\right)_T = -\frac{\partial^2 g}{\partial p \partial T} = -\left(\frac{\partial(\frac{1}{\rho})}{\partial T}\right)_p = -\frac{1}{\rho}\alpha_p. \tag{2d}$$

Using Eqs. (2a)–(2d), we express ds and $d\rho$ in terms of dT and dp,

$$T\,ds = c_p dT - \frac{\alpha_p T}{\rho}dp, \tag{3a}$$

$$\frac{1}{\rho}\,d\rho = \kappa_T dp - \alpha_p dT, \tag{3b}$$

which combined with Eq. (1a) leads to $d\varepsilon$ in terms of dT and dp,

$$\rho\,d\varepsilon = (c_p\rho - \alpha_p p)dT + (\kappa_T p - \alpha_p T)dp. \tag{3c}$$

Using Eqs. (3a)–(3c), small changes ds, $d\rho$, and $d\varepsilon$ in the dependent thermodynamic variables s, ρ, and ε away from equilibrium can thus be expressed in terms of changes in the independent thermodynamic variables T and p. In our numerical analysis, the default unperturbed equilibrium state is the one at ambient temperature $T_0 = 25.0\,^{\circ}\mathrm{C}$ and pressure $p_0 = 0.1013$ MPa.

B. Physical properties of water according to IAPWS

The theoretical treatment of thermoviscous acoustics requires detailed knowledge of the dependence on temperature and density (or temperature and pressure) of the physical properties of the fluid of choice. In the present paper, we use the parameter values for water supplied by the IAPWS in its thorough statistical treatment of large data sets provided by numerous experimental groups [24–26].

The values of the thermodynamic properties are taken from the IAPWS Formulation 1995 [24], the shear viscosity is taken from the IAPWS Formulation 2008 [25], the thermal conductivity is taken from the IAPWS Formulation 2011 [26], while the bulk viscosity is taken from Holmes, Parker, and Povey [27], who extended the work by Dukhin and Goetz [28]. The IAPWS data set spans a much wider range in temperature and ambient pressures than needed in our work, and it is somewhat complicated to handle. Consequently, to ease the access to the IAPWS data in our numerical implementation, we have carefully fitted the temperature dependence of all properties at atmospheric pressure by fifth-order polynomials in temperature in the range from 10 to 50 °C, as described in detail in Appendix A. In the specified range, the differences between our fits and the IAPWS data are negligible. In Table I, we have listed the physical properties of water at ambient temperature and pressure.

The thermodynamic coefficients of Eq. (3) are by definition evaluated at the equilibrium state $T = T_0$ and $p = p_0$, leaving all acoustics perturbations to enter only in the small deviations, e.g., $dT = T_1 + T_2$. On the other hand, the transport coefficients of the fluid depend on the acoustic perturbation. To avoid the ambiguity of the pressure p as either the ambient pressure outside the fluid or the intrinsic pressure (cohesive energy) of the fluid, we use Eq. (3b) to change the variable from pressure p to density ρ in our treatment of the IAPWS

TABLE I. IAPWS parameter values for pure water at ambient temperature 25°C and pressure 0.1013 MPa. For references, see Appendix A.

Parameter	Symbol	Value	Unit
Thermodynamic parameters:			
Mass density	ρ	9.970×10^{2}	kg m^{-3}
Heat capacity	c_p	4.181×10^{3}	J kg^{-1}K^{-1}
Speed of sound	c_s	1.497×10^{3}	m s^{-1}
Compressibility	κ_T	4.525×10^{-10}	Pa^{-1}
Thermal expansion	α_p	2.573×10^{-4}	K^{-1}
Heat capacity ratio	γ	1.011×10^{0}	
Transport parameters:			
Shear viscosity	η	8.900×10^{-4}	Pa s
Bulk viscosity	η^{b}	2.485×10^{-3}	Pa s
Thermal conductivity	k^{th}	6.065×10^{-1}	W m^{-1} K^{-1}
Thermodynamic derivatives:			
	$\frac{1}{\eta}\frac{\partial \eta}{\partial T}$	-2.278×10^{-2}	K^{-1}
	$\frac{1}{\eta}\frac{\partial \eta}{\partial \rho}$	-3.472×10^{-4}	kg^{-1} m^{3}
	$\frac{1}{\eta^{\mathrm{b}}}\frac{\partial \eta^{\mathrm{b}}}{\partial T}$	-2.584×10^{-2}	K^{-1}
	$\frac{1}{k^{\mathrm{th}}}\frac{\partial k^{\mathrm{th}}}{\partial T}$	2.697×10^{-3}	K^{-1}
	$\frac{1}{k^{\mathrm{th}}}\frac{\partial k^{\mathrm{th}}}{\partial \rho}$	2.074×10^{-3}	kg^{-1}m^{3}

data. To first order in the acoustic perturbation, we thus write the dynamic shear viscosity η, the bulk (second) viscosity η^{b}, and the thermal conductivity k^{th} as

$$\eta(T,\rho) = \eta_0(T_0,\rho_0) + \eta_1(T_0,T_1,\rho_0,\rho_1), \tag{4a}$$

$$\eta_1 = \left(\frac{\partial \eta}{\partial T}\right)_{T=T_0} T_1 + \left(\frac{\partial \eta}{\partial \rho}\right)_{\rho=\rho_0} \rho_1, \tag{4b}$$

$$\eta^{\mathrm{b}}(T,\rho) = \eta^{\mathrm{b}}_0(T_0,\rho_0) + \eta^{\mathrm{b}}_1(T_0,T_1,\rho_0,\rho_1), \tag{4c}$$

$$\eta^{\mathrm{b}}_1 = \left(\frac{\partial \eta^{\mathrm{b}}}{\partial T}\right)_{T=T_0} T_1 + \left(\frac{\partial \eta^{\mathrm{b}}}{\partial \rho}\right)_{\rho=\rho_0} \rho_1, \tag{4d}$$

$$k^{\mathrm{th}}(T,\rho) = k^{\mathrm{th}}_0(T_0,\rho_0) + k^{\mathrm{th}}_1(T_0,T_1,\rho_0,\rho_1), \tag{4e}$$

$$k^{\mathrm{th}}_1 = \left(\frac{\partial k^{\mathrm{th}}}{\partial T}\right)_{T=T_0} T_1 + \left(\frac{\partial k^{\mathrm{th}}}{\partial \rho}\right)_{\rho=\rho_0} \rho_1. \tag{4f}$$

For the acoustic amplitudes used in this model, the maximum relative perturbations, such as $|\eta_1|/\eta_0$, due to the temperature dependence of the transport coefficients, are 0.33%, 0.53%, and 0.034% for η, η^{b}, and k^{th}, respectively, and the perturbations due to the density dependence are 0.37% and 0.82% for η and k^{th}, respectively. We could not find any literature on the density dependence of η^{b} of water.

C. Governing equations

Besides the above thermodynamic relations, the governing equations of thermoviscous acoustics requires the introduction of the velocity field $\boldsymbol{v}$ of the fluid as well as the stress tensor $\boldsymbol{\sigma}$, which is given as [29]

$$\boldsymbol{\sigma} = -p\mathbf{1} + \boldsymbol{\tau}, \tag{5a}$$

$$\boldsymbol{\tau} = \eta[\nabla \boldsymbol{v} + (\nabla \boldsymbol{v})^{\mathrm{T}}] + \left[\eta^{\mathrm{b}} - \tfrac{2}{3}\eta\right](\nabla \cdot \boldsymbol{v})\mathbf{1}. \tag{5b}$$

Here, $\mathbf{1}$ is the unit tensor, and the superscript "T" indicates tensor transposition.

Mass conservation implies that the rate of change $\partial_t \rho$ of the density in a test volume with surface normal vector $\boldsymbol{n}$ is given by the influx (direction $-\boldsymbol{n}$) of the mass current density $\rho\boldsymbol{v}$. In differential form by Gauss's theorem, it is

$$\partial_t \rho = \nabla \cdot [-\rho \boldsymbol{v}]. \tag{6a}$$

Similarly, momentum conservation implies that the rate of change $\partial_t(\rho\boldsymbol{v})$ of the momentum density in the same test volume is given by the stress forces $\boldsymbol{\sigma}$ acting on the surface (with normal $\boldsymbol{n}$), and the influx (direction $-\boldsymbol{n}$) of the momentum current density $\rho\boldsymbol{v}\boldsymbol{v}$. In differential form, neglecting body forces $\boldsymbol{f}$, this becomes

$$\partial_t(\rho \boldsymbol{v}) = \nabla \cdot [\boldsymbol{\tau} - p\mathbf{1} - \rho \boldsymbol{v}\boldsymbol{v}]. \tag{6b}$$

Finally, energy conservation implies that the rate of change $\partial_t(\rho\varepsilon + \frac{1}{2}\rho v^2)$ of the energy density (internal plus kinetic) is given by the power of the stress forces $\boldsymbol{v}\cdot\boldsymbol{\sigma}$ on the surface (direction $\boldsymbol{n}$), and the influx (direction $-\boldsymbol{n}$) of both heat conduction power $-k^{\mathrm{th}}\nabla T$ and energy current density $(\rho\varepsilon + \frac{1}{2}\rho v^2)\boldsymbol{v}$. In differential form, neglecting heat sources in the volume, this becomes

$$\partial_t\left(\rho\varepsilon + \tfrac{1}{2}\rho v^2\right) = \nabla \cdot \left[\boldsymbol{v}\cdot\boldsymbol{\tau} - p\boldsymbol{v} + k^{\mathrm{th}}\nabla T - \rho\left(\varepsilon + \tfrac{1}{2}v^2\right)\boldsymbol{v}\right]. \tag{6c}$$

D. First-order equations of thermoviscous acoustics

The homogeneous, isotropic quiescent state (thermal equilibrium) is taken to be the zeroth-order state in the acoustic perturbation expansion. Following standard first-order perturbation theory, all fields g are written in the form $g = g_0 + g_1$, for which g_0 is the value of the zeroth-order state and g_1 is the acoustic perturbation, which must be much smaller than g_0. In our work, $|g_1|/g_0 \lesssim 10^{-3}$ [20]. We assume that the acoustic perturbations g_1 are oscillating harmonically with the angular frequency ω of the acoustic actuation,

$$g_1(\boldsymbol{r},t) = g_1(\boldsymbol{r})e^{-i\omega t}, \quad \partial_t g_1 = -i\omega g_1. \tag{7}$$

For the velocity, the value of the zeroth-order state is $\boldsymbol{v}_0 = \mathbf{0}$, and thus $\boldsymbol{v} = \boldsymbol{v}_1$. The zeroth-order terms solve the governing equations for the zeroth-order state and thus drop out of the equations. Keeping only first-order terms, we obtain the first-order equations.

The continuity Eq. (6a) becomes

$$\partial_t \rho_1 = -\rho_0 \nabla \cdot \boldsymbol{v}_1, \tag{8a}$$

which, by using Eq. (3b) in the form

$$\rho_1 = \rho_0[\kappa_T\, p_1 - \alpha_p\, T_1], \tag{8b}$$

is rewritten as

$$\alpha_p\, \partial_t T_1 - \kappa_T\, \partial_t p_1 = \nabla \cdot \boldsymbol{v}_1. \tag{8c}$$

The momentum Eq. (6b) likewise becomes

$$\rho_0 \partial_t \boldsymbol{v}_1 = \boldsymbol{\nabla} \cdot [\boldsymbol{\tau}_1 - p_1 \mathbf{1}], \tag{9a}$$

where $\boldsymbol{\tau}_1$ is given by

$$\boldsymbol{\tau}_1 = \eta_0[\boldsymbol{\nabla} \boldsymbol{v}_1 + (\boldsymbol{\nabla} \boldsymbol{v}_1)^{\mathrm{T}}] + \left[\eta_0^{\mathrm{b}} - \tfrac{2}{3}\eta_0\right](\boldsymbol{\nabla} \cdot \boldsymbol{v}_1)\,\mathbf{1}. \tag{9b}$$

The energy Eq. (6c) requires a little more work. To begin with, it can be written as

$$\rho_0 \partial_t \varepsilon_1 + \varepsilon_0 \partial_t \rho_1 = k_0^{\mathrm{th}} \nabla^2 T_1 - p_0 \boldsymbol{\nabla} \cdot \boldsymbol{v}_1 - \varepsilon_0 \rho_0 \boldsymbol{\nabla} \cdot \boldsymbol{v}_1. \tag{10a}$$

The two terms containing ε_0 cancel out due to the continuity Eq. (8a), and the term $\rho_0 \partial_t \varepsilon_1$ is rewritten using Eq. (1a), whereby

$$\rho_0 T_0 \partial_t s_1 + \frac{p_0}{\rho_0}\, \partial_t \rho_1 = k_0^{\mathrm{th}} \nabla^2 T_1 - p_0 \boldsymbol{\nabla} \cdot \boldsymbol{v}_1. \tag{10b}$$

The two terms containing p_0 cancel out due to the continuity Eq. (8a), and the term $\rho_0 T_0 \partial_t s_1$ is rewritten using the time derivative of Eq. (3a). This leads to

$$\rho_0 c_p\, \partial_t T_1 - \alpha_p T_0\, \partial_t p_1 = k_0^{\mathrm{th}} \nabla^2 T_1. \tag{10c}$$

Equations (8c), (9a), and (10c) are the resulting first-order thermoviscous equations for conservation of mass, momentum, and energy, respectively. In the frequency domain, they become

$$-i\omega\alpha_p\, T_1 + i\omega\kappa_T\, p_1 = \boldsymbol{\nabla} \cdot \boldsymbol{v}_1, \tag{11a}$$

$$-i\omega\rho_0\, \boldsymbol{v}_1 = \boldsymbol{\nabla} \cdot [\boldsymbol{\tau}_1 - p_1 \mathbf{1}], \tag{11b}$$

$$-i\omega\rho_0 c_p\, T_1 + i\omega\alpha_p T_0\, p_1 = k_0^{\mathrm{th}} \nabla^2 T_1. \tag{11c}$$

From Eqs. (11b) and (11c), neglecting the pressure terms, we can derive the length scales δ_{s} and δ_{t} for diffusion of momentum and heat, respectively,

$$\delta_{\mathrm{s}} = \sqrt{\frac{2\eta_0}{\rho_0\omega}} = \sqrt{\frac{2\nu}{\omega}} = 0.38\ \mu\mathrm{m}, \tag{12a}$$

$$\delta_{\mathrm{t}} = \sqrt{\frac{2k_0^{\mathrm{th}}}{\rho_0 c_p \omega}} = \sqrt{\frac{2D_{\mathrm{th}}}{\omega}} = 0.15\ \mu\mathrm{m}, \tag{12b}$$

where the subscript "s" indicates shear stress, subscript "t" indicates thermal, and $\nu = \eta_0/\rho_0$ and $D_{\mathrm{th}} = k^{\mathrm{th}}/(\rho_0 c_p)$ are the momentum and thermal diffusivities with numerical values derived from the parameter values at ambient temperature and pressure listed in Table I.

E. Second-order time-averaged equations of thermoviscous acoustics

Moving on to second-order perturbation theory, writing the fields as $g = g_0 + g_1 + g_2$, we note that the second-order acoustic perturbation g_2 may contain both oscillating terms and a time-constant term. The time averaging over one oscillation period of a field $g(t)$ is denoted $\langle g \rangle$. We note that all full time derivatives average to zero, $\langle \partial_t g(t) \rangle = 0$, and that in our work $|g_2|/|g_1| \lesssim 10^{-3}$.

In the following, all pure second-order fields are taken to be time-averaged and thus written plainly as g_2 without the angled brackets. With this notation, the second-order time-averaged continuity Eq. (6a) becomes

$$\boldsymbol{\nabla} \cdot [\rho_0 \boldsymbol{v}_2 + \langle \rho_1 \boldsymbol{v}_1 \rangle] = 0, \tag{13}$$

while the momentum Eq. (6b) takes the form

$$\boldsymbol{\nabla} \cdot [\boldsymbol{\tau}_2 - p_2 \mathbf{1} - \rho_0 \langle \boldsymbol{v}_1 \boldsymbol{v}_1 \rangle] = \mathbf{0}, \tag{14a}$$

where $\boldsymbol{\tau}_2$ is given by

$$\boldsymbol{\tau}_2 = \eta_0[\boldsymbol{\nabla} \boldsymbol{v}_2 + (\boldsymbol{\nabla} \boldsymbol{v}_2)^{\mathrm{T}}] + \left[\eta_0^{\mathrm{b}} - \tfrac{2}{3}\eta_0\right](\boldsymbol{\nabla} \cdot \boldsymbol{v}_2)\,\mathbf{1} + \langle \eta_1[\boldsymbol{\nabla} \boldsymbol{v}_1 + (\boldsymbol{\nabla} \boldsymbol{v}_1)^{\mathrm{T}}] \rangle + \left\langle \left[\eta_1^{\mathrm{b}} - \tfrac{2}{3}\eta_1\right](\boldsymbol{\nabla} \cdot \boldsymbol{v}_1)\,\mathbf{1} \right\rangle. \tag{14b}$$

It is in the two last terms that the first-order temperature and density dependence of the viscosities come into play through the perturbations η_1 and η_1^{b}. Note that the second-order temperature perturbation does not enter the governing equations for $\boldsymbol{v}_2$. Note also that both shear-induced (Rayleigh) streaming and bulk-absorption-induced Eckart streaming are included through the shear and bulk viscosity η and η^{b}, respectively.

The energy Eq. (6c) in its second-order time-averaged form is initially written as

$$\boldsymbol{\nabla} \cdot \left[\langle \boldsymbol{v}_1 \cdot \boldsymbol{\tau}_1 \rangle + k_0^{\mathrm{th}} \boldsymbol{\nabla} T_2 + \left\langle k_1^{\mathrm{th}} \boldsymbol{\nabla} T_1 \right\rangle - p_0\, \boldsymbol{v}_2 - \langle p_1 \boldsymbol{v}_1 \rangle - \varepsilon_0 \rho_0 \boldsymbol{v}_2 - \varepsilon_0 \langle \rho_1 \boldsymbol{v}_1 \rangle - \rho_0 \langle \varepsilon_1 \boldsymbol{v}_1 \rangle \right] = 0. \tag{15a}$$

The two terms with ε_0 cancel due to the continuity Eq. (13). Next, using Eq. (1a), we obtain the expression $\rho_0 \varepsilon_1 = \rho_0 T_0 s_1 + (p_0/\rho_0)\rho_1$, which upon insertion into Eq. (15a) leads to

$$\boldsymbol{\nabla} \cdot \left[\langle \boldsymbol{v}_1 \cdot \boldsymbol{\tau}_1 \rangle + k_0^{\mathrm{th}} \boldsymbol{\nabla} T_2 + \left\langle k_1^{\mathrm{th}} \boldsymbol{\nabla} T_1 \right\rangle - p_0\, \boldsymbol{v}_2 - \langle p_1 \boldsymbol{v}_1 \rangle - \rho_0 T_0 \langle s_1 \boldsymbol{v}_1 \rangle - \frac{p_0}{\rho_0} \langle \rho_1 \boldsymbol{v}_1 \rangle \right] = 0. \tag{15b}$$

The two p_0 terms cancel by the continuity Eq. (13). Then, from Eq. (3a) we find $\rho_0 T_0 s_1 = \rho_0 c_p\, T_1 - \alpha_p T_0\, p_1$, which by substitution into Eq. (15b) yields

$$\boldsymbol{\nabla} \cdot \left[k_0^{\mathrm{th}} \boldsymbol{\nabla} T_2 + \left\langle k_1^{\mathrm{th}} \boldsymbol{\nabla} T_1 \right\rangle + \langle \boldsymbol{v}_1 \cdot \boldsymbol{\tau}_1 \rangle - (1 - \alpha_p T_0) \langle p_1 \boldsymbol{v}_1 \rangle - \rho_0 c_p \langle T_1 \boldsymbol{v}_1 \rangle \right] = 0. \tag{15c}$$

Equations (13), (14a), and (15c) are the resulting time-averaged second-order thermoviscous acoustic equations for conservation of mass, momentum, and energy, respectively.

The time-averaged acoustic energy density E_{ac} in the fluid is given by [23]

$$E_{\mathrm{ac}} = \tfrac{1}{2}\kappa_s \left\langle p_1^2 \right\rangle + \tfrac{1}{2}\rho_0 \left\langle v_1^2 \right\rangle, \tag{16}$$

where $\kappa_s = \kappa_T/\gamma$ is the isentropic compressibility and $\gamma = c_p/c_V$ is the ratio of specific heat capacities.

For a product of two time-harmonic fields in the complex-valued representation Eq. (7), the time average can be

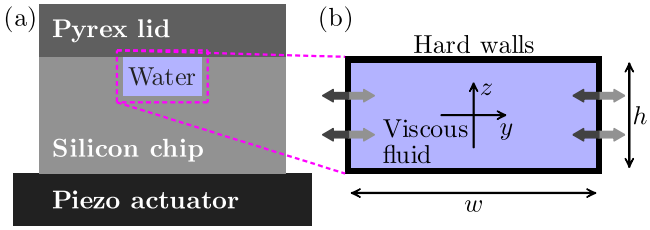

FIG. 1. (Color online) (a) Sketch of a physical acoustophoresis setup with a silicon microfluidic chip on top of a piezoactuator such as in Ref. [30]. (b) Sketch of the model system for the numerical scheme with the viscous fluid domain surrounded by hard walls. The thick arrows indicate in-phase oscillating displacement of the left and right walls. By default, we set the width $w = 380\ \mu$m and the height $h = 160\ \mu$m as in Ref. [30].

calculated as

$$\langle \rho_1(\boldsymbol{r},t)\, \boldsymbol{v}_1(\boldsymbol{r},t)\rangle = \tfrac{1}{2}\,\mathrm{Re}[\rho_1(\boldsymbol{r},0)\, \boldsymbol{v}_1^*(\boldsymbol{r},0)], \qquad (17)$$

where the asterisk denote complex conjugation.

III. NUMERICAL MODEL

The numerical scheme solves the governing equations for the acoustic field inside the two-dimensional water domain of a rectangular microchannel cross section, whereas the vibrations in the surrounding chip material and piezotransducer are not modeled. The water domain is surrounded by immovable hard walls, and the acoustic field is excited by oscillating velocity boundary conditions, representing an oscillating nm-sized displacement of the walls. A sketch of the physical system and the numerical model is shown in Fig. 1.

A. Governing equations

The governing equations are solved using the commercial software COMSOL MULTIPHYSICS [31]. To achieve greater flexibility, the equations are implemented through mathematics-weak-form-PDE modules and not through the built-in modules for acoustics and fluid mechanics. In contrast to our previous work [20], the second-order Eqs. (13), (14a), and (15c) are implemented in the flux density formulation, which by partial integration avoids the less accurate second-order derivatives appearing in the body-force formulation. To fix the numerical solution for the second-order mass and momentum conservation equations, the spatial average of the second-order pressure is forced to be zero by a Lagrange multiplier.

B. Boundary conditions

The first-order acoustic fields are solved in the frequency domain for a driven system, in which energy is added to the system by an oscillating velocity boundary condition and lost by thermal conduction through the walls. The walls are modeled as hard thermal conductors with infinite acoustic impedance and infinite thermal diffusivity. This approximation is reasonable given the parameter values listed in Table II. In the numerical model, this is implemented by zero velocity and ambient temperature at the walls,

TABLE II. Acoustic impedance and thermal diffusivity for water, silicon, and Pyrex glass at room-temperature values from Ref. [29].

Material	Acoustic impedance (10^6 kg m^{-2}s^{-1})	Thermal diffusivity (10^{-7} m^{2}s^{-1})
Water	1.5	1.4
Silicon	20	920
Pyrex glass	17	6.3

$$T = T_0 \quad \text{on all walls,} \qquad (18a)$$

$$\boldsymbol{v} = \boldsymbol{0} \quad \text{on all walls,} \qquad (18b)$$

$$\boldsymbol{n}\cdot\boldsymbol{v}_1 = v_{\mathrm{bc}}(y,z)e^{-i\omega t} \text{ added to actuated walls,} \qquad (18c)$$

$$\boldsymbol{n}\cdot\boldsymbol{v}_2 = -\left\langle \frac{\rho_1}{\rho_0}(\boldsymbol{n}\cdot\boldsymbol{v}_1)\right\rangle \text{ added to actuated walls.} \qquad (18d)$$

Here, $\boldsymbol{n}$ is the outward pointing surface normal, and Eq. (18d) ensures zero mass flux across the boundary. With the fixed temperature at the channel boundaries, we focus on the thermal properties of the acoustic effects, and we do not model any effects of heat generated by the piezotransducer. In the related experiments, the chip and the piezotransducer are thermally stabilized by a Peltier cooling element beneath the piezotransducer, which keeps the chip at a constant temperature using a temperature sensor and a PID controller; see Ref. [30] for a detailed explanation.

It is not trivial how to apply the oscillating velocity boundary condition. In our model, we wish to excite the horizontal half-wavelength resonance, which at the top and bottom walls leads to viscous boundary layers and the generation of streaming flow. To avoid direct influence on this flow from the actuation, we therefore choose to actuate only the left and right walls at $y = \pm w/2$. Moreover, an optimal coupling to the half-wavelength resonance is obtained by choosing the proper symmetry of the actuation, and therefore in terms of the components v_{y1} and v_{z1}, the boundary condition on $\boldsymbol{v}_1$ becomes

$$v_{y1}\left(\pm\frac{w}{2},z\right) = v_{\mathrm{bc}}e^{-i\omega t}, \qquad v_{z1}\left(\pm\frac{w}{2},z\right) = 0, \qquad (19)$$

where $v_{\mathrm{bc}} = \omega d$ is the amplitude of the actuation in terms of the displacement d, with $d = 0.1$ nm in all simulations. This velocity boundary condition is well defined and yields results consistent with experiments [14].

C. Convergence analysis

The weak form equations along with the boundary conditions are solved on a two-dimensional triangular mesh using the finite-element method; see Fig. 2. The resolution of the physical field is determined by the spatial resolution of the mesh and the polynomial order of the basis functions used to represent the field in each node in the mesh. To test the validity of the numerical model, we first check that the numerical solution has converged, i.e., ensuring that further refining of the mesh does not change the solution significantly.

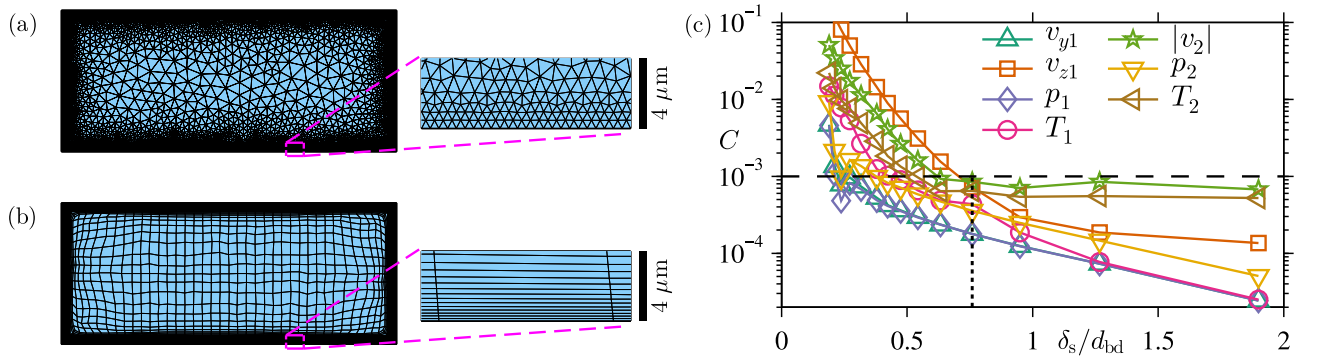

FIG. 2. (Color online) (a) The used triangular mesh with a gradually increasing element size from 0.5 μm at the boundaries to 20 μm in the bulk. This mesh, chosen as the default mesh, contains 30 246 elements. (b) Rectangular mesh with thin elongated 0.1-μm-by-10-μm elements at the boundaries and gradually changing to nearly square 10-μm-by-10-μm elements in the bulk. This mesh contains 3308 elements. (c) The convergence parameter C of Eq. (20) for all first- and second-order fields vs the numerical resolution defined by δ_s/d_{bd}, where d_{bd} is the mesh-element size at the boundary. The fields are solved on triangular meshes with different boundary element sizes but all with fixed bulk element size $d_{bk} = 20$ μm and growth rate $\alpha = 1.3$, while the reference solution is calculated for $d_{bd} = 0.15$ μm, $d_{bk} = 2$ μm, and $\alpha = 1.3$. The vertical dotted line indicates the solution for $d_{bd} = 0.5$ μm, which is chosen as the default value for the following simulations.

Due to the very different length scales of the channel dimensions and the boundary layer thickness an inhomogeneous mesh is necessary, and thus there is a number of ways to refine the mesh. We used three parameters: maximum mesh-element size at the boundaries d_{bd}, maximum mesh-element size in the bulk d_{bk}, and the maximum mesh-element growth rate α (maximum relative size of neighboring elements). The convergence of the fields was considered through the relative convergence parameter $C(g)$ defined in Ref. [20] by

$$C(g) = \sqrt{\frac{\int (g - g_{ref})^2 \, dy \, dz}{\int (g_{ref})^2 \, dy \, dz}}, \tag{20}$$

where $C(g)$ is the relative convergence of a solution g with respect to a reference solution g_{ref}. Convergence graphs for all fields as a function of d_{bd} are shown in Fig. 2(c). The mesh parameters for the reference solution are $d_{bd} = 0.15$ μm, $d_{bk} = 2$ μm, and $\alpha = 1.3$, whereas other solutions for given d_{bd} use $d_{bk} = 20$ μm and $\alpha = 1.3$. The basis functions for the first- and second-order velocity and temperature fields are all fourth order, while for the first- and second-order pressure they are third order. All fields exhibit good convergence, and we choose $C = 10^{-3}$ as our convergence criterion in the following. The corresponding default triangular mesh has $d_{bd} = 0.5$ μm; see Fig. 2(a). In Fig. 2(b), a mesh is shown with rectangular mesh elements that are nearly square in the bulk of the channel while very elongated near the walls. This mesh has been used for testing purposes as it contains approximately ten times fewer mesh elements compared to the default triangular mesh, and the resulting fields all show convergence parameters below $C = 10^{-3}$ with respect to the triangular reference mesh. All results have been calculated using the triangular mesh, but the square mesh provides a huge advantage regarding calculation speed and memory requirement.

IV. RESULTS

A. Resonance analysis

To determine the acoustic resonance frequency f_{res} corresponding to the horizontal half-wavelength resonance, we sweep the actuation frequency around the ideal frequency $f_0 = c_s/2w$, corresponding to the half-wavelength match $\lambda/2 = w$, and we calculate the acoustic energy density Eq. (16), shown in Fig. 3. The resonance frequency f_{res} is shifted slightly with respect to the ideal frequency f_0 due to the viscous loss in the boundary layers. This loss also determines the width of the resonance curve and thus the Q value of the acoustic cavity.

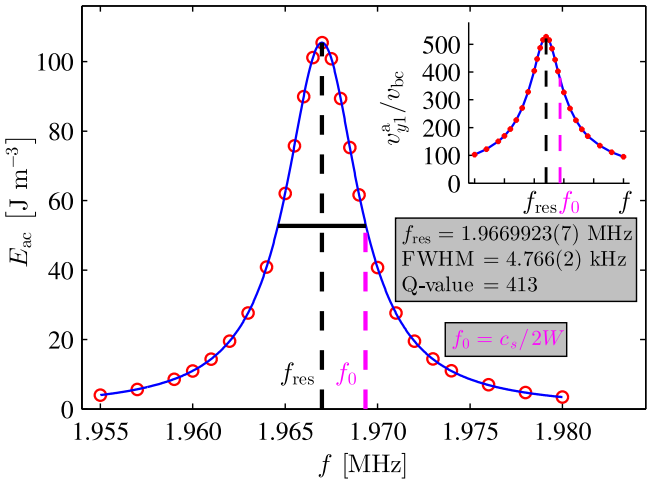

FIG. 3. (Color online) Graph of the acoustic energy density E_{ac} Eq. (16) as a function of the frequency f of the oscillating boundary condition. f_{res} is the resonance frequency at the center of the peak, while f_0 is the ideal frequency corresponding to matching a half-wavelength with the channel width. The inset shows the magnitude of the resonant oscillating first-order velocity field v_{y1}^a relative to the amplitude of the oscillating velocity boundary condition v_{bc} as a function of the actuation frequency f.

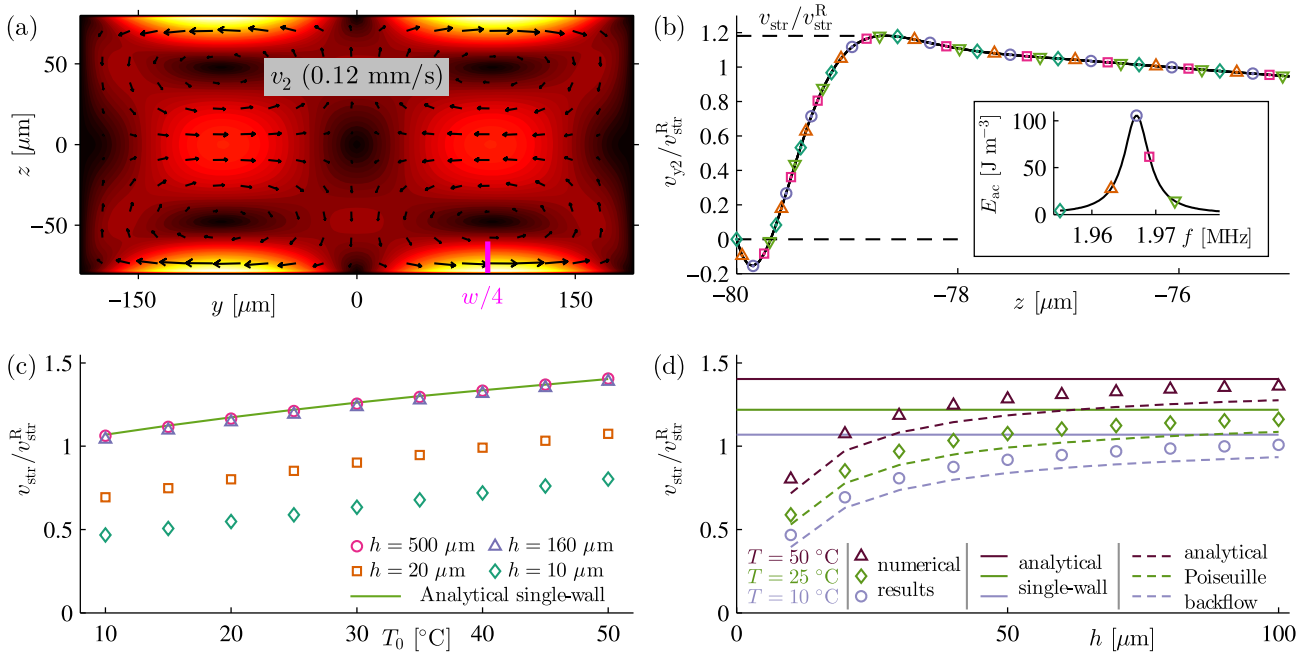

FIG. 4. (Color online) (a) Time-averaged second-order fluid velocity field $\boldsymbol{v}_2$ (vectors) and its magnitude [color plot ranging from 0 mm/s (black) to 0.13 mm/s (white)] in the vertical channel cross section calculated at $T_0 = 25$ ℃ and $f_{res} = 1.966\,992\,3$ MHz. (b) The horizontal velocity component v_{y2} plotted along $y = w/4$ indicated by the magenta line in (a). The velocity field has been calculated for the five actuation frequencies shown in the inset resonance curve, and normalized to the analytical Rayleigh streaming magnitude $v_{str}^R = (3/8)(v_{y1}^a)^2/c_s$, which is calculated based on the corresponding first-order solutions. The symbols are plotted in selected points illustrating the five numerical solutions (black lines) that coincide. (c) Normalized streaming magnitude v_{str}/v_{str}^R (symbols) vs equilibrium temperature T_0, calculated for different channel heights h. The full curve shows the analytical single-wall result by Ref. [15]. (d) Normalized streaming magnitude v_{str}/v_{str}^R (symbols) vs channel height h, calculated for different equilibrium temperatures T_0. The full curves show the analytical single-wall result by Ref. [15], while the dashed lines show the results of a one-dimensional analytical model with a Poiseuille backflow; see Eq. (21).

B. Time-averaged second-order velocity

The time-averaged second-order velocity field $\boldsymbol{v}_2$ is shown in Fig. 4(a), calculated for the default 380-μm-by-160-μm rectangular geometry, at $T_0 = 25$℃, and at the resonance frequency $f_{res} = 1.966\,992\,3$ MHz. It exhibits the well-known pattern of four flow rolls each $\lambda/4$ wide. To investigate the magnitude of the streaming velocity, Fig. 4(b) shows the velocity along a line perpendicular to the bottom wall at $y = w/4$. The streaming velocity field has been calculated for five different frequencies shown in the inset resonance curve. The streaming velocities have been normalized to the classical result by Lord Rayleigh for the magnitude of the acoustic streaming $v_{str}^R = (3/8)(v_{y1}^a)^2/c_s$, where v_{y1}^a is taken from the corresponding first-order solutions. The five numerical solutions (black lines) coincide completely, showing that the rescaled second-order velocity field is the same for off-resonance actuation frequencies. This is important for our further analysis, as we do not need to determine the exact resonance frequency as it changes due to variations in temperature T_0 and channel height h. The magnitude of the streaming velocity v_{str} is determined by the maximum value of v_{y2} along the line $y = w/4$ as indicated in Fig. 4(b).

In Fig. 4(c), we show the normalized magnitude of the streaming velocity v_{str}/v_{str}^R versus the equilibrium temperature T_0. The streaming velocity has been calculated for different channel heights indicated by different colors and symbols. The full line is the analytical single-wall solution by Rednikov and Sadhal [15] for a standing acoustic wave parallel to a single planar wall. For all channel heights, the streaming velocity shows an almost linear dependence with positive slope on the equilibrium temperature. The numerical results for the tall channel $h = 500$ μm agree well with the analytical single-wall prediction, while for more shallow channels the streaming velocity is significantly lower. At 25 ℃, the streaming velocity is 19% larger than the classical Rayleigh result, while for 50 ℃ this deviation has increased to 39%.

To elaborate on the dependence of the streaming velocity on the height of the channel, we plot in Fig. 4(d) the normalized streaming velocity versus the channel height for three equilibrium temperatures. The numerical results are shown by symbols, while the analytical single-wall predictions for each temperature are shown by full lines. The numerical results for the rectangular channel deviate from the analytical single-wall prediction as the channel height is decreased. To qualitatively explain this deviation, we make a simple one-dimensional analytical model along the z dimension of the rectangular channel in which we impose a boundary-driven flow. The first part of the model is a plug flow with an exponential dependence close to the wall, $v_{plug}(z) = v_0\{1 - \exp[-(z + h/2)/\delta_s]\}$ for $-h/2 < z < 0$. This approximates the z dependence of the streaming velocity field inside the viscous boundary layer, where v_0 corresponds to the analytical single-wall solution [15]. As the water is pushed toward the sidewall, a pressure

builds up and a Poiseuille backflow is established, which by mass conservation and no-slip boundary conditions becomes $v_{\mathrm{poi}}(z) \approx -v_0\{6(1/4 - z^2/h^2)\}$. By a first-order Taylor expansion of $v_{\mathrm{poi}}(z)$ at the wall $z = -h/2$, we can determine the maximum v_{str} of $v_{\mathrm{plug}}(z) + v_{\mathrm{poi}}(z)$ near the wall to first order in δ_s/h,

$$v_{\mathrm{str}} \approx v_0\left\{1 - 6\frac{\delta_s}{h}\left[1 + \ln\left(\frac{h}{6\delta_s}\right)\right]\right\}. \tag{21}$$

This provides an estimate for the magnitude of the acoustic streaming shown by dashed lines in Fig. 4(d), with the viscous boundary-layer thickness Eq. (12a) calculated for each of the three temperatures. This simple one-dimensional analytical model captures the trend of the numerical data well, though overall it predicts slightly lower streaming amplitudes. The deviation from the numerical data is ascribed primarily to the monotonic approximation $v_{\mathrm{plug}}(z)$ of the z dependence of the velocity inside the viscous boundary layer. The full z dependence of the streaming velocity inside the viscous boundary layer is nonmonotonic and overshoots slightly before leveling. This can be seen in Fig. 4(b), and thus the maximum velocity occurs at this overshoot and is consequently slightly larger than predicted by the approximate analytical model. For channel heights below 10 μm, the assumptions of a boundary-driven plug flow with a superimposed Poiseuille backflow begin to collapse as the height of the channel becomes comparable to the boundary-layer thickness, and a more elaborate analytical calculation of the streaming velocity field is necessary [12].

C. Time-averaged second-order temperature

In Fig. 5(a), we show the time-averaged second-order temperature field T_2 calculated for the default 380-μm-by-160-μm geometry at the resonance frequency. In Figs. 5(b) and 5(c), we show line plots of T_2 along the horizontal and vertical dashed lines in Fig. 5(a). T_2 has a saddle point in the center of the channel ($y = 0, z = 0$), two global maxima on the horizontal centerline $z = 0$, and a wide plateau on the vertical center line $y = 0$. The temperature field is forced to be zero at all boundaries due to the boundary condition of infinite heat conduction. The gradient of T_2 along line C indicates a decline in heat generation inside the boundary layer going from the center toward the left and right walls. The global maxima in the bulk result from heat generation in the bulk as discussed in Sec. V.

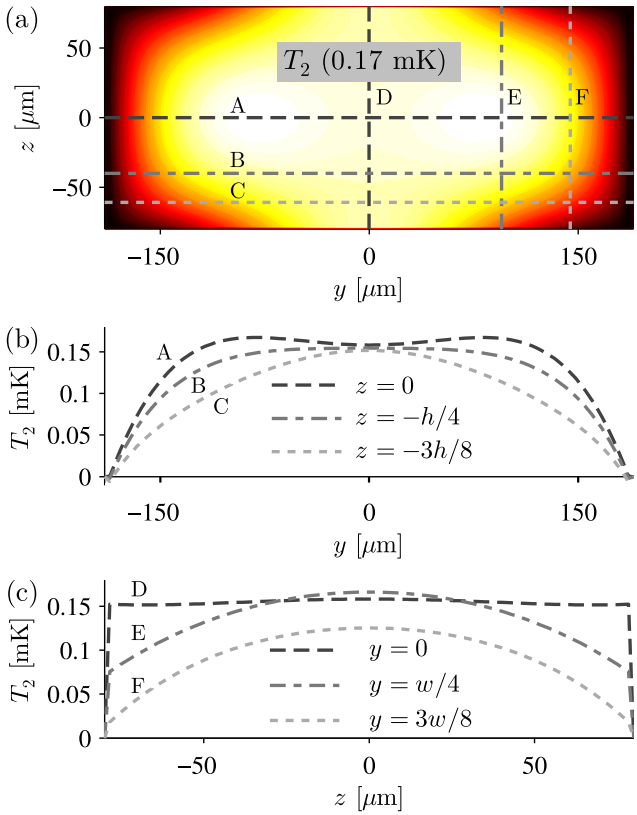

FIG. 5. (Color online) Time-averaged second-order temperature T_2 calculated for the default 380-μm-by-160-μm geometry, actuation frequency $f_{\mathrm{res}} = 1.966\,992\,3$ MHz, and equilibrium temperature $T_0 = 25$ °C. (a) Color plot (black 0 mK to white 0.17 mK) of T_2 in the channel cross section. (b) and (c) Line plots of T_2 along the horizontal and vertical dashed lines in (a), respectively.

V. DISCUSSION

In Fig. 6(a) we provide an overview of the energy transport and dissipation in the system by showing a sketch of the energy currents in the channel cross section. To explain the convection of energy, we consider the first-order velocity to be composed of a weak nonresonant part $\boldsymbol{v}_1^{\mathrm{bc}}$, which fulfills the oscillating velocity boundary conditions, and a strong resonant part $\boldsymbol{v}_1^{\mathrm{res}}$, which has zero amplitude at all walls [32]. In Fig. 6(b), we show the total energy current density, given by all the terms inside the divergence in Eq. (15c), in the bulk of the channel, thus not including the thin boundary layers at the top and bottom walls. The plot shows how mechanical energy is entering the system at the left and right walls, due to the oscillating boundary condition, and is convected toward the top and bottom walls. This transport is dominated by the term $\langle p_1 \boldsymbol{v}_1\rangle$ in Eq. (15c), particularly the nonresonant part $\langle p_1 \boldsymbol{v}_1^{\mathrm{bc}}\rangle$, since $\boldsymbol{v}_1^{\mathrm{res}}$ is out of phase with p_1 in the bulk. The y and z components of the energy current density inside the boundary layer at the bottom wall are shown in Figs. 6(c) and 6(d). The transport parallel to the wall, Fig. 6(c), results from $\langle p_1 \boldsymbol{v}_1^{\mathrm{res}}\rangle$, which is large, since $\boldsymbol{v}_1^{\mathrm{res}}$ is phase-shifted inside the boundary layer. The transport perpendicular to the wall, Fig. 6(d), results predominantly from the thermal diffusion term $-k_0^{\mathrm{th}}\boldsymbol{\nabla} T_2$.

To rationalize the amplitudes of the fields, we estimate the order of magnitude of the energy transport and dissipation in the system. The incoming energy current density from the oscillating velocity boundary condition at the left and right walls is given by the time-averaged product of the local pressure and velocity $\langle p_1 v_{y1}^{\mathrm{bc}}\rangle$. Multiplying this by the area $2h\ell$, we obtain the magnitude of the incoming power $P_{\mathrm{in}} \sim 2h\ell\frac{1}{2}p_1^{\mathrm{a}}v_{\mathrm{bc}}$. Here, the factor $\frac{1}{2}$ enters from time averaging, ℓ is the channel length, and the superscript "a" denotes the amplitude of the resonant field. From the inviscid part of the first-order momentum conservation Eq. (9a), we estimate the magnitude $p_1^{\mathrm{a}} \sim \rho_0 c_s v_{y1}^{\mathrm{a}}$ and therefore obtain $P_{\mathrm{in}} \sim h\ell\rho_0 c_s v_{y1}^{\mathrm{a}} v_{\mathrm{bc}}$.

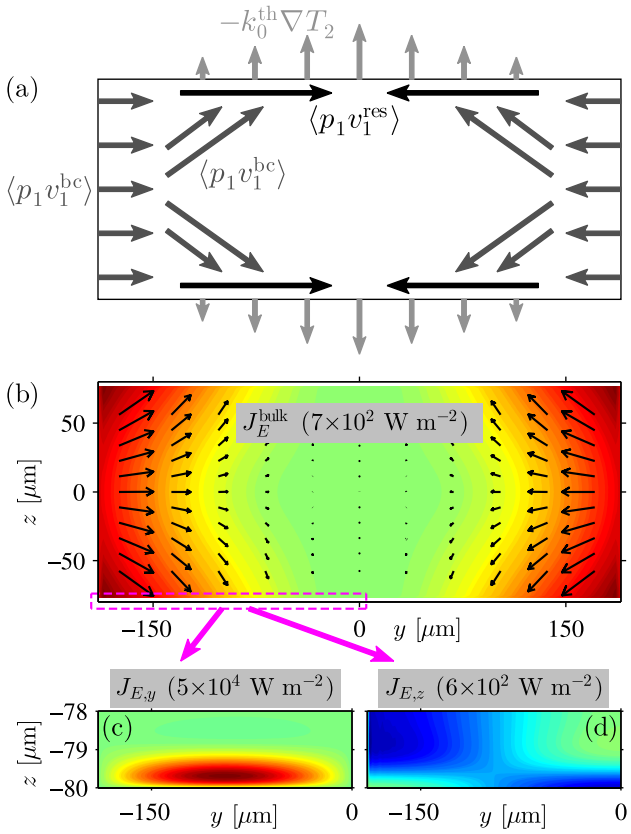

FIG. 6. (Color online) Time-averaged heat current densities in the channel cross section. (a) Sketch of the heat currents (arrows) with indication of the responsible terms in the time-averaged energy conservation Eq. (15). (b) Heat current density (arrows) and its magnitude [color plot ranging from zero (light green) to 7×10^2 W m^{-2} (dark red)] in the bulk of the channel. The strong currents inside the boundary layers are not shown. (c) Magnitude of the y component of the heat current density [color plot ranging from zero (light green) to 5×10^4 W m^{-2} (dark red)] inside the boundary layer at the bottom wall. (d) Magnitude of the z component of the heat current density [color plot ranging from -6×10^2 W m^{-2} (dark blue) to zero (light green)] inside the boundary layer at the bottom wall.

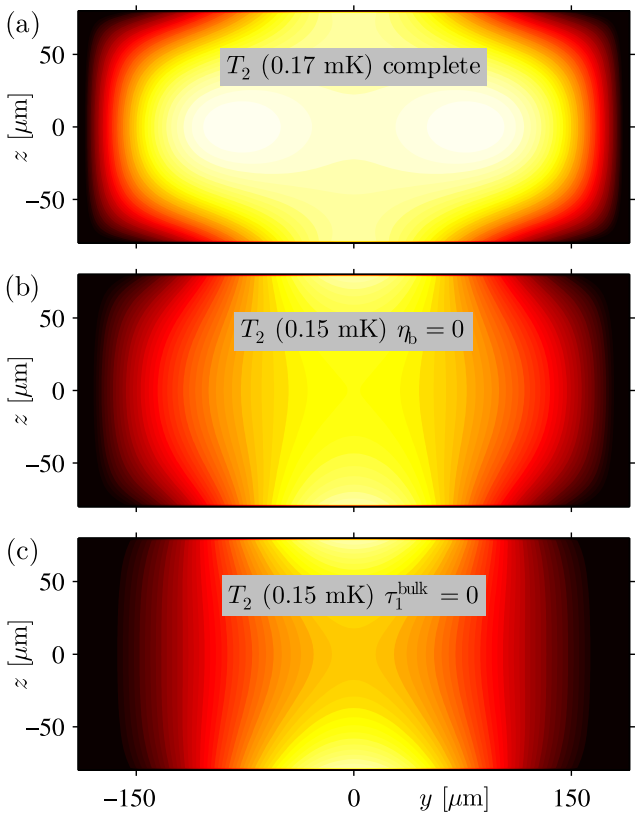

FIG. 7. (Color online) Color plot of the time-averaged second-order temperature T_2 [from zero (black) to maximum (white)] in three cases. (a) T_2 calculated from the complete governing equations, identical to Fig. 5(a). (b) T_2 calculated without bulk viscosity $\eta^{\rm b} = 0$. (c) T_2 calculated with zero viscous stress $\boldsymbol{\tau} = \mathbf{0}$ in the bulk defined by $|y| < (w/2 - 4\ \mu{\rm m})$ and $|z| < (h/2 - 4\ \mu{\rm m})$.

The dissipation of mechanical energy happens primarily in the viscous boundary layers of thickness $\delta_{\rm s}$ due to the work done by the viscous stress force density $(\boldsymbol{\nabla}\cdot\boldsymbol{\tau}_1)$ with power density $\langle(\boldsymbol{\nabla}\cdot\boldsymbol{\tau}_1)\cdot\boldsymbol{v}_1\rangle$. As the gradient of $\boldsymbol{v}_1$ perpendicular to the wall inside the boundary layer is large, the dominant term is $\langle\eta_0\frac{\partial^2 v_{y1}}{\partial z^2}\,v_{y1}\rangle \sim \eta_0\frac{1}{4}(v_{y1}^{\rm a})^2/\delta_{\rm s}^2$, where two factors of $\frac{1}{2}$ enter from spatial and time averaging. The total power dissipation is given by the product of the power density and the volume of the boundary layers, $P_{\rm s} \sim 2\delta_{\rm s} w\ell\eta_0\frac{1}{4}(v_{y1}^{\rm a})^2/\delta_{\rm s}^2$.

In steady state, $P_{\rm s}$ equals $P_{\rm in}$, from which we find the magnitude $v_{y1}^{\rm a}$ of the resonant field in terms of $v_{\rm bc}$ to be $v_{y1}^{\rm a} \sim \frac{2}{\pi}\frac{h}{\delta_{\rm s}}\frac{\lambda}{w}v_{\rm bc} \sim 500 v_{\rm bc}$ for our system, which is in good agreement with the numerical result for $v_{y1}^{\rm a}/v_{\rm bc}$ plotted in the inset of Fig. 3.

To rationalize the magnitude of the second-order temperature shift, we consider the diffusive energy transport through the top and bottom walls. The diffusive energy current density is $-k_0^{\rm th}\boldsymbol{\nabla}T_2$, and as heat diffuses to the perfectly conducting walls on a length scale of $\delta_{\rm t}$, the outgoing power is $P_{\rm out} \sim 2w\ell k_0^{\rm th}(\frac{1}{2}T_2^{\rm a}/\delta_{\rm t})$. Here, the spatial average of T_2 just outside the thermal boundary layers along the top and bottom walls has been approximated to $\frac{1}{2}T_2^{\rm a}$. In steady state, $P_{\rm out}$ equals $P_{\rm in}$ and the magnitude of the second-order temperature becomes $T_2^{\rm a} \sim \frac{2}{\pi^2}\frac{h^2}{\delta_{\rm t}\delta_{\rm s}}(\frac{\lambda}{w})^2\frac{1}{c_p}(v_{\rm bc})^2 \sim 0.13$ mK, which is comparable to the numerical result in Fig. 5.

From the simplified picture of strong heat generation inside the boundary layers, it may seem odd that the second-order temperature field in Fig. 5 has two global maxima in the bulk of the channel. This effect is due to the absorption in the bulk of the channel originating from the nonzero divergence of the stress force term $\langle\boldsymbol{v}_1\cdot\boldsymbol{\tau}_1\rangle$ in Eq. (15c) as shown in Fig. 7. In Fig. 7(a), we show the complete second-order temperature field T_2. Fig. 7(b) shows an artificial temperature field calculated without bulk viscosity, $\eta^{\rm b} = 0$. No maxima appear in the bulk, and the temperature field looks more as expected from the simplified view of heat generation in the boundary layers. However, there is still a small amount of heat generation in the bulk of the channel from the shear viscosity. In Fig. 7(c) this heat generation is suppressed by setting $\boldsymbol{\tau}_1 = \mathbf{0}$ in the bulk more than 4 μm from the walls, while maintaining the full $\boldsymbol{\tau}_1$ in the boundary layers. The resulting plot of T_2 shows how heat

is generated in boundary layers near the top and bottom walls and mainly conducted out of these, while some of the heat is conducted into the bulk and out through the left and right walls. The bulk viscosity η^{b} is often neglected when working at frequencies around 2 MHz because of its small contribution to the total dissipation, and the subsequent negligible influence on the resonance curve and the streaming velocity field. However, Fig. 7 clearly shows that the bulk absorption is important for the spatial structure of the time-averaged temperature field.

In Sec. II B we stated that the changes in the dynamic viscosity due to its temperature and density dependence are 0.33% and 0.37%, respectively, for the amplitudes of the acoustic oscillation used in this paper. It might seem surprising that, first, such a small perturbation of the viscosity can increase the magnitude of the streaming by 19% at 25 ℃ as stated in Sec. IV B (39% at 50 ℃), and secondly, the numerical results are in very good agreement with the analytical expression from Ref. [15], which does not include the density dependence of the dynamic viscosity of similar magnitude as the temperature dependence. The explanation lies within the spatial structure of the fields. From the time-averaged momentum Eq. (14), we see that the divergence of the stress tensor leads to a term containing the gradient of the viscosity perturbation $\langle \nabla \eta_1 \cdot [\nabla \boldsymbol{v}_1 + (\nabla \boldsymbol{v}_1)^{\mathrm{T}}] \rangle$. Here, η_1 is proportional to T_1 and ρ_1, and since T_1 changes on the small length scale of the boundary layer, whereas ρ_1 only changes on the long length scales of the channel width, we get $\nabla \eta_1 = \nabla \eta_1^{(T)} + \nabla \eta_1^{(\rho)} \sim \eta_1^{(T)}/\delta_{\mathrm{t}} + \eta_1^{(\rho)}/w \approx \eta_1^{(T)}/\delta_{\mathrm{t}}$, where the superscripts refer to the contribution from either the temperature or the density perturbation. Consequently, with respect to the acoustic streaming, the temperature dependence of the dynamic viscosity is much more important than the density dependence.

The significant increase of the acoustic streaming magnitude, due to the temperature-induced viscosity perturbation, influences the interplay between radiation forces and drag forces on suspended particles [20,33]. The steady temperature rise of less than 1 mK, on the other hand, has a negligible influence on acoustic handling of biological samples, however other applications of acoustofluidics, such as thermoacoustic engines, rely on the steady energy currents for pumping heat from a low-temperature source to a high-temperature sink, or inversely, for generating acoustic power from the heat flow between a high-temperature source and a low-temperature sink [34,35].

VI. CONCLUSION

In this work, we have presented a full numerical study of the acoustic streaming in the cross section of a long straight microchannel including the temperature and density dependence of the fluid viscosity and thermal conductivity. The temperature dependence of the streaming amplitude in the case of a deep microchannel agreed well with the analytical single-wall result from 2011 by Rednikov and Sadhal [15], whereas significant deviations were found for shallow channels. This strong dependence of the streaming amplitude on the channel height was explained qualitatively with a simple one-dimensional backflow model. Furthermore, we showed that a meaningful comparison of solutions at different temperatures and off-resonance frequencies could be performed by normalizing the second-order velocity field to the square of the first-order velocity amplitude.

We have also solved the time-averaged second-order energy conservation equation numerically and calculated the steady temperature rise in the channel, and we analyzed the energy transport in the system. For acoustophoretic devices, the temperature rise is less than 1 mK and has no consequences for either operation conditions or biological samples. However, in other applications such as thermoacoustic engines, the energy transport is important.

Finally, we have provided polynomial fits in the temperature range from 10 to 50 ℃ of the thermodynamic properties and transport properties of water at ambient atmospheric pressure based on data from IAPWS, which cover a much wider range of temperatures and pressures. This allows for easy implementation of the official parameter values for the properties of water in other models working under the same temperature and pressure conditions.

With the inclusion of the local perturbation in viscosity and thermal conductivity, due to their temperature and density dependence, we have solved the complete time-averaged second-order acoustic equations for a Newtonian fluid enclosed by vibrating walls, with the one exception of the unknown density dependence of the bulk viscosity. To further progress the numerical analysis of microchannel acoustic streaming, one should improve the modeling of the vibration of the walls, preferably including the elastic waves in the surrounding solid material. In the present model, the acoustic streaming velocity field depends strongly on the choice of actuation conditions on the walls.

ACKNOWLEDGMENTS

We thank Wolfgang Wagner, Ruhr-Universität Bochum, for providing us with the software FLUIDCAL, Version Water (IAPWS-95), for calculating the thermodynamic properties of water. This work was supported by the Danish Council for Independent Research (DFF): Technology and Production Sciences (Grant No. 11-107021).

APPENDIX A: IAPWS FORMULATION

To ease the use of the official IAPWS values for the thermodynamic and transport properties of water in our numerical analysis, we fit polynomials in temperature to the data. The precise fitting procedure and its validation are described in the following.

The data for the thermodynamic properties are obtained from an Excel implementation [36] of the IAPWS Formulation 1995 [24], in which the equation of state for water is fitted using a function with 56 parameters covering the range $T_{\mathrm{melt}} \leqslant T \leqslant 1273.15$ K and $p \leqslant 1000$ MPa. The shear viscosity is taken from the IAPWS Formulation 2008 [25], and the thermal conductivity is taken from the IAPWS Formulation 2011 [26], for which we have implemented the expressions stated in the papers to extract data values in the temperature and density range of interest to us. The data for the density derivatives of

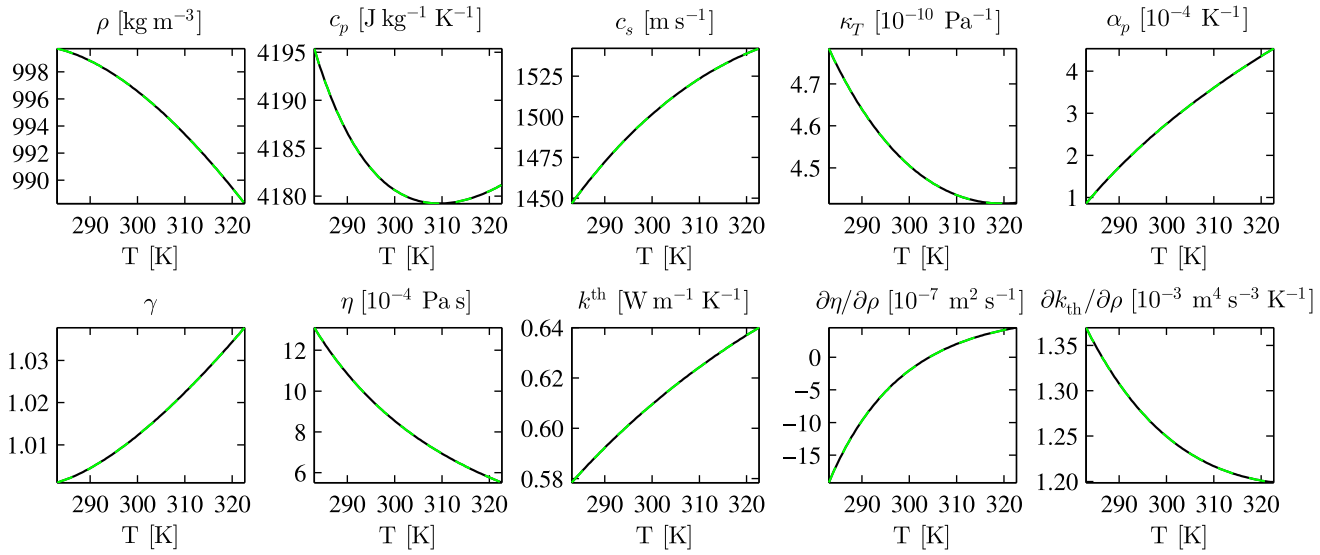

FIG. 8. (Color online) Fifth-order polynomial fits (dashed light green lines) to IAPWS data [24–26] (full black lines) of ten thermodynamic and transport parameters of water in the temperature range from 283 K (10 °C) to 323 K (50 °C).

the viscosity and the thermal conductivity have been obtained using a central difference $\partial\eta/\partial\rho \approx [\eta(T,\rho+d\rho)-\eta(T,\rho-d\rho)]/(2d\rho)$, with $d\rho = 0.001$ kg m^{-3}. The bulk viscosity is taken from Holmes, Parker, and Povey [27], who extended the work by Dukhin and Goetz [28]. The former paper provides a third-order polynomial fit in temperature to $\eta^{\rm b}$, thus rendering further fitting superfluous.

For each parameter, we extract 400 data points equally spaced in the temperature range from 283 to 323 K at ambient pressure $p = 0.101\,325$ MPa. From these 400 values, we only use every fourth point for the fitting of a fifth-order polynomial, while the remaining 300 data points are used for calculating the deviation of the fit from the data. The order of the polynomial has been chosen as a tradeoff between low deviation between fit and data, achieved at high polynomial order, and low uncertainty in the polynomial coefficients, achieved at low polynomial order. The fitted polynomial coefficients are then truncated to a finite precision of 11 significant digits. The number of significant digits has been chosen such that the finite precision of the fitting coefficients does not result in larger deviations between fit and data. We then calculated the relative deviation of the fit with respect

TABLE III. List of the coefficients C_i of the fifth-order polynomial fits to the IAPWS data for water [24–26], shown in Fig. 8. The temperature dependence of each of the ten thermodynamic or transport parameters g with SI unit $[g]$ is fitted in the temperature range from 283 K (10 °C) to 323 K (50 °C) by a polynomial of the form $g(\tilde{T})/[g] = C_0 + C_1\tilde{T} + C_2\tilde{T}^2 + C_3\tilde{T}^3 + C_4\tilde{T}^4 + C_5\tilde{T}^5$, with $\tilde{T} = T/(1\ \text{K})$. MD and AD denote the maximum and average relative deviation, respectively, of the fit from the data. Text files with the polynomial coefficients are provided in the Supplemental Material [37].

	ρ	c_p	c_s	κ_T	α_p
C_0	$-8.8657129122\times10^{+3}$	$2.9011416353\times10^{+5}$	$-3.1420310908\times10^{+4}$	$1.4812304299\times10^{-7}$	$-6.2142868017\times10^{-1}$
C_1	$1.4835428749\times10^{+2}$	$-4.4547002259\times10^{+3}$	$4.4207693183\times10^{+2}$	$-2.2647220701\times10^{-9}$	$9.6088951712\times10^{-3}$
C_2	$-8.9906362105\times10^{-1}$	$2.7826280608\times10^{+1}$	$-2.4555531077\times10^{+0}$	$1.3993170593\times10^{-11}$	$-5.9809671543\times10^{-5}$
C_3	$2.7498750299\times10^{-3}$	$-8.7096216461\times10^{-2}$	$7.0411177557\times10^{-3}$	$-4.3493756936\times10^{-14}$	$1.8708110371\times10^{-7}$
C_4	$-4.2441616455\times10^{-6}$	$1.3656418313\times10^{-4}$	$-1.0353739103\times10^{-5}$	$6.7914632960\times10^{-17}$	$-2.9366903765\times10^{-10}$
C_5	$2.6348942330\times10^{-9}$	$-8.5786317870\times10^{-8}$	$6.1949139692\times10^{-9}$	$-4.2558992023\times10^{-20}$	$1.8495258230\times10^{-13}$
MD	0.1×10^{-6}	1.2×10^{-6}	0.2×10^{-6}	5.3×10^{-6}	1.244×10^{-4}
AD	0.0×10^{-6}	0.3×10^{-6}	0.1×10^{-6}	1.4×10^{-6}	0.119×10^{-4}
	γ	η	$k^{\rm th}$	$\partial\eta/\partial\rho$	$\partial k_{\rm th}/\partial\rho$
C_0	$8.6095341563\times10^{+1}$	$3.8568288635\times10^{+0}$	$-4.5378052364\times10^{+1}$	$-3.7043919290\times10^{-2}$	$3.3029688424\times10^{-1}$
C_1	$-1.3297233662\times10^{+0}$	$-6.0269041999\times10^{-2}$	$7.0158464759\times10^{-1}$	$5.8520864113\times10^{-4}$	$-4.6998644326\times10^{-3}$
C_2	$8.3329451753\times10^{-3}$	$3.7823493660\times10^{-4}$	$-4.3372914723\times10^{-3}$	$-3.7051700834\times10^{-6}$	$2.7065291331\times10^{-5}$
C_3	$-2.6194143444\times10^{-5}$	$-1.1905791749\times10^{-6}$	$1.3522238266\times10^{-5}$	$1.1749472916\times10^{-8}$	$-7.8584696013\times10^{-8}$
C_4	$4.1304638557\times10^{-8}$	$1.8785807901\times10^{-9}$	$-2.1181858883\times10^{-8}$	$-1.8657255651\times10^{-11}$	$1.1504432763\times10^{-10}$
C_5	$-2.6113941825\times10^{-11}$	$-1.1881783857\times10^{-12}$	$1.3309059289\times10^{-11}$	$1.1866022487\times10^{-14}$	$-6.7916212133\times10^{-14}$
MD	1.6×10^{-6}	1.379×10^{-4}	1.0×10^{-6}	15.459×10^{-4}	0.8×10^{-6}
AD	0.4×10^{-6}	0.227×10^{-4}	0.3×10^{-6}	3.851×10^{-4}	0.1×10^{-6}

to each of the 400 data points and derive the maximum relative deviation (MD) and the average relative deviation (AD). The derivative of the shear viscosity with respect to the density is a special case since it crosses zero in the temperature interval, and thus the deviation between the fit and the data points is normalized to the mean of all the data points instead of the local data point. The data points and the polynomial fits for all fitted parameters are shown in Fig. 8, and the polynomial coefficients and the maximum and average relative deviation between fit and data are shown in Table III. The fitted coefficients are provided in the Supplemental Material [37].

[1] H. Bruus, J. Dual, J. Hawkes, M. Hill, T. Laurell, J. Nilsson, S. Radel, S. Sadhal, and M. Wiklund, Lab Chip **11**, 3579 (2011).
[2] M. Nordin and T. Laurell, Lab Chip **12**, 4610 (2012).
[3] P. Thevoz, J. D. Adams, H. Shea, H. Bruus, and H. T. Soh, Anal. Chem. **82**, 3094 (2010).
[4] M. Ohlin, A. E. Christakou, T. Frisk, B. Onfelt, and M. Wiklund, J. Micromech. Microeng. **23**, 035008 (2013).
[5] J. Shi, D. Ahmed, X. Mao, S.-C. S. Lin, A. Lawit, and T. J. Huang, Lab Chip **9**, 2890 (2009).
[6] A. Bussonniere, Y. Miron, M. Baudoin, O. Bou Matar, M. Grandbois, P. Charette, and A. Renaudin, Lab Chip **14**, 3556 (2014).
[7] P. Augustsson, C. Magnusson, M. Nordin, H. Lilja, and T. Laurell, Anal. Chem. **84**, 7954 (2012).
[8] T. Schwarz, G. Petit-Pierre, and J. Dual, J. Acoust. Soc. Am. **133**, 1260 (2013).
[9] L. Rayleigh, Philos. Trans. R. Soc. London **175**, 1 (1884).
[10] H. Schlichting, Phys. Z. **33**, 327 (1932).
[11] W. L. Nyborg, J. Acoust. Soc. Am. **30**, 329 (1958).
[12] M. Hamilton, Y. Ilinskii, and E. Zabolotskaya, J. Acoust. Soc. Am. **113**, 153 (2003).
[13] M. Hamilton, Y. Ilinskii, and E. Zabolotskaya, J. Acoust. Soc. Am. **114**, 3092 (2003).
[14] P. B. Muller, M. Rossi, Á. G. Marin, R. Barnkob, P. Augustsson, T. Laurell, C. J. Kähler, and H. Bruus, Phys. Rev. E **88**, 023006 (2013).
[15] A. Y. Rednikov and S. S. Sadhal, J. Fluid Mech. **667**, 426 (2011).
[16] W. L. Nyborg, J. Acoust. Soc. Am. **25**, 68 (1953).
[17] C. Lee and T. Wang, J. Acoust. Soc. Am. **85**, 1081 (1989).
[18] J. Lei, P. Glynne-Jones, and M. Hill, Lab Chip **13**, 2133 (2013).
[19] J. Lei, M. Hill, and P. Glynne-Jones, Lab Chip **14**, 532 (2014).
[20] P. B. Muller, R. Barnkob, M. J. H. Jensen, and H. Bruus, Lab Chip **12**, 4617 (2012).
[21] M. Antfolk, P. B. Muller, P. Augustsson, H. Bruus, and T. Laurell, Lab Chip **14**, 2791 (2014).
[22] L. D. Landau and E. M. Lifshitz, *Statistical Physics, Part 1*, 3rd ed. (Butterworth-Heinemann, Oxford, 1980), Vol. 5.
[23] A. D. Pierce, *Acoustics* (Acoustical Society of America, Woodbury, NY, 1991).
[24] W. Wagner and A. Pruss, J. Phys. Chem. Ref. Data **31**, 387 (2002).
[25] M. L. Huber, R. A. Perkins, A. Laesecke, D. G. Friend, J. V. Sengers, M. J. Assael, I. N. Metaxa, E. Vogel, R. Mares, and K. Miyagawa, J. Phys. Chem. Ref. Data **38**, 101 (2009).
[26] M. L. Huber, R. A. Perkins, D. G. Friend, J. V. Sengers, M. J. Assael, I. N. Metaxa, K. Miyagawa, R. Hellmann, and E. Vogel, J. Phys. Chem. Ref. Data **41**, 033102 (2012).
[27] M. J. Holmes, N. G. Parker, and M. J. W. Povey, J. Phys.: Conf. Ser. **269**, 012011 (2011).
[28] A. S. Dukhin and P. J. Goetz, J. Chem. Phys. **130**, 124519 (2009).
[29] H. Bruus, *Theoretical Microfluidics* (Oxford University Press, Oxford, 2008).
[30] P. Augustsson, R. Barnkob, S. T. Wereley, H. Bruus, and T. Laurell, Lab Chip **11**, 4152 (2011).
[31] COMSOL MULTIPHYSICS 4.4, www.comsol.com (2013).
[32] H. Bruus, Lab Chip **12**, 20 (2012).
[33] R. Barnkob, P. Augustsson, T. Laurell, and H. Bruus, Phys. Rev. E **86**, 056307 (2012).
[34] N. Rott, Z. Angew. Math. Phys. **26**, 43 (1975).
[35] G. Swift, J. Acoust. Soc. Am. **84**, 1145 (1988).
[36] U. Overhoff and W. Wagner, Fluidcal, version water (iapws-95), https://www.thermo.rub.de/en/prof-w-wagner/software/fluidcal.html (2013).
[37] See Supplemental Material at http://link.aps.org/supplemental/10.1103/PhysRevE.90.043016 for text files with the fitted polynomial coefficients for the temperature dependence of the thermodynamic and transport parameters, both in a general format `coefficients_general_format.txt` for copy-paste use, and a format `coefficients_comsol_format.txt` for direct import into COMSOL MULTIPHYSICS.

Appendix E

Paper submitted to Physical Review E, September 2015

A theoretical study of time-dependent, ultrasound-induced acoustic streaming in microchannels

Peter Barkholt Muller and Henrik Bruus

Abstract: Based on first- and second-order perturbation theory, we present a numerical study of the temporal build-up and decay of unsteady acoustic fields and acoustic streaming flows actuated by vibrating walls in the transverse cross-sectional plane of a long straight microchannel under adiabatic conditions and assuming temperature-independent material parameters. The unsteady streaming flow is obtained by averaging the time-dependent velocity field over one oscillation period, and as time increases, it is shown to converge towards the well-known steady time-averaged solution calculated in the frequency domain. Scaling analysis reveals that the acoustic resonance builds up much faster than the acoustic streaming, implying that the radiation force may dominate over the drag force from streaming even for small particles. However, our numerical time-dependent analysis indicates that pulsed actuation does not reduce streaming significantly due to its slow decay. Our analysis also shows that for an acoustic resonance with a quality factor Q, the amplitude of the oscillating second-order velocity component is Q times larger than the usual second-order steady time-averaged velocity component. Consequently, the well-known criterion $v_1 \ll c_s$ for the validity of the perturbation expansion is replaced by the more restrictive criterion $v_1 \ll c_s/Q$. Our numerical model is available in the supplemental material in the form of Comsol model files and Matlab scripts.

http://arxiv.org/abs/1509.02554v1

A theoretical study of time-dependent, ultrasound-induced acoustic streaming in microchannels

Peter Barkholt Muller* and Henrik Bruus†
Department of Physics, Technical University of Denmark, DTU Physics Building 309, DK-2800 Kongens Lyngby, Denmark
(Dated: Submitted to Phys. Rev. E, 8 September 2015)

Based on first- and second-order perturbation theory, we present a numerical study of the temporal build-up and decay of unsteady acoustic fields and acoustic streaming flows actuated by vibrating walls in the transverse cross-sectional plane of a long straight microchannel under adiabatic conditions and assuming temperature-independent material parameters. The unsteady streaming flow is obtained by averaging the time-dependent velocity field over one oscillation period, and as time increases, it is shown to converge towards the well-known steady time-averaged solution calculated in the frequency domain. Scaling analysis reveals that the acoustic resonance builds up much faster than the acoustic streaming, implying that the radiation force may dominate over the drag force from streaming even for small particles. However, our numerical time-dependent analysis indicates that pulsed actuation does not reduce streaming significantly due to its slow decay. Our analysis also shows that for an acoustic resonance with a quality factor Q, the amplitude of the oscillating second-order velocity component is Q times larger than the usual second-order steady time-averaged velocity component. Consequently, the well-known criterion $v_1 \ll c_s$ for the validity of the perturbation expansion is replaced by the more restrictive criterion $v_1 \ll c_s/Q$. Our numerical model is available in the supplemental material in the form of Comsol model files and Matlab scripts.

PACS numbers: 43.25.Nm, 43.20.Ks, 43.25.+y

I. INTRODUCTION

Acoustophoresis has successfully been used in many applications to manipulate particles in the size range from about 0.5 mm down to about 2 µm [1]. However, for smaller particles, the focusing by the acoustic radiation force is hindered by the drag force from the suspending liquid, which is set in motion by the generation of an acoustic streaming flow [2, 3]. This limits the use of acoustophoresis to manipulate sub-micrometer particles, relevant for application within medical, environmental, and food sciences, and it underlines a need for better understanding of acoustic streaming and ways to circumvent this limitation.

The phenomenon of acoustic streaming was first described theoretically by Lord Rayleigh [4] in 1884, and has later been revisited, among others, by Schlicting [5], Nyborg [6], Hamilton [7, 8], Rednikov and Sadhal [9], and Muller *et al.* [10], to extend the fundamental treatment of the governing equations and to solve the equations for various open and closed geometries.

Numerical methods have been applied in many studies to predict the streaming phenomena observed in various experiments. Muller *et al.* [2] developed a numerical scheme to solve the acoustic streaming in the cross section of a long straight microchannel, which resolved the viscous acoustic boundary layers and described the interplay between the acoustic scattering force and the streaming-induced drag force on suspended particles. This scheme was later extended to take into account the thermoviscous effects arising from the dependence of the fluid viscosity on the oscillating temperature field [11]. Lei *et al.* [12, 13] have developed a numerical scheme based on the effective slip-velocity equations, originally proposed by Nyborg in 1953 [14, 15], which avoid the resolution of the thin boundary layers but still enable qualitative predictions of the three-dimensional streaming flows observed in microchannels and flat microfluidic chambers. To obtain quantitative results from such models that does not resolve the acoustic boundary layers, Hahn *et al.* [16] developed an effective model to determine the loss associated with the viscous stresses inside the thermoacoustic boundary layers, and apply this loss as an artificial bulk absorption coefficient. This enables the calculation of correct acoustic amplitudes, without resolving the thin acoustic boundary layers. Acoustic streaming in the cross section of a straight PDMS microchannel exited by surface acoustic waves was studied numerically by Nama *et al.* [17], describing the influence of the acoustically soft PDMS wall on the particle focusability, and examining the possibilities of having two tunable counter-propagating surface acoustic waves.

All of the above mentioned studies consider steady acoustic streaming flows. This is reasonable as the streaming flow reaches steady state typically in a few milliseconds, much faster than other relevant experimental timescales. Furthermore, this allows for analytical solutions for the streaming velocity field in some special cases, and it makes it much easier to obtain numerical solutions. However, an experimental study by Hoyos and Castro [18] indicates that a pulsed actuation, instead of steady, can reduce the drag force from the streaming flow

* peter.b.muller@gmail.com
† bruus@fysik.dtu.dk

relative to the radiation force and thus allowing the latter also to dominate manipulation of sub-micrometer particles. This might provide an alternative method to the one proposed by Antfolk *et al.* [19], which used an almost square channel with overlapping resonances to create a streaming flow that did not counteract the focusing of sub-micrometer particles.

To theoretically study the effects of a pulsed ultrasound actuation, we need to solve the temporal evolution of the acoustic resonance and streaming, which is the topic of the present work. Numerical solutions of the time-domain acoustic equations were used by Wang and Dual [20] to calculate the time-averaged radiation force on a cylinder and the steady streaming around a cylinder, both in a steady oscillating acoustic field. However, they did not present an analysis of the unsteady build-up of the acoustic resonance and the streaming flow.

In this paper, we derive the second-order perturbation expansion of the time-dependent governing equations for the acoustic fields and streaming velocity, and solve them numerically for a long straight channel with acoustically hard walls and a rectangular cross section. The analysis and results are divided into two sections: (1) A study of the transient build-up of the acoustic resonance and streaming from a initially quiescent state towards a steady oscillating acoustic field and a steady streaming flow. (2) An analysis of the response of the acoustic field and the streaming flow to pulsed actuation, and quantifying whether this can lead to better focusability of sub-micrometer particles.

In previous studies, such as [2, 11, 17], only the periodic state of the acoustic resonance and the steady time-averaged streaming velocity are solved. When solving the time-dependent equations, we obtain a transient solution, which may also be averaged over one oscillation period to obtain an unsteady time-averaged solution.

II. BASIC ADIABATIC ACOUSTIC THEORY

In this section we derive the governing equations for the first- and second-order perturbations to unsteady acoustic fields in a compressible Newtonian fluid. We only consider acoustic perturbation in fluids, and treat the surrounding solid material as ideal rigid walls. Our treatment is based on textbook adiabatic acoustics [21] and our previous study Ref. [11] of the purely periodic state.

A. Adiabatic thermodynamics

We employ the adiabatic approximation, which assumes that the entropy is conserved for any small fluid volume [22]. Consequently, the thermodynamic state of the fluid is described by only one independent thermodynamic variable, which we choose to be the pressure p. See Table I for parameter values. The changes $\mathrm{d}\rho$ in the density ρ from the equilibrium state is given by

$$\mathrm{d}\rho = \rho\kappa_s \,\mathrm{d}p, \tag{1}$$

where the isentropic compressibility κ_s is defined as

$$\kappa_s = \frac{1}{\rho}\left(\frac{\partial\rho}{\partial p}\right)_s = \frac{1}{\rho c_s^2}. \tag{2}$$

TABLE I. IAPWS parameter values for pure water at ambient temperature 25 °C and pressure 0.1013 MPa. For references see Sec. II-B in Ref. [11].

Parameter	Symbol	Value	Unit
Acoustic properties:			
Mass density	ρ_0	9.971×10^{2}	$\mathrm{kg\,m^{-3}}$
Speed of sound	c_s	1.497×10^{3}	$\mathrm{m\,s^{-1}}$
Compressibility	κ_s	4.477×10^{-10}	$\mathrm{Pa^{-1}}$
Transport properties:			
Shear viscosity	η	8.900×10^{-4}	Pa s
Bulk viscosity	η^{b}	2.485×10^{-3}	Pa s

B. Governing equations

Mass conservation implies that the rate of change $\partial_t\rho$ of the density in a test volume with surface normal vector $\boldsymbol{n}$ is given by the influx (direction $-\boldsymbol{n}$) of the mass current density $\rho\boldsymbol{v}$. In differential form by Gauss's theorem it is

$$\partial_t\rho = \boldsymbol{\nabla}\cdot\big[-\rho\boldsymbol{v}\big]. \tag{3a}$$

Substituting $\partial_t\rho$ and $\boldsymbol{\nabla}\rho$ using Eq. (1), and dividing by ρ, the continuity equation (3a) becomes

$$\kappa_s\partial_t p = -\boldsymbol{\nabla}\cdot\boldsymbol{v} - \kappa_s\boldsymbol{v}\cdot\boldsymbol{\nabla}p. \tag{3b}$$

Similarly, momentum conservation implies that the rate of change $\partial_t(\rho\boldsymbol{v})$ of the momentum density in the same test volume is given by the stress forces $\boldsymbol{\sigma}$ acting on the surface (with normal $\boldsymbol{n}$), and the influx (direction $-\boldsymbol{n}$) of the momentum current density $\rho\boldsymbol{v}\boldsymbol{v}$. In differential form, neglecting body forces, this becomes

$$\partial_t(\rho\boldsymbol{v}) = \boldsymbol{\nabla}\cdot\big[\boldsymbol{\tau} - p\,\mathbf{1} - \rho\boldsymbol{v}\boldsymbol{v}\big], \tag{4a}$$

where the viscous stress tensor is defined as

$$\boldsymbol{\tau} = \eta\Big[\boldsymbol{\nabla}\boldsymbol{v} + (\boldsymbol{\nabla}\boldsymbol{v})^{\mathrm{T}}\Big] + \Big[\eta^{\mathrm{b}} - \frac{2}{3}\eta\Big](\boldsymbol{\nabla}\cdot\boldsymbol{v})\,\mathbf{1}. \tag{4b}$$

Here $\mathbf{1}$ is the unit tensor and the superscript "T" indicates tensor transposition. Using the continuity equation (3a), the momentum equation (4a) is rewritten into the well-known Navier–Stokes form,

$$\rho\partial_t\boldsymbol{v} = \boldsymbol{\nabla}\cdot\big[\boldsymbol{\tau} - p\,\mathbf{1}\big] - \rho(\boldsymbol{v}\cdot\boldsymbol{\nabla})\boldsymbol{v}, \tag{4c}$$

which is useful when solving problems in the time domain. The equations (3b) and (4c) constitutes the nonlinear governing equations which we will study by applying the usual perturbation approach of small acoustic amplitudes.

C. First-order time-domain equations

The homogeneous, isotropic, quiescent thermodynamic equilibrium state is taken to be the zeroth-order state in the acoustic perturbation expansion. Following standard perturbation theory, all fields g are written in the form $g = g_0 + g_1$, for which g_0 is the value of the zeroth-order state, and g_1 is the acoustic perturbation which by definition has to be much smaller than g_0. For the velocity, the value of the zeroth-order state is $\boldsymbol{v}_0 = \boldsymbol{0}$, and thus $\boldsymbol{v} = \boldsymbol{v}_1$. The zeroth-order terms solve the governing equations in the zeroth-order state and thus drop out of the equations. Keeping only first-order terms, we obtain the following first-order equations.

The first-order continuity equation (3b) becomes

$$\kappa_s \partial_t p_1 = -\boldsymbol{\nabla} \cdot \boldsymbol{v}_1, \tag{5}$$

and likewise, the momentum equation (4c) becomes

$$\rho_0 \partial_t \boldsymbol{v}_1 = \boldsymbol{\nabla} \cdot \big[\boldsymbol{\tau}_1 - p_1 \mathbf{1}\big], \tag{6a}$$

where $\boldsymbol{\tau}_1$ is given by

$$\boldsymbol{\tau}_1 = \eta_0 \Big[\boldsymbol{\nabla}\boldsymbol{v}_1 + (\boldsymbol{\nabla}\boldsymbol{v}_1)^{\mathrm{T}}\Big] + \Big[\eta_0^{\mathrm{b}} - \frac{2}{3}\eta_0\Big](\boldsymbol{\nabla}\cdot\boldsymbol{v}_1)\,\mathbf{1}. \tag{6b}$$

Equations (5) and (6) determine together with a set of boundary conditions the time evolution of the first-order acoustic fields p_1 and $\boldsymbol{v}_1$.

D. Second-order time-domain equations

Moving on to second-order perturbation theory, we write the fields as $g = g_0 + g_1 + g_2$, with g_1 and g_2 depending on both time and space. For simplicity and in contrast to Ref. [11], we do not include perturbations in η and η^{b}. This will cause the magnitude of the streaming to be slightly off, as does the adiabatic approximation, however the qualitative behavior is not expected to change. The second-order time-domain continuity equation (3b) becomes

$$\kappa_s \partial_t p_2 = -\boldsymbol{\nabla}\cdot\boldsymbol{v}_2 - \kappa_s \boldsymbol{v}_1 \cdot \boldsymbol{\nabla} p_1, \tag{7}$$

and the momentum equation (4c) takes the form

$$\rho_0 \partial_t \boldsymbol{v}_2 = -\rho_1 \partial_t \boldsymbol{v}_1 + \boldsymbol{\nabla}\cdot\big[\boldsymbol{\tau}_2 - p_2\,\mathbf{1}\big] - \rho_0(\boldsymbol{v}_1\cdot\boldsymbol{\nabla})\boldsymbol{v}_1, \tag{8a}$$

where $\boldsymbol{\tau}_2$ is given by

$$\boldsymbol{\tau}_2 = \eta_0 \Big[\boldsymbol{\nabla}\boldsymbol{v}_2 + (\boldsymbol{\nabla}\boldsymbol{v}_2)^{\mathrm{T}}\Big] + \Big[\eta_0^{\mathrm{b}} - \frac{2}{3}\eta_0\Big](\boldsymbol{\nabla}\cdot\boldsymbol{v}_2)\,\mathbf{1}. \tag{8b}$$

Using Eq. (1) in the form $\rho_1 = \rho_0\kappa_s p_1$ and the first-order momentum equation (6a), we rewrite Eq. (8a) to

$$\begin{aligned}\rho_0 \partial_t \boldsymbol{v}_2 =& \boldsymbol{\nabla}\cdot\big[\boldsymbol{\tau}_2 - p_2\,\mathbf{1} - \kappa_s p_1 \boldsymbol{\tau}_1 + \tfrac{1}{2}\kappa_s p_1^2\,\mathbf{1}\big] \\ &+ \kappa_s \boldsymbol{\nabla} p_1 \cdot \boldsymbol{\tau}_1 - \rho_0(\boldsymbol{v}_1\cdot\boldsymbol{\nabla})\boldsymbol{v}_1.\end{aligned} \tag{8c}$$

This particular form of the second-order momentum equation is chosen to minimize numerical errors as described in Section III A.

E. Periodic frequency-domain equations

When solving for the periodic state at $t \to \infty$, it is advantageous to formulate the first-order equations in the frequency domain. The harmonic first-order fields are all written as $g_1(\boldsymbol{r},t) = \mathrm{Re}\big\{g_1^{\mathrm{fd}}(\boldsymbol{r})\mathrm{e}^{-\mathrm{i}\omega t}\big\}$, where g_1^{fd} is the complex field amplitude in the frequency domain. The first-order frequency-domain equations are derived from Eqs. (5) and (6a) by the substitution $\partial_t \to -\mathrm{i}\omega$,

$$\boldsymbol{\nabla}\cdot\boldsymbol{v}_1^{\mathrm{fd}} - \mathrm{i}\omega\kappa_s p_1^{\mathrm{fd}} = 0, \tag{9}$$

$$\boldsymbol{\nabla}\cdot\big[\boldsymbol{\tau}_1^{\mathrm{fd}} - p_1^{\mathrm{fd}}\mathbf{1}\big] + \mathrm{i}\omega\rho_0\boldsymbol{v}_1^{\mathrm{fd}} = \boldsymbol{0}. \tag{10}$$

The steady time-averaged streaming flow is obtained from the time-averaged second-order frequency-domain equations, where $\langle g_2^{\mathrm{fd}}\rangle$ denotes time averaging over one oscillation period of the periodic second-order field. The time-average of products of two harmonic first-order fields g_1^{fd} and $\tilde{g}_1^{\mathrm{fd}}$ is given by $\langle g_1^{\mathrm{fd}}\tilde{g}_1^{\mathrm{fd}}\rangle = \frac{1}{2}\,\mathrm{Re}\big[\big(g_1^{\mathrm{fd}}\big)^*\tilde{g}_1^{\mathrm{fd}}\big]$, as in Ref. [11], where the asterisk denotes complex conjugation. In the periodic state, the fields may consist of harmonic terms and a steady term, and thus all full time-derivatives average to zero $\langle\partial_t g_2^{\mathrm{fd}}\rangle = 0$. The time-averaged second-order frequency-domain equations are derived from Eqs. (7) and (4a),

$$\boldsymbol{\nabla}\cdot\langle\boldsymbol{v}_2^{\mathrm{fd}}\rangle + \kappa_s\langle\boldsymbol{v}_1^{\mathrm{fd}}\cdot\boldsymbol{\nabla}p_1^{\mathrm{fd}}\rangle = 0, \tag{11}$$

$$\boldsymbol{\nabla}\cdot\big[\langle\boldsymbol{\tau}_2^{\mathrm{fd}}\rangle - \langle p_2^{\mathrm{fd}}\rangle\,\mathbf{1} - \rho_0\langle\boldsymbol{v}_1^{\mathrm{fd}}\boldsymbol{v}_1^{\mathrm{fd}}\rangle\big] = \boldsymbol{0}. \tag{12}$$

F. Acoustic energy and cavity Q-factor

The total acoustic energy of the system in the time domain $E_{\mathrm{ac}}(t)$ and in the frequency domain $\langle E_{\mathrm{ac}}^{\mathrm{fd}}(\infty)\rangle$ is given by

$$E_{\mathrm{ac}}(t) = \int_V \left[\frac{1}{2}\kappa_s p_1^2 + \frac{1}{2}\rho_0 v_1^2\right]\mathrm{d}V, \tag{13a}$$

$$\langle E_{\mathrm{ac}}^{\mathrm{fd}}(\infty)\rangle = \int_V \left[\frac{1}{2}\kappa_s\langle p_1^{\mathrm{fd}}p_1^{\mathrm{fd}}\rangle + \frac{1}{2}\rho_0\langle\boldsymbol{v}_1^{\mathrm{fd}}\cdot\boldsymbol{v}_1^{\mathrm{fd}}\rangle\right]\mathrm{d}V. \tag{13b}$$

Moreover, the time derivative of $E_{\mathrm{ac}}(t)$ is

$$\begin{aligned}\partial_t E_{\mathrm{ac}} &= \int_V \partial_t\left[\frac{1}{2}\kappa_s p_1^2 + \frac{1}{2}\rho_0 v_1^2\right]\mathrm{d}V \\ &= \int_V \left[\kappa_s p_1 \partial_t p_1 + \rho_0 \boldsymbol{v}_1\cdot\partial_t\boldsymbol{v}_1\right]\mathrm{d}V \\ &= \int_V \Big\{\boldsymbol{\nabla}\cdot\Big[\boldsymbol{v}_1\cdot(\boldsymbol{\tau}_1 - p_1\mathbf{1})\Big] - \boldsymbol{\nabla}\boldsymbol{v}_1 : \boldsymbol{\tau}_1\Big\}\mathrm{d}V,\end{aligned} \tag{14a}$$

where we have used Eqs. (5) and (6a). Applying Gauss's theorem on the first term in Eq. (14a), we arrive at

$$\begin{aligned}\partial_t E_{\mathrm{ac}} &= \int_A \Big[\boldsymbol{v}_1\cdot(\boldsymbol{\tau}_1 - p_1\mathbf{1})\Big]\cdot\boldsymbol{n}\;\mathrm{d}A - \int_V \boldsymbol{\nabla}\boldsymbol{v}_1 : \boldsymbol{\tau}_1\;\mathrm{d}V \\ &= P_{\mathrm{pump}} - P_{\mathrm{dis}},\end{aligned} \tag{14b}$$

where P_{pump} is the total power delivered by the forced vibration of the sidewalls, and P_{dis} is the total power dissipated due to viscous stress. The quality factor Q of a resonant cavity is given by

$$Q = 2\pi \frac{\text{Energy stored}}{\text{Energy dissipated per cycle}} = \omega \frac{\langle E_{\text{ac}}^{\text{fd}} \rangle}{\langle P_{\text{dis}}^{\text{fd}} \rangle}. \quad (15)$$

G. Summary of theory

Throughout this paper we refer to two kinds of solutions of the acoustic energy and velocity fields: unsteady non-periodic solutions obtained from Eqs. (5)-(8) and steady periodic solutions obtained from Eqs. (9)-(12). When presenting the unsteady non-periodic solutions, they are often normalized by the steady periodic solution, to emphasize how close it has converged towards this solution.

III. NUMERICAL MODEL

The numerical scheme solves the governing equations for the acoustic field inside a water domain enclosed by a two-dimensional rectangular microchannel cross section. The vibrations in the surrounding chip material and piezo transducer are not modeled. The water domain is surrounded by immovable hard walls, and the acoustic field is excited by oscillating velocity boundary conditions, representing an oscillating nm-sized displacement of the walls. A sketch of the numerical model is shown in Fig. 1(a). We exploit the symmetry along the horizontal center axis $z = 0$, reducing our computational domain by a factor of two. The system is also symmetric about the vertical center axis $y = 0$, however, our attempts to use this symmetry introduced numerical errors, and consequently it was not exploited in the numerical model. The model used to calculate the steady streaming flow in the time-periodic case is a simplification of the model presented in Ref. [11], whereas the model used to solve the time-dependent problem is new.

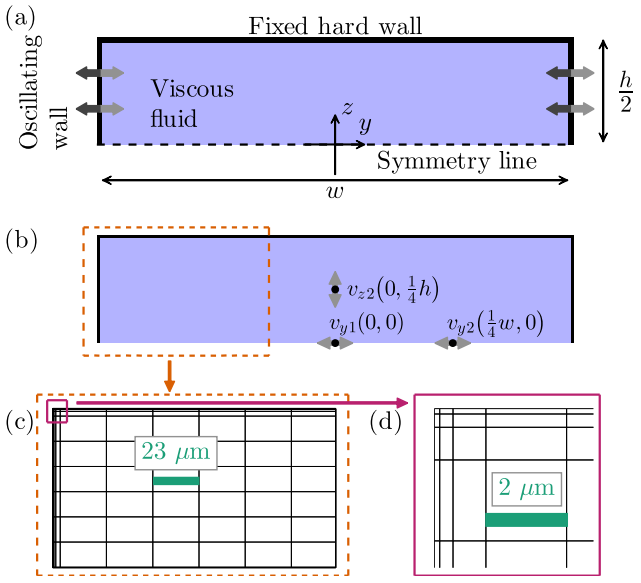

FIG. 1. (Color online) (a) Sketch of the rectangular computational domain in the yz-plane representing the upper half of a rectangular cross section of a long straight microchannel of width $w = 380$ µm and height $h = 160$ µm as in [23]. The thick arrows indicate in-phase oscillating velocity actuation at the left and right boundaries. (b) The three black points indicate positions at which the velocity components (gray arrows), defined in Eq. (29), are probed. (c) Sketch of the spatial mesh used for the discretization of the physical fields. (d) A zoom-in on the mesh in the upper left corner.

A. Governing equations

The governing equations are solved using the commercial software Comsol Multiphysics [24] based on the finite element method [25]. To achieve greater flexibility and control, the equations are implemented through mathematics-weak-form-PDE modules and not through the built-in modules for acoustics and fluid mechanics. The governing equations are formulated to avoid evaluation of second-order spatial derivatives and of time-derivatives of first-order fields in the second-order equations, as time-derivatives carry larger numerical errors compared to the spatial derivatives. To fix the numerical solution of the second-order equations, a zero spatial average of the second-order pressure is enforced by a Lagrange multiplier. For the time-domain simulations we use the generalized alpha solver [26], setting the alpha parameter to 0.5 and using a fixed time step Δt. Furthermore, to limit the amount of data stored in Comsol, the simulations are run from Matlab [27] and long time-marching schemes are solved in shorter sections by Comsol. Comsol model files and Matlab scripts are provided in the Supplemental Material [28].

B. Boundary conditions

The acoustic cavity is modeled with stationary hard rigid walls, and the acoustic fields are exited on the side walls by an oscillating velocity boundary condition with oscillation period t_0 and angular frequency ω,

$$t_0 = \frac{2\pi}{\omega}. \quad (16)$$

The symmetry of the bottom boundary is described by zero orthogonal velocity component and zero orthogonal gradient of the parallel velocity component. The explicit

boundary conditions for the first-order velocity become

$$\begin{aligned}
&\text{top:} && v_{y1} = 0, && v_{z1} = 0, && \text{(17a)}\\
&\text{bottom:} && \partial_z v_{y1} = 0, && v_{z1} = 0, && \text{(17b)}\\
&\text{left-right:} && v_{y1} = v_{\mathrm{bc}} \sin(\omega t), && v_{z1} = 0. && \text{(17c)}
\end{aligned}$$

The boundary conditions on the second-order velocity are set by the zero-mass-flux condition $\boldsymbol{n} \cdot \rho \boldsymbol{v} = 0$ on all boundaries, as well as zero parallel velocity component on the top, right and left wall boundaries, and zero orthogonal derivative of the parallel component of the mass flux on the bottom symmetry boundary. The explicit boundary conditions for the second-order velocity become

$$\begin{aligned}
&\text{top:} && v_{y2} = 0, && v_{z2} = 0, && \text{(18a)}\\
&\text{bottom:} && \partial_z\big(\rho_0 v_{y2} + \rho_1 v_{y1}\big) = 0, && v_{z2} = 0, && \text{(18b)}\\
&\text{left-right:} && \rho_0 v_{y2} + \rho_1 v_{y1} = 0, && v_{z2} = 0. && \text{(18c)}
\end{aligned}$$

C. Spatial resolution

The physical fields are discretized using fourth-order basis functions for $\boldsymbol{v}_1$ and $\boldsymbol{v}_2$ and third-order basis functions for p_1 and p_2. The domain shown in Fig. 1(a) is covered by basis functions localized in each element of the spatial mesh shown in Fig. 1(c). Since the streaming flow is solved in the time domain, the computational time quickly becomes very long compared to the computational time of solving the usual steady streaming flow. Thus we have optimized the use of precious few mesh elements to obtain the best accuracy of the solution. We use an inhomogeneous mesh of rectangular elements ranging in size from 0.16 µm at the boundaries to 24 µm in the bulk of the domain. The convergence of the solution g with respect to a reference solution g_{ref} was considered through the relative convergence parameter $C(g)$ defined in Ref. [11] by

$$C(g) = \sqrt{\frac{\int \big(g - g_{\mathrm{ref}}\big)^2 \,\mathrm{d}y\,\mathrm{d}z}{\int \big(g_{\mathrm{ref}}\big)^2 \,\mathrm{d}y\,\mathrm{d}z}}. \qquad (19)$$

In Ref. [11], $C(g)$ was required to be below 0.001 for the solution to have converged. The solution for the steady time-averaged velocity $\langle \boldsymbol{v}_2^{\mathrm{fd}}(\infty)\rangle$, calculated with the mesh shown in Fig. 1(c) and 1(d), has $C = 0.006$ with respect to the solution calculated with the fine triangular reference mesh in Ref. [11], which is acceptable for the present study.

D. Temporal resolution

The required temporal resolution for time-marching schemes is normally determined by the Courant–Friedrichs–Lewy (CFL) condition [29], also referred to as just the Courant number

$$\mathrm{CFL} = \frac{c_s\,\Delta t}{\Delta r} \leq \mathrm{CFL}_{\max}, \qquad (20)$$

where Δt is the temporal discretization and Δr is the spatial discretization. This means that the length over which a disturbance travels within a time step Δt should be some fraction of the mesh element size, ultimately ensuring that disturbances do not travel through a mesh element in one time step. A more accurate interpretation of the CFL-condition is that it ensures that the error on the approximation of the time-derivative is smaller than the error on the approximation of the spatial-derivatives. Consequently, the value of $\mathrm{CFL}_{\max}$ depends on the specific solver and on the order of the basis functions. For fourth-order basis functions and the generalized alpha solver, Ref. [29] reports a value of $\mathrm{CFL}_{\max}^{\mathrm{4th}} = 0.05$, which is an empirical result for a specific model. Due to the inhomogeneity of the mesh, two values for the upper limit for the temporal resolution can be calculated based on Eq. (20); $\Delta t = 8 \times 10^{-10}$ ns $\approx t_0/600$ for the bulk mesh size of 24 µm and $\Delta t = 5 \times 10^{-12}$ ns $\approx t_0/95000$ for the boundary mesh size of 160 nm.

To determine a reasonable trade-off between numerical accuracy and computational time, we study the convergence of the transient solution towards the steady solution for different values of the temporal resolution $t_0/\Delta t$. The acoustic energy $E_{\mathrm{ac}}(t)$ is shown in Fig. 2(a) for different values of Δt and normalized by the steady time-averaged energy $\langle E_{\mathrm{ac}}^{\mathrm{fd}}(\infty)\rangle$ of the frequency-domain calculation, and it is thus expected to converge to the unity for long times. In Fig. 2(b), $E_{\mathrm{ac}}(1000t_0)/\langle E_{\mathrm{ac}}^{\mathrm{fd}}(\infty)\rangle$ is plotted versus the temporal resolution $t_0/\Delta t$, which shows how the accuracy of the time-domain solution increases as the temporal resolution is increased. In all subsequent simulations we have chosen a time step of $\Delta t = t_0/256$, the circled point in Fig. 2(b), for which the time-domain energy converge to 99.4% of the energy of the steady calculation. The chosen value for the time step is larger than the upper estimate $t_0/600$ of the necessary Δt based on the CFL-condition. This might be because our spatial domain is smaller than the wavelength, and consequently a finer spatial resolution is needed, compared to what is usually expected to spatially resolve a wave.

We have noted that the fastest convergence is obtained when actuating the system at its (numerically determined) resonance frequency f_{res}. When shifting the actuation frequency half the resonance width $\frac{1}{2}\Delta f$ away from f_{res}, the energy $E_{\mathrm{ac}}(t)$ for $\Delta t = t_0/256$ converged to only 95% of the steady value $\langle E_{\mathrm{ac}}^{\mathrm{fd}}(\infty)\rangle$ (calculated in the frequency domain), thus necessitating smaller time steps to obtain reasonable convergence.

The computations where performed on a desktop PC with Intel Xeon CPU X5690 3.47 GHz 2 processors, 64-bit Windows 7, and 128 GB RAM. The computations took approximately one hour for each time interval of width $100t_0$ with $\Delta t = t_0/256$, and the computational

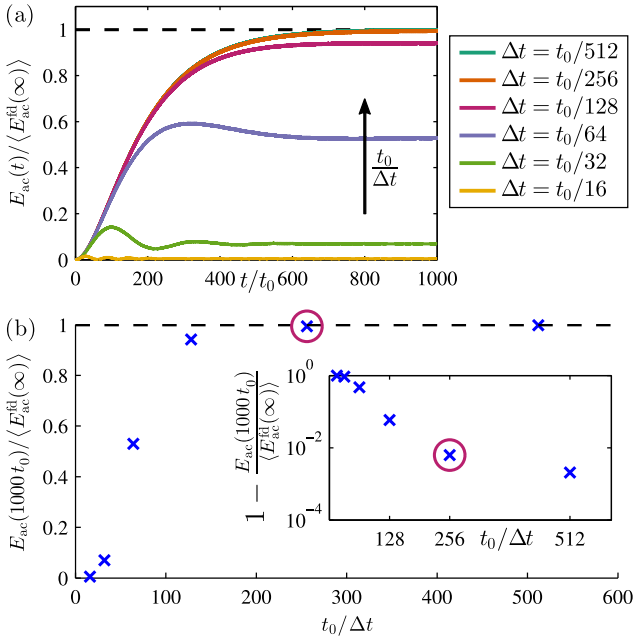

FIG. 2. (Color online) Numerical convergence and temporal resolution. (a) Graphs of the build-up of acoustic energy $E_{\rm ac}(t)$ in the time-domain simulations calculated with different fixed time steps Δt. The energy of the time-domain simulations is normalized with respect to the energy $\langle E^{\rm fd}_{\rm ac}(\infty)\rangle$ of the steady solution in the frequency domain, and should thus converge towards unity. In all simulations the actuation frequency equals the resonance frequency discussed in Section IV A. (b) Acoustic energy $E_{\rm ac}(1000\,t_0)$ at $t = 1000\,t_0$, normalized by $\langle E^{\rm fd}_{\rm ac}(\infty)\rangle$, and plotted versus the temporal resolution $t_0/\Delta t$ of the oscillation. The inset is a semilog plot of the relative deviation of $E_{\rm ac}(1000\,t_0)$ from $\langle E^{\rm fd}_{\rm ac}(\infty)\rangle$. The circled point in each graph indicates the time step $\Delta t = t_0/256$ used in all subsequent simulations.

time was not limited by RAM, as only less than 2 GB RAM was allocated by Comsol for the calculations.

IV. ONSET OF ACOUSTIC STREAMING

In this section the fluid is initially quiescent. Then, at time $t = 0$, the oscillatory velocity actuation is turned on, such that within the first oscillation period its amplitude increases smoothly from zero to its maximum value $v_{\rm bc}$, which it maintains for the rest of the simulation. We study the resulting build-up of the acoustic resonance and the acoustic streaming flow.

A. Resonance and build-up of acoustic energy

To determine the resonance frequency, the steady acoustic energy $\langle E^{\rm fd}_{\rm ac}(\infty)\rangle$ Eq. (13b) was calculated for a range of frequencies based on the frequency-domain equations (9)-(10). In Fig. 3 the numerical results (circles) are shown together with a Gaussian fit (full line), while the inset exhibits the fitted resonance frequency $f_{\rm res}$, the full width Δf at half maximum, and the quality factor $Q = f_{\rm res}/\Delta f$.

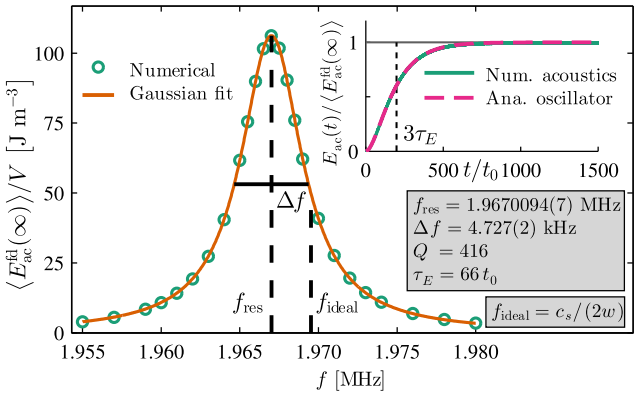

FIG. 3. (Color online) Resonance curve and build-up of acoustic energy. (a) The numerical acoustic energy density $\langle E^{\rm fd}_{\rm ac}(\infty)\rangle/V$ (circles) for different frequencies of the boundary actuation and a Gaussian fit (full line) to the numerical data. $f_{\rm res}$ is the fitted resonance frequency at the center of the peak, while $f_{\rm ideal}$ is the frequency corresponding to matching a half-wavelength with the channel width. The inset shows the numerical build-up of the acoustic energy (full line) for actuation at the resonance frequency, $\omega = 2\pi f_{\rm res}$, along with the analytical prediction Eq. (23) (dashed line) for a single harmonic oscillator with the same resonance frequency and quality factor $Q = f_{\rm res}/\Delta f$.

The build-up of the acoustic energy in the cavity is well captured by a simple analytical model of a single sinusoidally-driven damped harmonic oscillator with time-dependent position $x(t)$,

$$\frac{{\rm d}^2x}{{\rm d}t^2} + 2\Gamma\omega_0\frac{{\rm d}x}{{\rm d}t} + \omega_0^2 x = \frac{1}{m}F_0\sin(\omega t). \qquad (21)$$

Here, Γ is the non-dimensional loss factor, ω_0 is the resonance frequency of the oscillator, $\frac{1}{m}F_0$ is the amplitude of the driving force divided by the oscillator mass, and ω is the frequency of the forcing. The loss factor is related to the quality factor by $\Gamma = 1/(2Q)$, and in the underdamped case $\Gamma < 1$, the solution becomes

$$x(t) = A\Bigg[\sin(\omega t+\phi) - \frac{\omega\,{\rm e}^{-\Gamma\omega_0 t}}{\omega_0\sqrt{1-\Gamma^2}}\sin\left(\sqrt{1-\Gamma^2}\,\omega_0 t+\phi\right)\Bigg]. \qquad (22)$$

The amplitude A and the phase shift ϕ between the forcing and the response are known functions of $\frac{F_0}{m}$, ω_0, ω, and Γ, which are not relevant for the present study. From Eq. (22) we obtain the velocity ${\rm d}x/{\rm d}t$, leading to the total energy E of the oscillator,

$$E = \tfrac{1}{2}m\omega_0^2x^2 + \tfrac{1}{2}m\left(\frac{{\rm d}x}{{\rm d}t}\right)^2. \qquad (23)$$

Based on Eqs. (22) and (23), the characteristic timescale τ_E for the build-up of the acoustic energy is found to be

$$\tau_E = \frac{1}{2\Gamma\omega_0} = \frac{Q}{\omega_0}. \tag{24}$$

The build-up of the energy in the single harmonic oscillator, calculated at $\omega = \omega_0$ with $\Gamma = 1.20 \times 10^{-3}$, is shown in the inset of Fig. 3 together with the build-up of acoustic energy $E_{\rm ac}(t)$ of the microfluidic channel solved numerically at resonance, $\omega = 2\pi f_{\rm res}$. The analytical and numerical results are in good agreement, and we conclude that the build-up of acoustic energy in the channel cavity can be modeled as a single harmonic oscillator. The energy builds up to 95% of its steady value in about $500\,t_0 \approx 8\,\tau_E$.

B. Decomposition of the velocity field

The task of calculating the build-up of the acoustic streaming flow is a multi-scale problem, because the amplitude of the oscillating acoustic velocity field is several orders of magnitude larger than the magnitude of the streaming flow. This is indeed the very reason that we can apply the perturbation expansion

$$\boldsymbol{v} = \boldsymbol{v}_1 + \boldsymbol{v}_2, \tag{25}$$

and decompose the non-linear governing equations into a set of linear first-order equations and a set of second-order equations. However, there is also another level of difference in velocity scaling. In the purely periodic state, the velocity can be Fourier decomposed as

$$\boldsymbol{v}(\boldsymbol{r},t) = \boldsymbol{v}_1^{\omega}(\boldsymbol{r})\sin(\omega t) + \boldsymbol{v}_2^{2\omega}(\boldsymbol{r})\sin(2\omega t) + \boldsymbol{v}_2^{0}(\boldsymbol{r}), \tag{26}$$

where $\boldsymbol{v}_1^{\omega}(\boldsymbol{r})$ is the steady amplitude of the first-order harmonic component, $\boldsymbol{v}_2^{2\omega}(\boldsymbol{r})$ is the steady amplitude of the second-order frequency-doubled component, and $\boldsymbol{v}_2^{0}(\boldsymbol{r})$ is the magnitude of the second-order steady velocity component referred to as the acoustic streaming flow. The orders of magnitude of the three velocity components in the periodic state are given by

$$v_1^{\omega} \sim Q v_{\rm bc}, \quad v_2^{2\omega} \sim \frac{Q^3 v_{\rm bc}^2}{c_s}, \quad v_2^{0} \sim \frac{Q^2 v_{\rm bc}^2}{c_s}. \tag{27}$$

The order of v_1 is derived in the one-dimensional acoustic cavity example presented in Ref. [30], the order of v_2^0 is given by the well-known Rayleigh theory, while the order of $v_2^{2\omega}$ is a new result derived in Appendix A. The magnitude of $v_2^{2\omega}$ is a factor of Q larger than what is expected from dimensional analysis of the second-order equation (8c). Consequently, the criterion $|v_2| \ll |v_1|$ for the perturbation expansion becomes

$$Q^2 v_{\rm bc} \ll c_s, \tag{28}$$

which is more restrictive than the usual criterion based on the first-order perturbation expansion, $Q v_{\rm bc} \ll c_s$. Thus, the perturbation expansion becomes invalid for smaller values of $v_{\rm bc}$ than previously expected.

In the transient regime we cannot Fourier decompose the velocity field. Instead, we propose a decomposition using envelope functions inspired by Eq. (26),

$$\boldsymbol{v}(\boldsymbol{r},t) = \boldsymbol{v}_1^{\omega}(\boldsymbol{r},t)\sin(\omega t) + \boldsymbol{v}_2^{2\omega}(\boldsymbol{r},t)\sin(2\omega t) + \boldsymbol{v}_2^{0}(\boldsymbol{r},t). \tag{29}$$

Here, the amplitudes are slowly varying in time compared to the fast oscillation period t_0. We can no longer separate $\boldsymbol{v}_2^{2\omega}$ and $\boldsymbol{v}_2^{0}$ before solving the second-order time-dependent equations (7) and (8). To obtain the time-dependent magnitude of the quasi-steady streaming velocity mode $\boldsymbol{v}_2^0$, we need to choose a good velocity probe, and we thus form the unsteady time-average of $\boldsymbol{v}_2(\boldsymbol{r},t)$,

$$\big\langle \boldsymbol{v}_2(\boldsymbol{r},t) \big\rangle = \int_{t-t_0/2}^{t+t_0/2} \boldsymbol{v}_2(\boldsymbol{r},t')\,\mathrm{d}t'. \tag{30}$$

The time-averaging is done with a fifth-order Romberg integration scheme [31] using data points with a uniform spacing of $t_0/16$ in the time interval of width t_0.

C. Steady and unsteady streaming flow

In this section we compare the unsteady time-averaged second-order velocity field $\big\langle \boldsymbol{v}_2(\boldsymbol{r},t) \big\rangle$, from the time-domain simulations, with the steady time-averaged second-order velocity field $\big\langle \boldsymbol{v}_2^{\rm fd}(\boldsymbol{r},\infty) \big\rangle$, from the frequency-domain simulation. Figure 4(a) and (b) each shows a snapshot in time of the transient $\boldsymbol{v}_1$ and $\boldsymbol{v}_2$, respectively. For $\boldsymbol{v}_2(\boldsymbol{r},t)$, the oscillatory component $\boldsymbol{v}_2^{2\omega}(\boldsymbol{r},t)\sin(2\omega t)$ dominates, as it is two orders of magnitude larger than the quasi-steady component $\boldsymbol{v}_2^{0}(\boldsymbol{r},t)$. However, at late times, here $t = 3000\,t_0$, the amplitude $\boldsymbol{v}_2^{2\omega}(\boldsymbol{r},t)$ has converged, and in $\big\langle \boldsymbol{v}_2(\boldsymbol{r},t) \big\rangle$ the oscillatory component average to zero and only the quasi-steady component remains.

The unsteady time average $\big\langle \boldsymbol{v}_2(\boldsymbol{r},t) \big\rangle$ evaluated at $t = 3000\,t_0$ is shown in Fig. 4(c), exhibiting a single flow roll, in agreement with the classical Rayleigh streaming flow. In Fig. 4(d) is shown the steady $\big\langle \boldsymbol{v}_2^{\rm fd}(\infty) \big\rangle$ from the frequency-domain simulation. Figure 4(c) and 4(d) use the same color scaling for the velocity magnitude, to evaluate the convergence of the unsteady streaming flow $\big\langle \boldsymbol{v}_2(3000\,t_0) \big\rangle$ towards the steady streaming flow $\big\langle \boldsymbol{v}_2^{\rm fd}(\infty) \big\rangle$, and the two solutions agree well both qualitatively and quantitatively. The convergence parameter C, Eq. (19), of $\big\langle \boldsymbol{v}_2(3000\,t_0) \big\rangle$ with respect to $\big\langle \boldsymbol{v}_2^{\rm fd}(\infty) \big\rangle$ is $C = 0.01$, and if we multiply $\big\langle \boldsymbol{v}_2 \big\rangle$ by a free factor, taking into account that $\big\langle \boldsymbol{v}_2 \big\rangle$ has not fully converged at $t = 3000\,t_0$, the convergence parameter can be reduced to $C = 0.008$. The remaining small difference between the unsteady $\big\langle \boldsymbol{v}_2(3000\,t_0) \big\rangle$ and the steady $\big\langle \boldsymbol{v}_2^{\rm fd}(\infty) \big\rangle$ is attributed to the finite temporal resolution of the time marching scheme. We can thus conclude that the time-domain streaming simulation converges well towards the

frequency-domain simulation, and this constitutes the primary validation of the unsteady non-periodic simulations.

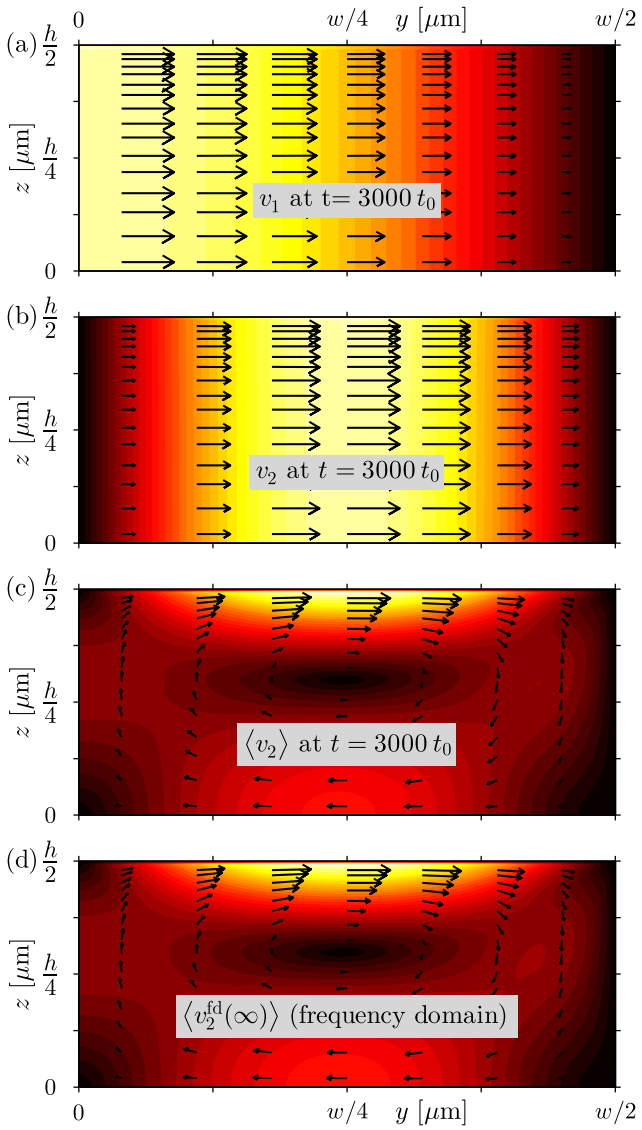

FIG. 4. (Color online) (a) Snapshot of the oscillatory first-order velocity field $\boldsymbol{v}_1$ (vectors) and its magnitude [color plot ranging from 0 m/s (black) to 0.7 m/s (white)] at $t = 3000\,t_0$. (b) Snapshot of the oscillatory second-order velocity field $\boldsymbol{v}_2$ (vectors) and its magnitude [color plot ranging from 0 m/s (black) to 0.02 m/s (white)] at $t = 3000\,t_0$. (c) Snapshot of the unsteady time-averaged second-order velocity field $\langle \boldsymbol{v}_2 \rangle$ (vectors), Eq. (30), and its magnitude [color plot ranging from 0 mm/s (black) to 0.1 mm/s (white)] at $t = 3000\,t_0$. (d) Steady time-averaged second-order velocity field $\langle \boldsymbol{v}_2^{\mathrm{fd}}(\infty) \rangle$ (vectors), Eqs. (11) and (12), and its magnitude [color scaling as in (c)]. In both the time-domain and the frequency-domain simulations the parameters of the oscillating velocity boundary condition was $\omega = 2\pi f_{\mathrm{res}}$ and $v_{\mathrm{bc}} = \omega d$, with wall displacement $d = 1\,\mathrm{nm}$.

D. Build-up of the velocity field

To visualize the build-up of the acoustic fields over short and long timescales, we have chosen the three point probes shown in Fig. 1(b). The oscillating first-order velocity field is probed in the center of the channel $(0, 0)$, far from the walls in order to measure the bulk amplitude of the acoustic field. The horizontal component of the second-order velocity v_{y2} is probed on the horizontal symmetry axis at $(\frac{1}{4}w, 0)$, where the oscillatory component $\boldsymbol{v}_2^{2\omega}$ has it maximum amplitude. The vertical component of the second-order velocity v_{z2} is probed on the vertical symmetry axis at $(0, \frac{1}{4}h)$ where the oscillatory component $\boldsymbol{v}_2^{2\omega}$ is small and of the same order as the quasi-steady component $\boldsymbol{v}_2^0$, making the unsteady time-averaged second-order velocity at this point a good probe for the quasi-steady streaming velocity.

In Fig. 5 is shown the build-up of the velocity probes (a-c) and their time-averages (d-f) for the first 20 oscillations. The thick lines are the oscillating velocities while, the thin lines are the envelopes of the oscillations. Already within the first 20 oscillation periods we see in Fig. 5(f) the build-up of a quasi-steady velocity component. The unsteady time-averaged horizontal velocity $\langle v_{y2} \rangle$, Fig. 5(e), is still primarily oscillatory, showing that for this probe the oscillatory component $\boldsymbol{v}_2^{2\omega}$ is much larger than the quasi-steady component $\boldsymbol{v}_2^0$.

The temporal evolution of the velocity probes on the longer time scale up to $t = 1500\,t_0$ is shown in Fig. 6. In Fig. 6(a) and (b) the amplitudes of the oscillatory first- and second-order velocity components are seen to stabilize around $t = 700\,t_0 \sim 10\,\tau_E$. The steady amplitudes of the velocity probes Fig. 6 agree with the theoretical predictions of Eq. (27), yielding orders of magnitude $v_1^{\omega}/c_s \sim 3 \times 10^{-4}$ (Fig. 6(a)), $v_2^{2\omega}/c_s \sim 5 \times 10^{-5}$ (Fig. 6(b)), and $v_2^0/c_s \sim 1 \times 10^{-7}$ (Fig. 6(e) and 6(f)). The time-average of v_{y1} tends to zero for long times as it is purely oscillatory, whereas the time-average of v_{y2} tends to the magnitude of the quasi-steady component $\boldsymbol{v}_2^0$, because the large but now steady oscillatory component $\boldsymbol{v}_2^{2\omega}$ average to zero. The dashed lines in Fig. 6(e) and (f) represent the magnitude of the steady time-averaged second-order velocity $\langle \boldsymbol{v}_2^{\mathrm{fd}}(\infty) \rangle$ from the frequency-domain simulation.

V. ACOUSTIC STREAMING GENERATED BY PULSED ACTUATION

In the following we study the effects of switching the oscillatory boundary actuation on and off on a timescale much longer than the oscillation period t_0 in either single- or multi-pulse mode. The aim is to investigate whether such an approach can suppress the influence of the streaming flow on suspended particles relative to that of the radiation force.

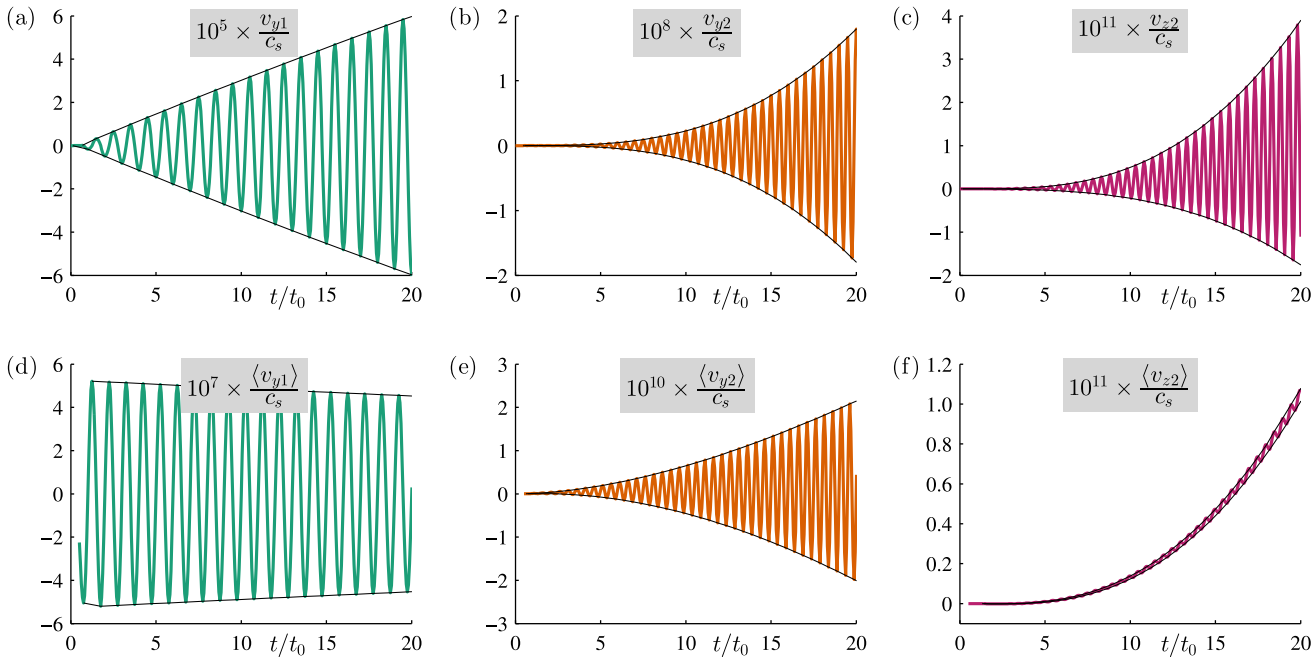

FIG. 5. (Color online) Velocity probes for the initial time interval $0 < t < 20\,t_0$. (a-c) probes for the first- and second-order velocity (a) $v_{y1}(0,0)$, (b) $v_{y2}(w/4,0)$, and (c) $v_{z2}(0,h/4)$. (d-f) Running time-average Eq. (30) on an interval one oscillation period wide of the velocity probes in (a-c). The thick lines show the oscillating velocity probes while the thin lines emphasize the envelopes of the oscillations.

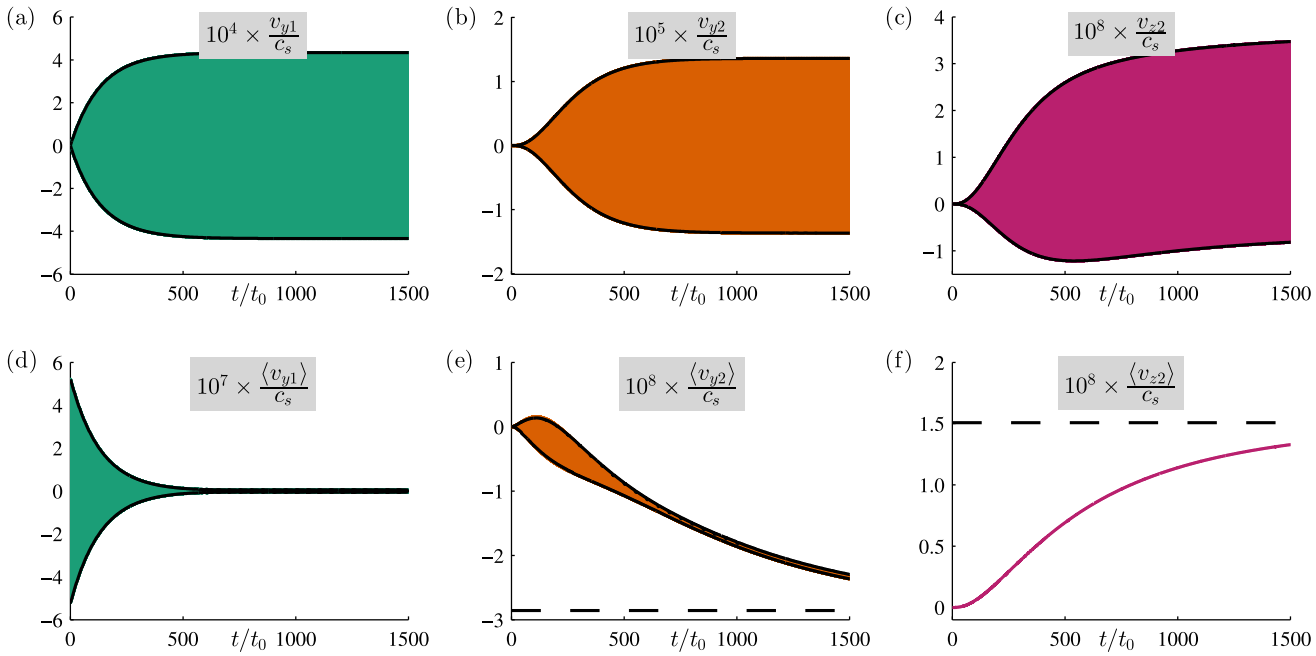

FIG. 6. (Color online) The velocity probes from Fig. 5, but now extended to the long time interval $0 < t < 1500\,t_0$, showing the convergence towards a periodic state. The dashed lines in (e) and (f) indicate the magnitude of the steady time-averaged second-order velocity from the frequency-domain simulation Eqs. (11) and (12).

TABLE II. Characteristic timescales. The values are obtained by using the kinematic viscosity $\nu = \eta/\rho_0 = 8.93\times10^{-7}$ m^2/s (Table I), the Q-factor $Q = 416$ (Fig. 3), and the channel height $h = 160$ µm (Fig. 1).

Timescale	Expression	Value
Oscillation time	t_0	5.1×10^{-7} s $\approx$ 1 t_0
Resonance relaxation time	$\tau_E = \frac{Q}{2\pi} t_0$	3.4×10^{-5} s $\approx$ 66 t_0
Momentum diffusion time	$\tau_\nu = \frac{1}{2\nu}\left(\frac{h}{8}\right)^2$	2.8×10^{-4} s $\approx$ 558 t_0

A. Single-pulse scaling analysis

A striking feature of Fig. 6, is the separation of timescales between the roughly exponential build-up of the acoustic resonance in Fig. 6(a) and of the streaming flow in Fig. 6(f). It appears that the resonance, and hence the acoustic radiation force on a suspended particle, is fully established almost ten times faster than the streaming flow and the resulting drag force on a suspended particle. To investigate this further, we look at the scaling provided by the three timescales relevant for the problem of transient acoustic streaming, all listed in Table II: the oscillation time t_0 of the acoustic wave, the resonance relaxation time τ_E of the acoustic cavity, and the momentum diffusion time τ_ν governing the quasi-steady streaming flow.

The momentum diffusion time is $\tau_\nu = \frac{1}{2\nu}\left(\frac{1}{8}h\right)^2$, where $\nu = \frac{\eta}{\rho_0}$ is the kinematic viscosity, and $\frac{1}{8}h$ is approximately half the distance between the top boundary and the center of the streaming flow roll. Inserting the relevant numbers, see Table II, we indeed find that $\tau_E \approx 66\, t_0$ is much faster than $\tau_\nu \approx 558 t_0$. However, this separation in timescales does not guarantee a suppression of streaming relative to the radiation force. One problem is that the streaming is driven by the shear stresses in the boundary layer, and these stresses builds up much faster given the small thickness of the boundary layer. This we investigate further in the following subsection. Another problem is that the large momentum diffusion time τ_ν implies a very slow decay of the streaming flow, once it is established. The latter effect, we study using the following analytical model. Consider a quantity f (streaming velocity or acoustic energy), with a relaxation time τ and driven by a pulsed source term P of pulse width t_{pw}. The rate of change of f is equivalent to Eq. (14b),

$$\partial_t f = P - \frac{1}{\tau} f, \tag{31a}$$

$$P = \begin{cases} \frac{1}{\tau} f_0, & \text{for } 0 < t < t_{\mathrm{pw}}, \\ 0, & \text{otherwise}, \end{cases} \tag{31b}$$

where $\frac{1}{\tau} f_0$ is a constant input power. This simplified analytical model captures the roughly exponential build-up and decay characteristics of our full numerical model, and allows for analytical studies of the time-integral of $f(t)$. For a final time $t > t_{\mathrm{pw}}$ we find

$$\int_0^t f(t')\,\mathrm{d}t' = f_0 t_{\mathrm{pw}} - f_0 \tau \left[\mathrm{e}^{-\frac{1}{\tau}(t-t_{\mathrm{pw}})} - \mathrm{e}^{-\frac{1}{\tau}t}\right]. \tag{32}$$

From this we see that when $t \gg \tau + t_{\mathrm{pw}}$ the time-integral of $f(t)$ is approximately $f_0 t_{\mathrm{pw}}$ and not dependent on the relaxation time τ. Consequently, if both the acoustic energy and the acoustic streaming can be described by exponential behavior with the respective relaxation times τ_E and τ_ν, the ratio of their time-integrated effects is the same whether the system is driven by a constant actuation towards their steady time-periodic state or by a pulsed actuation with pulse width t_{pw}. This simplified analytical model indicates that there is little hope of decreasing acoustic streaming relative to the acoustic radiation force by applying pulsed actuation, in spite of the order of magnitude difference between the relaxation times for the acoustic energy and the streaming.

B. Single-pulse numerical analysis

We investigate the features of pulsed actuation more detailed in the following by numerical analysis. In Fig. 7 is shown the temporal evolution of the total acoustic energy $\langle E_{\mathrm{ac}} \rangle$ and the magnitude of the acoustic streaming flow $\langle v_{\mathrm{str}} \rangle$ for the three cases: (i) the build-up towards the periodic state, (ii) a single long actuation pulse, and (iii) a single short actuation pulse. The magnitude of the acoustic streaming is measured by the unsteady time-averaged velocity probe

$$\langle v_{\mathrm{str}} \rangle = \langle v_{z2}(0, \frac{1}{4}h) \rangle, \tag{33}$$

and the unsteady energy and streaming probes obtained from the time-domain simulation are normalized by their corresponding steady time-averaged values from the frequency-domain simulation.

We introduce the streaming ratio χ to measure the influence of streaming-induced drag on suspended particles relative to the influence of the acoustic radiation force for the unsteady time-domain solution, in comparison to the periodic frequency-domain solution. To calculate the relative displacement Δs of particles due to each of the two forces, respectively, we compare their time integrals. Since the radiation force scales with the acoustic energy density, we define the streaming ratio $\chi(t)$ as

$$\chi(t) = \frac{\displaystyle\int_0^t \frac{\langle v_{\mathrm{str}}(t') \rangle}{\langle v_{\mathrm{str}}^{\mathrm{fd}}(\infty) \rangle}\,\mathrm{d}t'}{\displaystyle\int_0^t \frac{\langle E_{\mathrm{ac}}(t') \rangle}{\langle E_{\mathrm{ac}}^{\mathrm{fd}}(\infty) \rangle}\,\mathrm{d}t'} \sim \frac{\dfrac{\Delta s_{\mathrm{str}}}{\Delta s_{\mathrm{str}}^{\mathrm{fd}}}}{\dfrac{\Delta s_{\mathrm{rad}}}{\Delta s_{\mathrm{rad}}^{\mathrm{fd}}}}, \tag{34}$$

where Δs_{str} and Δs_{rad} are the total particle displacements in the time from 0 to t due to the streaming-induced drag force and the acoustic radiation force, respectively. In the periodic state $\chi = 1$, and to obtain

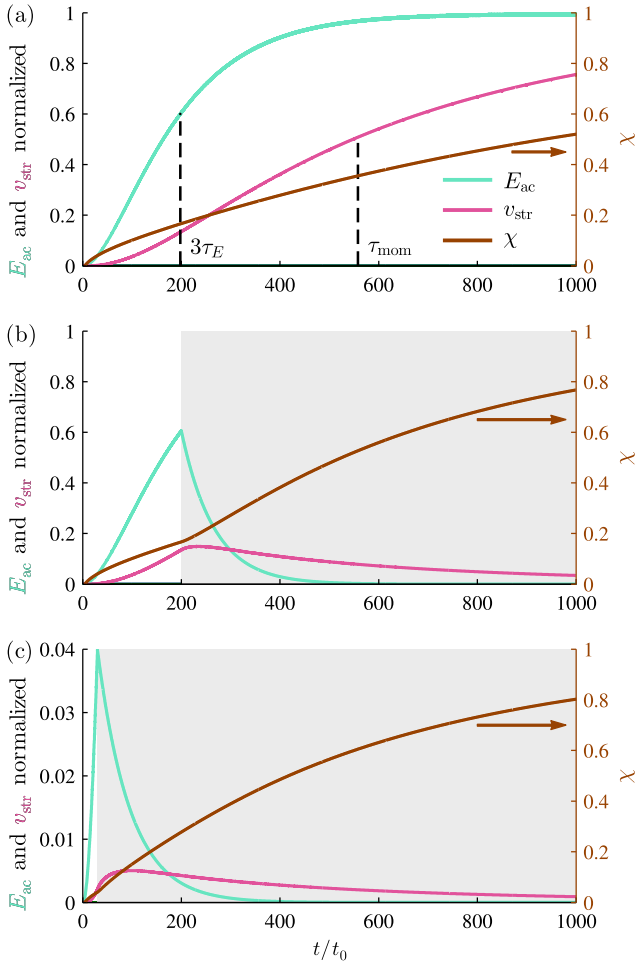

FIG. 7. (Color online) Acoustic energy $\langle E_{ac}(t)\rangle/\langle E_{ac}^{fd}(\infty)\rangle$ Eq. (13) (light green), streaming velocity $\langle v_{str}(t)\rangle/\langle v_{str}^{fd}(\infty)\rangle$ Eq. (33) (medium purple), and streaming ratio $\chi(t)$ Eq. (34) (dark brown, right ordinate axis). The gray background indicates the time intervals where the actuation is turned off. (a) Constant actuation for $0 < t < 3000\,t_0$. (b) Actuation on for $0 < t < 200\,t_0$ followed by no actuation for $200\,t_0 < t < 1000\,t_0$. (c) Actuation on for $0 < t < 30\,t_0$ followed by no actuation for $30\,t_0 < t < 1000\,t_0$.

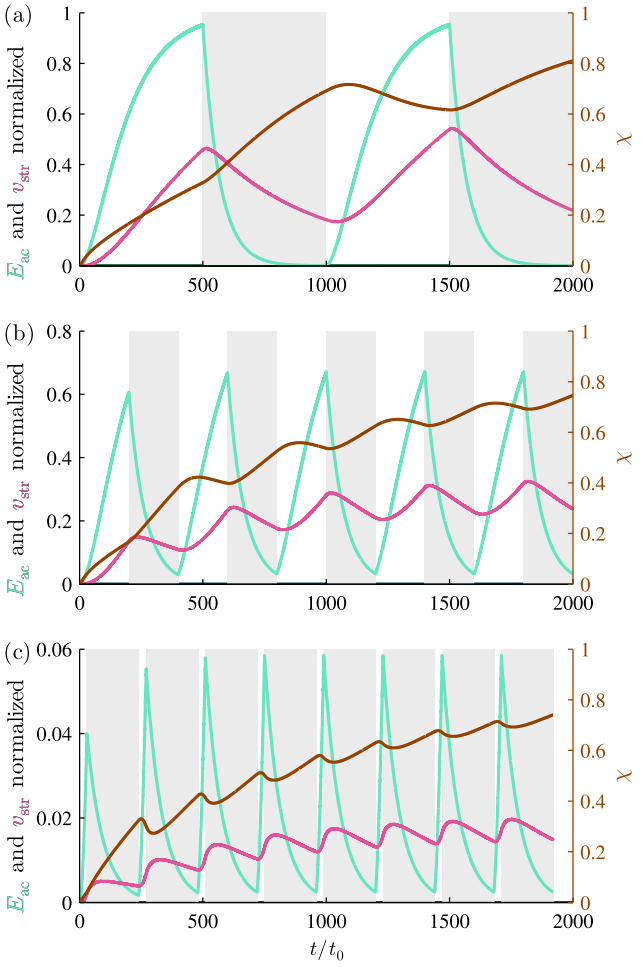

FIG. 8. (Color online) The same probes as in Fig. 7 but for the following pulsed actuation schemes: (a) actuation is on for $500\,t_0$ followed by no actuation for $500\,t_0$ repeatedly, (b) actuation is on for $200\,t_0$ followed by no actuation for $200\,t_0$ repeatedly, and (c) actuation is on for $30\,t_0$ followed by no actuation for $210\,t_0$ repeatedly.

radiation force-dominated motion of smaller particles, we need to achieve a smaller value of χ. Obtaining a value of $\chi = 0.8$ at time t_{end}, implies that the ratio of the relative displacement due to the streaming-induced drag force and the radiation force for the time interval $0 < t < t_{end}$ is 20% lower than in the periodic state, corresponding to a 20% reduction of the critical particle size for acoustophoretic focusing, defined in Ref. [2], assuming the particles can be focused during the time interval $0 < t < t_{end}$.

Figure 7(a) shows $\langle E_{ac}\rangle$, $\langle v_{str}\rangle$ and χ during the build-up towards the periodic state. χ approaches unity slower than $\langle v_{str}\rangle$ because χ is an integration of the streaming and radiation contributions, whereas v_{str} probes the instantaneous magnitude of the streaming flow. Figure 7(b) and 7(c) show $\langle E_{ac}\rangle$, $\langle v_{str}\rangle$, and χ when the actuation is turned off at $t = 200\,t_0$ and $t = 30\,t_0$, respectively. When the actuation is turned off, $\langle E_{ac}\rangle$ decays faster than $\langle v_{str}\rangle$ and thus χ begins to increase more rapidly, reaching $\chi = 0.8$ around $t = 1000\,t_0$ in both cases. From the results shown in Fig. 7 it does not seem advantages to turn off the actuation, as this only causes χ to increase faster than for constant actuation. Figure 7(c) further shows that when the actuation is turned off, $\langle E_{ac}\rangle$ immediately begins to decay, whereas $\langle v_{str}\rangle$ continues to increase for some time, due to the present acoustic energy in the system that still provides a driving force for the streaming flow.

C. Multi-pulse numerical analysis

From the single pulse results shown in Fig. 7 there is no indication of any optimum for the pulse duration or repetition period, and in general it provides little hope that pulsed actuation should lead to lower values of χ. Figure 8 shows $\langle E_{\mathrm{ac}} \rangle$, $\langle v_{\mathrm{str}} \rangle$, and χ for three pulsed schemes with pulse duration $500\,t_0$, $200\,t_0$, and $30\,t_0$ and pause duration $500\,t_0$, $200\,t_0$, and $210\,t_0$, respectively. For all three pulsed schemes, χ increases faster than for the constant actuation Fig. 7(a), thus not indicating any increased suppression of the streaming.

VI. DISCUSSION

Solving numerically the time-dependent problem of the acoustic cavity and the build-up of acoustic streaming, presents new challenges, which are not present in the purely periodic problem. Firstly, the numerical convergence analysis now involves both the spatial and temporal resolutions. This we addressed in a sequential process by first analyzing the spatial mesh with the periodic frequency-domain solution, and thereafter doing a thorough convergence analysis with respect to the temporal resolution. Secondly, the convergence of the transient solution towards the periodic state was poor for actuation frequencies away from the resonance frequency of the system. This makes off-resonance simulation computationally costly, as it requires a better temporal resolution, and it complicates comparison of simulations at resonance with simulations off resonance. Thirdly, small numerical errors accumulate during the hundred thousand time steps taken during a simulation from a quiescent state to a purely periodic state. These errors need to be suppressed by the numerical time-domain solver, which in the generalized-alpha solver is done through the alpha parameter. Simulation with higher temporal resolution required lower values of the alpha parameter to have more suppression of accumulated numerical errors.

The model system used in this study is a simplification of an actual device. The vibration of only the side walls, and not the top and bottom walls, stands in contrast to the physical system, in which the whole device is vibrating in a non-trivial way, difficult to predict, and only the overall amplitude and the frequency of the actuation is controlled experimentally. Furthermore, our model only treats the two-dimensional cross section of a long straight channel, whereas experimental studies have shown that there are dynamics along the length of the channel [23]. Nevertheless, successful comparison, both qualitatively and quantitatively, have been reported between the prediction of this simplified numerical model and experimental measurements of Rayleigh streaming in the cross sectional plane of a microchannel [10], which makes it reasonable to assume that the time-dependent simulations also provide reliable predictions.

It is also important to stress that our model only describes the fluid and not the motion of the suspended particles. Integrating the forces acting on the particles becomes vastly more demanding when the streaming flow is unsteady, because the drag forces from the oscillating velocity components $\boldsymbol{v}_1$ and $\boldsymbol{v}_2^{2\omega}$ do average out, as they do in the case of a purely time-periodic state. To include this contribution in the particle tracking scheme, the forces on the particles need to be integrated with a time step of a fraction of the oscillation period, which makes the solution of particle trajectories over several seconds a very demanding task using brute-force integration of the equations of motion.

Our analysis of the pulsed actuation schemes showed that the slow decay of the streaming flow makes pulsation inefficient in reducing the streaming-induced drag force compared to the radiation force. Such a reduction may, however, be obtained by a rapid switching between different resonances each resulting in similar radiation forces but different spatial streaming patterns which on averages cancel each other out, thus fighting streaming with streaming. An idea along these lines was presented by Ohlin *et al.* Ref. [32], who used frequency sweeping to diminish the streaming flows in liquid-filled wells in a multi-well plate for cell analysis. However, the prediction of particle trajectories under such multi-resonance conditions requires an extensive study as described above.

Experimentally, the use of pulsed actuation to decrease streaming flow has been reported by Hoyos *et al.* Ref. [18]. However, this study is not directly comparable to our analysis, as we treat the build-up of Rayleigh streaming perpendicular to the pressure nodal plane, whereas Hoyos *et al.* study the streaming flow in this plane. Such in-nodal-plane streaming flows have been studied numerically by Lei *et al.* [12, 13], though only with steady actuation. The contradicting results of our theoretical study and the experimental study of Hoyos *et al.* may thus rely on the differences of the phenomena studied.

VII. CONCLUSION

In this work, we have presented a model for the transient acoustic fields and the unsteady time-averaged second-order velocity field in the transverse cross-sectional plane of a long straight microchannel. The model is based on the usual perturbation approach for low acoustic field amplitudes, and we have solved both first- and second-order equations in the time domain for the unsteady transient case as well as in the frequency domain for the purely periodic case. This enabled us to characterize the build-up of the oscillating acoustic fields and the unsteady streaming flow.

Our analysis showed that the build-up of acoustic energy in the channel follows the analytical prediction obtained for a single damped harmonic oscillator with sinusoidal forcing, and that a quasi-steady velocity component is established already within the first few oscillations and increases in magnitude as the acoustic energy builds

up. We have also found that for a resonance with quality factor Q, the amplitude of the oscillatory second-order velocity component is a factor of Q larger than what is expected from dimensional analysis, which results in a more restrictive criterion for the validity of the perturbation expansion, compared to the usual one based on the first-order perturbation expansion.

Furthermore, contrary to a simple scaling analysis of the time scales involved in the fast build-up of radiation forces and slow build-up of drag-induced streaming forces, we have found that pulsating oscillatory boundary actuation does not reduce the time-integrated streaming-induced drag force relative to the time-integrated radiation force. As a result, pulsating actuation does not prevent streaming flows perpendicular to the pressure nodal plane from destroying the ability to focus small particles by acoustophoresis.

ACKNOWLEDGMENTS

This work was supported by the Danish Council for Independent Research, Technology, and Production Sciences (grant no. 11-107021).

Appendix A: Amplitude of the second-order oscillatory velocity field

Extending to second order the one-dimensional example given in Ref. [30], we derive in this appendix the order of magnitude of the second-order oscillatory component $v_2^{2\omega}$, which was stated in Eq. (27).

Like $\langle g_2 \rangle$ denotes time-averaging over one oscillation period, Eq. (30), and in the periodic state equals the zero-order temporal Fourier component of the field, then $g_2^{2\omega}(\boldsymbol{r})$ denotes the complex amplitude of the oscillatory second-order mode and is given by the second-order Fourier component

$$g_2^{2\omega}(\boldsymbol{r}) = \frac{1}{T}\int_{t-T/2}^{t+T/2} g_2(\boldsymbol{r},t')\mathrm{e}^{-i2\omega t'}\,\mathrm{d}t'. \tag{A1}$$

By using the general formula for the real part of any complex number Z, $\mathrm{Re}[Z] = \frac{1}{2}(Z+Z^*)$, the product $A(\boldsymbol{r},t)B(\boldsymbol{r},t)$ of two oscillating fields $A(\boldsymbol{r},t) = \mathrm{Re}\left[A\mathrm{e}^{-\mathrm{i}\omega t}\right]$ and $B(\boldsymbol{r},t) = \mathrm{Re}\left[B\mathrm{e}^{-\mathrm{i}\omega t}\right]$ can be decomposed into a steady component and an oscillatory component

$$\begin{aligned} A(t)B(t) &= \tfrac{1}{2}\Big(A\mathrm{e}^{-\mathrm{i}\omega t} + A^*\mathrm{e}^{\mathrm{i}\omega t}\Big)\tfrac{1}{2}\Big(B\mathrm{e}^{-\mathrm{i}\omega t} + B^*\mathrm{e}^{\mathrm{i}\omega t}\Big) \\ &= \tfrac{1}{2}\,\mathrm{Re}\Big[A^*B\Big] + \tfrac{1}{2}\,\mathrm{Re}\Big[AB\mathrm{e}^{-\mathrm{i}2\omega t}\Big], \end{aligned} \tag{A2}$$

from which we introduce the following notation

$$\big\langle AB\big\rangle \equiv \tfrac{1}{2}\,\mathrm{Re}\Big[A^*B\Big], \tag{A3}$$

$$\big(AB\big)^{2\omega} \equiv \tfrac{1}{2}AB, \tag{A4}$$

where A and B could be any first-order fields.

The governing equations for the oscillatory second-order component $\boldsymbol{v}_2^{2\omega}$ can be derived from Eqs. (7) and (8) and in the one-dimensional problem treated in Ref. [30], where the top and bottom walls are not taken into account, they become

$$-\mathrm{i}2\omega\kappa_s p_2^{2\omega} = -\partial_y v_2^{2\omega} - \kappa_s\big(v_1\partial_y p_1\big)^{2\omega} \tag{A5a}$$

$$\begin{aligned} -\mathrm{i}2\omega\rho_0 v_2^{2\omega} = &-\partial_y p_2^{2\omega} + \big(\tfrac{4}{3}\eta + \eta^{\mathrm{b}}\big)\,\partial_y^2 v_2^{2\omega} \\ &- \big(\rho_1(-\mathrm{i}\omega v_1)\big)^{2\omega} - \rho_0\big(v_1\partial_y v_1\big)^{2\omega}. \end{aligned} \tag{A5b}$$

Applying the 2ω-rule of Eq. (A4) and the mass continuity Eq. (5), the two last terms of Eq. (A5b) cancel. Inserting Eq. (A5a) into Eq. (A5b), the governing equation for $v_2^{2\omega}$ becomes

$$4k_0^2 v_2^{2\omega} + (1 - \mathrm{i}4\Gamma)\partial_y^2 v_2^{2\omega} + \frac{1}{2}\kappa_s\partial_y(v_1\partial_y p_1) = 0, \tag{A6}$$

where Γ is the non-dimensional bulk damping coefficient given by $\Gamma = \frac{\omega\eta}{2\rho_0 c_s^2}\Big(\frac{4}{3} + \frac{\eta^{\mathrm{b}}}{\eta}\Big)$, and $k_0 = \frac{\omega}{c_s}$ is the wavenumber. For the fundamental half-wave resonance, the spatial dependence of the source term $\partial_y(v_1\partial_y p_1)$ is $\sin(2k_0 y)$, and the guess for the inhomogeneous solution to Eq. (A6) thus becomes

$$v_2^{2\omega,\mathrm{inhom}} = C\sin(2k_0 y). \tag{A7}$$

Inserting the inhomogeneous solution Eq. (A7) into the governing equation (A6), we note that the first term cancels with the "1" in the parentheses of the second term, and the order of magnitude of the inhomogeneous solution thus becomes

$$|v_2^{2\omega}| = C \sim \frac{1}{\Gamma}\kappa_s|v_1||p_1| \sim \frac{1}{\Gamma^3}\frac{v_{\mathrm{bc}}^2}{c_s} \sim Q^3\frac{v_{\mathrm{bc}}^2}{c_s}, \tag{A8}$$

which is the result stated in Eq. (27).

[1] H. Bruus, J. Dual, J. Hawkes, M. Hill, T. Laurell, J. Nilsson, S. Radel, S. Sadhal, and M. Wiklund, Lab Chip **11**, 3579 (2011).

[2] P. B. Muller, R. Barnkob, M. J. H. Jensen, and H. Bruus, Lab Chip **12**, 4617 (2012).

[3] R. Barnkob, P. Augustsson, T. Laurell, and H. Bruus, Phys Rev E **86**, 056307 (2012).

[4] L. Rayleigh, Philos Trans R Soc London **175**, 1 (1884).

[5] H. Schlichting, Phys Z **33**, 327 (1932).

[6] W. L. Nyborg, J Acoust Soc Am **30**, 329 (1958).

[7] M. Hamilton, Y. Ilinskii, and E. Zabolotskaya, J Acoust Soc Am **113**, 153 (2003).

[8] M. Hamilton, Y. Ilinskii, and E. Zabolotskaya, J Acoust Soc Am **114**, 3092 (2003).

[9] A. Y. Rednikov and S. S. Sadhal, J Fluid Mech **667**, 426 (2011).

[10] P. B. Muller, M. Rossi, A. G. Marin, R. Barnkob, P. Augustsson, T. Laurell, C. J. Kähler, and H. Bruus, Phys Rev E **88**, 023006 (2013).

[11] P. B. Muller and H. Bruus, Phys Rev E **90**, 043016 (2014).

[12] J. Lei, P. Glynne-Jones, and M. Hill, Lab Chip **13**, 2133 (2013).

[13] J. Lei, M. Hill, and P. Glynne-Jones, Lab Chip **14**, 532 (2014).

[14] W. L. Nyborg, J Acoust Soc Am **25**, 68 (1953).

[15] C. Lee and T. Wang, J Acoust Soc Am **85**, 1081 (1989).

[16] P. Hahn and J. Dual, Physics of Fluids **27**, 062005 (2015).

[17] N. Nama, R. Barnkob, Z. Mao, C. J. Kähler, F. Costanzo, and T. J. Huang, Lab Chip **15**, 2700 (2015).

[18] M. Hoyos and A. Castro, Ultrasonics **53**, 70 (2013).

[19] M. Antfolk, P. B. Muller, P. Augustsson, H. Bruus, and T. Laurell, Lab Chip **14**, 2791 (2014).

[20] J. Wang and J. Dual, J. Phys. A: Math. Theor. **42**, 285502 (2009).

[21] A. D. Pierce, *Acoustics* (Acoustical Society of America, Woodbury, 1991).

[22] L. D. Landau and E. M. Lifshitz, *Statistical Physics, Part 1*, 3rd ed., Vol. 5 (Butterworth-Heinemann, Oxford, 1980).

[23] P. Augustsson, R. Barnkob, S. T. Wereley, H. Bruus, and T. Laurell, Lab Chip **11**, 4152 (2011).

[24] COMSOL Multiphysics 4.4, www.comsol.com, (2013).

[25] S. C. Brenner and L. R. Scott, *The Mathematical Theory of Finite Element Methods* (Springer, 2008).

[26] *Comsol Multiphysics Reference Manual version 4.4*.

[27] Matlab 2012a, www.mathworks.com, (2012).

[28] See Supplemental Material at [URL] for Comsol model files, both in a simple version `Muller2015_TimeDepAcoust_simple.mph`, and a full version `Muller2015_TimeDepAcoust_full.mph`, that allows for sectioning in smaller time intervals using the supplied Matlab script `Muller2015_TimeDepAcoust_full.m` with the functions `AVGromb16PBM.m` and `polint.m`.

[29] Comsol Multiphysics Model Library, "Nonlinear Acoustics — Modeling of the 1D Westervelt Equation," (2013).

[30] H. Bruus, Lab Chip **12**, 20 (2012).

[31] W. H. Press, S. A. Teukolsky, W. T. Vetterling, and B. P. Flannery, *Numerical Recipies in C - The Art of Scientific Computing, 2nd edition* (Cambridge University Press, 2002).

[32] M. Ohlin, A. Christakou, T. Frisk, B. Önfelt, and M. Wiklund, in *Proc. 15th MicroTAS, 2 - 6 October 2011, Seattle (WA), USA*, edited by J. Landers, A. Herr, D. Juncker, N. Pamme, and J. Bienvenue (CBMS, 2011) pp. 1612–1614.

Bibliography

[1] H. Bruus, J. Dual, J. Hawkes, M. Hill, T. Laurell, J. Nilsson, S. Radel, S. Sadhal, and M. Wiklund. *Forthcoming lab on a chip tutorial series on acoustofluidics: Acoustofluidics-exploiting ultrasonic standing wave forces and acoustic streaming in microfluidic systems for cell and particle manipulation.* Lab Chip **11**, 3579–3580 (2011).

[2] N. Riley. *Steady streaming.* Annu Rev Fluid Mech **33**, 43–65 (2001).

[3] L. Rayleigh. *On the circulation of air observed in Kundt's tubes, and on some allied acoustical problems.* Philos Trans R Soc London **175**, 1–21 (1884).

[4] A. Kundt. *Ueber eine neue art akustischer staubfiguren und über die anwendung derselben zur bestimmung der schallgeschwindigkeit in festen körpern und gasen.* Ann Phys Chem **127**, 497–523 (1866).

[5] H. Schlichting. *Berechnung ebener periodischer grenzeschichtströmungen.* Phys Z **33**, 327–335 (1932).

[6] W. L. Nyborg. *Acoustic streaming near a boundary.* J Acoust Soc Am **30**, 329–339 (1958).

[7] C. Lee and T. Wang. *Near-boundary streaming around a small sphere due to 2 orthogonal standing waves.* J Acoust Soc Am **85**, 1081–1088 (1989).

[8] A. Y. Rednikov and S. S. Sadhal. *Acoustic/steady streaming from a motionless boundary and related phenomena: generalized treatment of the inner streaming and examples.* J Fluid Mech **667**, 426–462 (2011).

[9] M. Hamilton, Y. Ilinskii, and E. Zabolotskaya. *Thermal effects on acoustic streaming in standing waves.* J Acoust Soc Am **114**, 3092–3101 (2003).

[10] M. Hamilton, Y. Ilinskii, and E. Zabolotskaya. *Acoustic streaming generated by standing waves in two-dimensional channels of arbitrary width.* J Acoust Soc Am **113**, 153–160 (2003).

[11] P. B. Muller, M. Rossi, A. G. Marin, R. Barnkob, P. Augustsson, T. Laurell, C. J. Kähler, and H. Bruus. *Ultrasound-induced acoustophoretic motion of microparticles in three dimensions.* Phys Rev E **88**, 023006 (2013).

[12] L. V. King. *On the acoustic radiation pressure on spheres.* P Roy Soc Lond A Mat **147**, 212–240 (1934).

[13] K. Yosioka and Y. Kawasima. *Acoustic radiation pressure on a compressible sphere.* Acustica **5**, 167–173 (1955).

[14] L. P. Gorkov. *On the forces acting on a small particle in an acoustical field in an ideal fluid.* Sov Phys–Dokl **6**, 773–775 (1962). Doklady Akademii Nauk SSSR 140, 88 (1961).

[15] M. Settnes and H. Bruus. *Forces acting on a small particle in an acoustical field in a viscous fluid.* Phys Rev E **85**, 016327 (2012).

[16] J. T. Karlsen and H. Bruus. *Forces acting on a small particle in an acoustical field in a thermoviscous fluid.* Phys Rev E **submitted** (2015).

[17] H. Bruus, *Theoretical Microfluidics*, (Oxford University Press, Oxford, 2008).

[18] M. Nordin and T. Laurell. *Two-hundredfold volume concentration of dilute cell and particle suspensions using chip integrated multistage acoustophoresis.* Lab Chip **12**, 4610–4616 (2012).

[19] F. Petersson, A. Nilsson, C. Holm, H. Jönsson, and T. Laurell. *Separation of lipids from blood utilizing ultrasonic standing waves in microfluidic channels.* Analyst **129**, 938–43 (2004).

[20] C. Grenvall, P. Augustsson, J. R. Folkenberg, and T. Laurell. *Harmonic microchip acoustophoresis: A route to online raw milk sample precondition in protein and lipid content quality control.* Anal Chem **81**, 6195–6200 (2009).

[21] B. Hammarstrom, T. Laurell, and J. Nilsson. *Seed particle enabled acoustic trapping of bacteria and nanoparticles in continuous flow systems.* Lab Chip **12**, in press (2012, doi: 101039/C2LC40697G).

[22] M. Ohlin, A. E. Christakou, T. Frisk, B. Onfelt, and M. Wiklund. *Influence of acoustic streaming on ultrasonic particle manipulation in a 100-well ring-transducer microplate.* J Micromech Microeng **23**, 035008 (2013).

[23] P.-H. Huang, N. Nama, Z. Mao, P. Li, J. Rufo, Y. Chen, Y. Xie, C.-H. Wei, L. Wang, and T. J. Huang. *A reliable and programmable acoustofluidic pump powered by oscillating sharp-edge structures.* Lab Chip **14**, 4319–4323 (2014).

[24] R. Barnkob, P. Augustsson, T. Laurell, and H. Bruus. *Measuring the local pressure amplitude in microchannel acoustophoresis.* Lab Chip **10**, 563–570 (2010).

[25] P. Augustsson, R. Barnkob, S. T. Wereley, H. Bruus, and T. Laurell. *Automated and temperature-controlled micro-piv measurements enabling long-term-stable microchannel acoustophoresis characterization.* Lab Chip **11**, 4152–4164 (2011).

[26] R. Barnkob, P. Augustsson, T. Laurell, and H. Bruus. *Acoustic radiation- and streaming-induced microparticle velocities determined by microparticle image velocimetry in an ultrasound symmetry plane.* Phys Rev E **86**, 056307 (2012).

[27] S. Lakaemper, A. Lamprecht, I. A. T. Schaap, and J. Dual. *Direct 2D measurement of time-averaged forces and pressure amplitudes in acoustophoretic devices using optical trapping.* Lab Chip **15**, 290–300 (2015).

[28] P. B. Muller, R. Barnkob, M. J. H. Jensen, and H. Bruus. *A numerical study of microparticle acoustophoresis driven by acoustic radiation forces and streaming-induced drag forces.* Lab Chip **12**, 4617–4627 (2012).

[29] P. B. Muller and H. Bruus. *Numerical study of thermoviscous effects in ultrasound-induced acoustic streaming in microchannels.* Phys Rev E **90**, 043016 (2014).

[30] P. B. Muller and H. Bruus. *A theoretical study of time-dependent, ultrasound-induced acoustic streaming in microchannels.* Phys Rev E (submitted September 2015).

[31] M. Antfolk, P. B. Muller, P. Augustsson, H. Bruus, and T. Laurell. *Focusing of submicrometer particles and bacteria enabled by two-dimensional acoustophoresis.* Lab Chip **14**, 2791 (2014).

[32] R. Barnkob. *Physics of microparticle acoustophoresis — Bridging theory and experiment.* Ph.D. thesis, Technical University of Denmark (2012).

[33] N. Nama, R. Barnkob, Z. Mao, C. J. Kähler, F. Costanzo, and T. J. Huang. *Numerical study of acoustophoretic motion of particles in a pdms microchannel driven by surface acoustic waves.* Lab Chip **15**, 2700 (2015).

[34] J. Lei, P. Glynne-Jones, and M. Hill. *Acoustic streaming in the transducer plane in ultrasonic particle manipulation devices.* Lab Chip **13**, 2133–2143 (2013).

[35] J. Lei, M. Hill, and P. Glynne-Jones. *Numerical simulation of 3d boundary-driven acoustic streaming in microfluidic devices.* Lab Chip **14**, 532–541 (2014).

[36] S. M. Hagsäter, T. G. Jensen, H. Bruus, and J. P. Kutter. *Acoustic resonances in microfluidic chips: full-image micro-PIV experiments and numerical simulations.* Lab Chip **7**, 1336–1344 (2007).

[37] P. Hahn and J. Dual. *A numerically efficient damping model for acoustic resonances in microfluidic cavities.* Physics of Fluids **27**, 062005 (2015).

[38] P. Hahn, O. Schwab, and J. Dual. *Modeling and optimization of acoustofluidic microdevices.* Lab Chip **14**, 3937–3948 (2014).

[39] L. D. Landau and E. M. Lifshitz, *Statistical Physics, Part 1*, vol. 5, 3rd ed., (Butterworth-Heinemann, Oxford, 1980).

[40] L. D. Landau and E. M. Lifshitz, *Fluid Mechanics*, vol. 6, 2nd ed., (Pergamon Press, Oxford, 1993).

[41] H. Bruus. *Acoustofluidics 2: Perturbation theory and ultrasound resonance modes.* Lab Chip **12**, 20–28 (2012).

[42] J. T. Karlsen. *Theory of thermoviscous acoustofluidics in microsystems.* Master's thesis, Technical University of Denmark (2014).

[43] P. B. Muller. *Acoustofluidics in microsystems: investigation of acoustic streaming.* Master's thesis, DTU Nanotech, Department of Micro- and Nanotechnology (2012).

[44] W. Wagner and A. Pruss. *The IAPWS formulation 1995 for the thermodynamic properties of ordinary water substance for general and scientific use.* J Phys Chem Ref Data **31**, 387–535 (2002).

[45] L. H. Olesen. *Computational fluid dynamics in microfluidic systems.* Master's thesis, Technical University of Denmark (2003).

[46] S. C. Brenner and L. R. Scott, *The Mathematical Theory of Finite Element Methods*, (Springer, 2008).

[47] *Comsol Multiphysics Reference Manual version 4.4.*

[48] Comsol Multiphysics Model Library. *Nonlinear Acoustics — Modeling of the 1D Westervelt Equation* (2013).

[49] M. Hoyos and A. Castro. *Controlling the acoustic streaming by pulsed ultrasounds.* Ultrasonics **53**, 70 (2013).